Technische Universität München

How New Particles Change Stars and how Stars Change Particles

Dissertation

by

Stefan Stelzl

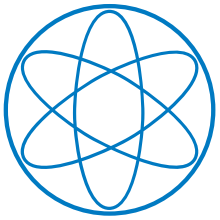

Physik-Department T75, TUM

Technische Universität München

Fakultät für Physik

How New Particles Change Stars and how Stars Change Particles

Stefan Stelzl

Vollständiger Abdruck der von der Fakultät für Physik der Technischen Universität München zur Erlangung des akademischen Grades eines

Doktors der Naturwissenschaften

genehmigten Dissertation.

Vorsitzender:		Prof. Dr. Peter Fierlinger
Prüfer der Dissertation:	1.	Prof. Dr. Andreas Weiler
	2.	Prof. Dr. Björn Garbrecht

Die Dissertation wurde am 26.07.2022 bei der Technischen Universität München eingereicht und durch die Fakultät für Physik am 07.09.2022 angenommen.

How New Particles Change Stars and how Stars Change Particles

Wie neue Teilchen Sterne ändern und wie Sterne Teilchen ändern

Stefan Stelzl

Abstract

The non-observation of colored new states at the LHC puts severe constraints on symmetry based models addressing the naturalness of the Higgs mass. In the first part of this thesis, we explore an exceptional twin Higgs model, that, while not predicting any color-charged particles below a few TeV, has an exciting phenomenology and promising detection prospects at the HL-LHC. In the second part of this thesis we explore the rich phenomenology of the interplay between finite baryon density found in stars and light BSM scalar fields. This interplay leads to many fascinating effects, from changing the QCD axion couplings via false vacuum decay to large changes in the structure of stellar remnants. We use these phenomena to put novel constraints on well-motivated BSM models.

Zusammenfassung

Das Fehlen von Beobachtungen neuer Teilchen mit Farbladung am LHC ist eine starke Einschränkung für symmetriebasierten Modelle, die sich mit der Natürlichkeit der Higgsmasse befassen. Im ersten Teil dieser Arbeit untersuchen wir ein exzeptionelles twin-Higgs Modell, das, ohne farbgeladenen Teilchen unter einigen TeV vorherzusagen, eine aufregende Phänomeno-logie und vielversprechende Detektionsaussichten am HL-LHC hat. Im zweiten Teil dieser Arbeit untersuchen wir die reichhaltige Phänomenologie des Zusammenspiels zwischen endlicher Baryonendichte und leichten BSM-Skalarfeldern. Dieses Wechselspiel führt zu vielen faszinierenden Effekten, von der Änderung der Kopplung des QCD-Axions über Vakuumzerfall bis hin zur Änderung der Struktur von Sternen. Wir nutzen diese Phänomene, um gut motivierte BSM-Modelle zu testen.

Contents

Introduction **7**

I Composite Twin Higgs **11**

1 Motivation and Introduction **13**

2 Composite Higgs and Twin Higgs **15**
2.1 The Hierarchy Problem 15
2.2 Composite Higgs 17
2.2.1 The Composite Higgs Framework 17
2.2.2 Partial Compositeness 19
2.3 Twin Higgs 21
2.3.1 The Twin Higgs construction 21
2.3.2 Composite Twin Higgs based on $SO(8)/SO(7)$ 22

3 Composite Twin Higgs in $SO(7)/G_2$ Coset **25**
3.1 Higgs Sector 25
3.2 Gauge and fermion sectors 26
3.2.1 Fraternal 27
3.2.2 Minimal 29
3.3 Scalar Potentials 31
3.3.1 EWSB and Higgs mass 33
3.3.2 Twin pseudo-NGBs 34
3.4 Phenomenology 35
3.4.1 Indirect Effects 36
3.4.2 Direct Production 37
3.4.3 Fraternal Z' 46
3.5 Conclusions 47

Appendices Part I **49**
I.A $SO(7)$ and G_2 representation 49

II Interplay between Light New Physics and Matter Density **51**

4 Motivation and Introduction **53**

5 The QCD Axion, ALPs and the Relaxion **55**
5.1 The Strong $\mathcal{CP}$ Problem and the QCD Axion . . . 55
5.2 The QCD Axion Couplings in ChPT . . . 56
5.2.1 Axion Couplings in QCD . . . 56
5.2.2 QCD Axion Couplings in ChPT . . . 58
5.2.3 Astrophysical Bounds on the QCD Axion . . . 60
5.3 Light QCD Axions . . . 61
5.4 The Relaxion - A Dynamical Solution to the EW Hierarchy Problem . . . 61

6 The Structure of Stellar Remnants **63**
6.1 White Dwarfs . . . 63
6.2 Neutron Stars . . . 64

7 QCD Axion Couplings to Nucleons at Finite Density **67**
7.1 Heavy Baryon Chiral Perturbation Theory at Finite Density . . . 67
7.1.1 Power Counting in Heavy Baryon Chiral Perturbation Theory . . . 67
7.1.2 Finite Density Propagator and Density Loops . . . 69
7.2 The Axion-Nucleon Coupling at Finite Density . . . 70
7.2.1 $\nu = 2$ Diagrams . . . 71
7.2.2 Dominant $\nu = 3$ Diagrams . . . 73
7.2.3 Results . . . 74
7.3 Implications on Stellar Bounds on Axions . . . 76

8 Phase Transitions from Stars **79**
8.1 Density induced Vacuum Instabilities . . . 79
8.1.1 General Scalar Potential . . . 80
8.1.2 Spherically Symmetric Dense Systems . . . 83
8.1.3 Bubble Formation and Evolution . . . 85
8.1.4 Phenomenological Implications . . . 95
8.2 Bounds on Relaxion Models from Density Induced Phase Transitions . . . 97
8.2.1 The Relaxion Potential . . . 98
8.2.2 The Relaxion at Finite Density . . . 100
8.2.3 Bounds on Relaxions . . . 104
8.3 Discussion and Conclusions . . . 115

9 Structure of Stellar Remnants in the Presence of Light Scalars **117**
9.1 Heavy Neutron Stars from Lights Scalars . . . 117
9.1.1 Free Fermi Gas and a Light Scalar . . . 118
9.1.2 Case Studies . . . 132
9.1.3 Conclusions . . . 146
9.2 White Dwarfs as a Probe of Light QCD Axions . . . 146
9.2.1 New Ground State: The Axion WD System . . . 146
9.2.2 Confrontation with Observational Data . . . 149
9.2.3 Conclusions . . . 150

Appendices Part II **153**
II.A Axion Couplings at Finite Density . . . 153
II.A.1 Construction of the Lagrangian . . . 153
II.A.2 Sample Calculation of V_1 . . . 160

II.A.3 Helpful Integrals . . . 161
II.A.4 The Full Analytic Results at Zero Temperature . . . 163
II.A.5 The Influence of (small) Temperature . . . 164
II.B Density induced Instabilities . . . 164
II.B.1 Linear Profile Approximation . . . 164
II.B.2 Gravitational Force . . . 165
II.B.3 Linear Tension Approximation . . . 166
II.B.4 Ultra-high Densities . . . 167
II.B.5 Sudden Approximation . . . 168
II.B.6 Formation and Escape of $N \gg 1$ Bubbles . . . 169
II.B.7 Opposite-sign Back-reaction . . . 170
II.B.8 Bubble Interactions with the Environment . . . 171
II.C Backreaction of Light Scalars on Stellar Remnants . . . 172
II.C.1 Negligible Gradient Approximation in TOV Equations . . . 172
II.C.2 Temperature Dependence of WD M - R Relation . . . 176

III Conclusions **177**

Bibliography **185**

Introduction

The discovery of the Higgs boson in 2012 [1,2] constitutes a milestone in modern particle physics. The spontaneous symmetry breaking due to the Higgs gives a mass to the electroweak gauge bosons and explains the short range of the interaction. At the same time, the Higgs boson is needed to make the theory of the electroweak interactions unitary at high energies [3]. For the first time since the discovery of the 'particle zoo' in the 1960s, we now have a consistent and complete description of all known forces and particles of nature: the Standard Model of Particle Physics.

However, at the same time, the discovery of the Higgs boson along with the non-discovery of any other new physics at or around the electroweak scale raises as many questions as it answers. The Higgs boson mass is not protected from quantum corrections, and, as such, should be as high as the cutoff of the theory. This is the electroweak Hierarchy Problem. A natural mechanism to protect the Higgs mass parameter without fine tuning like composite Higgs or Supersymmetry so far was not found at the weak scale.

Another problem that is not addressed by the Standard Model is why the strong interactions do not violate charge and parity symmetry. This problem can also be stated in terms of a parameter of the Standard Model: why is $\bar{\theta} \lesssim 10^{-10}$? Within the Standard Model, there is no explanation for the smallness or absence of $\mathcal{CP}$ violation in the strong interactions. A particularly elegant solution to this problem is to promote $\bar{\theta}$ to a dynamical field, the QCD axion. The original proposal by Peccei, Quinn, Weinberg, and Wilczek [4–7] was soon experimentally excluded, however, there is a straightforward way to make the QCD axion extremely weakly coupled, thereby evading the bounds, called the invisible axion.

There are even more hints that tell us that the Standard Model is not a complete theory up to very high energies at which we need a UV completion for gravity. There is the Cosmological Constant, which, similar to the Higgs mass, is not protected from quantum corrections. Even if there is a more complete theory above the weak scale that cuts off all UV contributions to it, this still leaves us with a ridiculous amount of fine tuning. We have observational evidence that there is about five times as much dark matter as there is visible matter in our universe, yet, the Standard Model has no candidate for it. We have measured non-zero neutrino masses, yet, we do not know if they are of Majorana or Dirac type.

All of this tells us that we still have a long way to go. The Standard Model clearly is an effective theory which is valid below some cutoff. However, as we have seen with the QCD axion, there is also plenty of reason to look also for light new physics. In recent years the idea of explaining the smallness of the Higgs mass not via symmetry but with a dynamical mechanism gained a lot of attention [8, 9]. These dynamics typically include light scalar fields.

We have some guidelines to look for new physics, however, it is important to keep an open mind and look at as many places as possible. In this thesis, we pick two different routes: in Part I, we look at a symmetry-based mechanism to stabilise the Higgs mass. Then in Part II, we look at light weakly coupled new scalar fields and how their interaction with matter can be

detected.

We start Part I with a brief introduction to the electroweak Hierarchy Problem. We then see in Sec. 2.2 how this can be alleviated within the framework of composite Higgs (CH). Here the Higgs is a pseudo-Nambu-Goldstone boson (GB) of a broken approximate symmetry $G \to H$. This way, the Higgs possesses an approximate shift symmetry and can naturally be lighter than the cutoff f, at which the Higgs is no longer the right degree of freedom, very similar to pions in QCD. However, as we see, the absence of any resonances at the LHC already puts pressure on the tuning in CH models. This motivates us to look in Sec. 2.3 at the twin Higgs (TH) construction. In this construction, one introduces a Z_2 copy of the Standard Model. The 'twins' of the SM fermions, which cut off the Higgs loops are not charged under color but under twin color, while color-charged resonances can be pushed up to a few TeV. This is one realisation of the so-called neutral-naturalness paradigm, where the new physics responsible for the Higgs naturalness is not charged under the SM gauge group. We briefly review the original construction of composite twin Higgs (CTH) based on the coset $SO(8)/SO(7)$.

In Chapter 3 we then turn to the Coset $SO(7)/G_2$. This exceptional twin Higgs model is the last missing construction with the minimal amount of GBs, where exact twin parity can be enforced along with custodial symmetry. In this model, the photon is its own twin and the twin fermions carry hypercharge. The Higgs is embedded as a spinorial **8** of $SO(7)$.

We identify two different scenarios, the 'fraternal', in which we introduce twin partners for all SM gauge bosons and at least one generation of fermions, and the 'minimal', in which we only introduce the twin top and bottom, while we assume that for example the $SU(2)_{\tilde{L}}$ is broken at a scale much above the confinement scale. The fraternal model, due to the symmetry breaking structure, leads to a Z' boson with large couplings to the SM. The strong collider bounds on this Z' push this scenario into the fine-tuned region and we then focus on the minimal model. In this case, the formerly eaten twin Goldstone bosons are now physical scalar fields that are electrically charged. We calculate the contributions to the scalar potentials and the resulting fine-tuning in both scenarios before we explore the exciting phenomenology of this model.

The phenomenology consists of long lived charged particles, the twin scalars and, if present, the twin tau. With the HL-LHC, the long lived charged particle search could probe the relevant parameter space. The lightest twin quark behaves as a quirk, a heavy stable particle interacting with an unbroken non-abelian gauge group, that, once pair produced, does not hadronize but forms meta-stable strings. The strings quickly de-excite and decay predominantly to twin glueballs, with a non-negligible fraction however decaying to di-photons. The twin glueballs are long lived and lead to displaced vertices to diphotons. We finally discuss the detection prospects of these displaced vertices in the ATLAS as well as in the proposed MATHUSLA detector.

In Part II, we switch topics and focus on the phenomenology of weakly coupled light scalars, especially on their interaction with Standard Model matter density. The collective effects arising from the density background can overcome the small coupling. This can give rise to a plethora of exciting new phenomena that we explore. We are especially interested in a shift symmetry breaking coupling that can be written as a scalar field dependent nucleon mass, or in other words, a coupling of the scalar to the so-called nucleon scalar density. This Lorentz invariant coupling reduces in the non-relativistic limit to a coupling of the scalar field to nucleon number density.

We start in Chapter 5 by introducing the QCD axion as a solution to the strong $\mathcal{CP}$ problem. We also review how to introduce the low energy description of QCD, chiral perturbation theory (ChPT), add the axion to it, and calculate its couplings to nucleons at leading order. We then introduce a paradigmatic model of dynamical solutions to the electroweak Hierarchy Problem, the relaxion. In Chapter 6, we give a very brief introduction to the simplest toy models of stellar

remnants, i.e. a free Fermi gas describing white dwarfs and neutron stars.

In Chapter 7 we calculate the couplings of the QCD axion at finite density and temperature. On the way, we derive the ChPT Lagrangian with the QCD axion to NLO and systematically calculate loop diagrams with a density and temperature dependent propagator. In the limit $T \to 0$, this can be done analytically, while for finite T we have to evaluate the loop integrals numerically. We focus on the density corrections to the KSVZ axion where in vacuum there is an accidental cancellation in the axion-neutron coupling. This cancellation is alleviated at finite density, where the coupling goes towards its natural value. We end this Chapter by discussing the relevance of our findings on astrophysical constraints on the QCD axion.

In Chapter 8 we focus on light scalars with a meta-stable ground state. We investigate how the vacuum can be destabilised by finite density effects. We look at a simple toy model with two minima and investigate the dynamics of the scalar field if the barrier is density dependent. We find conditions of when a dense object leads to a phase transition that penetrates our universe and find stringent cosmological constraints on phase transitions that happen after star formation. We then use our findings to place novel bounds on several benchmark relaxion models. Relaxion models by construction fulfill all the properties needed to be subject to density induced instabilities: The minimum the field ends up in is metastable and due to the sensitivity of the Higgs, the relaxion necessarily couples to a density background. We find the regions of parameter space in which this coupling is large enough to destabilise the relaxion field and use this to exclude previously unconstrained parameter space. We also point out the regions of parameter space where a phase transition is not excluded by cosmological considerations.

In Chapter 9 we investigate models of scalar fields where the potential is such that, while the field gets sourced at finite density, a bubble can never escape from the dense object. We especially focus on the back-reaction of the scalar field on the dense object. One prime example are light QCD axions, where by accident the potential is smaller than for the usual QCD axion, while the couplings to matter are the same. To make the qualitative features of the effect as transparent as possible, we investigate the simple toy model of a neutron star, the free Fermi gas of neutrons. There is a simplifying limit that we use for most of our discussions, namely that gradient energy stored in the field is small compared to other energies.

In this limit, we investigate the equation of state with surprising results: while, as expected, there is a region in parameter space where the field is sourced only at large enough densities leading to hybrid stars, there also exists a region in parameter space where it is energetically favorable for the neutrons to be in a dense state with the scalar field bubble formed compared to infinitely separated neutrons. In these models, this is the absolute ground state of matter. Nuclei are only metastable, and, if we bring many of them close enough, they would undergo a phase transition into this ground state. However, due to gradient effects, as long as the necessary field excursions are much above the QCD scale, this new ground state is not accessible, except in very dense large objects as neutron stars. As we work out, this can have large effects on the structure of neutron stars.

Finally at the end of Chapter 9 we investigate the same effects not in neutron stars, but in white dwarfs. White dwarfs are stellar remnants whose equation of state is reasonably well understood: they consist of electrons that make up the degeneracy pressure and nuclei making up the mass. In the same way as above, light QCD axions can lead to a new ground state accessible within white dwarfs. We study the impact of these on the mass-radius curve of white dwarfs and compare with data of measured white dwarfs. This allows us to put novel bounds on the light QCD axion parameter space.

We then conclude in Part III, where we summarize our main results. We also give a brief outlook on work in progress and future directions.

This thesis is largely based on the following publications

[10] J. Serra, S. Stelzl, R. Torre and A. Weiler, *Hypercharged Naturalness*, JHEP **10**, 060 (2019), [arXiv:1905.02203].

[11] R. Balkin, J. Serra, K. Springmann, S. Stelzl and A. Weiler, *Runaway relaxion from finite density*, JHEP **06**, 023 (2022), [arXiv:2106.11320].

[12] R. Balkin, J. Serra, K. Springmann, S. Stelzl and A. Weiler, *Density Induced Vacuum Instability*, [arXiv:2105.13354].

and work in progress

[13] K. Springmann, M. Stadlbauer, S. Stelzl and A. Weiler, *QCD axion couplings at finite density*, in preparation.

[14] R. Balkin, J. Serra, K. Springmann, S. Stelzl and A. Weiler, *Heavy Neutron Stars from Light Scalars*, in preparation.

[15] R. Balkin, J. Serra, K. Springmann, S. Stelzl and A. Weiler, *White Dwarfs as a Probe of light QCD Axions*, in preparation.

In particular, some figures contained in this thesis have previously appeared or will soon appear in one of these articles.

Part I

Composite Twin Higgs

Chapter 1

Motivation and Introduction

In the absence of any sign of beyond the Standard Model physics at the LHC and the resulting increasing pressure on some proposed solutions to the Higgs Hierarchy Problem, the paradigm of neutral naturalness has emerged. In this paradigm a neutral sector with non-standard low-energy signatures is responsible for the insensitivity of the scalar Higgs field to higher mass scales.

Recent progress in this direction ranges from theories where the gauge quantum numbers of the BSM states that cut off the UV contributions to the Higgs potential are unconventional, the prime realization of this idea being the so-called twin Higgs [16–19], to scenarios in which a non-trivial cosmological history explains the preference for a light Higgs sector [8,20]. The motivation of the former alternative, which we focus on in this part of the thesis, is easy to understand: the dominant exploration of the high-energy territory is due to the LHC, a hadron machine where colored particles can be produced with large cross sections. It has already shown its constraining power on such type of new physics, e.g. colored top partners in composite Higgs models (see e.g. [21–23] for reviews), whose mass should now exceed a TeV [24, 25]. Similar bounds also apply to colored supersymmetric particles. While this could indicate that the characteristic scale of the new dynamics is higher than expected from naturalness considerations, there is also the possibility that nature has chosen a non-standard manifestation of the TeV solutions to the Hierarchy Problem, i.e. one without the presence of light colored states.

Indeed, in composite twin Higgs models, the Higgs arises as a Nambu-Goldstone boson (NGB) from the spontaneous breaking of a global symmetry at a scale $f \approx$ TeV, as in standard theories of composite Higgs, yet, the leading SM loop contributions to the Higgs potential are cut off by uncolored states. These uncolored states are the twins of the SM particles, owing to a Z_2 symmetry that relates them. In particular, as we will see, the large explicit breaking of the Higgs shift-symmetry from the top Yukawa coupling no longer results in a squared Higgs mass proportional to $(y_t/4\pi)^2\, m_*^2$, with $m_* = g_* f$ the typical mass of the colored composite resonances: a color-neutral twin top introduces an additional breaking of the shift-symmetry which due to twin parity results in a $(y_t/g_*)^2$ reduction of this contribution. A twin top mass $m_{\tilde{t}} \simeq m_t/\sqrt{\xi}$ with $\xi = v^2/f^2$ is predicted, while the resonances can be pushed to m_*, beyond LHC reach without affecting the fine-tuning of the EW scale. Consequently, the collider phenomenology of twin Higgs models is substantially different from that of a standard composite-NGB Higgs, see e.g. [26–30].

In this part of the thesis, we present a new realization of the twin Higgs paradigm, in fact the last missing construction with minimal NGB content and a full twin Higgs mechanism, i.e. with a twin parity that could be enforced exactly. The model is based on a global $SO(7)$ symmetry broken to the exceptional group G_2, and its main novel phenomenological characteristic is that

the twin fields carry hypercharge and have the same electric charge as the SM states. This feature gives rise to new and exciting signals at colliders, which include long-lived charged particles, twin quarks behaving as microscopic quirks, that after pair production form bound states that annihilate into SM final states, dileptons and γh, Zh, or twin gluons, and some twin glueballs which, while likely stable on collider scales, eventually decay almost exclusively to diphotons. Although some of these signatures have been already experimentally explored, here they are linked to the naturalness of the EW scale, a strong motivation that deserves further exploration at the LHC, in particular in its high-luminosity phase: since production cross sections are of electromagnetic size, large data samples mean excellent prospects to probe this scenario.

Finally, let us briefly comment on how our exceptional twin Higgs compares with previous models of neutral naturalness. Because the twin quarks are uncolored but carry hypercharge as well as twin color, their phenomenological signatures are similar to those of folded supersymmetry [31] or the quirky little Higgs [32]. However, the scenario we present below is not supersymmetric, and, in contrast to the quirky little Higgs, it enjoys a custodial symmetry. Furthermore, the twin sector is hypercharged but $SU(2)_L$-neutral so its phenomenology is dominated by a coupling to photons and Z's. In particular, the twin top, which is the minimal light degree of freedom for a successful implementation of the twin Higgs mechanism, can be produced at colliders with γ, Z-mediated cross sections that, although small, could be eventually probed by the HL-LHC, for instance in γh, Zh final states.

We start this part of the thesis with an introduction to composite Higgs and composite twin Higgs models in Chapter 2. Using this foundation, in Chapter 3 we explore the novel symmetry breaking pattern of $SO(7)/G_2$: we construct the embedding of the fermions and gauge bosons in this coset in two different scenarios, calculate the scalar potentials and then explore the exciting phenomenology of this symmetry breaking.

Chapter 3 is heavily based on [10], from where all Figures and parts of the text have been taken.

Chapter 2

Composite Higgs and Twin Higgs

This chapter introduces the theoretical framework in which we work in this part of the thesis. After introducing the electroweak (EW) Hierarchy Problem in Section 2.1, we discuss one of its most popular solutions, the composite Higgs framework. Afterwards we discuss the second important ingredient for this part of the thesis, the twin Higgs mechanism. We then review how combining these two ideas gives rise to composite twin Higgs models, which can significantly reduce the fine-tuning compared to ordinary composite Higgs models.

2.1 The Hierarchy Problem

In the discussion of the Hierarchy Problem, we loosely follow the discussion of [23], for a broader view see e.g. recent essays on the topic, [33, 34], as well as the original papers [35–37]. The Standard Model (SM) is an effective field theory that descibes nature extraordinarily well at the scales we can measure it, i.e. up to energy scales of several TeV. However, as gravity becomes strongly coupled around the Planck scale, at energies $E \sim 4\pi M_p$, the SM has to be extended at latest around this scale. This does not mean that there can not be any earlier layers of UV completion, e.g. to include neutrino masses, flavor or electroweak symmetry breaking (EWSB).

Viewing the SM as an effective theory, apart from the gauge group $SU(3) \times SU(2) \times U(1)$, there is not much we can tell about it. It is a series of local, gauge invariant operators of energy dimension d that have coefficients that from dimensional analysis must be proportional to $\propto \Lambda_{SM}^{4-d}$.

Let us start with the dimension $d = 4$ operators: They descibe almost everything we see in nature, the EW interactions, QCD, quarks and lepton masses. Together with the $d = 2$ and $d = 0$ operators that we describe later, they from the renormalizable part of the SM. Most of the success of the SM comes from the 'accidental' symmetries in its renomalizable part. 'Accidental' symmetries are symmetries that have no symmetry principle behind them and only arise at a given order because there exists no operator to this order that breaks them and is compatible with the gauge symmetries. In the renormalizable part of the SM, baryon and lepton family number are exact 'accidental' symmetries.

Let us now look at operators with $d > 4$: The contribution of these operators to low energy observables are suppressed by $\frac{E^{d-4}}{\Lambda_{SM}^{4-d}}$. Lepton number is broken at $d = 5$ by the Weinberg operator [38],

$$\frac{1}{\Lambda_{SM}} \left(\bar{L}_L H^c\right) \left(L_L^c H^c\right), \tag{2.1}$$

where L_L is the lepton doublet, H is the Higgs doublet, and the superscript c denotes the charge conjugate. With an order one coefficient it gives rise to the right ballpark neutrino masses for

$\Lambda_{SM} \sim 10^{14}$GeV. The Weinberg operator is the unique dimension five operator that can be added to the SM. Going to the next dimension, $d = 6$, baryon number is broken. Assuming $O(1)$ coefficients, the absence of proton decay gives us $\Lambda_{SM} \gtrsim 10^{16}$GeV.

From these considerations it is perfectly plausible that the SM is a good theory until very high scales, $\Lambda_{SM} \sim 10^{15}$GeV. There are several limitations in the standard model, e.g. the non-generic flavor structure or the need to incorporate dark matter (DM), however non of these are strong enough to challenge the idea of heavy new physics. The only limitation that is able is the Hierarchy Problem, as we will see now.

So far we have not discussed the operators of $d < 4$. There are two operators in the SM that we have to consider, i.e. the Higgs mass $\propto \Lambda_{SM}^2 H^\dagger H$ and the Cosmological Constant (CC) $\propto \Lambda_{SM}^4$. These operators are not suppressed by the scale of new physics but enhanced by it. We will focus on the Higgs mass here, while we comment on the CC later. We have measured the Higgs mass $m_H = 125$GeV, so the mass parameter $\mu^2 = \frac{m_H^2}{2} = (89\text{GeV})^2$. So the question is, why is there such an enormous hierarchy between the expected and the measured parameter? Why is

$$\frac{\mu^2}{\Lambda_{SM}^2} \sim 10^{-28} \ll 1 \ ? \tag{2.2}$$

This separation of scales is the essence of the Hierarchy Problem. However, we can make the Hierarchy Problem more precise. For this let us compare to Fermi's theory of the weak interaction. There, in the low energy theory, the coupling strength is determined by G_F. We now know the UV completion, i.e. the SM, and we can calculate $G_F = \frac{g_W^2}{4\sqrt{2} m_W^2}$ in terms of the microscopic parameters g_W and m_W.

Now let us look again at the Higgs mass parameter. If we assume that the UV completion is known, then we can calculate the Higgs mass parameter as

$$m_H^2 = \int_0^\infty dE \frac{dm_H^2}{dE}(E; p), \tag{2.3}$$

where p are the input parameters of the full theory. This integral sums up different contributions to the Higgs mass from different energy scales in the true theory. Let us split the contributions to the ones where the SM is a valid theory and the ones above,

$$\begin{aligned} m_H^2 &= \int_0^{\sim\Lambda_{SM}} dE \frac{dm_H^2}{dE}(E; p) + \int_{\sim\Lambda_{SM}}^\infty dE \frac{dm_H^2}{dE}(E; p) && (2.4) \\ &= m_H^2 \delta_{SM} + m_H^2 \delta_{BSM} && (2.5) \end{aligned}$$

The standard model contribution $m_H^2 \delta_{SM}$ is calculable, while the beyond the Standard Model (BSM) contribution is completely unknown. The low energy contribution can be approximated by calculating one loop contributions from the top, the electroweak gauge bosons and the Higgs boson loops as shown in Fig. 2.1 leading to

$$m_H^2 \delta_{SM} = \frac{3y_t^2}{8\pi^2}\Lambda_{SM}^2 - \frac{3g_W^2}{8\pi^2}\left(\frac{1}{4} + \frac{1}{8\cos^2(\theta_W)}\right)\Lambda_{SM}^2 - \frac{3\lambda^2}{8\pi^2}\Lambda_{SM}^2 \tag{2.6}$$

These one loop diagrams are quadratically sensitive to the cutoff of the theory. If we consider the SM alone, this calculation is not very sensible, as the quadratically divergent terms are regulated and renormalized, however as an estimation of the low energy contribution to the full calculation of the Higgs mass parameter it makes perfectly sense. It is here that we can again see the Hierarchy Problem very clearly: The Higgs mass parameter in the full theory has two

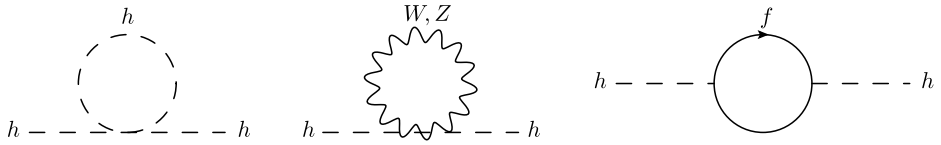

Figure 2.1: Sketch of the fraternal spectrum of the exceptional twin Higgs.

completely separate contributions, one from the low energy theory and one from high energies. As the contribution as low energies is calculable and very large, we know that a cancellation has to take place between the two terms. This cancellation can be described by the tuning

$$\Delta_H = \frac{3y_t^2}{8\pi^2}\left(\frac{\Lambda_{SM}^2}{m_H^2}\right) \tag{2.7}$$

The problem now becomes very clear: Even if we have a theory that formally predicts the Higgs mass, if $\Lambda_{SM} \gg m_H$ we can never really calculate it. Assuming $\Lambda_{SM} \sim 10^{15}$GeV, in calculating the Higgs mass, there would be a cancellation in 24 digits, so we would need calculate both contributions to this accuracy. We will never achieve such an accuracy, neither in the experimental determination of the parameters nor in the theoretical calculation of the loop contributions.

Depending on the value of Δ_H, the Higgs mass can be easier or harder to predict in the full theory, making the Hierarchy Problem less or more severe. It is the experimental high energy frontier that tells us what to expect for Δ_H, either by pushing Λ_{SM} to higher and higher values or by discovering new physics that addresses the Hierarchy Problem.

2.2 Composite Higgs

The idea behind the CH framework is dates back to the '80s [39–44] and is very simple: Instead of being an elementary point-like particle as in the SM, in CH models the Higgs particle is a bound state originating from a new strongly interacting sector. As a bound state, the Higgs particle a finite size l_H. In the same way that charged pions or the proton are transparent to photons with energy much above their inverse size, the Higgs mass now does not get loop contributions from energies above l_H^{-1}. In analogy to the QCD scale, the scale l_H^{-1} is naturally generated due to dimensional transmutation. For introductions and recent reviews see e.g. [21–23, 45]. This section loosely follows [23].

2.2.1 The Composite Higgs Framework

In order for the size of the Higgs to naturally be around the electroweak scale, we introduce a new 'composite sector'. The dynamics of this composite sector take place in the non-perturbative regime and dynamically generates a scale $m_* \sim l_H^{-1}$. This sector originates at $\Lambda_{\text{UV}} \gg \Lambda_{EW}$. As the whole point of this strong sector is to make the Higgs mass insensitive to the UV, the value of Λ_{UV} does not matter. At Λ_{UV}, the theory is close to a renormalization group (RG) fixed point and due to the logarithmic running of the coupling, exponentially large separation of scales can easily be achieved, depending on how close to the fixed point one starts in the UV.

The other ingredient to produce realistic models is an 'elementary sector'. All SM particles except for the Higgs are part of this elementary sector. This includes the weakly coupled EW

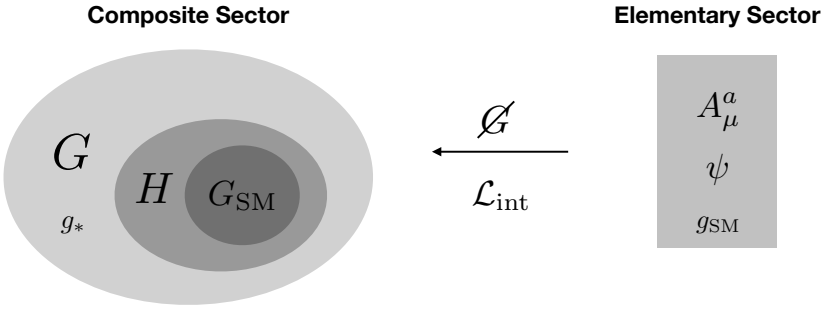

Figure 2.2: Sketch of the CH setup: A composite sector with global symmetry G which breaks to H at the scale f, where the standard model gauge group is part of the unbroken subgroup H as well as an elementary sector with the SM gauge bosons and fermions. The gauge and fermion interaction between the two sectors break the global symmetry G explicitly and lead to a potential for the Goldstone boson (GB), as we see below.

gauge fields, the leptons and quarks. Obviously the most important terms in the Lagrangian are $d = 4$ terms, the kinetic terms of the fermions, the gauge bosons, and the interaction between the 'elementary' and 'composite' sectors. The strong sector is assumed to be invariant under a global symmetry group G with the electroweak $SU(2)_L \times U(1)_Y$ as a subgroup.[1] The weak gauging of this subgroup corresponds to coupling the electroweak gauge bosons W^a and B to the corresponding currents of the strong sector. A sketch of the general setup is shown in Fig. 2.2 This is in strong analogy to the $SU(N_f)_L \times SU(N_f)_R$ global symmetry of QCD with the photon as an external gauge boson of the diagonal $U(1)_{EM}$. There is however the difference that for simplicity we assume that G is an exact symmetry of the strong sector, while in QCD the global symmetry is explicitly broken by the quark masses. As only part of the global symmetry group is gauged be the external fields, the gauging however breaks the global symmetry explicitly. This explicit breaking is communicated to the strong sector through the interactions.

In analogy with QCD, at the confinement scale m_*, the strong sector spontaneously breaks the global symmetry group G to an unbroken subgroup H. This leads to GB living in the coset G/H, similar to the pions in QCD. While in early attempts of CH models the Higgs was a generic resonance around the scale m_* [35, 36], this is phenomenologically excluded as experimental bounds push m_* well above the TeV scale. A natural CH has to be a GB and as such can have masses well below m_*, again, in analogy to the pions in QCD with $m_\pi \ll$ GeV. The explicit breaking of G due to the elementary sector leads to a potential for the GB Higgs, which in turn leads to EWSB.

To be more concrete, let us look at a strong sector that breaks $G \to H$ at the scale m_*, giving rise to GB living in the coset G/H. Let us assume that the electroweak $SU(2) \times U(1)$ is part of the unbroken H, while to coset G/H is large enough to accommodate at least for the Higgs doublet. We denote the generators of G by T^A, the unbroken generators that span H by T^a and the broken ones in the coset G/H by $T^{\hat{a}}$. We also define a vacuum orientation $\boldsymbol{F}$ which is a reference vacuum of all the degenerate vacua. The reference vacuum is chosen such that it

[1] In order for the oblique corrections not to be large, we actually assume that the custodial $SO(4)$ is a subgroup of G.

is annihilated by the unbroken generators, i.e.

$$T^a \boldsymbol{F} = 0 \qquad \text{and} \qquad T^{\hat{a}} \boldsymbol{F} \neq 0. \tag{2.8}$$

The GBs correspond to fluctuations along the broken directions and can be parametrized as

$$\phi(x) = \exp[i\theta(x)^{\hat{a}} T^{\hat{a}}] \boldsymbol{F}. \tag{2.9}$$

The four real degrees of freedom of the Higgs are part of the $\theta^{\hat{a}}$. The vacuum expectation value (VEV) of one of its components should break the electroweak group to the electromagnetic subgroup as in the SM. As long as we do not take the G breaking effects into account, there is no potential for the Higgs, as the $\theta^{\hat{a}}$ are exact GBs. In this case the VEVs of $\theta^{\hat{a}}$ are completely arbitrary but unphysical as they can be rotated away by an H transformation. However, including G breaking effects of the gauge bosons (and fermions as we see below), a potential for the GB is generated. Geometrically, θ is the vacuum misalignment angle between the reference vacuum $\boldsymbol{F}$, which we chose perpendicular to H and the true vacuum. This means that all EWSB effects are determined by θ, more precisely

$$v = f \sin\theta \qquad \text{with} \qquad f = |\boldsymbol{F}|. \tag{2.10}$$

A priori we would expect $\theta \sim 1$ and thus $v \sim f$. We want however a separation of scales, $\theta \ll 1$ in order to have the Higgs far below the cutoff. This is usually written in terms of

$$\xi = \frac{v^2}{f^2} = \sin^2\theta \ll 1, \tag{2.11}$$

where ξ is an adjustable parameter that determines most of the phenomenology of the CH models. In the limit $\xi \to 0$, the strong sector decouples and the Higgs looks elementary. In order for CH models to be phenomenologically viable one usually assumes some accidental cancellation in the contributions to the Higgs potential that lead to $\xi \lesssim 0.1$, so a small amount of fine tuning.

There exists a general framework to construct the full theory below the symmetry breaking scale, the Callan-Coleman-Wess-Zumino (CCWZ) construction [46, 47]. This formalism allows one to construct the full low energy effective theory characterized by a symmetry breaking pattern $G \to H$, including the explicit breaking effects. It is completely based on symmetries and describes the GBs as well as their interactions. We do not review it here but refer the reader e.g. to [23] or the original papers.

2.2.2 Partial Compositeness

So far we only talked on how to couple the gauge fields to the strong sector. In this subsection we describe how the elementary fermions can be coupled to the strong sector and thus at low energies to the Higgs. The naive way to couple fermions to an operator of the strong sector is with a bilinear coupling, e.g. for the top quark

$$\mathcal{L}_{\text{naive}} = \frac{\lambda_t}{\Lambda_{\text{UV}}^{d-1}} \bar{q}_L O_s t_r, \tag{2.12}$$

where d is the scaling dimension of O_s. Running this down to the scale m_*, the quark Yukawa's can be estimated as

$$y_t \sim \lambda_t[m_*] \sim \lambda_t \left(\frac{m_*}{\Lambda_{\text{UV}}}\right)^{d-1}. \tag{2.13}$$

For $d > 1$, and $\lambda_t < 16\pi$, it is thus hard to have a large hierarchy between $\Lambda_{\rm UV}$ and m_* and at the same time having a large top quark Yukawa. As discussed in more detail in [23], taking $d = 1+\epsilon$ can lead to reintroducing the Hierarchy Problem again, while for $d > 2$, where the Hierarchy Problem is absent, the bilinear coupling of fermions to the composite sector generically leads to a very low $\Lambda_{\rm UV}$ and thus phenomenologically unacceptably large flavor violations. An elegant way out is partial compositeness of fermions, first discussed in [48]: The fermions are coupled linearly to an operator of the composite sector, i.e.

$$\mathcal{L}_{\rm pc} = \frac{\lambda_l}{\Lambda_{\rm UV}^{d_l-5/2}}\bar{q}_l O_l + \frac{\lambda_r}{\Lambda_{\rm UV}^{d_r-5/2}}\bar{t}_r O_r. \tag{2.14}$$

The main differences to above are that now the couplings are linear in the elementary fermions, and that the composite operators now are fermionic (in contrast to bosonic above). Running this down to the scale m_*, we find

$$\lambda_i[m_*] = \lambda_i \left(\frac{m_*}{\Lambda_{\rm UV}}\right)^{d_i-5/2}. \tag{2.15}$$

In contrast to before, here there is nothing that prevents us from taking d close to $5/2$, as it does not introduce a fine tuning problem. This means that we can generate a large hierarchy between $\Lambda_{\rm UV}$ and m_* while having large couplings. At the scale m_*, the strong sector confines and gives rise, apart from the GBs, to resonances with masses of the order of m_*. To each local operator of the strong sector, there corresponds at least one such resonance that it can excite. This means that there exist resonances Q, T, with

$$\langle 0|O_l|Q\rangle \neq 0 \qquad \langle 0|O_r|T\rangle \neq 0. \tag{2.16}$$

The T and Q are called 'partners' and are charged under QCD, as they mix with q_l and t_r. This means that the strong sector needs to be endowed with additional global $SU(3)$. At the same time, due to the linear coupling, these partners need to have the same electroweak quantum numbers as the quarks. The partners get a mass $\sim m_*$ as the strong sector confines, and as they are charged, they have to be vector-like fermions with a Dirac mass term. Around the confinement scale, the mass terms of the different fields can be estimated as

$$\mathcal{L} = -m_*\bar{T}T - m_*\bar{Q}Q - \lambda_l[m_*]\frac{m_*}{g_*}\left(\bar{q}_l Q + \text{h.c.}\right) - \lambda_r[m_*]\frac{m_*}{g_*}\left(\bar{t_r}T + \text{h.c.}\right), \tag{2.17}$$

where the precise form, i.e. the factors of $\frac{m_*}{g_*}$ come from the assumption of having one scale and one coupling, for more details see [23]. We can now diagonalize the mass matrix to find two massless states, identified with the standard model quarks, which are now partially composite, and two heavy resonances with Dirac mass. The light physical states are

$$|\text{physical}_i\rangle = \cos\theta_i\ |\text{elementary}_i\rangle + \sin\theta_i\ |\text{composite}_i\rangle, \tag{2.18}$$

with $\sin\theta_i = \frac{\lambda_i}{\sqrt{g_*^2+\lambda_i^2}}$. This puts us now in the position to estimate the Yukawa couplings of the quarks: part of the physical quarks are composite and this composite states couple to the Higgs with a coupling constant g_*, giving

$$y_t = \sin\theta_l \sin\theta_r g_* \sim \frac{\lambda_r\lambda_l}{g_*}, \tag{2.19}$$

where in the last line we assumed $\lambda_i \ll g_*$.

In order to proceed, we have to specify more details of the operators O_l and O_r. In particular, we need to know the transformation properties under the global group G. A priori any representation can be picked and it is a model-building exercise to chose. However, as the operators run down from the UV scale, only the ones with lowest scaling dimension survive at low energies, giving rise to a single representation. One can then investigate these case by case starting from the smallest representations. Generically, the Yukawa coupling of the Higgs to the fermions changes compared to the standard model value, $y_i^{\text{CH}} = y_i^{\text{SM}}(1 + O(\xi))$, however, by an amount that is $\xi = \frac{v^2}{f^2}$ suppressed. Note that in order to give the partners the right EW quantum numbers, one has to introduce an additional global $U(1)_X$ under which the strong sector is invariant.

2.3 Twin Higgs

Following Eq. (2.7), allowing some tuning, new states that cut off the top loop have to appear around $\Lambda^2 \sim \frac{8\pi}{3y_t^2}\Delta_H m_H^2$. However this does not tell us anything about the nature of these states. In CH models, these are the fermionic top partners, while in supersymmetric models they are bosonic. In both cases they are charged under $SU(3)$ und thus easily produced at hadron colliders.

However there exists the interesting alternative that the states responsible to cut off the top loop are not charged under the SM. A prime example of these neutral naturalness models are twin Higgs models [16–19], where the states that cut off the top loop are not charged under the SM gauge group, but under a Z_2 symmetric copy of it, its twin gauge group. As such, the twin particles are poorly produced at (hadron) colliders. The theory still contains states that are charged under the SM, but these can be boosted in mass by a factor of $\frac{g_*}{g_{\text{SM}}}$, where g_* describes the coupling strength of the new dynamics and g_{SM} is a SM coupling. Then the first charged states appear at a mass

$$m_* \sim \frac{4\pi}{3y_t^2}\frac{g_*^2}{g_{SM}^2}\Delta m_H^2. \tag{2.20}$$

In the light of the Hierarchy Problem, it is very motivated to make the twin Higgs a composite model, s.t. we can push g_* to high values. Then the first colored states can be pushed out of the reach of LHC already with mild tuning.

2.3.1 The Twin Higgs construction

In this subsection we outline some essential aspects of the TH idea, hereby following closely [49]. For now let us take the SM and its exact duplicate, the $\widetilde{\text{SM}}$ that are related by a Z_2 symmetry. While in practice this Z_2 has to be broken in order to get a viable phenomenology and cosmology, for the sake of the discussion of naturalness and electroweak symmetry breaking we can assume that it is exact. The most general Lagrangian invariant under the above symmetries is

$$\mathcal{L} = m_{\mathcal{H}}^2\left(H^\dagger H + \tilde{H}^\dagger\tilde{H}\right) + \frac{\lambda_{\mathcal{H}}}{4}\left(H^\dagger H + \tilde{H}^\dagger\tilde{H}\right)^2 + \frac{\hat{\lambda}_h}{8}\left(\left(H^\dagger H\right)^2 + \left(\tilde{H}^\dagger\tilde{H}\right)^2\right). \tag{2.21}$$

Similar to the SM it has an accidental custodial symmetry, $SO(4)\times\widetilde{SO}(4)$. In the limit $\hat{\lambda}_h \to 0$, the Z_2 enhances the custodial symmetry to $SO(8)$. In this limit if the twin Higgs would get a VEV $\langle\tilde{H}\rangle = \frac{f}{\sqrt{2}}$, then the Higgs would be completely massless. Note however in order to have a tunable Higgs VEV, a small amount of Z_2 breaking is necessary. Of course the standard model gauge couplings as well as the Yukawa's break the $SO(8)$ symmetry explicitly. However, we can

consider the scenario where the $SO(8)$ preserving dynamics is stronger than the small $SO(8)$ breaking effects. In this case, $\hat{\lambda}_h$ can be treated as a small perturbation. To zeroth order, i.e. neglecting the breaking effects, we can expand around $\langle \tilde{H} \rangle = \frac{\sqrt{2} m_{\mathcal{H}}}{\sqrt{\lambda_{\mathcal{H}}}} \equiv \frac{f}{\sqrt{2}}$ and $\langle H \rangle = 0$. We find a radial mode σ with mass $m_\sigma = \sqrt{2} m_{\mathcal{H}}$, the three GB of the twin Higgs get eaten by the twin electroweak gauge group, giving the twin gauge bosons a mass of $m_{\tilde{W}} \sim gf$, while the twin electromagnetic $U(1)$ is unbroken and the Higgs is massless. At leading order in $\hat{\lambda}_h$, the Higgs gets a potential and we find for the Higgs quartic and the mass term

$$\lambda_h \sim \hat{\lambda}_h \qquad \text{and} \qquad \delta m_H^2 \sim \frac{\lambda_h}{2\lambda_{\mathcal{H}}} m_{\mathcal{H}}^2. \tag{2.22}$$

In terms of the physical masses, one finds exactly the same relation, $\delta m_h^2 = \frac{\lambda_h}{2\lambda_{\mathcal{H}}} m_\sigma^2$ and for the tuning we find $\epsilon = \frac{m_h^2}{\delta m_h^2} = 2\frac{v^2}{f^2} = 2\xi$.

It is clear that the crucial parameter is $\lambda_h/\lambda_{\mathcal{H}}$: The sensitivity of the physical Higgs mass to the mass of the radial mode is determined by it. The other important model-building question is how the mass of the radial mode depends on the scale of new SM charged physics, m_*. In the simple models that we consider, where the twin Higgs comes from a composite sector with just one coupling and one scale, we have $m_\sigma \sim m_*$ and $\lambda_{\mathcal{H}} \sim g_*^2$. For more involved models that can push the scale m_* above the mass of the radial mode, see e.g. [49]. This gives us, together with the fact that in TH models the RG-induced quartic from top-loops $\Delta\lambda_h \sim \frac{3y_t^2}{\pi^2} \ln(m_*/m_t)$ more than saturates the experimental value, an estimate of

$$\delta m_h^2 = \frac{3y_t^2}{2\pi^2 g_*^2} m_*^2 \ln(m_*/m_t). \tag{2.23}$$

Apart from the logarithm, this nicely confirms the naive expectation in Eq. (2.20).

2.3.2 Composite Twin Higgs based on $SO(8)/SO(7)$

The CTH based on the symmetry breaking structure $SO(8)/SO(7)$ was investigated in [50–52]. For later reference we summarize here some of the main ingredients following mainly [52].

The strong sector is assumed to be endowed with a global $SO(8) \times U(1)_X \times \widetilde{U}(1)_{\tilde{X}} \times Z_2$ symmetry. As usual in composite Higgs models, a $U(1)_X$ is needed for the right hypercharge assignments of the fermions, while for the twin fermions we introduce its twin. The Higgs and its twin are included as a fundamental of $SO(8)$, such that after the symmetry breaking we have 7 GBs. Some of the block-diagonal $SO(4) \times \widetilde{SO}(4)$ generators are gauged, in particular the EW gauge group is included in the custodial $SO(4)$, while the gauged twin $\widetilde{SU}(2)_L$ is part of the $\widetilde{SO}(4)$. Six of the GB get eaten by the electroweak gauge group and its twin, while only the physical Higgs survives. The SM gauge group being part of the custodial $SO(4)$ ensures that the oblique corrections to the T parameter are small.

The fermions are coupled via partial compositeness. A suitable choice is to couple the q_L and t_R to an **8** and a singlet of $SO(8)$ respectively. The twins couple the same way, i.e. the $\tilde{q}_L$ couples to an **8** while the $\tilde{t}_R$ couples to a singlet. As we want the twins to be color neutral, we also introduce twin color, $\widetilde{SU}(3)$, under which the strong sector is invariant. The q_L and $\tilde{q}_L$ are embedded as incomplete **8**-plets,

$$\begin{aligned} Q_L &= \frac{1}{\sqrt{2}} \begin{pmatrix} ib_L & b_L & it_L & -t_L & 0 & 0 & 0 & 0 \end{pmatrix}^T, \\ \widetilde{Q}_L &= \frac{1}{\sqrt{2}} \begin{pmatrix} 0 & 0 & 0 & 0 & i\tilde{b}_L & \tilde{b}_L & i\tilde{t}_L & -\tilde{t}_L \end{pmatrix}^T, \end{aligned} \tag{2.24}$$

and their coupling to the composite sector explicitly breaks the $SO(8)$, similar to the gauging. Both of these give rise to a potential for the GB Higgs, which we now discuss. Let us look at the interaction of the gauge fields with currents of the strong sector

$$\mathcal{L} = g_2 W_\mu J_L^\mu + \tilde{g}_2 \tilde{W}_\mu \tilde{J}_L^\mu. \tag{2.25}$$

We promote the fields to spurions by writing the interaction in a formally $SO(8)$ invariant way and then follow [53] to classify the independent invariants that we can write down. Constructing the only possible combination at $O(g^2)$ and plugging back in the spurions, we find

$$V_g = C_g \left[\frac{3}{4} g_2^2 \sin^2(H/f) + \frac{3}{4} \tilde{g}_2^2 \cos^2(H/f) \right], \tag{2.26}$$

where the coefficient C_g can either be estimated by naive dimensional analysis (NDA) or computed in an explicit model, like the two-site model in [52]. Here we can see the TH mechanism at work: In the case of exact twin parity, $g_2 = \tilde{g_2}$, the potential is independent of the Higgs. Twin parity in this model however is not exact, e.g. we did not gauge twin Hypercharge. This leads to a potential

$$V_g = C_g \left[\frac{3}{4} g_1^2 \sin^2(H/f) \right]. \tag{2.27}$$

Let us now look at the potential induced by the fermionic sector, as it is the most important one for the tuning: At $O(y_L^2)$, there is again only one independent invariant,[2] leading to

$$V_y = C_y y_L^2 \sin^2(H/f) + \tilde{C}_y \tilde{y}_L^2 \cos^2(H/f), \tag{2.28}$$

where with exact twin parity we can relate $C_y = \tilde{C}_y$, again leading to a cancellation in the potential. At $O(y_L^4)$, there arises a contribution that does not vanish even for exact twin parity: Again, the symmetries determine the form of the potential to look as

$$V_y = \left(C_1 y_L^4 + \tilde{C}_1 \tilde{y}_L^4 \right) \left[\sin^4(H/f) + \cos^4(H/f) \right] + \left(C_2 y_L^4 - \tilde{C}_2 \tilde{y}_L^4 \right) \left[\sin^2(H/f) - \cos^2(H/f) \right]. \tag{2.29}$$

This completes the ultra-violet (UV) contributions to the Higgs potential, however, there is one additional contribution coming from the running of the Higgs quartic down from the scale m_*. It is log enhanced and given by

$$V_y^{\mathrm{IR}} = \frac{3}{16\pi^2} \left[m_t(H)^4 \log\left(\frac{m_*^2}{m_t(H)^2} \right) + m_{\tilde{t}}(H)^4 \log\left(\frac{m_*^2}{m_{\tilde{t}}(H)^2} \right) \right] \tag{2.30}$$

with the top and twin top masses

$$m_t(H)^2 = \frac{y_t^2}{2} f^2 \sin^2(H/f) \qquad \text{and} \qquad m_{\tilde{t}}(H)^2 = \frac{y_{\tilde{t}}^2}{2} f^2 \cos^2(H/f). \tag{2.31}$$

With these contributions to the Higgs potential, a realistic EWSB is possible with moderate tuning that is consistent with current bounds. Most importantly, the presence of particles charged under the strong interactions is pushed to high masses above a few TeV, thereby eliminating the possibility of directly producing the top partners of standard CH models at the LHC. At the same time, the possibility of directly producing the twin particles opens up, which can add to the Higgs to invisible decay rate. On the other hand, similar to ordinary CH models, the couplings of the Higgs are modified in CTH models and precision tests of the Higgs couplings can constrain them.

[2] As the t_R is included as a singlet in an $SO(8)$ invariant way, there is no contribution from y_T.

Chapter 3

Composite Twin Higgs in $SO(7)/G_2$ Coset

In this chapter we present an exceptional twin Higgs model with the minimal symmetry structure for an exact implementation of twin parity along with custodial symmetry, which is based on the coset $SO(7)/G_2$. Twin particles here are mirrors of the Standard Model yet they carry hypercharge, while the photon is identified with its own twin. After presenting the particle spectrum of the theory, we estimate the different contributions to the scalar potential and the corresponding tuning that is necessary in the Higgs sector. We then explore the phenomenological signatures of hypercharged naturalness: long-lived charged particles, a colorless twin top with electric charge 2/3 that after being pair-produced, bounds via the twin of the strong interactions and can annihilate to dileptons or a Higgs plus a photon or a Z, and glueballs produced from Higgs decays and twin-quarkonium annihilation that either decay displaced, or are stable on collider scales and eventually decay to diphotons. We also discuss the future prospects for detection of these signatures.

The results of this chapter discussed below are published before in [10], where all figures and large parts of the text are taken.

3.1 Higgs Sector

The composite twin Higgs mechanism relies on the Higgs arising as a NGB from the spontaneous breaking of a global symmetry. We assume that such a breaking is driven by a strongly interacting sector that confines at a scale m_* close to the TeV. The characteristic mass and coupling of the composite resonances is set by m_* and g_* respectively, related by the symmetry-breaking order parameter, f, as $m_* = g_* f$.

The novel features of the scenario under investigation comes from a different global symmetry breaking pattern, $SO(7) \to G_2$, with respect to previous twin Higgs models. This breaking has the peculiarity of being the smallest that gives rise to seven NGBs while leaving an unbroken custodial symmetry, $SU(2)_L \times SU(2)_R \subset G_2$.[1] The twin Higgs mechanism can still work in this minimal coset, with the complex Higgs doublet H and its twin $\widetilde{H}$ embedded in the spinorial **8** representation of $SO(7)$. Interestingly, $SO(7)$ has rank three and contains as a subgroup the product $SU(2)_L \times SU(2)_{\widetilde{L}} \times SU(2)_{\widehat{R}}$, where the unbroken $SU(2)_R$ is the diagonal combination of the $SU(2)_{\widetilde{L}}$ and $SU(2)_{\widehat{R}}$. As it will become clear in the following, the discrete Z_2 symmetry, the

[1] The other relevant 7-spheres are $SO(8)/SO(7)$, $SU(4)/SU(3)$ and $SO(5)/SO(3)$, where only the first respects custodial symmetry. The coset $SO(7)/G_2$ has also been explored in [54, 55] in the context of ordinary composite-Higgs models.

twin parity, in this coset requires the SM particles and their twins to share the same quantum numbers under $SU(2)_{\widehat{R}}$, which in turn implies they have identical electric charges, with the SM photon being its own twin.

We parametrize the $SO(7)/G_2$ coset with the Σ vector

$$\Sigma = U(\pi)\Sigma_0 = \begin{pmatrix}\pi_1 & \pi_2 & \pi_3 & \pi_4 & \pi_5 & \pi_6 & \pi_7 & \sigma\end{pmatrix}^T\,,\quad \sigma = \sqrt{1-\pi_{\hat{a}}^2}\,, \tag{3.1}$$

associated with the vacuum expectation value of a spinor of $SO(7)$, that is $\Sigma_0 \sim \mathbf{8}$.[2] Given the decomposition $\mathbf{8} = (\mathbf{2},\mathbf{1},\mathbf{2}) + (\mathbf{1},\mathbf{2},\mathbf{2})$ under $SU(2)_L \times SU(2)_{\widetilde{L}} \times SU(2)_{\widehat{R}}$, the Higgs and its twin can be identified as

$$(\mathbf{2},\mathbf{1},\mathbf{2}):\ H = \frac{f}{\sqrt{2}}\begin{pmatrix}\pi_2 + i\pi_1 \\ h - i\pi_3\end{pmatrix}\,,\quad (\mathbf{1},\mathbf{2},\mathbf{2}):\ \widetilde{H} = \frac{f}{\sqrt{2}}\begin{pmatrix}\pi_6 + i\pi_5 \\ \sigma - i\pi_7\end{pmatrix}\,, \tag{3.2}$$

where $h \equiv \pi_4$. It then follows that under the custodial $SU(2)_L \times SU(2)_R$ symmetry, the Higgs has the proper quantum numbers, i.e. $H \sim (\mathbf{2},\mathbf{2})$, while the twin Higgs decomposes as $\widetilde{H} \sim (\mathbf{1},\mathbf{1}) \oplus (\mathbf{1},\mathbf{3})$, which correspond to the singlet radial component, σ, and a triplet of $SU(2)_R$. The kinetic terms take the same form as in other spherical cosets,

$$\frac{f^2}{2}|\partial_\mu \Sigma|^2 = \frac{f^2}{2}(\partial_\mu \pi_{\hat{a}})^2 + \frac{f^2}{2}\frac{(\pi_{\hat{a}}\partial_\mu \pi_{\hat{a}})^2}{1-\pi_{\hat{b}}^2}\,. \tag{3.3}$$

Twin parity in the strong sector is realized as a discrete $SO(7)$ transformation of the form

$$\mathcal{P} = \begin{pmatrix} & \mathbb{1}_4 \\ \mathbb{1}_4 & \end{pmatrix}\,, \tag{3.4}$$

whose action on Σ has the form $H \leftrightarrow \widetilde{H}$. This parity also interchanges the $SU(2)_L$ and $SU(2)_{\widetilde{L}}$, while acting trivially on $SU(2)_{\widehat{R}}$. This explains why the twin NGBs, $\tilde{\omega}^\pm \equiv f(\pi_6 \pm i\pi_5)/\sqrt{2}$ and $\tilde{\omega}_0 \equiv f\pi_7$ have the same electric charge as those NGBs that are eventually eaten by the $W^\pm$ and the Z.

Let us finally recall that as we have seen above, in composite twin Higgs models the strong sector is also symmetric under $SU(3)_C \times SU(3)_{\widetilde{C}} \times Z_2$ transformations, with the Z_2 exchanging $C \leftrightarrow \widetilde{C}$. Moreover to reproduce the hypercharges of the SM fermions an extra $U(1)_X$ abelian symmetry is introduced, along with its counterpart $U(1)_{\widetilde{X}}$ and with twin parity enforcing $X \leftrightarrow \widetilde{X}$.[3]

3.2 Gauge and fermion sectors

To specify the couplings of the external elementary (i.e. weakly coupled in comparison to g_*) SM gauge and fermion fields and their twins to the strong sector, we need to identify the operator content of the strong sector. Besides the scalar operator responsible for the spontaneous breaking of $SO(7)$ to G_2, there is a vector current associated to each global symmetry of the strong

[2] $SO(7)$ matrices in the spinor representation can be found in App. I.A. As usual the Goldstone matrix is given by $U(\hat{\pi}) = \exp(i\sqrt{8/3}\,\hat{\pi}_{\hat{a}}T^{\hat{a}})$, and we redefined $\pi_{\hat{a}} = \hat{\pi}_{\hat{a}}\sin\widehat{\Pi}$, with $\widehat{\Pi} = \sqrt{\hat{\pi}_{\hat{a}}\hat{\pi}^{\hat{a}}}$, while $\Sigma_0 = (0\ 0\ 0\ 0\ 0\ 0\ 0\ 1)^T$ to arrive at Eq. (3.1).

[3] There is the more minimal alternative consisting in a single $U(1)_X$ shared by the SM and their twins, with the Z_2 acting trivially on it. We however opt for the introduction of $U(1)_{\widetilde{X}}$ in order to distinguish the composite operators that couple to the SM (right-handed) leptons from their twins, see below.

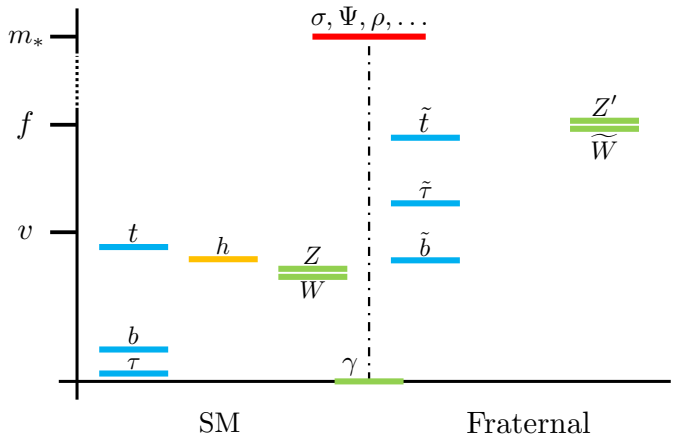

Figure 3.1: Sketch of the fraternal spectrum of the exceptional twin Higgs.

dynamics: $\mathcal{J}^A \sim \mathbf{21}$ of $SO(7)$, which under G_2 decomposes in unbroken $\mathcal{J}^a \sim \mathbf{14}$ and broken $\mathcal{J}^{\hat{a}} \sim \mathbf{7}$ components, $\mathcal{J}_\mu^{X,\widetilde{X}}$, and the color and twin color currents $\mathcal{J}_\mu^{C,\widetilde{C}}$. As seen above, this weak gauging of the global symmetries then gives rise to the coupling of the elementary gauge fields with the corresponding composite currents, i.e. $g_i A_\mu^i \mathcal{J}^{\mu i}$. Besides, as we have seen above, in order to implement partial compositeness [48], we assume the strong sector contains fermionic operators Ψ in non-trivial representations of $SO(7) \times SU(3)_C \times SU(3)_{\widetilde{C}} \times U(1)_X \times U(1)_{\widetilde{X}}$. The interaction of the elementary fermion fields ψ with the strong dynamics proceeds via linear mixing of the form $y\bar{\psi}\Psi$ (see Sec. 2.2.2). The actual set of fermionic operators depends on which twin fermions are present at energies around m_*, that in turn depends on which of the global symmetries are gauged. We discuss the most interesting possibilities in the following.

3.2.1 Fraternal

A full analogue of the standard twin Higgs models discussed above, which are based on a global $SO(8)$ symmetry and where twin partners are introduced for all the SM gauge bosons and for at least one complete generation of SM fermions [27], can also be constructed upon the symmetry group $SO(7)$. However, because of the smaller rank of $SO(7)$ compared to $SO(8)$, the gauge content of the twin sector is necessarily reduced. In particular, elementary massless vectors gauge $SU(2)_L \times SU(2)_{\widetilde{L}} \times U(1)_{\widehat{Y}}$, with

$$\widehat{Y} = T^3_{\widehat{R}} + X + \widetilde{X}\,, \tag{3.5}$$

where $T^3_{\widehat{R}}$ is the diagonal generator $U(1)_{\widehat{R}} \subset SU(2)_{\widehat{R}}$.[4]

Since $\langle \widetilde{H} \rangle \sim f$ spontaneously breaks $SU(2)_{\widetilde{L}} \times U(1)_{\widehat{R}}$ to $U(1)_R \subset SU(2)_R$, the three gauge bosons associated to the broken directions become massive, while the unbroken hypercharge group is identified with the diagonal combination of $U(1)_{\widetilde{L}} \times U(1)_{\widehat{Y}}$, where $U(1)_{\widetilde{L}} \subset SU(2)_{\widetilde{L}}$, given by

$$Y = T^3_R + X + \widetilde{X}\,, \quad T^3_R = T^3_{\widetilde{L}} + T^3_{\widehat{R}}\,. \tag{3.6}$$

Only after the Higgs field develops a VEV, $\langle H \rangle \sim v$, the $SU(2)_L \times U(1)_Y$ EW symmetry gets broken to $U(1)_Q$ and the W and Z also become massive. From this symmetry breaking pattern

[4] Giving up on exact twin parity a different global symmetries could be also be gauged, e.g. $\widehat{Y} = T^3_{\widehat{R}} + X$, in which case the twins would have different hypercharges than the ones considered in this work.

it follows that electric charge is given by

$$Q = T_L^3 + Y = T_L^3 + T_{\widetilde{L}}^3 + T_{\widehat{R}}^3 + X + \widetilde{X}\,, \tag{3.7}$$

thus twin parity implies that the SM particles and their twins have the same electric charge.

The masses of the gauge bosons follow from Eq. (3.3) by introducing covariant derivatives $\partial_\mu \to D_\mu = \partial_\mu - i g_i A_\mu^i T^i$, with $g_i A_\mu^i T^i = g W_\mu^\alpha T_L^\alpha + \tilde{g}\widetilde{W}_\mu^\alpha T_{\widetilde{L}}^\alpha + \hat{g}\widehat{B}_\mu \widehat{Y}$. In the unitary gauge,

$$\begin{aligned}\frac{f^2}{2}|D_\mu \Sigma|^2 = \frac{f^2}{2}\frac{(\partial_\mu h)^2}{1-h^2} + \frac{g^2 f^2}{4} h^2 \left[W_\mu^+ W^{\mu -} + \left(\frac{\hat{g}}{g}\widehat{B}_\mu - W_\mu^3 \right)^2 \right] \\ + \frac{\tilde{g}^2 f^2}{4}(1-h^2)\left[\widetilde{W}_\mu^+ \widetilde{W}^{\mu -} + \left(\frac{\hat{g}}{\tilde{g}}\widehat{B}_\mu - \widetilde{W}_\mu^3 \right)^2 \right],\end{aligned} \tag{3.8}$$

where $h = (v + \hat{h})/f$, with $v \approx 246\text{GeV}$ and $\hat{h}$ the Higgs boson. This equation clearly shows the upshot of twin parity, which exchanges $SU(2)_L$ and $SU(2)_{\widetilde{L}}$ and $h \leftrightarrow \sigma = \sqrt{1-h^2}$. As a result, we can consistently impose a discrete Z_2 symmetry acting on the elementary gauge fields as $W_\mu^\alpha \leftrightarrow \widetilde{W}_\mu^\alpha$ and trivially on $\widehat{B}_\mu$, which enforces $g = \tilde{g}$ while leaving $\hat{g}$ free. This constitutes a novel implementation of the twin Higgs mechanism in the gauge sector, leading to important phenomenological departures from the SM, but no massless twin photon. To see this right away, let us work in the limit $\xi \equiv v^2/f^2 \to 0$, that is neglecting EW symmetry-breaking effects. The SM hypercharge gauge field is given by $B = c_{\tilde{\theta}}\widehat{B} + s_{\tilde{\theta}}\widetilde{W}^3$ with $\tan\tilde{\theta} = s_{\tilde{\theta}}/c_{\tilde{\theta}} = \hat{g}/\tilde{g}$ and gauge coupling $g' = \tilde{g} s_{\tilde{\theta}}$. The orthogonal combination, $Z' = c_{\tilde{\theta}}\widetilde{W}^3 - s_{\tilde{\theta}}\widehat{B}$, gets a mass term

$$m_{Z'} = \sqrt{\tilde{g}^2 + \hat{g}^2}\frac{f}{2} = \frac{\tilde{g}}{c_{\tilde{\theta}}}\frac{f}{2} \tag{3.9}$$

and, by virtue of the mixing $s_{\tilde{\theta}}$ with $\widehat{B}$, it couples to the SM fermions, which carry non-zero $\widehat{B}$-charges (the same as their twins), given by $\widehat{Y} = Y - T_{\widetilde{L}}^3 = Q - (T_L^3 + T_{\widetilde{L}}^3)$, see Table 3.1. As we will show in Section 3.4.3, such a Z' contributes to the EW precision tests (specifically to the Y-parameter) but, most importantly, can be produced at the LHC with significant cross sections.[5] The only other extra gauge boson, the $\widetilde{W}^\pm$, gets a mass $m_{\widetilde{W}} = \tilde{g} f\sqrt{1-\xi}/2$ and it has electric charge ± 1, being the twin of the SM $W^\pm$. The contribution of the twin gauge bosons to the Higgs potential will be discussed in Section 3.3.

Regarding the elementary fermions, anomaly cancellation requires a twin partner for every SM fermion of at least one complete generation: in practice this means we include the third generation, since the twin top is the crucial player leading to a successful cancellation of the Higgs potential induced by the top loop. The EW gauge quantum numbers of the twin particles are dictated by twin parity and are given in Table 3.1. Of particular importance for the phenomenology of this scenario is the fact that the twin fermions have the same electric charge as their SM partners.

Besides, as in previous twin Higgs models, the twin quarks are not colored but instead carry twin color, i.e. they are fundamentals **3** of $SU(3)_{\widetilde{C}}$, which is gauged by the twin gluons. Twin parity exchanges them with the SM gluons, from where it follows $g_3 = \tilde{g}_3$, up to terms that explicit break the twin parity.

The SM fermions and their twins get mass via their interactions with the strong sector, that we assume to be of partial compositeness type, at least for the top sector. The top quark fields t_R,

[5] Including EWSB terms does not change this conclusion, because the associated corrections to the mass and couplings of the Z' are suppressed by $\xi \lesssim 0.1$.

	$SU(2)_L$	$SU(2)_{\widetilde{L}}$	$U(1)_{\widehat{Y}}$	$U(1)_Y$
H	**2**	**1**	1/2	1/2
$\widetilde{H}$	**1**	**2**	1/2	±1 , 0
W	**3**	**1**	0	0
$\widetilde{W}$	**1**	**3**	0	±1 , 0
$\widehat{B}$	**1**	**1**	0	0
q_L	**2**	**1**	1/6	1/6
t_R	**1**	**1**	2/3	2/3
b_R	**1**	**1**	−1/3	−1/3
$\tilde{q}_L$	**1**	**2**	1/6	$\frac{2}{3}$, $-\frac{1}{3}$
$\tilde{t}_R$	**1**	**1**	2/3	2/3
$\tilde{b}_R$	**1**	**1**	−1/3	−1/3
ℓ_L	**2**	**1**	−1/2	−1/2
τ_R	**1**	**1**	−1	−1
$\tilde{\ell}_L$	**1**	**2**	−1/2	0 , −1
$\tilde{\tau}_R$	**1**	**1**	−1	−1

Table 3.1: EW gauge quantum numbers of the SM fields and their twins. In the minimal scenario, with no twins for the SM W and Z, only $SU(2)_L \times U(1)_Y$ are gauged and the twin low-energy content reduces to $\tilde{t}_{L,R}$ and $\tilde{\omega}^{\pm,0} \subset \widetilde{H}$.

q_L and their twins $\tilde{t}_R$, $\tilde{q}_L$ then linearly couple, with strengths $y_{L,R}$ and $\tilde{y}_{L,R}$, to the corresponding composite operators. For a proper implementation of the twin Higgs mechanism, the latter should transform under $SO(7) \times SU(3)_C \times SU(3)_{\widetilde{C}} \times U(1)_X \times U(1)_{\widetilde{X}}$ as $\Psi_t \sim (\mathbf{1},\mathbf{3},\mathbf{1})_{(\frac{2}{3},0)}$, $\Psi_q \sim (\mathbf{8},\mathbf{3},\mathbf{1})_{(\frac{2}{3},0)}$ and $\widetilde{\Psi}_t \sim (\mathbf{1},\mathbf{1},\mathbf{3})_{(0,\frac{2}{3})}$, $\widetilde{\Psi}_q \sim (\mathbf{8},\mathbf{1},\mathbf{3})_{(0,\frac{2}{3})}$. We recall that the spinorial representation of $SO(7)$ decomposes as $\mathbf{8} = \mathbf{1} + \mathbf{7}$ under G_2.

At low energies the interactions of q_L and $\tilde{q}_L$ can be simply obtained via the embeddings

$$\begin{aligned} Q_L &= v_b b_L + v_t t_L = \frac{1}{\sqrt{2}} \begin{pmatrix} ib_L & b_L & it_L & -t_L & 0 & 0 & 0 & 0 \end{pmatrix}^T , \\ \widetilde{Q}_L &= \tilde{v}_b \tilde{b}_L + \tilde{v}_t \tilde{t}_L = \frac{1}{\sqrt{2}} \begin{pmatrix} 0 & 0 & 0 & 0 & i\tilde{b}_L & \tilde{b}_L & i\tilde{t}_L & -\tilde{t}_L \end{pmatrix}^T , \end{aligned} \tag{3.10}$$

while those of t_R and $\tilde{t}_R$ are trivial, being $SO(7)$ singlets. For instance, the top Yukawa couplings, generated at the scale m_* with $y_t \sim y_L y_R / g_*$ and likewise for $\tilde{y}_t$, are given by

$$y_t f \bar{t}_R \Sigma^\dagger Q_L + \tilde{y}_t f \bar{\tilde{t}}_R \Sigma^\dagger \widetilde{Q}_L + \text{h.c.} = -y_t \bar{t}_R H q_L - \tilde{y}_t \bar{\tilde{t}}_R \widetilde{H} \tilde{q}_L + \text{h.c.} , \tag{3.11}$$

from where we find for the twin-top mass $m_{\tilde{t}} = \tilde{y}_t f \sqrt{1-\xi}/\sqrt{2}$. It is evident that a Z_2 symmetry acting on the elementary fields as $q_L, t_R \leftrightarrow \tilde{q}_L, \tilde{t}_R$ leads to $y_t = \tilde{y}_t$. The rest of SM fermions and their twin partners get masses in a similar manner, with twin parity enforcing the equality of their Yukawa couplings and thus $m_\psi = m_{\tilde{\psi}} \sqrt{\xi/(1-\xi)}$. However, since as long as $\tilde{y}_\psi \ll y_t$ the associated contribution to the Higgs potential will be negligible (see Section 3.3), the approximate equality $y_\psi = \tilde{y}_\psi$ need not be enforced for all of them.

3.2.2 Minimal

The construction presented in the previous section demonstrates that it is feasible to build a twin Higgs model based on $SO(7)$ as global symmetry where twin parity is exact. However, as

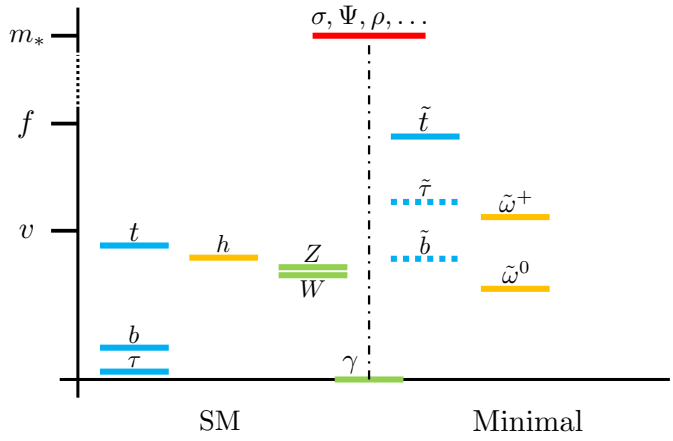

Figure 3.2: Sketch of the minimal spectrum of the exceptional twin Higgs.

we will see below, the experimental constraints on the twin Z' are quite severe, disfavouring a twin-symmetric model in view of fine-tuning considerations. Besides, it is well known that the twin parity cannot be an exact symmetry at m_* if the Higgs VEV is to be misaligned from the Z_2-symmetric vacuum $\langle H\rangle^2 + \langle \tilde{H}\rangle^2 = f^2$. We therefore consider in this section a realization that is more minimal in terms of the (elementary) twin particle content.

We assume that the gauged $SU(2)_{\tilde{L}}$ symmetry has been spontaneously broken at a scale $\Lambda_{\not{Z}_2}$ significantly above the strong sector confinement scale, such that at m_* only $SU(2)_L \times U(1)_Y$ is gauged, in a similar fashion as the recent twin Higgs constructions of [56, 57]. This has several important consequences: the formerly eaten twin NGBs $\tilde{\omega}^{\pm,0}$ are now physical and become massive (much in the same way as the QCD pions because of EWSB), and the twin fermion content can be reduced to the absolute essential, that is a (vector-like) twin top.

The kinetic terms for the twin Goldstones, along with derivative Higgs and self-interactions, follow from the kinetic term Eq. (3.3),

$$\frac{f^2}{2}|D_\mu \Sigma|^2 = |D_\mu H|^2 + |D_\mu \tilde{\omega}^+|^2 + \frac{1}{2}(\partial_\mu \tilde{\omega}^0)^2 + \frac{\left(2\partial_\mu |H|^2 + 2\partial_\mu |\tilde{\omega}^+|^2 + \partial_\mu (\tilde{\omega}^0)^2\right)^2}{f^2 - 2|H|^2 - 2|\tilde{\omega}^+|^2 - (\tilde{\omega}^0)^2}\,, \tag{3.12}$$

where $D_\mu \tilde{\omega}^+ = \partial_\mu \tilde{\omega}^+ - i g' B_\mu \tilde{\omega}^+$. Note that $\tilde{\omega}^+$ has electric charge $+1$, while $\tilde{\omega}^0$ is neutral. It is clear that in this scenario there can be no twin cancellation of the gauge radiative correction to the Higgs potential. However this can be kept small, i.e. without compromise for fine-tuning, as long as EW composite resonances are sufficiently light (see Section 3.3).

The top and its twin couple to the strong sector as in Eq. (3.10), but we can consider the twin bottom as no longer present in the low-energy spectrum but decoupled above m_*,[6] or that, even if it is light, its couplings differ from those of $\tilde{t}$. As a result the Yukawa couplings are now given by

$$-\, y_t \bar{t}_R H q_L - \frac{\tilde{y}_t}{\sqrt{2}} \bar{\tilde{t}}_R \left(i\tilde{\omega}^0 + \sqrt{f^2 - 2|H|^2 - 2|\tilde{\omega}^+|^2 - (\tilde{\omega}^0)^2} \right) \tilde{t}_L + \text{h.c.}\,. \tag{3.13}$$

Given the explicit breaking of the twin parity from the absence of the twin $\widetilde{W}$'s and the twin bottom, it is no longer the case that $y_{L,R} = \tilde{y}_{L,R}$ (thus neither that $y_t = \tilde{y}_t$) at m_*. As we will

[6] Note that below $\Lambda_{\not{Z}_2}$, where the only gauged symmetries are the SM ones and twin color, the twin bottom as well as the twin top have vector-like charges.

show in Section 3.3, this indicates there is an upper bound on the scales (like Λ_{Z_2}) where the sources of Z_2 breaking originate, such that the twin cancellation of the top radiative correction to the Higgs potential is still effective.

3.3 Scalar Potentials

In this section we discuss the radiative generation of the Higgs potential and examine the conditions as well as the amount of fine-tuning needed to achieve EWSB. We also compute the potential of the additional pseudo-NGBs in the case that the twin symmetries are not gauged.

Fraternal: Let us discuss first the gauge contributions to the Higgs potential in the fraternal model, where the $SU(2)_L \times SU(2)_{\widetilde{L}} \times U(1)_{\widehat{R}}$ symmetries are gauged. The leading order (LO) terms in the gauge couplings arise at $O(g_i^2)$ from 1-loop diagrams with either the W's, the twin $\widetilde{W}$'s or the $\widehat{B}$,

$$V_{g^2}^{\rm UV} = C_g \sum_i g_i^2 \, \Sigma^\dagger T^i T^i \Sigma = c_g \frac{3 m_\rho^2}{32\pi^2} \frac{3}{2} \left(g^2 |H|^2 + \tilde{g}^2 |\widetilde{H}|^2 \right) , \tag{3.14}$$

where we estimated the coefficient C_g based on naive dimensional analysis (NDA), with an $O(1)$ uncertainty encoded in the parameter c_g. This radiative correction is quadratically sensitive to the compositeness scale, which we parametrized by $m_\rho \sim g_\rho f/2 \lesssim m_*$. In the twin-symmetric limit $g = \tilde{g}$, Eq. (3.14) does not depend on the Higgs, which is the essence of the twin Higgs mechanism. Note also that in our realization the twin cancellation of the $O(\hat{g}^2)$ correction is automatic, since $\widehat{B}$ is its own twin or, in other words, H and $\widetilde{H}$ have identical $U(1)_{\widehat{R}}$ charges. In consequence, also the usual hypercharge contribution to the Higgs potential is absent.

In contrast with most composite-NGB-Higgs models, (3.14) is in fact the most relevant correction to the Higgs potential in our fraternal $SO(7)$ twin Higgs model. This is because of the experimental constraints on the Z', the mass eigenstate of the $\widetilde{W}^3$-$\widehat{B}$ system up to $O(\xi)$ terms, see Section 3.4.3 for the details. Since the couplings of the Z' to SM fields scale with $s_{\tilde{\theta}} = g'/\tilde{g}$ and its mass Eq. (3.9) is well approximated by $\tilde{g} f/2$, the bounds can only be satisfied either if the twin gauge coupling $\tilde{g}$ is substantially above g, thus breaking twin parity and spoiling the cancellation of Eq. (3.14), or if f is pushed to several TeVs. As we show in Section 3.4.3, both cases imply a significant fine-tuning of the Higgs potential.

Minimal: In view of these considerations, we now turn to the scalar potential in the minimal model, where only $SU(2)_L \times U(1)_Y$ are gauged. The LO gauge contribution formally reads as the l.h.s. of Eq. (3.14), but now evaluates to

$$V_{g^2}^{\rm UV} = c_g \frac{3 m_\rho^2}{64\pi^2} \left[(3g^2 + g'^2) |H|^2 + 2 g'^2 |\tilde{\omega}^+|^2 \right] , \tag{3.15}$$

where the last term is from a B loop, since the twin $\tilde{\omega}^\pm$ carries hypercharge. The contribution to the Higgs potential is similar to the LO gauge correction in standard composite-NGB-Higgs models, where in fact it is usually considered subleading and relatively unimportant compared to the corrections arising from the top (at least in partial compositeness). In contrast, Eq. (3.15) is certainly important in the present twin Higgs model, since it can introduce the required amount of Z_2-breaking to accomplish $v/f \ll 1$, as explained below. EW gauge corrections at $O(g_i^4)$ are generically subleading and we neglect them in the following.

The other important contributions to the scalar potential arise from the explicit $SO(7)$ symmetry-breaking terms sourced by the top and its twin, two different types of which are relevant: those generated at m_*, which we denote as UV (as Eq. (3.15) for gauge fields), and those generated from IR loops, independent of the details of the strong dynamics. Let us discuss them in turn.

The LO corrections from 1-loop UV diagrams with q_L and $\tilde{t}_L$ arise at $O(y_L^2)$ and $O(\tilde{y}_L^2)$ and are given by [7]

$$V_{y^2}^{\rm UV} = C_y y_L^2 \sum_{\psi=t,b} \Sigma^\dagger v_\psi v_\psi^\dagger \Sigma + \widetilde{C}_y \tilde{y}_L^2 \Sigma^\dagger \tilde{v}_t \tilde{v}_t^\dagger \Sigma = c_y \frac{6 m_\Psi^2}{32\pi^2} \left[(y_L^2 - \tilde{y}_L^2)|H|^2 - \tilde{y}_L^2 |\tilde{\omega}^+|^2 \right] , \qquad (3.16)$$

where we used NDA to estimate the size of $C_y = \widetilde{C}_y$, with the equality between the coefficients following from twin parity in the strong sector. Note that while the overall sign of this contribution (i.e. the sign of $c_y = O(1)$) cannot be predicted without explicit information on the strong dynamics, a prediction is obtained instead for the relative sign of the mass terms of the Higgs and of the charged scalar. The latter arises because no $\tilde{b}_L$ loop has been included, since e.g. it acquired a vector-like mass (i.e. independent of f) $\widetilde{m}_b > m_*$ [58] or because its couplings to the strong sector depart from those of $\tilde{t}_L$, these two states are no longer related by a gauged $SU(2)_{\widetilde{L}}$ symmetry. In other words, if at m_* a twin bottom were present (i.e. in the fraternal model or if $\widetilde{m}_b \ll m_*$) and its coupling to the strong sector were still fixed by $\tilde{y}_L$, then the $|\tilde{\omega}^+|^2$ term would be absent. In contrast, a potential for the neutral scalar $\tilde{\omega}^0$ is automatically absent because neither y_L nor $\tilde{y}_L$ break the corresponding $U(1)_{\widetilde{L}-\widehat{R}}$ shift symmetry. Finally, an exact twin parity would enforce $\Delta y_L^2 \equiv y_L^2 - \tilde{y}_L^2 = 0$, thus exactly cancelling the $|H|^2$ term. This cancellation is the *raison d'être* of twin Higgs models, and in the present realization does indeed take place at LO in the elementary (weak) couplings. However, since the Z_2 symmetry is not exact, Δy_L^2 will generically be non-vanishing at the relevant scale, m_*, due to renormalization group evolution (RGE) from the Z_2-breaking couplings, i.e. at NLO. In our case these are the EW gauge couplings g, g', which contribute as

$$(\Delta y_L^2)_g = y_L^2 \frac{3Ag^2 + A'g'^2}{16\pi^2} \log \frac{\Lambda_{\not{Z}_2}}{m_*} . \qquad (3.17)$$

The coefficients A and A' parametrize our ignorance on the strong dynamics at scales above m_* and are a priori $O(1)$ in size. Another potential source of Z_2 breaking in the top sector at one loop depends on the vector-like mass of the twin b. If $\widetilde{m}_b \gg m_*$, then loops of $q_L = (t_L\ b_L)$ cannot be matched by those of $\tilde{t}_L$, inducing $(\Delta y_L^2)_b \sim (y_L^4/16\pi^2) \log \widetilde{m}_b/m_*$. We note that this correction is model dependent and, in particular, there is no experimental reason to completely decouple the twin bottom. Besides, if twin colored fermions are decoupled, a differential running of the $SU(3)_C$ and $SU(3)_{\widetilde{C}}$ gauge couplings is induced, which eventually adds to Δy_L^2 (formally a 2-loop effect, i.e. NNLO, but could easily be numerically important).

Other potentially relevant UV radiative corrections to the potential arise from 1-loop diagrams with 4 insertions of either y_L or $\tilde{y}_L$,

$$\begin{aligned} V_{y^4}^{\rm UV} &= D_y y_L^4 \Big(\sum_{\psi=t,b} \Sigma^\dagger v_\psi v_\psi^\dagger \Sigma \Big)^2 + \widetilde{D}_y \tilde{y}_L^4 \left(\Sigma^\dagger v_{\tilde{t}} v_{\tilde{t}}^\dagger \Sigma \right)^2 \\ &= d_y \frac{6}{32\pi^2} \left[y_L^4 |H|^4 + \tilde{y}_L^4 \left(f^2/2 - |H|^2 - |\tilde{\omega}^+|^2 \right)^2 \right] , \end{aligned} \qquad (3.18)$$

[7] There are no equivalent contributions at this order from t_R or $\tilde{t}_R$ since neither y_R nor $\tilde{y}_R$ break any shift symmetries, being both fields embedded in a singlet of $SO(7)$.

where $D_y = \widetilde{D}_y$ from twin parity. Even if Z_2 symmetric, (3.18) contains both a Higgs mass and quartic terms. The latter could be particularly important in order to reproduce the physical Higgs mass, depending on the size of the IR contributions to the Higgs potential, which we discuss in the following.

Below m_*, loops of the top and its twin give further corrections to the scalar potential via the Yukawa couplings in (3.13). The leading logarithmic (LL) term reads as in standard twin Higgs models,

$$V_{\rm LL}^{\rm IR} = \frac{3}{16\pi^2}\left[y_t^4|H|^4\log_t + \tilde{y}_t^4\left(f^2/2 - |H|^2 - |\tilde{\omega}^+|^2\right)^2\log_{\tilde{t}}\right], \tag{3.19}$$

where $\log_t \equiv \log(m_*^2/m_t^2)$ and likewise for $\log_{\tilde{t}}$. This contribution to the Higgs potential is generically identified as the leading one in twin Higgs models, being logarithmically enhanced in comparison to UV terms such as (3.18). In our scenario the same would be true for the charged twin potential if it was not for Eq. (3.18), which is quadratically sensitive to m_* (there identified with m_Ψ).

Finally, we should note that NLL corrections to Eq. (3.19) from RGE due to the top/twin-top Yukawas and color/twin-color interactions have been shown in [49, 56, 59] to be numerically important, in particular for extracting the physical Higgs mass. We expect a similar analysis could be performed in our scenario, leading to similar results, at least qualitatively if not quantitatively. In this work we simply bear in mind such corrections when presenting our $O(1)$ estimates in the next section.

3.3.1 EWSB and Higgs mass

The set of contributions to the Higgs potential presented above can be simply parametrized as (focusing only on the relevant component h) [52],

$$V(h)/f^4 = \alpha h^2 + \beta\left(h^4\log\frac{a}{h^2} + (1-h^2)^2\log\frac{a}{1-h^2}\right), \tag{3.20}$$

where

$$\beta = \frac{3y_t^4}{64\pi^2}, \quad \log a = \log\frac{2m_*^2}{y_t^2 f^2} + d_y\frac{y_L^4}{y_t^4} \tag{3.21}$$

and we have taken $\tilde{y}_t = y_t$ and $y_L = \tilde{y}_L$ in (3.19) and (3.18) respectively, which is a good approximation at the order we are working. The Z_2-breaking term α depends on whether the model is fraternal or minimal,

$$\text{Fraternal:} \quad \alpha = c_g\frac{9g_\rho^2(g^2-\tilde{g}^2)}{512\pi^2} + c_y\frac{3g_\Psi^2\Delta y_L^2}{32\pi^2}, \tag{3.22}$$

$$\text{Minimal:} \quad \alpha = c_g\frac{3g_\rho^2(3g^2+g'^2)}{512\pi^2} + c_y A\frac{3g_\Psi^2 y_L^2}{32\pi^2}\frac{3g^2+g'^2}{16\pi^2}\log\frac{\Lambda_{\not Z_2}}{m_*}, \tag{3.23}$$

where we have taken $m_\rho = g_\rho f/2$ and $m_\Psi = g_\Psi f$ in (3.14, 3.15) and (3.16), respectively, and assumed $A = A'$ in Eq. (3.17).

The first point to note is that in our scenario the Higgs quartic is approximately the same as in standard twin Higgs models. In particular the IR contribution to the physical Higgs mass provides a significant fraction of the observed value,

$$\frac{(\delta m_h^2)^{\rm IR}}{m_h^2} = \frac{3y_t^4v^2}{8\pi^2}\log\frac{m_*^4}{m_t^2 m_{\tilde{t}}^2} \approx 0.9, \tag{3.24}$$

where we have evaluated the top Yukawa at high scales, $y_t(1\,\text{TeV}) \approx 0.85$, in order to roughly include NLL effects, and taken $m_* = 5\,\text{TeV}$ and $m_{\tilde{t}}^2 \simeq m_t^2/\xi$ with $\xi = v^2/f^2 = 0.1$. It is then clear that UV corrections, proportional to d_y in (3.21), can easily and naturally provide the missing fraction of m_h.

Therefore, to a good approximation the degree of fine-tuning required in our construction is determined by how unlikely it is to achieve a realistic EWSB, something that is directly controlled by the size of the h^2 terms in Eq. (3.20). As in most twin Higgs models, there is a minimum amount of tuning (Δ) as a direct consequence of twin parity: the Z_2-symmetric term in Eq. (3.20) leads to $\Delta_{\text{min}} = 2\xi$, while ξ is bounded from above from direct and indirect measurements of the Higgs couplings. Another way to see this is that twin parity implies that the minimum of the potential is at $\langle h^2 \rangle = \xi = 1/2$, thus some other finely-tuned Z_2-breaking contribution is needed to misalign the vacuum at $\xi \ll 1$. This is in fact the reason why sources of explicit Z_2-breaking are needed in twin Higgs models, whose leading effect in the Higgs potential we have encoded in the term proportional to α ($\alpha > 0$ in order to accomplish such a misalignment). Note that in the case that α is controlled by a single Z_2-breaking source of the right size to reproduce a given value of ξ, then the associated tuning is simply given by Δ_{min}. However, in more complicated situations with several Z_2-breaking sources, it is possible that a tuning between them is needed to achieve a given ξ, thus increasing the overall tuning. A better measure of fine-tuning, applicable to either case, is $\Delta_i = m_h^2/4\alpha_i f^2$.

Fraternal: The fraternal scenario illustrates both of these possibilities. The twin gauge coupling $\tilde{g}$ could be larger than g such that, provided $c_g < 0$, the first term in (3.22) can be tuned to the Z_2-symmetric piece ($2\beta \log a$), how much tuned determined by Δ_{min}; the hierarchy between f and v is however no longer determined by the bounds on the Higgs couplings, but by the bounds on the Z' mass (Section 3.4.3), leading to $\Delta_{\text{min}} \lesssim 1\%$ for $g_\rho \gtrsim 4$ (thus $m_\rho \gtrsim 6\,\text{TeV}$). Otherwise, f can be kept relatively low consistently with the Z' bounds if there is another source of Z_2-breaking, e.g. the second term in (3.22), and $\tilde{g}$ is sufficiently large. In such a case the tuning is no longer tied to v/f, but instead is well approximated by $m_h^2/4\alpha f^2$, clearly worse than Δ_{min} for fixed m_ρ.

Minimal: The situation in the minimal model is certainly better, since

$$\Delta_g = \frac{32\pi^2}{3c_g(3g^2+g'^2)}\frac{m_h^2}{m_\rho^2} \approx 15\%\frac{1}{c_g}\left(\frac{3\,\text{TeV}}{m_\rho}\right)^2 , \tag{3.25}$$

$$\Delta_y = \frac{128\pi^4}{3c_y A(3g^2+g'^2)y_L^2 \log_{\not{Z}_2}}\frac{m_h^2}{m_\Psi^2} \approx 30\%\frac{1}{c_y A}\frac{1}{y_L^2}\frac{10}{\log_{\not{Z}_2}}\left(\frac{4\,\text{TeV}}{m_\Psi}\right)^2 , \tag{3.26}$$

that is, none of the Z_2-breaking terms in (3.23) leads to a fine-tuning significantly worse than $\Delta_{\text{min}} = 20\%$ for reasonable parameters: relatively heavy vector and fermionic resonances and a large separation between the Z_2-breaking UV scale and m_*, $\log_{\not{Z}_2} \equiv \log(\Lambda_{\not{Z}_2}/m_*)$ with e.g. $\Lambda_{\not{Z}_2}/m_* = 2.5 \times 10^4$.

3.3.2 Twin pseudo-NGBs

Let us focus first on the mass of the charged twin scalar present in the minimal model. This arises from both gauge and top/twin-top radiative corrections, Eq. (3.15) and Eqs. (3.16, 3.18, 3.19) respectively. The largest of these is the UV $O(\tilde{y}_L^2)$ contribution in (3.16), which is quadratically sensitive to the cutoff, there parametrized by m_Ψ. As long as the coefficient c_y is negative,[8] then

[8] A coefficient $c_y < 0$ implies that the contribution from Eq. (3.16) to α in the Higgs potential is also negative, assuming the perturbative result that the parameter A in the RGE of Δy_L^2, Eq. (3.17), is positive. Even if this it

the mass-squared is positive and of size

$$m^2_{\tilde{\omega}^+} \sim \frac{3m^2_\Psi \tilde{y}^2_L}{16\pi^2} \approx (550\text{GeV})^2 \left(\frac{\tilde{y}_L}{1}\right)^2 \left(\frac{m_\Psi}{4\,\text{TeV}}\right)^2 . \tag{3.27}$$

The other corrections give rise to smaller contributions: the gauge contribution is suppressed by $O(g'^2/y^2_L)$ and yields $\Delta m^2_{\tilde{\omega}^+} \sim (100\text{GeV})^2(m_\rho/3\,\text{TeV})^2$, while the IR twin-top contribution (which is negative) is suppressed by $O(m^2_t/m^2_\Psi)$. After EWSB there also small corrections from the quartic coupling $|H|^2|\tilde{\omega}^+|^2$, suppressed by ξ. Other contributions to the $\tilde{\omega}^+$ mass could also be present, e.g. from loops of twin taus, if these are in the IR spectrum.

The attentive reader will have already noticed that none of the radiative corrections discussed above gave rise to a potential for the neutral twin scalar. This was to be expected, since neither gauging only $U(1)_Y$ nor considering a left-handed twin bottom with couplings different than those of the twin top (or just a decoupled $\tilde{b}$), breaks the $U(1)_{\widetilde{L}-\widehat{R}}$ shift symmetry protecting the $\tilde{\omega}^0$. However, an exact global $U(1)$ is not at all guaranteed, on the contrary quite generically a source of explicit symmetry breaking will be present, lifting the $\tilde{\omega}^0$. In fact, it is easy to imagine examples for such a source. One instance, perhaps not the best but certainly simple, is to consider a f-independent mass for the twin top $\widetilde{m}_t \bar{\tilde{t}}_R \tilde{t}_L$, generated below $\Lambda_{\not{Z}_2}$ where no gauge symmetry forbids it, but naturally small $\widetilde{m}_t \ll m_*$ since still protected by a chiral symmetry [58]. Such a mass in fact breaks explicitly $U(1)_{\widetilde{L}-\widehat{R}}$, and gives rise to an extra radiative correction to the scalar potential

$$\begin{aligned} V^{\text{UV}}_{\widetilde{m}} &= \widetilde{C}_{\widetilde{m}} \tilde{y}_L \tilde{y}_R \Sigma^\dagger \tilde{v}_t \widetilde{m}_t + \text{h.c.} \\ &= c_{\widetilde{m}} \frac{3m^2_*}{16\pi^2} \frac{y_t \widetilde{m}_t \sqrt{2}}{f} \left[\sin\gamma\, \tilde{\omega}^0 - \cos\gamma \sqrt{f^2 - 2|H|^2 - 2|\tilde{\omega}^+|^2 - (\tilde{\omega}^0)^2}\right] , \end{aligned} \tag{3.28}$$

where we used NDA to estimate the size of $C_{\widetilde{m}}$, $\tilde{y}_t \sim \tilde{y}_L \tilde{y}_R/g_* \simeq y_t$, and included a possible phase difference γ between $\tilde{y}_t$ and $\widetilde{m}_t$. Besides the tadpole term (which vanishes for $\sin\gamma = 0$), (3.29) contains a $\tilde{\omega}^0$ mass of size (taking $\cos\gamma = 1$ and $c_{\widetilde{m}} > 0$)

$$m^2_{\tilde{\omega}^0} \sim (85\text{GeV})^2 \left(\frac{\widetilde{m}_t}{10\text{GeV}}\right) \left(\frac{750\text{GeV}}{f}\right) \left(\frac{m_*}{5\,\text{TeV}}\right)^2 . \tag{3.29}$$

The f-independent mass for the twin top is just one example of how the singlet twin could be lifted. Yet one should be aware that regardless of how $\tilde{\omega}^0$ gets a potential, it should be such that the Higgs potential is not significantly altered, not to raise the fine-tuning of the EW scale. In our example this would happen if $\widetilde{m}_t \gtrsim 100\text{GeV}$, which explains why the reference value used in Eq. (3.29). Of course $\widetilde{m}_t$ could be much smaller and the neutral twin much lighter accordingly. Let us note in this regards that $\tilde{\omega}^0$ does not linearly couple to SM fermions, but if kinematically allowed it opens a new Higgs-decay channel, which would force $f \gtrsim 1.2\,\text{TeV}$ to ensure consistency with LHC data.

3.4 Phenomenology

In this section we discuss the collider signals of the exceptional twin Higgs model. While we focus mostly on its minimal incarnation, the main constraints on the fraternal scenario will also be discussed at the end of this section to understand why it is less attractive.

at odds with the requirement (to misalign $\xi \ll 1$) that $\alpha > 0$, this is in fact not an issue, since α in the minimal scenario is easily dominated by the gauge term, as shown in Eq. (3.25).

While sharing some of standard signatures of twin Higgs models, such as the modification of the Higgs couplings and non-standard Higgs decays, our model has novel phenomenological features stemming from the fact that the twin particles carry hypercharge. We will first examine the indirect effects of the twin states on the well-measured properties of the SM particles. These are primarily the Y-parameter (which encodes new physics contributions to the hypercharge propagator), the running of the hypercharge gauge coupling g', and the Higgs decay rate to photons. These departures from the SM arise at the 1-loop level (with the exception of those mediated by the twin Z' in the fraternal model). Other indirect effects, common in constructions where the Higgs is a (custodially protected) composite pNGB, such as the S-parameter or deviations in other Higgs couplings, will not be discussed here further and we will merely recall when necessary their implications on the parameters of the strong sector, f and $m_* \sim m_\rho, m_\Psi$ [49].[9]

Direct production of the twin particles at colliders gives rise to the most interesting, though in some cases challenging, signatures of the exceptional twin Higgs. The twin quarks, being hypercharged, can be pair-produced via Drell-Yan (DY) and, because of the existence of twin strong interactions, exhibit the typical characteristics of the so-called quirks [32, 63, 64]. Such quirks are microscopic and lead to the formation of bound states that predominantly decay either to twin glueballs or back to the SM, while the glueballs in turn decay via an off-shell Higgs or, whenever this channel is forbidden, to photons. Another attractive signature arises from the charged twin pNGB $\tilde{\omega}^\pm$ or the twin leptons: they are pair-produced in DY and likely stable on detector scales, thus subject to current long-lived charged particle (LLCP) searches. Finally, we also present the stringent constraints on the twin Z'. These are the main reason why the minimal model is preferred, since such bounds are absent and one is left with a light but almost inert $\tilde{\omega}^0$, whose phenomenology is that of a twin axion-like particle that only couples to SM hypercharge, the study of which we defer to a future study.[10]

3.4.1 Indirect Effects

Since the twin particles carry hypercharge, they induce at the loop level a non-standard self-energy for the hypercharge field.[11] At leading order in a momentum expansion, such type of corrections are customarily parametrized by the dimension-6 operator $-(Y/4m_W^2)(\partial_\rho B_{\mu\nu})^2$. Indeed, $N_{\tilde{\psi}}$ heavy fermions of mass $m_{\tilde{\psi}}$ and hypercharge $q_{\tilde{\psi}}$ generate a Y-parameter of size

$$Y_{\tilde{\psi}} = \frac{g'^2}{80\pi^2}\frac{m_W^2}{m_{\tilde{\psi}}^2}\Delta b_Y\,, \quad \Delta b_Y = \frac{4}{3}N_{\tilde{\psi}}q_{\tilde{\psi}}^2\,. \tag{3.30}$$

For e.g. the twin top, $N_{\tilde{t}} = 3$, $q_{\tilde{t}} = \frac{2}{3}$ and $m_{\tilde{t}} \simeq m_t/\sqrt{\xi}$, leading to a very small contribution, $Y_{\tilde{t}} \sim 1 \times 10^{-5}$ for $\xi = 1/4$, in comparison to the per mille constraints from LEP [65] and more recently from the LHC [66, 67]. In fact, for any type of twin fermion we find that $Y_{\tilde{\psi}}$ is below LEP sensitivity for masses $m_{\tilde{\psi}} \gtrsim 100$GeV. For an even lighter twin fermion, encoding its effects in the Y-parameter is no longer adequate, nor it is for the twin top at the LHC [67]. In these cases however, constraints could a priori still be placed by considering the contribution

[9] We will refrain as well from discussing the flavor aspects of our construction, which are in any case not significantly different than in other composite-twin Higgs models [60]; see also [61, 62] for a general discussion of flavor in partial compositeness.

[10] As a matter of fact, ω_0 would be a bona-fide twin axion if other sources of mass beyond the twin-color anomaly, such as that in Eq. (3.29), vanished. It would then solve the twin-strong-CP problem, if there was any to begin with.

[11] For the present purpose this is identified with the vector state coupled to the SM fermions via the usual $U(1)_Y$ current, that is the $\widehat{B}$ field.

to the running of the hypercharge gauge coupling, encoded in the beta function coefficient Δb_Y in (3.30). However, the present accuracy on neutral DY processes is too low to see any such effect [68]. The charged pNGB $\tilde{\omega}^\pm$ also give a small contribution to the Y-parameter at one loop, which reads as in Eq. (3.30) with $m_{\tilde{\psi}}^2 \to 2m_{\tilde{\omega}^+}^2$, see Eq. (3.27), and $\Delta b_Y = 1/3$.

More important are the 1-loop contributions of the twins to the Higgs decay to diphotons. In composite Higgs models deviations of such a rate are generically $O(\xi)$ and a consequence of the modified couplings of the Higgs to the top and the W. The latter are also present in twin Higgs models, since they are intrinsic of the NGB nature of the Higgs [69]. On top of these, because the twin particles are electrically charged in our scenario, a direct $O(\xi)$ contribution is generated as well, specifically from a twin top loop. Since $m_{\tilde{t}} \gg m_h$, such an effect can be parametrized by the dimension-6 operator $(c_\gamma g'^2/m_W^2)|H|^2 B_{\mu\nu}B^{\mu\nu}$ with

$$(c_\gamma)_{\tilde{t}} = -\frac{q_{\tilde{t}}^2 g^2}{32\pi^2}\frac{\xi}{1-\xi}\,. \tag{3.31}$$

Note that in contrast to standard composite Higgs models [69], this operator is not suppressed by y_t^2/g_*^2.[12] The associated contribution to the $h\gamma\gamma$ vertex is $(c_{\gamma\gamma})_{\tilde{t}}/(c_{\gamma\gamma})_t \simeq -\xi/(1-\xi)$, where $(c_{\gamma\gamma})_t$ is the top loop contribution in the SM; a result that matches the expectation from twin parity once $\xi = 1/2$. The contribution from the twin top therefore, being opposite in sign to the top's, increases by $O(\xi)$ the Higgs coupling to photons. Since the standard corrections lead to a reduction of $h\gamma\gamma$, $c_{\gamma\gamma} \simeq (c_{\gamma\gamma})_{\rm SM}\sqrt{1-\xi}$, the twin-top loop alleviates, rather than aggravates, the departure from the SM prediction, a fact that can become relevant as the precision on Higgs couplings measurements improves. Besides, since the twin top is uncolored, it does not affect the Higgs coupling to gluons, thus breaking the correlation between $h\gamma\gamma$ and hgg usually found in composite Higgs models.

3.4.2 Direct Production

All our production cross sections have been computed using the MSTW2008NNLO parton distribution functions [70].

A Long-lived Charged Particles

Some of the hypercharged twin particles are potentially stable on detector scales. This is the case of the charged twin scalar in the minimal model, since its leading interactions with the SM respect an accidental Z_2 symmetry $\tilde{\omega}^\pm \to -\tilde{\omega}^\pm$, while we expect the decay channels $\tilde{\omega} \to \tilde{t} + \tilde{b}, \tilde{\tau} + \tilde{\nu}_\tau$ to be kinematically closed, the latter because the experimental bound on a collider-stable twin tau is stronger than for $\tilde{\omega}$, as we show in the following (thus the decay $\tilde{\tau} \to \tilde{\omega} + \tilde{\nu}_\tau$ is open). Besides, we recall that minimality does not require neither the twin bottom nor the twin tau to be present in the IR, while in the fraternal model both of them are required for anomaly cancellation.

Searches at the LHC for such type of particles have been carried out at $\sqrt{s} = 13\,\text{TeV}$, the latest analysis from ATLAS with $36.1\,\text{fb}^{-1}$ of data [71]. In Fig. 3.3 we show the corresponding constraints on the production cross sections for a $|Q| = 1$ charged scalar (left panel), identified with a stau in the ATLAS analysis, and a $|Q| = 1$ DY charged fermion (right panel), identified with a chargino. These constraints readily apply to our twin $\tilde{\omega}^+$ and $\tilde{\tau}$, respectively. The comparison of the predicted cross section with the experimental bound for the former shows

[12] We have explicitly checked that such a suppression is found instead in the contribution to c_γ from a loop of the charged pNGB $\tilde{\omega}^\pm$.

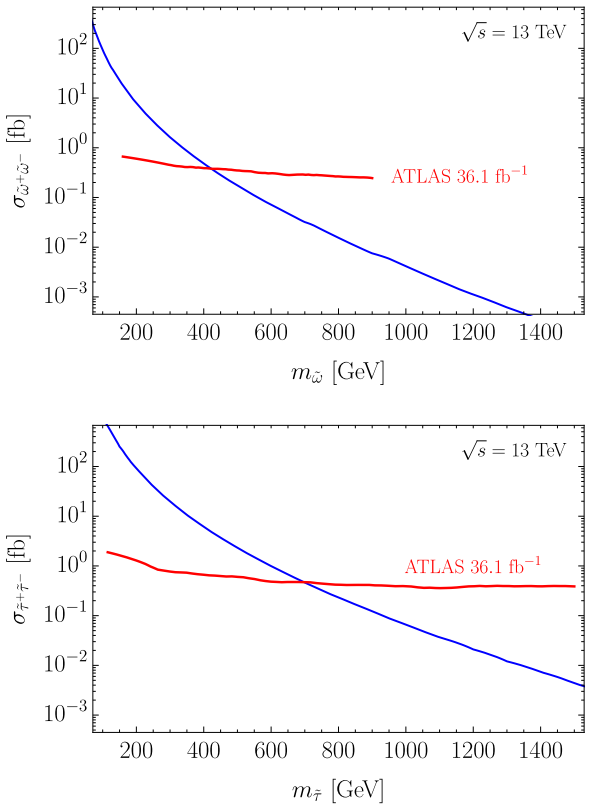

Figure 3.3: Upper 95% CL limits on the cross section for DY pair-production of $|Q| = 1$ heavy stable scalars (left) and fermions (right) from an ATLAS search in 36.1 fb^{-1} of data at $\sqrt{s} = 13$ TeV [71] (red). The theoretical predictions for the twin pNGB $\tilde{\omega}^{\pm}$ and the twin tau $\tilde{\tau}$ are also shown (blue).

that masses below 420GeV are excluded. This should be compared with our expectation for the twin scalar mass $m_{\tilde{\omega}^+} \sim 550$GeV, Eq. (3.27). Even though the current bound does not quite reach such values, a factor of a few improvement in experimental sensitivity would start probing the relevant parameter space. For what regards the twin tau, the situation is certainly different, since twin parity would imply $m_{\tilde{\tau}} \simeq m_\tau/\sqrt{\xi}$, while data indicates that only masses above 700GeV are allowed. Of course, explicitly breaking twin parity in the lepton sector is a priori an option. However, the experimental bound is so stringent that the twin-tau Yukawa should be larger than the twin-top's to avoid it, thus a large contribution to the Higgs potential should be expected. This extra complication is yet another reason why the fraternal implementation of our scenario is disfavoured versus the minimal model, where the bounds on the charged scalar are less consequential and the $\tilde{\tau}$ could be lifted by giving it a vector-like mass.

While LLCPs could be regarded as a differential phenomenological feature of the exceptional twin Higgs, it is important to note that neither the stability of $\tilde{\tau}$ nor of $\tilde{\omega}^+$ are due to super-selection rules. Indeed, at low energies these states only carry electric charge and therefore decays such as $\tilde{\tau} \to \tau + \gamma, Z$ or $\tilde{\omega} \to \ell + \nu, q' + q, W + \gamma, Z$ are allowed. Let us discuss in some detail the decay of the twin tau (a similar discussion holds for $\tilde{\omega}^+$). The first point to note is that, since $\tilde{\tau}$ and τ have different X (and $\widetilde{X}$) charges, the interaction mediating the decay cannot be generated by the strong dynamics alone, thus it should have its origin at some UV

scale Λ. One instance is an interaction of the form $\bar{\tau}_R \sigma^{\mu\nu} \widetilde{H} \tilde{\ell}_L \widehat{B}_{\mu\nu}$, which could be generated at low energies with a coefficient $\hat{g}/m_* \Lambda$, leading to a $\tilde{\tau}$ decay rate

$$\Gamma_{\tilde{\tau}\to\tau+\gamma} \sim \frac{e^2 m_{\tilde{\tau}}^3}{8\pi g_*^2 \Lambda^2} \approx (0.2\,\mathrm{cm})^{-1} \left(\frac{m_{\tilde{\tau}}}{100\mathrm{GeV}}\right)^3 \left(\frac{2\pi}{g_*}\right)^2 \left(\frac{10^7\mathrm{GeV}}{\Lambda}\right)^2 . \tag{3.32}$$

Therefore, model-dependent UV considerations could render the twin tau (and/or $\tilde{\omega}^+$) short-lived, displaced, or long-lived. It would be interesting to study these types of signatures at the LHC, e.g. similar to those of an excited tau if the twin tau decays promptly. Finally, we restate that given the constraints in Fig. 3.3, the decay $\tilde{\tau} \to \tilde{\omega} + \tilde{\nu}_\tau$ would also proceed in the minimal model, and dominate over (3.32).

B Hypercharged Quirks

The lightest twin quark of the exceptional twin Higgs behaves as a quirk [63], a heavy stable particle that interacts via a new unbroken non-abelian gauge group and carries SM charges, in our case twin color and hypercharge, respectively. Once pair-produced, via DY in our scenario, quirks do not hadronize but instead form (meta-)stable strings. This is because any of the twin quarks are heavy in comparison with the scale where twin-color interactions become strong, i.e. $m_{\tilde{q}} \gg \tilde{\Lambda}_{\mathrm{QCD}}$: in such a case the breaking of the string by pair production takes an exponentially large time, $t_{\mathrm{break}} \sim (4\pi^3/m_{\tilde{q}}) \exp(c\, m_{\tilde{q}}/\tilde{\Lambda}_{\mathrm{QCD}})^2$, with c an $O(1)$ factor that depends on the precise definition of $\tilde{\Lambda}_{\mathrm{QCD}}$. The absence of twin quarks lighter than $\tilde{\Lambda}_{\mathrm{QCD}}$ follows from several considerations. On the one hand, naturalness of the Higgs potential indicates that the SM and twin-color gauge couplings are not substantially different at m_*, $\tilde{g}_s \approx g_s$, thus $\tilde{\Lambda}_{\mathrm{QCD}}$ will not be far apart from the scale $\Lambda_{\mathrm{QCD}} \approx 250\,\mathrm{MeV}$ where the SM color becomes strong. The difference arises mainly from Z_2-breaking radiative effects that originate from the different colored content of $SU(3)_C$ and $SU(3)_{\widetilde{C}}$ below m_*, since we assumed a single generation of twin quarks (and $m_{\tilde{q}} \neq m_q$). Such an effect leads to $\tilde{\Lambda}_{\mathrm{QCD}} \sim 2 - 10\mathrm{GeV}$, depending on m_*, on the exact values of $\tilde{g}_s$ and g_s at m_*, and on the twin quark masses [27]. On the other hand, experimental constraints on the twin quarks force them to be considerably heavier than $\tilde{\Lambda}_{\mathrm{QCD}}$. In particular, the precise measurement at LEP1 of the Z decay width, $\Delta\Gamma_Z/\Gamma_Z \approx 9 \cdot 10^{-4}$ [72], rules out twin quarks (with $Y_{\tilde{q}} = 2/3$ or $-1/3$) for which the decay channel $Z \to \tilde{\bar{q}}\tilde{q}$ is kinematically open, that is $m_{\tilde{q}} \lesssim m_Z/2 \approx 45\mathrm{GeV}$. This constraint is only relevant for the twin bottom, since it implies $m_{\tilde{b}} > m_b/\sqrt{\xi}$, away from the Z_2-symmetric relation, while the twin top is always heavier. In summary, we conclude that $m_{\tilde{q}}/\tilde{\Lambda}_{\mathrm{QCD}} \gtrsim 4$ and that t_{break} is very large, much longer, as we show next, than the time it takes for the string to annihilate, which is the other possible fate of the string.[13]

The typical annihilation time depends a priori on the annihilation rates of the different states of energy and angular momentum the string can be in. In practice a good proxy is to consider only the low-lying low angular momentum ($\ell = 0$) bound states, whose lifetime is proportional

[13] Heavier twin quarks, up to $m_{\tilde{q}} \approx 103.5\mathrm{GeV}$, should have also been pair produced at LEP2 through an off-shell photon or Z. However, being the cross sections of $O(g'^2)$ and the quirks losing a significant fraction of their energy through electromagnetic radiation (see below), we expect LEP did not have the required sensitivity. Besides, even though the twin quarks modify at one loop SM processes like dilepton pair production (this being the same effect we encoded in the Y-parameter for twin masses beyond LEP reach, see Section 3.4.1), we checked the effect is below experimental uncertainties [73]. We note that twin-QCD dynamics could also affect such processes, e.g. via Z-glueball mixing, however we expect the effects to be small; also, the decay $Z \to \tilde{g}\tilde{g}\tilde{g}$ is below current constraints on non-standard Z decays, $\mathrm{BR}(Z \to X_{\mathrm{BSM}}) \lesssim 10^{-4}$.

to the classical crossing time of the quirks (or length of the string),

$$T \sim \frac{m_{\tilde{q}}}{\tilde{\Lambda}^2_{\rm QCD}} \approx 3\times 10^{-24}\,{\rm sec}\left(\frac{m_{\tilde{q}}}{100{\rm GeV}}\right)\left(\frac{5{\rm GeV}}{\tilde{\Lambda}_{\rm QCD}}\right)^2, \tag{3.33}$$

i.e. our twin strings are microscopic, $L \sim 0.1\,{\rm fm}$. This approach might naively seem at odds with the fact that most twin quarks will be produced relativistic, $\sqrt{\hat{s}} - 2m_{\tilde{q}} \sim m_{\tilde{q}}$, therefore in highly excited states. However excited bound states have annihilation rates suppressed by their large angular momentum [63]. Therefore the low-lying states are eventually reached after the quirks radiate away most of their energy into (relatively) soft twin glueballs and photons [74]. For the latter the typical radiation time can be estimated as $t^{\rm QED}_{\rm rad} \sim (3/8\pi q^2_{\tilde{q}}\alpha) m^3_{\tilde{q}}/\tilde{\Lambda}^4_{\rm QCD} \approx (2/q^2_{\tilde{q}}) \times 10^{-22}\,{\rm sec}$ for the same parameters as in (3.33) and $q_{\tilde{q}}$ the twin electric charge. This means that the de-excitation process is fast, in particular no displaced vertices in quirk pair-production and annihilation should be expected. Besides, twin glueball emission is also expected to contribute to the process, at least for energies where the kinematical suppression from the non-zero glueball mass is irrelevant.[14]

Let us focus therefore on the lightest twin quarkonium bound states with $\ell = 0$, which are a pseudoscalar η^{-+} and a vector Υ^{--}, both electrically neutral (see also [75, 76]).[15] Their mass is given to a good approximation by $m_{\eta,\Upsilon} \approx 2m_{\tilde{q}}$, while their decay rates can be found e.g. in [77–79]. Of special significance is the fact that the decay of Υ^{--} to a pair of twin gluons is forbidden, thus enhancing its branching ratio to SM final states. Neglecting the masses of the daughter particles as well as m_Z,

$$\begin{aligned}
&\Gamma_{\Upsilon^{--}\to\gamma h,\, Zh} \simeq \frac{\alpha q^2_{\tilde{q}}\tilde{y}^2_q|\psi(0)|^2}{\pi m^2_\Upsilon}\left\{1,\, t^2_{\theta_W}\right\}, \quad \Gamma_{\Upsilon^{--}\to f\bar{f}} \simeq \frac{4N_c\alpha^2[(Q^{\Upsilon f}_V)^2 + (Q^{\Upsilon f}_A)^2]|\psi(0)|^2}{m^2_\Upsilon}, \\
&\Gamma_{\Upsilon^{--}\to\tilde{g}\tilde{g}\tilde{g}} \simeq \frac{40\tilde{\alpha}^3_s(\pi^2-9)|\psi(0)|^2}{81\pi m^2_\Upsilon},
\end{aligned} \tag{3.34}$$

where $Q^{\Upsilon f}_V = q_{\tilde{q}}(q_f + q^V_{Zf}/c^2_{\theta_W})$ and $Q^{\Upsilon f}_A = q_{\tilde{q}}\, q^A_{Zf}/c^2_{\theta_W}$ with q_i the electric charge of i and $q^{V,A}_{Zf}$ the vector and axial Z-charges of the SM fermions, e.g. for $f = e$, $q^V_{Ze} = \frac{1}{2}(-\frac{1}{2} + 2s^2_{\theta_W})$ and $q^A_{Ze} = -\frac{1}{4}$. The twin-QCD structure constant $\tilde{\alpha}_s$ is to be evaluated at m_Υ,[16] and $\psi(0)$ is the radial wave function of the bound state at the origin. For a Υ^{--} made of twin bottoms ($q_{\tilde{q}} = -\frac{1}{3}$), the decay to three twin gluons is the largest for all twin quarks masses of interest, $m_{\tilde{q}} \in (0.1, 1)\,{\rm TeV}$, while for a bound state of twin tops ($q_{\tilde{q}} = \frac{2}{3}$), decays to γh and Zh dominate, owing to a large twin Yukawa coupling. Importantly, decays to SM fermions are always non-negligible, e.g. ${\rm BR}(\Upsilon^{--} \to e^+e^-) \approx 4 - 10\%$, where the lower end is found for a twin top, quite independently of its mass. In contrast, the η^{-+} decays almost exclusively to two twin gluons, while its other allowed decay channels, to a pair of SM neutral gauge bosons (i.e. $\gamma\gamma, ZZ, Z\gamma$), are suppressed by the small electromagnetic coupling constant, e.g.

$$\Gamma_{\eta^{-+}\to\tilde{g}\tilde{g}} = \frac{8\tilde{\alpha}^2_s|\psi(0)|^2}{3m^2_\eta}, \quad \Gamma_{\eta^{-+}\to\gamma\bar{\gamma}} = \frac{12\alpha^2 q^4_{\tilde{q}}|\psi(0)|^2}{m^2_\eta}. \tag{3.35}$$

[14] Here we follow [63, 64] where it is argued that the energetic strings quickly acquire large values of ℓ, thus suppressing annihilation and favoring the process of de-excitation by glueball or photon emission. If this were not the case and annihilation took place before reaching the lowest bound states, the twin string would be best described as a broad resonance.

[15] As usual the parity and charge-conjugation properties of the bound states are given by $P = (-1)^{\ell+1}$ and $C = (-1)^{\ell+s}$ respectively, s being the spin.

[16] To extract $\tilde{\alpha}_s$, we match it to the QCD coupling constant g_s at $m_* = 5\,{\rm TeV}$, i.e. $\tilde{g}_s(5\,{\rm TeV}) = g_s(5\,{\rm TeV})$, to then run it down to the relevant scale, taking into account that only one generation of twin quarks contributes to the running (and the twin top threshold).

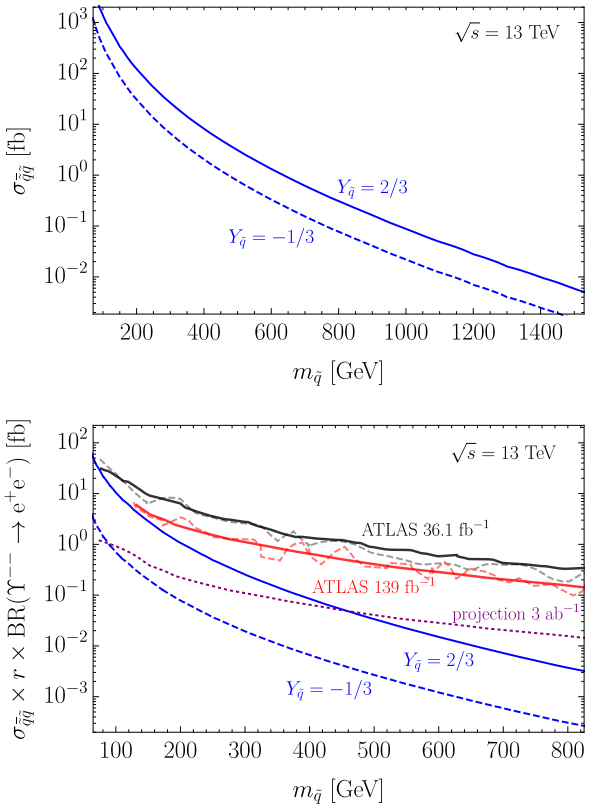

Figure 3.4: (Left) Pair production cross sections of twin quarks with hypercharge $Y_{\tilde{q}} = \frac{2}{3}$ (solid) or $Y_{\tilde{q}} = -\frac{1}{3}$ (dashed). (Right) Upper 95% CL limit on Z' cross section times branching ratio to dileptons from ATLAS searches in 36.1 fb^{-1} [80] (black solid) and in 139 fb^{-1} [81] (red solid) of data at $\sqrt{s} = 13$ TeV, where the Z' is identified with the bound state $\Upsilon^{--} \sim \bar{\tilde{q}}\tilde{q}$ of mass $m_\Upsilon = 2m_{\tilde{q}}$, with theory predictions for $Y_{\tilde{q}} = \frac{2}{3}$ (blue solid) and $Y_{\tilde{q}} = -\frac{1}{3}$ (blue dashed). Also shown the projected bound after 3 ab^{-1} of integrated luminosity (see text for details).

For the relevant range of quirk masses $\mathrm{BR}(\eta^{-+} \to \gamma\gamma) \approx q_{\tilde{q}}^4(1-4)\%$, which means that even for a twin-top bound state the branching ratio is always below the per cent.

The substantial branching ratio of the Υ^{--} to dileptons make its production at the LHC one of the most promising avenues for detection of the twin quarks. To assess the sensitivity of current LHC searches for dilepton resonances, we plot in Fig. 3.4 (left panel) the production cross section of pairs of twin quarks with hypercharge either as that of the twin top, $Y_{\tilde{q}} = \frac{2}{3}$, or as the twin bottom, $Y_{\tilde{q}} = -\frac{1}{3}$ (recall $q_{\tilde{q}} = Y_{\tilde{q}}$). We keep the mass $m_{\tilde{q}}$ a free parameter, but we recall that in our twin Higgs model $m_{\tilde{t}} \simeq m_t/\sqrt{\xi}$ while $m_{\tilde{b}}$ only needs to be large enough for $Z \to \bar{\tilde{b}}\tilde{b}$ to be kinematically forbiden, but otherwise it is not bounded by naturalness considerations; we effectively vary $m_{\tilde{q}}$ by changing the corresponding vector-like mass $\widetilde{m}_q$ (i.e. keeping the Yukawa coupling $\tilde{y}_q$ to its Z_2-symmetric value). The fraction of events that go through the formation and decay of Υ^{--} bound states rather than of η^{+-} is expected to depend on their total decay rates, $\Gamma_{\Upsilon,\eta}$, as $r = 3\Gamma_\Upsilon/(3\Gamma_\Upsilon + \Gamma_\eta)$ [82], where the factor of three accounts for the number of degrees of freedom in the vector bound state versus in the pseudoscalar. Because of the large decay rate of the η^{+-} to $\tilde{g}\tilde{g}$, we find r is always below 25% for a twin-top bound state and below 5% for the twin bottom. With these results we have computed the cross section for production and decay

to e^+e^- (and $\mu^+\mu^-$) of the Υ^{--}, which we show in Fig. 3.4 (right panel) for a bound state made of twin quarks with either top-like of bottom-like hypercharges. Comparing them with the latest ATLAS bounds on a Z' decaying to dileptons [81], we find that the current $139\,\text{fb}^{-1}$ of data at $\sqrt{s} = 13\,\text{TeV}$ are not quite enough to probe the small cross sections associated with the hypercharged quirks. However, the order of magnitude increase in sensitivity needed to probe the relevant twin-top cross sections could potentially be achieved at the LHC with $3\,\text{ab}^{-1}$ of integrated luminosity, as we also shown in Fig. 3.4. Such a expected a limit has been obtained from a naive luminosity rescaling, after contrasting the improvement of the expected bounds from $36\,\text{fb}^{-1}$ [80] to $139\,\text{fb}^{-1}$ [81] of data (note that the HL-LHC projections in [83] do not go below 2 TeV resonance masses). In addition, searches for γh resonances are also relevant in view of the large branching ratios of the twin-top Υ^{--} to this final state. Current analyses [84] set a constraint $\sigma \cdot \text{BR} \lesssim 10\,\text{fb}$, roughly one order of magnitude above the cross section predicted in our scenario for $m_\Upsilon \sim 1\,\text{TeV}$, which makes this a very interesting signature for the high-luminosity phase of the LHC.

Similarly, the cross section for production and decay to diphotons of the pseudoscalar, $\sigma_{\tilde{q}\bar{\tilde{q}}} \cdot (1-r) \cdot \text{BR}(\eta^{-+} \to \gamma\gamma) \approx 1.6 \times 10^{-2}\,\text{fb}$ for $m_\eta = 1\,\text{TeV}$ and $Y_{\tilde{q}} = \frac{2}{3}$, is for the most part down by one/two orders of magnitude compared to current LHC bounds on diphoton resonances [85]. Once again the interesting conclusion is that the HL-LHC should have enough sensitivity to probe a twin-top bound state decaying to $\gamma\gamma$ of mass as expected from twin parity, therefore reaching the relevant parameter space. We note that the situation is certainly different if twin quarks had larger hypercharges, for instance if $Y_{\tilde{q}} = 2$ current diphoton searches would already exclude $m_{\tilde{q}} \lesssim 1\,\text{TeV}$.

C Twin Glueballs

In our exceptional twin Higgs, twin glueballs are the lightest states of the twin sector. They are produced from Higgs decays, as in other scenarios of neutral naturalness [27, 86], as well as from the decays of the twin-quark bound states, as discussed in the previous section.[17] While the former process dominates for heavy twin quarks, it is interesting that the decays of twin-bottom bound states lighter than approximately 300GeV dominate the inclusive glueball production at $\sqrt{s} = 13\,\text{TeV}$: $\sigma_{\tilde{g}}^{(h)} \approx 67\,\text{fb}\,(\xi/0.1)^2$ while $\sigma_{\tilde{g}}^{(\Upsilon+\eta)}$ is very near the total quirk production cross section, shown on the left panel of Fig. 3.4, since bound-state annihilation to glueballs always dominates.

The mass, lifetime and decay modes of a given glueball are determined by its quantum numbers, see e.g. [87, 88]. Therefore, the actual signatures associated to glueball production depend on which and how many glueballs are produced from the aforementioned decays. These questions however cannot be reliably answered without a proper understanding of the non-perturbative twin-color dynamics (see however [89]). We will therefore focus our attention on the lightest glueball 0^{++}, whose dominant decays are mediated by the Higgs, via the dimension-6 operator $|H|^2 \widetilde{G}_{\mu\nu}\widetilde{G}^{\mu\nu}$, as well as on the lightest glueball for which such decays are forbidden, i.e. the 0^{-+}, which decays almost exclusively to two photons. Both of these glueballs, of mass $m_{0^{++}} \equiv m_0 \approx 6.9\tilde{\Lambda}_{\text{QCD}}$ and $m_{0^{-+}} \approx 1.5 m_0$, are expected to represent a significant low-energy population of the energetic twin gluons originally produced, with the 0^{++} expected to dominate if the kinetic energy of the twin gluons is low, being the lightest. Other glueballs could also yield interesting and somewhat distinct phenomenology, however the 0^{++} and 0^{-+} are good representatives of the particularities of our exceptional twin Higgs with respect to previous

[17] Another potential source of glueballs is from the previous deexcitation of the quirks, which we neglect here since it is unclear if such radiation would dominate over the electromagnetic one.

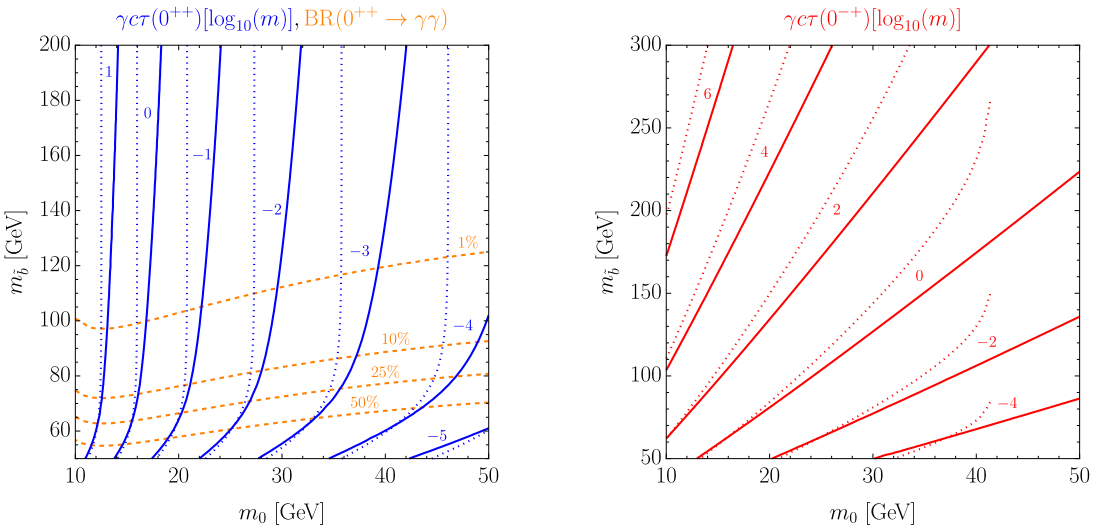

Figure 3.5: (Left) Branching ratio of the lightest glueball 0^{++} to diphotons (orange) and lab decay length (blue) from production via either Higgs decays (dotted) or η^{-+} decays (solid), for $\xi = 0.1$. (Right) Lab decay length of the lightest parity-odd glueball 0^{-+} (red), of mass $m_{0^{-+}} \approx 1.5\, m_0$, from production via either Higgs decays (dotted) or η^{-+} decays (solid). The decay lengths have been computed under the assumption that the parent particle produces two glueballs only, thus they should be understood as upper bounds.

models. For instance, we checked that the 2^{++} glueball decays predominantly to diphotons and is stable on collider scales, as the 0^{-+}, see Eq. (3.37).

Significant branching ratios to diphotons is in fact the identifying feature of the glueballs in our scenario. These arise via dimension-8 operators of the form $c\, F_{\mu\nu}F^{\mu\nu}\widetilde{G}_{\rho\sigma}\widetilde{G}^{\rho\sigma}$ generated by a twin-quark loop, of size

$$c \sim \frac{\alpha\, \tilde{\alpha}_s Y_{\tilde{q}}^2}{m_{\tilde{q}}^4}\,, \tag{3.36}$$

which is therefore enhanced at low twin-quark masses. For this reason in the following we will consider the twin bottom as a key player in glueball phenomenology, and comment when relevant on the differences that would arise if the $\tilde{b}$ is decoupled and only the twin top contributes, e.g. Eq. (3.36) would be enhanced due to the larger hypercharge of $\tilde{t}$ but suppressed by its larger mass. In the left panel of Fig. 3.5 we show the branching fraction to diphotons of the lightest glueball in the $(m_0, m_{\tilde{b}})$ plane, in the range of glueball mass expected from our estimates of $\tilde{\Lambda}_{\rm QCD}$. As anticipated, only for light twin bottoms this channel dominates over the standard Higgs-mediated decay to a pair of SM bottoms. The decay length of the 0^{++} can be approximated, for sufficiently large $m_{\tilde{b}}$ and/or ξ by $c\tau_{0^{++}} \approx (0.4\,\text{m})(15\text{GeV}/m_0)^7(0.1/\xi)^2$ as in standard twin Higgs constructions. Therefore, such glueballs are relativity long-lived, giving rise to displaced vertices in a significant fraction of the parameter space. This decay length, but in the lab frame, is also shown in the left panel of Fig. 3.5, where the boost factor is either from the decay of a Higgs (blue dotted) or the decay of the twin-bottom bound states (blue solid), to two, and only two, glueballs. More realistically, such decays will give rise to more glueballs, meaning these lengths should be considered as upper bounds. One of the new and exciting features of our glueballs is found in the right panel of Fig. 3.5, where we show the lab decay length of the 0^{-+}, which almost exclusively decays to $\gamma\gamma$ and it is very long-lived, in fact stable on collider

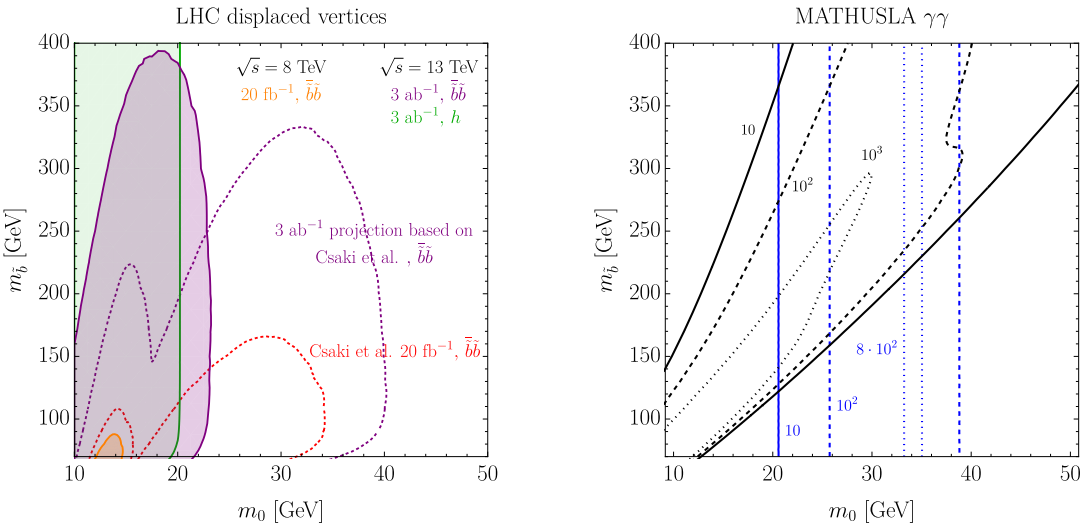

Figure 3.6: (Left) Current and projected LHC constraints on the 0^{++} glueball mass m_0 and the twin-bottom mass $m_{\tilde{b}}$ from searches for displaced vertices, for $\xi = 0.1$. The bounds shown correspond to 0^{++} production from annihilation of twin-bottom bound states at 8 TeV in 20 fb^{-1} of ATLAS data [93] (orange), and projected searches from [94] at 13 TeV with 20 fb^{-1} (dotted red) and 3 ab^{-1} (dotted purple), as well as from the HL-LHC [95] (purple). Shown also the HL-LHC bounds on 0^{++} production from Higgs decays (green). (Right) Expected number of glueballs decaying to diphotons inside the MATHUSLA detector, from twin gluons produced at the 13 TeV LHC after 3 ab^{-1} of integrated luminosity, via decays of the Higgs and twin-bottom bound-states (black) or Higgs and twin-top bound-states with $m_{\tilde{t}} \simeq m_t/\sqrt{\xi}$ (blue), for $\xi = 0.1$.

scales in a large portion of parameter space. This can be easily understood from the fact that its rest-frame decay length scales as

$$c\tau_{0^{-+}} \approx (55\,\mathrm{m}) \left(\frac{m_{\tilde{b}}}{150\mathrm{GeV}}\right)^8 \left(\frac{20\mathrm{GeV}}{m_0}\right)^9 \left(\frac{-1/3}{Y_{\tilde{b}}}\right)^4 , \tag{3.37}$$

which in the lab frame translates to up to 250 m. Since the dependence on either m_0 or $m_{\tilde{b}}$ is very strong, these glueballs could give rise either to displaced photons or to missing energy signatures in the detector. In the latter case, the glueballs would eventually decay to a pair of photons, which could potentially be detected by one of the proposed detectors dedicated to long-lived particle searches [90–92]. Besides, notice that if the twin bottom is decoupled, $c\tau_{0^{-+}}$ would be substantially larger, since the decay would only be mediated by the heavier twin top.

Before discussing the experimental prospects for such collider-stable glueballs, let us understand the sensitivity of current and future LHC data to the 0^{++} glueballs. Since these are long-lived but always decay within the detector, they give rise to displaced vertices. This kind of signals have been studied in detail in several works, e.g. [94, 96–99], and we reinterpret here some of their results to account for the effects of our hypercharged twin quarks. In the left panel of Fig. 3.6 we show the constraints on m_0 and $m_{\tilde{b}}$ from several searches for displaced vertices. These in general focus on decays either in the inner detector, $c\tau\gamma \lesssim 25$ cm (γ the boost factor), therefore sensitive to heavier 0^{++} glueballs, or in the hadronic calorimeter and/or muon spectrometer, that is 2 m $\lesssim c\tau\gamma \lesssim$ 10 m and thus of relevance for lighter glueballs. The current most sensitive experimental analysis that is well suited to the features of our twin glueballs is from ATLAS at 8 TeV and with 20 fb^{-1} of data [93] (small orange region in Fig. 3.6). While

this search barely reaches the interesting region, the theory projections of [94] for 13 TeV and $20\,\text{fb}^{-1}$ (dotted red line) show that with current data one could already probe twin-bottom masses up to 150GeV, at least for glueballs that decay within the inner detector.[18] We should note however that these projections are somewhat uncertain, in particular to date there is no experimental analysis demonstrating the sensitivity to such heavy glueballs, while the region at small m_0, which overlaps with the ATLAS 8 TeV analysis [93], has not been corroborated by a recent 13 TeV analysis that studies glueballs decaying in the hadronic or the outer edge of the electromagnetic calorimeters [100]. We have checked that this experimental analysis, based on $10.8\,\text{fb}^{-1}$ of data, does not yield any constraint on out parameter space. Besides, the analysis of [94] is not sensitive to glueballs originating from Higgs decays (for $\xi \lesssim 0.1$), but only to those from the annihilation of twin-bottom bound states. In Fig. 3.6 we also show the region covered by a naive (by $1/\sqrt{L}$) rescaling of the projections of [94] to $L = 3\,\text{ab}^{-1}$ (dotted purple). This simple extrapolation shows that the high-luminosity phase of the LHC could considerably extend the coverage up to $m_{\tilde{b}} \sim 300$GeV. Moreover, we have also recasted the HL-LHC projections from [95], which shows sensitivity to light 0^{++} glueballs produced from twin-bottomonium annihilation up to $m_{\tilde{b}} \sim 400$GeV (purple region), as well as glueballs from Higgs decays (green). The latter region is independent of $m_{\tilde{b}}$ since the twin bottom does not contribute significantly to the Higgs branching ratio into twin gluons, being instead solely determined by ξ. Indeed, for $\xi \lesssim 0.01$ the green region in Fig. 3.6 disappears. In addition, both the constraints associated to Higgs and twin quarkonium annihilation extend to higher m_0 values for smaller ξ, since the decay rate of the 0^{++}, dominated by Higgs exchange, decreases. Let us also comment on the dependence of these constraints on the electric charge of the twin quarks, in particular for $Y_{\tilde{t}} = 2/3$ as it corresponds to the twin top. A larger $Y_{\tilde{q}}$ implies a larger production cross section of the twin quarks for the same mass, thus the main effect is that the constraints from searches for displaced vertices extend to heavier $m_{\tilde{q}}$. We find that $3\,\text{ab}^{-1}$ could probe up to $m_{\tilde{t}} \sim 520$GeV for light glueballs or $m_{\tilde{t}} \sim 450$GeV for heavy ones, close to the twin-top mass expected from twin parity; we could forecast that a dedicated search would achieve the required sensitivity. Let us add that in the above we have always assumed that two, and only two, 0^{++} glueballs are produced during twin-color glueballization.

The very slow decay of twin glueballs such as the 0^{-+}, see Eq. (3.37), could potentially be detected by a surface detector such as MATHUSLA [90], granted its efficiency to identify photons is not negligible. In the right panel of Fig. 3.6 we show a (very) rough estimate of the number of photons that would decay inside the detector: $L \cdot \sigma_{0^{-+}} \cdot P(d)$, with $L = 3\,\text{ab}^{-1}$, the 13 TeV cross section $\sigma_{0^{-+}}$ includes glueballs from twin gluons produced in both Higgs ($\xi = 0.1$) and twin-bottomonium decays, and $P(d) = e^{-d_i/d}(1 - e^{-(d_i+\Delta d)/d})\Omega_M/4\pi$ is our naive estimate of the probability for the glueball to decay inside MATHUSLA, where $d_i \approx 225\,\text{m}$ (distance from the interaction point to center of the closer horizontal edge of the detector), $\Delta d \approx 45\,\text{m}$ (the corresponding maximum distance to the farther edge of the detector), d is to be identified with the lab-frame decay length of the glueball, $(c\tau\gamma)_{0^{-+}}$, and $\Omega_M \approx 0.3$ the solid angle covered by the detector.[19] Once again we have assumed for simplicity that at least two, but only two, 0^{-+} glueballs arise from the hard-scattered twin gluons. We therefore conclude that large numbers of glueballs, up to $O(10^3)$ after $3\,\text{ab}^{-1}$ of integrated luminosity, could potentially decay to diphotons within MATHUSLA. Interestingly, this conclusion does not depend on the presence of light twin bottoms in the spectrum, as shown by the blue contours in Fig. 3.6, corresponding to glueballs

[18] Even though most strategies, and in particular those of [94], focus on displaced vertices from Higgs decays, we naively assume that similar sensitivities can be achieved for glueballs from twin-quark bound-state decays.

[19] A proper estimate would take into account that the distances to the closer and farther edges of the detector depend on the direction of incidence of the glueball.

from the decays of Higgs and twin-top bound states at their twin-symmetric mass ($\xi = 0.1$).

We conclude this section by noticing that another potentially relevant signature of our glueballs is given by the process $pp \to \tilde{g}\tilde{g} \to 0^{++}0^{-+} + X$, where the 0^{++} decays displaced to $\gamma\gamma$ (even if this is a subleading decay channel, see Fig. 3.5), while 0^{-+} escapes the detector and thus shows up as missing energy [101, 102].

3.4.3 Fraternal Z'

In the fraternal model, the spontaneous breaking of $SU(2)_{\widetilde{L}} \times U(1)_{\widehat{Y}}$ to $U(1)_Y$ gives rise to a tree-level contribution to Y-parameter, which decouples with both the twin gauge coupling $\tilde{g}$ and the symmetry-breaking scale f as

$$Y_{Z'} = \frac{g^2 g'^2 \xi}{\tilde{g}^4(1-\xi)} \simeq \frac{g'^2}{\tilde{g}^2}\frac{m_W^2}{m_{Z'}^2}\,, \tag{3.38}$$

where on the r.h.s. we neglected subleading terms in ξ and $g'/\tilde{g}$. The constraint from LEP $Y \lesssim 1 \cdot 10^{-3}$ then leads to an important upper bound on the parameter combination $\tilde{g}^4 f^2$. Nevertheless, except for very large $\tilde{g}$ or unless some ad hoc assumption is made on the decays of the Z', this constraint is milder than the one arising from direct Z' searches at the LHC, as shown in the right panel of Fig. 3.7.

We recall that the twin Z' is the axial combination of the $\widehat{B}$ and $\widetilde{W}^3$ gauge bosons, with mass $m_{Z'} \sim \tilde{g} f/2$. Its couplings to the SM and twin fermions can be written as

$$\tilde{g} Z'^{\mu} \left(c_{\tilde{\theta}} \mathcal{J}^Q_\mu(\tilde{\psi}) - \frac{1}{c_{\tilde{\theta}}} \mathcal{J}^{\widehat{Y}}_\mu(\tilde{\psi}) - \frac{s^2_{\tilde{\theta}}}{c_{\tilde{\theta}}} \mathcal{J}^Y_\mu(\psi) \right) + O(\xi)\,, \tag{3.39}$$

where $s_{\tilde{\theta}} = g'/\tilde{g}$ and $\mathcal{J}^{Q,\widehat{Y},Y}$ are the $U(1)_{Q,\widehat{Y},Y}$ currents made of either SM fermions ψ or twin fermions $\tilde{\psi}$, with twin parity enforcing $\widehat{Y}(\tilde{\psi}_i) = Y(\psi_i)$ and $Q(\tilde{\psi}_i) = Q(\psi_i)$. The $O(\xi)$ term stands for corrections induced after EWSB, which we safely neglected in the following. From the last term in brackets one can immediately see that the Z' can be produced from a SM fermion pair, e.g. $q\bar{q}$ at the LHC, with a cross section that scales as $\sigma_{Z'} \sim g'^2 (g'/\tilde{g})^2$ for fixed Z' mass and $\tilde{g} \gg g'$. In this limit the width of the Z' is dominated by decays to twin fermions, with branching ratios to SM fermions scaling as $\mathrm{BR}(\bar{\psi}\psi) \sim (g'/\tilde{g})^2$. Therefore, for large values of $\tilde{g}$ both production and SM decays are suppressed.

We find the strongest direct constraints on the Z' arise from ATLAS searches for a resonant peak in dilepton $(e^+e^-, \mu^+\mu^-)$ invariant mass distributions [80, 81]. The bounds on $\sigma \cdot \mathrm{BR}$ are shown in the left panel of Fig. 3.7, along with the theoretical prediction for three different values of the twin $SU(2)_{\widetilde{L}}$ gauge coupling and assuming one full generation of twin fermions the Z' can decay to.[20] In the twin-symmetric case $\tilde{g} = g$, we find $m_{Z'} \gtrsim 4.1\,\mathrm{TeV}$, a stringent bound that, according to Eq. (3.9), implies $f \gtrsim 10\,\mathrm{TeV}$, way beyond natural values. This motivates larger values of $\tilde{g}$, for which the constraints on $m_{Z'}$ are milder and the corresponding amount of fine-tuning is smaller. This is shown in the right panel of Fig. 3.7, where we plot the excluded regions from LHC direct searches and from the Y-parameter Eq. (3.38) in the $(f,\, \tilde{g}/g)$ plane, along with contours of fixed $m_{Z'}$ and tuning Δ_g associated to the gauge contributions to the Higgs potential for $g_\rho = 6$; values of $\Delta_g \gtrsim 0.5\%$ can be achieved for $\tilde{g} \gtrsim 2g$.

In view of these results, the question arises of how $\tilde{g}$ could happen to be larger than g at low energies. The naive possibility of decoupling two full twin generations at a high-energy scale

[20] The constraints would be mildly weaker if three twin generations instead of one were to be considered.

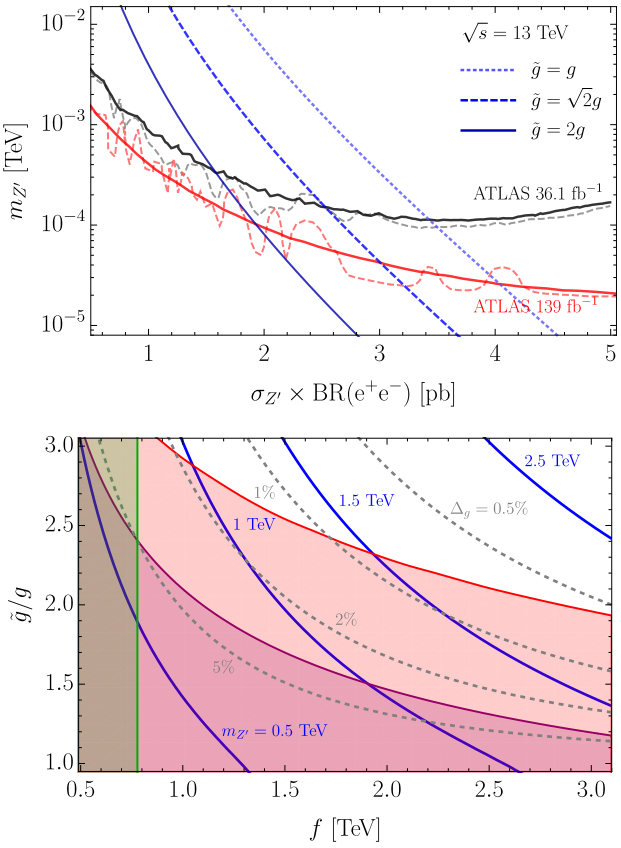

Figure 3.7: (Left) Upper 95% CL limits on Z' cross section times branching ratio to dileptons as a function of the Z' mass from a published search in 36.1 fb^{-1} of data at $\sqrt{s} = 13$ TeV [80] (expected bound as black solid and observed as dashed) and from a more recent search with 139 fb^{-1} [81] (red), as well as the prediction for the twin Z' for different $SU(2)_{\tilde{L}}$ gauge couplings: $\tilde{g} = g, \sqrt{2}g, 2g$ (blue dotted, dashed, solid respectively). (Right) In the plane of Higgs decay constant f and $\tilde{g}/g$, excluded regions from Z' bounds (red shaded), the Y-parameter (purple shaded) and $\xi < 0.1$ (green shaded). Also shown contours of constant twin Z' mass (blue solid) and Higgs tuning (grey dashed), the latter computed with $g_\rho = 6$.

above m_* where $\tilde{g} \approx g$, is at odds with the requirement of approximately equal color and twin-color gauge couplings at m_*. Therefore, other ideas seem to be required (e.g. large threshold corrections or extra $SU(2)_L$-charged matter). These difficulties nevertheless suggest that the easiest realization of our twin Higgs scenario is the minimal one, in which the twin $SU(2)_{\tilde{L}}$ gauge symmetry has been broken above m_*.

3.5 Conclusions

In this Chapter, we have presented a twin Higgs construction that nicely exemplifies the exciting prospects for discovery of these unorthodox low-energy manifestations of theories solving the Hierarchy Problem, where the states that account for the little hierarchy between the Higgs mass and the cutoff m_* of the Higgs sector are colorless but hypercharged. This is a consequence of the symmetry structure of the strong sector, whose dynamics is ultimately responsible for shielding

the EW scale from UV thresholds while giving rise the Higgs in the IR. Besides a Z_2 parity that exchanges color and its twin, a global $SO(7)$ symmetry, spontaneously broken to the G_2, delivers a Higgs and a twin Higgs that carries hypercharge. These couple to the SM fermions and their twins, in particular to a twin top with 2/3 of electric charge, eliminating the leading sensitivity of the Higgs potential to m_*. While this exceptional twin Higgs model admits a full mirroring of the SM, we find that only when the twin gauge bosons are decoupled above m_*, the Higgs VEV and mass can be reproduced with a mild level of fine-tuning, to a good approximation given by $2\xi \approx 10\%$. The misalignment $\xi = v^2/f^2$ between the EW scale and the Higgs decay constant is a common requisite in all the constructions with a composite-NGB Higgs, since its couplings to the SM depart from those of an elementary Higgs proportionally to ξ, and such departures are constrained by both EW precision tests and Higgs couplings measurements.

The exceptional twin Higgs leads to novel phenomenology that we call hypercharged naturalness. The leading indirect effect is found in the loop-induced Higgs coupling to photons, which receives an additional contribution from the twin top making it more SM-like in comparison to other composite Higgs models. The fondness of the twins for hypercharge, that is for photons and Z's, shows up in a striking way in processes where the twins are directly produced. In the fraternal scenario, this quickly drives the model into fine-tuned territory, due to the relatively light Z' that couples to the SM quarks and leptons via the mixing with the B. Much more compelling however is the case where we strip our construction to the bare minimum: the twin pNGBs, the twin top and possibly the twin bottom. While the neutral pseudoscalar ω^0 is almost inert, the electrically charged scalar $\omega^\pm$ is long-lived or stable on collider scales, giving rise to charged tracks that the LHC could soon detect. The twin top/bottom exhibits quirky phenomenology: once pair-produced they lose energy until they are brought back together by the twin-QCD interactions, eventually forming low-lying twin-quarkonium states, either a pseudoscalar η^{-+} or a vector Υ^{--}. The former annihilates mostly to twin gluons, thus becoming another source of twin glueballs besides those from Higgs decays as in other twin Higgs models. The latter either annihilates to SM fermions, thus it could be detected as a Z'-like resonance (although with much smaller cross sections than the fraternal Z'), or to γh and Zh, which can be considered a smoking gun of our exceptional twin Higgs. The production cross sections are small but kinematically accessible at the LHC, and prospects for a detection at the HL-LHC are promising. Finally, the twin glueballs, in particular the lightest 0^{++}, exhibit similar phenomenology as those in other twin Higgs models: they are long-lived if the twin-QCD scale is not considerably above $\Lambda_{\rm QCD}$. Amusingly, some of the glueballs such as the 0^{-+} decay almost certainly to diphotons, and they are very long-lived, especially for a heavy twin bottom. In such a case, these glueballs would leave the LHC detectors as missing energy, and eventually reappear as a pair of photons, to be picked up by a future detector such as MATHUSLA.

Appendices part I

I.A $SO(7)$ and G_2 representation

In this appendix we construct the basis of generators for $SO(7)$ in its spinor **8** representation. We start with the Γ matrices, here written as outer products of the Pauli matrices,

$$\begin{aligned}
\Gamma_1 &= \sigma_1 \otimes \sigma_0 \otimes \sigma_2 \,, \\
\Gamma_2 &= \sigma_2 \otimes \sigma_0 \otimes \sigma_0 \,, \\
\Gamma_3 &= \sigma_1 \otimes \sigma_2 \otimes \sigma_1 \,, \\
\Gamma_4 &= \sigma_1 \otimes \sigma_2 \otimes \sigma_3 \,, \\
\Gamma_5 &= \sigma_3 \otimes \sigma_1 \otimes \sigma_2 \,, \\
\Gamma_6 &= \sigma_3 \otimes \sigma_2 \otimes \sigma_0 \,, \\
\Gamma_7 &= \sigma_3 \otimes \sigma_3 \otimes \sigma_2 \,.
\end{aligned} \tag{I.A.1}$$

From these, a basis of generators is obtained as

$$M_{ij} = \frac{1}{4i} \left[\Gamma_i, \Gamma_j\right] . \tag{I.A.2}$$

It is convenient to define the linear combinations

$$T_L^1 = \tfrac{1}{2}\left(M_{14} - M_{23}\right) , \;\; T_L^2 = \tfrac{1}{2}\left(M_{13} + M_{24}\right) , \;\; T_L^3 = \tfrac{1}{2}\left(M_{12} - M_{34}\right) , \tag{I.A.3}$$

$$T_{\widetilde{L}}^1 = \tfrac{1}{2}\left(M_{14} + M_{23}\right) , \;\; T_{\widetilde{L}}^2 = \tfrac{1}{2}\left(M_{13} - M_{24}\right) , \;\; T_{\widetilde{L}}^3 = -\tfrac{1}{2}\left(M_{12} + M_{34}\right) , \tag{I.A.4}$$

$$T_{\widehat{R}}^1 = M_{67} \,, \;\; T_{\widehat{R}}^2 = -M_{57} \,, \;\; T_{\widehat{R}}^3 = M_{56} \,, \tag{I.A.5}$$

which can be identified as the generators of the $SU(2)_L \times SU(2)_{\widetilde{L}} \times SU(2)_{\widehat{R}}$ subgroups of $SO(7)$. We have normalized the generators as $\mathrm{Tr}[T^A T^B] = \delta^{AB}$, except for those generating $SU(2)_{\widehat{R}}$, which again for convenience we define with s.t. $\mathrm{Tr}[T_{\widehat{R}}^i T_{\widehat{R}}^j] = 2\delta^{ij}$.

The unbroken $SU(2)_{R=\widetilde{L}+\widehat{R}}$ subgroup in G_2 and the corresponding axial combination in $SO(7)/G_2$ are identified as

$$T_R^i = T_{\widetilde{L}}^i + T_{\widehat{R}}^i \,, \tag{I.A.6}$$

$$T^{\hat{a}=i+4} = \tfrac{1}{\sqrt{3}}\big(T_{\widetilde{L}}^i - T_{\widehat{R}}^i\big) \,, \tag{I.A.7}$$

with norm $\mathrm{Tr}[T_R^i T_R^j] = 3\delta^{ij}$. The Higgs generators are

$$\begin{aligned}
T^{\hat{a}=2} &= -\tfrac{1}{\sqrt{6}}\left(M_{15} - M_{26} - M_{37}\right) , \;\; T^{\hat{a}=1} = \tfrac{1}{\sqrt{6}}\left(M_{16} + M_{25} + M_{47}\right) , \\
T^{\hat{a}=4} &= -\tfrac{1}{\sqrt{6}}\left(M_{17} + M_{35} - M_{46}\right) , \;\; T^{\hat{a}=3} = \tfrac{1}{\sqrt{6}}\left(M_{27} - M_{36} - M_{45}\right) ,
\end{aligned} \tag{I.A.8}$$

while the rest of unbroken generators, in G_2, are

$$\tfrac{1}{2}\left(M_{15}+M_{26}\right)\ ,\ \ \tfrac{1}{2}\left(M_{16}-M_{25}\right)\ ,\ \ \tfrac{1}{2}\left(M_{35}+M_{46}\right)\ ,\ \ \tfrac{1}{2}\left(M_{36}-M_{45}\right)\ , \tag{I.A.9}$$

$$\tfrac{1}{2\sqrt{3}}\left(M_{15}-M_{26}+2M_{37}\right)\ ,\ \ \tfrac{1}{2\sqrt{3}}\left(M_{16}+M_{25}-2M_{47}\right)\ ,$$

$$\tfrac{1}{2\sqrt{3}}\left(2M_{17}-M_{35}+M_{46}\right)\ ,\ \ -\tfrac{1}{2\sqrt{3}}\left(2M_{27}+M_{36}+M_{45}\right)\ . \tag{I.A.10}$$

Part II

Interplay between Light New Physics and Matter Density

Chapter 4

Motivation and Introduction

The rich physics of light scalar fields is behind their central role in many scenarios that address the shortcomings of the standard models of cosmology and particle physics, such as the nature of dark matter and dark energy and the electroweak hierarchy and strong-CP problems.

Among those, a particularly well motivated candidate of physics beyond the standard model is the QCD axion [4, 6, 7]. There are many planned and ongoing experiments to look for the QCD axion, with the strongest current constraints coming from astrophysics [103]. Especially the dense environments of supernovae and neutron stars can be used as axion laboratories.

Another interesting aspect of scalar dynamics is associated with the presence of multiple minima of the scalar potential, leading to a plethora of phenomena like false vacuum decay [104,105], early universe phase transitions [106,107], or vacuum selection of a small cosmological constant [108–110] or a small electroweak scale [8, 111–114]. The discovery that our vacuum is just one of many in a landscape would have profound implications for our understanding of particle physics.

Similar to the well-known case of finite temperature, in which the properties of a scalar field change due to its coupling to a thermal bath, in this part of the thesis we wish to explore the much less studied question of the properties of scalar fields in a background of finite density.

Finite density effects on scalar potentials have long been considered for the QCD order parameters, see e.g. [115,116], as well as in the context of chameleon theories, see e.g. [117] for a review. Moreover, it has been recently shown that the potential and the couplings of the QCD axion [118], and of certain deformations thereof [119], change in systems with large baryonic densities, such as neutron stars. In these examples, the coupling of the scalar to a background matter density can displace the field away from its value in vacuum.

As we will see, the displacement of the scalar field also back-reacts on the system with large density. While this can be used to put strong constraints on BSM models that significantly change white dwarfs, neutron stars are much less constrained. The change of the properties of neutron stars is an especially exciting prospect in light of the future NS mergers expected to be seen in LIGO and the increasingly larger stellar remnant catalogue [120–122].

Another intriguing possibility is that the background density displaces the field all the way to a deeper minimum. In this case the dense objects can seed phase transitions in our universe. This leads to strong constraints on some models but also the exciting possibility to detect a change of vacuum. After investigating this is a two minimum toy model, we apply our findings to relaxion models, where we can place novel bounds on previously unconstrained parameter space.

This part of the thesis is organized as follows: in Chapter 5, we introduce the QCD axion, axion-like particle (ALP)s and the relaxion. In Chapter 6 we give a very brief introduction

to stellar remnants. Then in Chapter 7 we investigate how the couplings of the QCD axion change in a density background. In Chapter 8, we investigate how finite density effects on scalar potentials with multiple minima can give rise to field displacements large enough to reach the value of a lower energy minimum. Finally in Chapter 9, we investigate the back-reaction of confined bubble of the scalar field on the matter density.

Chapter 7 is heavily based on [13], Chapter 8 on [11, 12] and Chapter 9 on [14, 15], from which parts of the text and most of the figures are taken.

Chapter 5

The QCD Axion, ALPs and the Relaxion

In this Chapter we introduce the strong $\mathcal{CP}$ problem and the QCD axion as its solution. We investigate the couplings of the QCD axion to matter within ChPT. After a short detour to astrophysical bounds on the QCD axion, we then have a look at a light version of the QCD axion, whose couplings are as the ones of the QCD axion but whose mass are lighter and seemingly tuned [123, 124]. We finish this chapter by a short introduction to the relaxion, an ALP that dynamically solves the EW Hierarchy Problem.

5.1 The Strong $\mathcal{CP}$ Problem and the QCD Axion

The absence of CP violation in the strong interaction is what is known as the strong $\mathcal{CP}$ problem. Let us see in more detail how this problem arises: Let us start with the two flavor QCD Lagrangian,

$$\mathcal{L} = \sum_q \bar{q}\left(i\not{D} + m_q e^{i\gamma_5\theta_q}\right)q - \frac{1}{4}\mathrm{Tr}\left[GG\right] + \theta\frac{g^2}{16\pi^2}\mathrm{Tr}\left[G\tilde{G}\right] \tag{5.1}$$

This Lagrangian has two potential sources of CP violation, the topological term $\mathrm{Tr}\left[G\tilde{G}\right]$ and the angles θ_q. Naively it seems that $\mathrm{Tr}\left[G\tilde{G}\right]$ is a total derivative and thus this term has no influence on the equations of motion and therefore can be discarded. However let us look at chiral rotations: It is well known that the $U(1)_A$ symmetry $q \to e^{i\gamma^5\alpha}$ is anomalous: While it leads to $\theta_q \to \theta_q + 2\alpha$, it can be shown that at the quantum level it also shifts the theta term $\theta \to \theta - 2\alpha$, see e.g. [125]. Because of this, only the linear combination $\bar{\theta} = \theta + \theta_q$ is physical. One can for example show that the vacuum energy of QCD depends on $\bar{\theta}$ [126]. In the dilute instanton approximation one finds [127]

$$E(\theta) = -2Ke^{-8\pi^2/g^2}\cos\left(\bar{\theta}\right). \tag{5.2}$$

Among the $\mathcal{CP}$ violating effects, the most sensitive probe is the neutron electric dipole moment (EDM). The neutron EDM can be defined by the non-relativistic Hamiltonian

$$H = -d_n\boldsymbol{E}\hat{S}, \tag{5.3}$$

with a current bound of $|d_n^{\mathrm{exp}}| < 3.0 \cdot 10^{-26} e$ cm [128]. We can write this in terms of a Lorentz invariant Lagrangian as

$$\mathcal{L} = -d_n\frac{i}{2}\bar{n}\sigma_{\mu\nu}\gamma_5 n F^{\mu\nu}. \tag{5.4}$$

While there are many different techniques to calculate the neutron EDM such as ChPT, QCD sum rules, holography and lattice, we are only interested in an order of magnitude estimation. The operator in question must be generated via an EM loop and an insertion of the phase in the quark matrix. Being a dimension 5 operator, we find using NDA and expanding to linear order in $\bar{\theta}$

$$\mathcal{L} = -\frac{e}{16\pi^2}\frac{i\bar{\theta}m_q}{m_n^2}\bar{n}\sigma_{\mu\nu}\gamma_5 n F^{\mu\nu}. \tag{5.5}$$

While this naive estimation leads to a bound $\bar{\theta} \lesssim 10^{-8}$, a precise calculation based on QCD sum rules [129] leads to the bound $\bar{\theta} \lesssim 10^{-10}$. The smallness of $\bar{\theta}$, i.e. the smallness or absence of the violation of $\mathcal{CP}$ in the strong interactions is the so-called strong $\mathcal{CP}$ problem. While there exist different ideas to solve the strong $\mathcal{CP}$ problem, we focus on a very simple approach: We promote the angle $\bar{\theta} \to \bar{\theta} + \frac{a}{f}$, where a is a dynamical field, the axion and f is a scale called axion decay constant to get the right dimensions. Looking at Eq. (5.2), we find that the vacuum solution is

$$\left\langle \bar{\theta} + \frac{a}{f} \right\rangle = 0, \tag{5.6}$$

so the QCD axion dynamically solves the strong $\mathcal{CP}$ problem. Already from Eq. (5.2), we see that the only parameter determining the QCD axion mass is the decay constant f. Note that in the UV, one introduces a globel $U(1)_{\text{PQ}}$ symmetry, which gets spontaneously broken at the scale f. The QCD axion is the corresponding GB. While in the original proposal [4, 6, 7], the scale f was tied to the EW scale, it soon became clear that this is ruled out experimentally [130]. This lead to the proposal of the so-called invisible axions, in which f is a free parameter. Two benchmark models are the KSVZ [131, 132]and the DFSZ [133, 134] axion, which differ in their couplings to matter. However, in both cases all couplings to the standard model are suppressed by $\frac{1}{f}$.

While we focussed here on the QCD axion, light pseudoscalars appear quite numerously in models beyond the standard model, for example in string theory compactifications, e.g. [135]. It is therefore motivated to not just look for the QCD axion, but also for other light pseudoscalars that do not fulfill the relation between mass and decay constant in Eq. (5.24). These are called axion-like particles (ALPs). They do not fulfil the same relation between mass and decay constant as the QCD axion, and, at the same mass, their couplings to the SM can be very different.

5.2 The QCD Axion Couplings in ChPT

In this section we write down the low energy description of QCD, i.e. ChPT, where we include nucleons as well as the QCD axion as an external field, see e.g. [136]. We use this to determine the couplings of the QCD axion to nucleons. At the end of this section we have a short look at the bounds on these couplings from astrophysical observations.

5.2.1 Axion Couplings in QCD

The Lagrangian of QCD with the axion is given by

$$\mathcal{L} = \mathcal{L}_{\text{QCD}} + \frac{1}{2}(\partial_\mu a)^2 + c_{a\gamma\gamma}\frac{a}{f}F\tilde{F} + \left(\frac{a}{f} + \bar{\theta}\right)\frac{g^2}{16\pi^2}\text{Tr}\left[G\tilde{G}\right] + \frac{\partial^\mu a}{2F}J_\mu^{\text{PQ}}, \tag{5.7}$$

with

$$\mathcal{L}_{\text{QCD}} = -\frac{1}{4}G^{\mu\nu}G_{\mu\nu} + i\bar{q}\not{D}q - \bar{q}\mathcal{M}_q q \tag{5.8}$$

and

$$J_\mu^{\rm PQ} = \sum_q c_q^0 \bar{q}\gamma^\mu\gamma_5 q, \tag{5.9}$$

where the c_q^0 depend on the specific axion realization in the UV (e.g KSVZ or DFZS).

In the limit of vanishing quark masses, this Lagrangian is invariant under

$$SU(N_f)_L \times SU(N_f)_R \times U(1)_V \times U(1)_A, \tag{5.10}$$

however with the $U(1)_A$ being broken at the quantum level. As we go to lower energies, QCD becomes strongly coupled and a quark condensate $\langle \bar{q}_R q_L\rangle \neq 0$ develops. This quark condensate spontaneously breaks

$$SU(N_f)_L \times SU(N_f)_R \times U(1)_V \to SU(N_f)_{L+R} \times U(1)_V. \tag{5.11}$$

From here on we specify on the case of two light flavors, i.e. we treat the mass of the strange quark as heavy. Then this breaking generates three Goldstone bosons, the pions. We now want to write down the low energy description with the axion included. To do this let us perform a chiral rotation on the quark fields, i.e.

$$q \to \exp\left[i\frac{a}{2f}\gamma_5 Q_a\right] q \tag{5.12}$$

with $\mathrm{Tr}Q_a = 1$. As this rotation is anomalous, it eliminates the axion gluon coupling and the axion is rotated into the quark mass term. We then find

$$\mathcal{L}_{\rm QCD} = \mathcal{L}_{\rm QCD,0} - (\bar{q}_L \mathcal{M}_a q_R + \text{ h.c. }) + \frac{1}{2}(\partial^\mu a)^2 + \frac{1}{4} a g_{a\gamma\gamma} F^{\mu\nu}\tilde{F}_{\mu\nu} + \frac{\partial^\mu a}{2f_a} J_\mu^{\rm PQ}, \tag{5.13}$$

with

$$\mathcal{M}_a \equiv e^{\frac{ia(x)Q_a}{2f_a}} \mathcal{M}_q e^{\frac{ia(x)Q_a}{2f_a}} = e^{\frac{ia(x)Q_a}{f_a}} \mathcal{M}_q, \tag{5.14}$$

$$J_{\rm PQ}^\mu = \sum_q c_q \bar{q}\gamma^\mu\gamma_5 q, \tag{5.15}$$

$$c_q \equiv c_q^0 - [Q_a]_q\,. \tag{5.16}$$

From now on we use $Q_a = \frac{\mathrm{diag}[1,z]}{1+z}$, where $z \equiv \frac{m_u}{m_d}$. This choice eliminates the mixing between the axion and the pion in the chiral Lagrangian which we construct later. We then find the rotated couplings to quarks,

$$\begin{aligned} c_{u-d} &= \frac{1}{2}\left(c_u^0 - c_d^0 - \frac{1-z}{1+z}\right), \\ c_{u+d} &= \frac{1}{2}\left(c_u^0 + c_d^0 - 1\right). \end{aligned} \tag{5.17}$$

We identify the interactions of the axions with the quarks as external fields and classify them according to their transformation properties as isovector axial vector a_μ and vector v_μ or isoscalar axial vector a_μ^s and vector v_μ^s as well as scalar and pseudoscalar fields s and p to find

$$\begin{aligned} \mathcal{L}_{a-q} &= -\bar{q}_L \mathcal{M}_a q_R + \text{ h.c. } + \left(\bar{q}\gamma^\mu \frac{\partial_\mu a}{2f_a}\left(c_{u-d}\tau_3 + c_{u+d}\mathbb{1}\right)\gamma_5 q\right)_{q=(u,d)^{\rm T}} \\ &= -\bar{q}_L(s-ip)q_R + \text{ h.c. } + \left(\bar{q}\gamma^\mu\left(v_\mu + v_\mu^s\right)q\right)_{q=(u,d)^{\rm T}} + \left(\bar{q}\gamma^\mu\left(a_\mu + a_\mu^s\right)\gamma_5 q\right)_{q=(u,d)^{\rm T}}, \end{aligned} \tag{5.18}$$

with

$$\begin{aligned} v_\mu &= 0, & v_\mu^s &= 0 \\ a_\mu &= c_{u-d}\frac{\partial_\mu a}{2f_a}\tau_3, & a_\mu^s &= c_{u+d}\frac{\partial_\mu a}{2f_a}\mathbb{1}, \\ s &= \mathrm{Re}\,\mathcal{M}_a, & p &= -\,\mathrm{Im}\,\mathcal{M}_a. \end{aligned} \tag{5.19}$$

5.2.2 QCD Axion Couplings in ChPT

To write down the most general theory compatible with the symmetries of the system, we use again the CCWZ construction [46, 47]. We parametrize the vacuum with a field that is an element of the broken part of the symmetry of the Lagrangian. In this case the broken symmetry is $SU(2)_A$. We parametrize the vacuum by

$$U(\pi(x)) = e^{i\frac{\pi^a(x)\tau^a}{f_\pi}}. \tag{5.20}$$

This field transforms as $U' = R'UL'^\dagger$ under a chiral transformation. We will not explicitly construct the Lagrangian but instead refer the reader to recent reviews on ChPT, e.g. [137]. To leading order, we find

$$\mathcal{L}_\pi^{(2)} = \frac{1}{4}f_\pi^2\left\{\mathrm{Tr}\left[\nabla_\mu U^\dagger \nabla^\mu U + \chi^\dagger U + \chi U^\dagger\right]\right\}, \tag{5.21}$$

where $\nabla_\mu U$ is a covariant derivative given by

$$\nabla_\mu U = \partial_\mu U - ia_\mu U - iUa_\mu - 2ia_\mu^s U. \tag{5.22}$$

At the next to leading order the terms are given by

$$\mathcal{L}_\pi^{(4)} = \sum_{i=1}^{10} L_i P_i + \sum_{j=1}^{2} H_j \tilde{P}_j, \tag{5.23}$$

where explicit expressions can be found in [138]. Using equation (5.21) one can integrate out the pions at tree level to find the axion mass [118, 136]

$$m_a^2 = \frac{m_\pi^2 f_\pi^2}{f_a^2}\frac{m_u m_d}{(m_u+m_d)^2}. \tag{5.24}$$

Let us now also include baryons into our effective description. For this, we introduce the isospin doublet

$$\mathcal{N} = (p, n)^{\mathrm{T}}. \tag{5.25}$$

A convenient way to systematically construct the most general Lagrangian including baryons is the following: We introduce the object

$$u = \sqrt{U} = \exp\left(i\frac{\pi^a\tau_a}{2f_\pi}\right), \tag{5.26}$$

and construct building blocks for the Lagrangian [139]. First, there is a connection

$$\Gamma_\mu = \frac{1}{2}\left[u^\dagger, \partial_\mu u\right] - \frac{i}{2}u^\dagger\left(v_\mu + a_\mu\right)u - \frac{i}{2}u\left(v_\mu - a_\mu\right)u^\dagger. \tag{5.27}$$

Then another building block is

$$\begin{aligned} u_\mu &= i\left(u^\dagger \nabla_\mu u - u \nabla_\mu u^\dagger\right) = i\left\{u^\dagger, \nabla_\mu u\right\} = i u^\dagger \nabla_\mu U u^\dagger \\ &= i\left\{u^\dagger, \partial_\mu u\right\} + u^\dagger\left(v_\mu + a_\mu\right) u - u\left(v_\mu - a_\mu\right) u^\dagger. \end{aligned} \tag{5.28}$$

Since the axion couples not just to an isovector axial current but also to an isoscalar axial current, there is another term with the same transformation property as the one before which one can construct,

$$\begin{aligned} \hat{u}_\mu &= u^\dagger\left(v_\mu^s + a_\mu^s\right) u - u\left(v_\mu^s - a_\mu^s\right) u^\dagger \\ &= u^\dagger a_\mu^s u + u a_\mu^s u^\dagger \\ &= 2 a_\mu^s. \end{aligned} \tag{5.29}$$

Note that the superscript s indicates that it is the isoscalar part of the external gauge field. As we construct explicitly in App. II.A.1, to leading order the Lagrangian is given by

$$\mathcal{L}_{\pi N}^{(1)} = \bar{\mathcal{N}}\left(i\gamma_\mu D^\mu - m + \frac{g_A}{2}\gamma^\mu\gamma_5 u_\mu + \frac{g_0}{2}\gamma^\mu\gamma_5\hat{u}_\mu\right)\mathcal{N}, \tag{5.30}$$

where $D_\mu\mathcal{N} = \partial_\mu\mathcal{N} + \Gamma_\mu\mathcal{N}$ is the covariant derivative. We can now expand the building blocks to first order in the axion field,

$$\begin{aligned} u_\mu =& -\left(\frac{\partial_\mu \pi^a}{f_\pi}\right)\tau^a + c_{u-d}\left(\frac{\partial_\mu a}{f_a}\right)\tau_3 + \frac{1}{6 f_\pi^3}\left(\pi^a\pi^a(\partial_\mu\pi^b)\tau^b + \pi^a\tau^a(\partial_\mu\pi^b)\pi^b\right) + \\ &+ \frac{c_{u-d}\partial_\mu a}{2 f_a f_\pi^2}\pi^a\pi^b\left(\tau^b\delta^{3a} - \tau^3\delta^{ab}\right) + \ldots \\ \hat{u}_\mu =& c_{u+d}\left(\frac{\partial_\mu a}{f_a}\right)\mathbb{1}. \end{aligned} \tag{5.31}$$

This gives us the interaction of the QCD axion with nucleons. Let us simplify further and go to the non-relativistic limit, the so-called heavy baryon chiral perturbation theory (HBChPT). We split the for momentum of the nucleon p^μ into a large piece mv^μ and a residual piece smaller piece l^μ

$$p^\mu = m v^\mu + l^\mu, \quad \text{with} \quad v\cdot l \ll m. \tag{5.32}$$

This splitting enables us to expand the Lagrangian (5.30) in powers of $\frac{l}{m}$ and $\frac{l}{4\pi f_\pi}$. The four momentum v^μ has the properties $v^2 = 1$ and $v^0 \geq 1$, and we can define the projectors

$$P_{v\pm} := \frac{1 \pm \not{v}}{2}. \tag{5.33}$$

At the same time we can split the baryon doublet into two pieces

$$N_v \equiv e^{imv\cdot x} P_{v+}\mathcal{N}, \quad H_v \equiv e^{imv\cdot x} P_{v-}\mathcal{N}, \tag{5.34}$$

a heavy and a light piece. Integrating out the heavy piece H_v using the projection operators, we find the effective Lagrangian of the light fermion,

$$\hat{\mathcal{L}}_{\pi N}^{(1)} = \bar{N}\left\{iv\cdot D + g_A S\cdot u + g_0 S\cdot\hat{u}\right\}N, \tag{5.35}$$

where

$$S_v^\mu = \frac{i}{2}\gamma_5\sigma^{\mu\nu}v_\nu = -\frac{1}{2}\gamma_5\left(\gamma^\mu\not{v} - v^\mu\right), \quad \sigma^{\mu\nu} := \frac{i}{2}[\gamma^\mu, \gamma^\nu]. \tag{5.36}$$

From this, we can now read off the coupling of the axion to protons and neutrons. After expanding in terms of the axion, we find

$$\begin{aligned}\mathcal{L} &\supset g_A \bar{N} S^\mu u_\mu N + g_0 \bar{N} S^\mu \hat{u}_\mu N \\ &= \bar{N} S^\mu \left(\frac{\partial_\mu a}{f_a}\right) \left(c_{u-d} g_A \tau_3 + g_0 c_{u+d}\right) N \\ &= -\bar{N} \left(\frac{\boldsymbol{\sigma}\cdot\boldsymbol{\nabla} a}{2 f_a}\right) \left(c_{u-d} g_A \tau_3 + g_0 c_{u+d}\right) N.\end{aligned} \tag{5.37}$$

From this we define the dimensionless coupling to protons and neutrons as

$$c_p = c_{u-d} g_A + g_0 c_{u+d} \tag{5.38}$$

and

$$c_n = -c_{u-d} g_A + g_0 c_{u+d} \tag{5.39}$$

One particularly important aspect is seen in the KSVZ or hadronic axion, where we have $c_q^0 = 0$: there is a cancellation in the neutron couplings between the two individual contributions, s.t. we find $c_n^{\text{KSVZ}} = 0.02(3)$, so the coupling is suppressed compared to it's expected $O(1)$ value by almost two orders of magnitude. We will see in chapter 7, that this accidental cancellation is lifted at high densities, and that this can have a significant impact on the astrophysical bounds from dense systems like supernovae and neutron stars discussed below.

5.2.3 Astrophysical Bounds on the QCD Axion

The strongest bounds on the axion decay constant and therefore also on the axion mass come from astrophysical observations. In this subsection we review the reasoning behind the bound from SN1987A and comment briefly on NS cooling. For other astrophysical bounds such as white dwarf and red giant cooling, see e.g. [140–143].

The only galactic supernova that we have observed with modern detectors is the NS1987A. We observed alongside with the optical counterpart a distinct neutrino signal in several detectors [144]. The neutrino burst lasted 10 s and agrees reasonably well with theoretical predictions. In recent years self-consistent simulations of core-collapse supernovae (CCSN) are available, see e.g. [145], and agree quite well with data. This implies that any additional energy loss due to the emission of light particles beyond the SM is tightly constrained. A simple criterion by Raffelt [146] states that the energy loss in axions evaluated at $\rho = 3{\cdot}10^{14}\,\text{g}\,\text{cm}^{-3}$ and $T = 30\,\text{MeV}$ is bounded by

$$\epsilon_a \lesssim 1 \times 10^{19} \text{erg g}^{-1}\text{s}^{-1}. \tag{5.40}$$

This can then be compared to the expectation of the energy loss from axion emission. The dominant channel for axion emission is [147] the one-pion exchange diagram (see Fig. 7.8). The emissivity at tree level is well known and together with some simplifications (e.g. set the pion mass to zero) lead to a bound of $f_a \gtrsim 4 \times 10^8$ GeV for the KSVZ axion. Recently, this bound has been revisited including some effects that were neglected before, like non-zero pion mass in the propagator and density dependent nucleon mass [148]. Including these effects changes the bound slightly to

$$g_{an}^2 + 0.61 g_{ap}^2 + 0.53 g_{an} g_{ap} \lesssim 8.26 \times 10^{-19} \tag{5.41}$$

Note however that for all these calculations the vacuum couplings of the QCD axion to nucleons was used. In Chapter 7 we derive the leading order corrections to the couplings of the axion at finite density. We then briefly revisit this bound to include this new effect.

Similar to SN cooling, there also exist bounds from the observation of NS cooling. As before, an additional channel to lose energy is tightly constrained, leading to very strong bounds on the axion coupling, see e.g. [149–152]. In this case, because of the composition of neutron stars, the bound however is much more sensitive on g_{an} and not as much on the coupling to protons g_{ap}. This makes it hard to place robust bounds on the axion decay constant or mass in the case of the KSVZ axion: The coupling of the KSVZ axion is compatible with zero for all f. However, as we also will see in Sec. 7, this is changed if we consider density corrections to the coupling of the axion to neutrons.

5.3 Light QCD Axions

As we have seen above, the mass of the QCD axion is given by Eq. (5.24). This mass comes from non-perturbative effects of QCD. In principle there could be other contributions to the mass of the QCD axion, however these contributions are typically not aligned with the QCD contribution, such that they typically would re-introduce the strong $\mathcal{CP}$ problem. This is the so-called axion quality problem. Because of this, other sources for the axion potential are very constrained and the prediction of the QCD axion mass is quite robust. However quite recently a symmetry based mechanism was found that leads to lighter QCD axions [123, 124]. The model is based on a discrete $\mathcal{Z}_N$ symmetry,

$$\begin{aligned} \mathcal{Z}_N : \mathrm{SM}_k &\to \mathrm{SM}_{k+1(\mathrm{mod}N)} \\ a &\to a + \frac{2\pi k}{N} f_a, \end{aligned} \tag{5.42}$$

where the symmetry is non-linearly realised on the axion. One of the SM is our own, while the others are mirror copies, while all give an aligned contribution to the axion mass, such that for all odd N, the minimum of the axion potential is still at $a = 0$. It is non-trivial to resum all the contributions and we just state the result for large N following [124]

$$m_a^2 \simeq \frac{m_\pi^2 f_\pi^2}{f_a^2} \frac{z^N}{\pi} N^{3/2} \sqrt{\frac{1-z}{1+z}}, \tag{5.43}$$

where $z = \frac{m_u}{m_d} \simeq 0.48$. It is this apparent down-tuning of the QCD axion mass that can give rise to many interesting phenomenological effects, some of which we will explore Sec. 9.1.

5.4 The Relaxion - A Dynamical Solution to the EW Hierarchy Problem

Another model that we want to introduce here is the relaxion. It is an ALP that dynamically solves the EW Hierarchy Problem. In this section we review the relaxion in its original formulation [8], however see e.g. [153–159] for other realisations and stopping mechanisms. The relaxion mechanism solves the Hierarchy Problem up to some cut off M by coupling the Higgs squared term with an ALP in the following manner

$$V(\phi, h) = -\frac{1}{2}\left(M^2 + gM\phi\right) h^2 + \frac{\lambda}{4} h^4 - gM^3\phi - \frac{c_1}{2} g^2 M^2 \phi^2 - \Lambda_B^4(\langle h \rangle) \cos\left(\frac{\phi}{f}\right). \tag{5.44}$$

Here g is a small coupling that breaks the shift-symmetry of ϕ. Note that the continuous shift symmetry of ϕ is broken to the discrete one $\phi \to \phi + 2\pi n$ by the periodic term in the potential.

The relaxion slow rolls down the potential during inflation. It starts at large field values $\phi \sim -2M/g$, thereby scans the Higgs mass $m_h^2 = -(M^2 + gM\phi)$. Once $m_h^2 = 0$, or equivalently $\phi_c = -M/g$, EWSB occurs. Thus, for values $\phi \geq \phi_c$, the Higgs gets minimised at

$$\langle h \rangle = v(\phi) = M\sqrt{\frac{1 + g\phi/M}{\lambda}}. \tag{5.45}$$

The backreaction scale $\Lambda_B^4(\langle h \rangle)$ grows with the Higgs VEV, s.t. after the Higgs get a small VEV, the ϕ potential has a minimum. As the field is slow rolling during inflation, it will stop as soon as a first minimum appears. There are two simple benchmark models for the origin of the barriers: They can originate from QCD, if the field ϕ is the QCD axion. This however has some problems accompanying it: The QCD axion dynamically sets θ_{QCD} as seen above. However, the relaxion minimum is not at $\theta \simeq 0$, but due to the linear slope at $\theta \simeq \pi/2$. Therefore, if one wants to realise the QCD relaxion mechanism, one has to invest in some further model-building, e.g. decreasing the linear slope after inflation by ~ 10 orders of magnitude. An easy way out is to consider a new confining gauge group beyond the SM that generates a (Higgs dependent) potential for the ALP. In this case, if the confinement does not break electroweak symmetry, the potential depends quadratically on the Higgs, i.e. $\Lambda_B^4(h) \sim \Lambda_{\rm C}^4 \frac{h^2}{v^2}$. We refer to this as the non-QCD relaxion below.

While we discuss the precise form of the potential close to the minimum below in Chap. 8, here we review some of the constraints on the Hubble parameter during inflation, which lead us to an upper bound on the cutoff M.

The rolling of ϕ is described by slow-roll during inflation, such that its EOM gives

$$\dot{\phi} = -\frac{V'(\phi)}{3H}. \tag{5.46}$$

Typical quantum fluctuations of the order $\Delta\phi \sim H/2\pi$ smear the axion field over some range in field space. A too large smearing can be avoided assuming classical dominance in the field evolution (using the above equation with $d\phi \sim H$, $dt \sim H^{-1}$)

$$H < \frac{V'(\phi)}{H^2} \rightarrow H < \left(gM^3\right)^{1/3}. \tag{5.47}$$

Appart from constraint (5.47), there are two other conditions on the Hubble scale of inflation. The first is that the vacuum energy during inflation is greater than the vacuum energy change along the ϕ potential, namely M^4, so

$$H > \frac{M^2}{M_{\rm Pl}}. \tag{5.48}$$

Furthermore the Hubble scale of inflation has to be lower than the confinement scale, otherwise the barriers will never form, therefore

$$H < \Lambda_B^4. \tag{5.49}$$

Taking the constraints (5.47), (5.48) and (5.49) one can derive an upper limit on the cut-off

$$M < \left(\frac{\Lambda_B^4 M_{\rm Pl}^3}{f}\right)^{1/6}. \tag{5.50}$$

Thus the relaxion can solve the EW Hierarchy Problem dynamically up to this cutoff. As we will see below in Chap. 8, the relaxion potential is very sensitive to finite density effects. We will there derive novel bounds on the relaxion parameter space originating from density induced phase transitions.

Chapter 6

The Structure of Stellar Remnants

As we have already seen in 5.2.3, dense systems are interesting laboratories to test light new physics. Some of the strongest bounds on the QCD axion couplings come from SN and NS cooling. However, as we will in the next chapters, we have to be careful when setting these bounds: Finite density can have a large influence on new light scalars, for example by changing its coupling to SM particles (Chapter 7). For some models, high density can even trigger a phase transition (Chapter 8). At the same time, these new light scalars can have a large influence on the structure of dense objects, in particular stellar remnants (Chapter 9). To set the stage for these interesting effects, in this Chapter we give a brief introduction to stellar remnants, i.e. to white dwarfs and neutron stars, for a pedagogical introduction see e.g. [160].

In all stars, there is an equilibrium between the crushing force of gravity and the stabilizing pressure that comes either from temperature (e.g. main sequence stars) or from Fermi degeneracy pressure (degenerate stars). The relativistic equations that govern such a system are the so-called Tolman-Oppenheimer-Volkoff (TOV) equations (see e.g. [160]),

$$\begin{aligned} p' &= -\frac{GM\varepsilon}{r^2}\left[1+\frac{p}{\varepsilon}\right]\left[1-\frac{2GM}{r}\right]^{-1}\left[1+\frac{4\pi r^3 p}{M}\right], \\ M' &= 4\pi r^2 \varepsilon, \end{aligned} \tag{6.1}$$

where G is Newtons constant, $M(r)$ the enclosed mass and all derivatives are taken with respect to the radial coordinate.

To describe different stars, we have to know the properties of matter at these densities. These are then encoded in the equation of state (EOS), which relates ε and p. Once an EOS is known, the TOV equations can be numerically integrated to find curves of stellar equilibrium.

6.1 White Dwarfs

White dwarfs are degenerate stars which are the end states of stars with masses below $\sim 8M_\odot$, which were not heavy enough to become a neutron star or black hole [160]. Most of their pressure comes from electron degeneracy pressure, while their mass comes from the non-relativistic nuclei.

Because of charge neutrality the number density of electrons is related to the number density of nucleons, $n_N \simeq \mu_e \rho_e$, where $\mu_e = A/Z$ is the ratio of nucleons per electron. Since white dwarfs are composed of light nuclei, ranging from helium ^{4}He to magnesium ^{24}Mg, the ratio of electrons per nucleons is to good approximation $\mu_e \simeq 2$.

In the following we take a very simple model which can reproduce the main features of white dwarfs: the non-interacting Fermi gas of degenerate electrons and a gas of nuclei. For simplicity,

we take positively charged non-relativistic nuclei with twice the nucleon mass $m_\psi = 2m_N$. The pressure is dominated by the electron contribution, $p = p_e + p_\psi \simeq p_e$, while the nuclei constitute, to good approximation, the entire energy density, $\varepsilon = \varepsilon_e + \varepsilon_\psi \simeq \varepsilon_\psi \simeq m_\psi \rho_\psi$.

Charge neutrality implies $\rho_\psi = \rho_e \equiv \rho$, which we can use to relate the electron Fermi momentum and the nucleon energy density via $k_F = (3\pi^2 \varepsilon/\mu_e m_N)^{1/3}$, which is enough to give the equation of state

$$p(\varepsilon) = \frac{2}{3} \int_0^{k_F(\varepsilon)} \frac{\mathrm{d}^3 k}{(2\pi)^3} \frac{k^2}{\sqrt{k^2 + m_e^2}}. \tag{6.2}$$

Note that we are working in the zero temperature limit.

The equation of state completes the set of equations that describe the balance between the electron degeneracy pressure and gravity, the TOV equations 6.1. One can numerically solve this system for different central pressures $p(r = 0)$. This gives rise to all stable white dwarf configurations which lie on a curve in the mass-radius plane, the so-called mass-radius relation shown in Fig. 6.1. Note that configurations with $\partial M/\partial R > 0$ are not stable. We can estimate the typical radius of white dwarfs as $R_{WD} \simeq \sqrt{8\pi} M_p/(m_e m_p) \sim O(1) \times 10^3$km, while the maximal energy density in white dwarfs is the central density of the most massive stable object and is approximately $\varepsilon_{\max}^{WD} \simeq (O(10)\,\mathrm{MeV})^4$.

6.2 Neutron Stars

Neutron stars are the smallest and densest stars known. While the detailed structure of neutron stars is complicated and unknown (see e.g. [161] for a recent review), to get an order of magnitude estimate, one can model a neutron star as non-interacting neutrons stabilized against gravity by their Fermi pressure. However, we know that at such high densities neglecting interactions is not a very good approximation. Especially the strong force becomes non-perturbative at such high densities and because of this the actual equation of state of neutron star matter is not know from first principle. At the same time modelling dense systems on the lattice is not possible due to the so-called sign problem [162]. This inevitably leads to $O(1)$ theory uncertainties when modelling neutron stars.

We now review the free Fermi gas of neutrons as a first approximation of the EOS of neutron stars. The treatment is very similar to the treatment of white dwarf above. However, this time the pressure as well as the energy density comes from relativistic neutrons, and are given by

$$\varepsilon_n(\rho) \equiv 2 \int^{k_f(\rho)} \frac{\mathrm{d}^3 k}{(2\pi)^3} \sqrt{\mathbf{k}^2 + m_n^2}\,, \tag{6.3a}$$

$$p_n(\rho) \equiv \frac{2}{3} \int^{k_f(\rho)} \frac{\mathrm{d}^3 k}{(2\pi)^3} \frac{k^2}{\sqrt{\mathbf{k}^2 + m_n^2}}\,. \tag{6.3b}$$

From this one can numerically find the EOS, $p(\varepsilon)$, which has to be plugged into Eq 6.1. As for white dwarfs, to find the mass radius curve of equilibrium configurations, one again solves the TOV equations with the corresponding EOS for different central pressures $p(r = 0)$. The result is also shown in Fig. 6.1. Typical densities are of order of nuclear saturation density $\rho_0 \simeq 0.16/\mathrm{fm}^3$, while typical radii can be estimated as $R \simeq \sqrt{8\pi} M_p/m_n^2 \sim O(\text{few})$km.

Note, as already discussed above, the free Fermi gas EOS is a very simplistic model for a neutron star. It cannot reproduce many of the measured properties, e.g. the maximal mass of the free Fermi gas EOS is $\sim 0.7 M_\odot$. However, neutron stars with masses above $2M_\odot$ have been measured [163], and our toy model of the free Fermi gas is no more than an order of magnitude

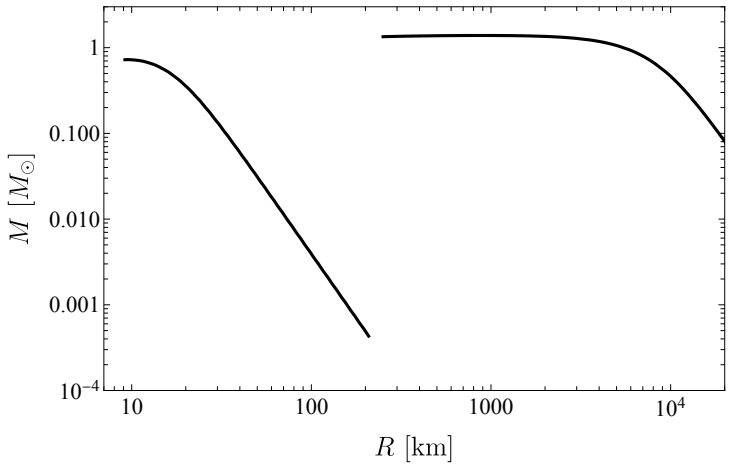

Figure 6.1: Configurations of stellar equilibrium. Right branch: White dwarfs modelled as a free Fermi gas of nuclei and electrons as described in the text. Left branch: Neutron stars as described by a free Fermi gas of neutrons.

estimation of the properties of neutron stars. We nevertheless use these estimates below, in order to study the interplay of some BSM models with high nucleon density.

Chapter 7

QCD Axion Couplings to Nucleons at Finite Density

As we have seen above, some of the strongest bounds on the QCD axion come from supernovae [148, 242] (see Sec. 5.2.3), while bounds from neutron star cooling are in the same ballpart [149–152]. In previous calculations of the axion emission inside these objects, the vacuum couplings of the axion have been employed. It is however well known that couplings in the chiral Lagrangian are density dependent. The density dependence of g_A in Gamov-Teller transitions has been calculated in [164]. Using this density dependence of the couplings of the axion in these dense objects were estimated in [118]. In this Chapter we systematically calculate the axion coupling at finite density in HBChPT.

We start this Chapter by a short review of HBChPT at finite density where we also review the power counting scheme of HBChPT introduced by Weinberg [108]. We then see that in order to get the dominant density corrections to the axion coupling, we need the NLO Lagrangian, which is constructed in App. II.A.1. In Sec. 7.2 we calculate the density corrections to the couplings in the zero temperature limit as well as at finite temperature. In Sec. 7.3 we comment on the relevance of the deformations of the couplings on astrophysical bounds on the QCD axion.

The content of this chapter is based on work in progress [13].

7.1 Heavy Baryon Chiral Perturbation Theory at Finite Density

We have already introduced HBChPT already in Sec. 5.2.2. In this section we first review the power counting scheme introduced by Weinberg [165]. Then we calculate the nucleon propagator at finite density and identify the leading contributions to the axion nucleon coupling at finite density.

7.1.1 Power Counting in Heavy Baryon Chiral Perturbation Theory

In order to systematically see which diagrams do or do not contribute to a process at a given order, we need to organize our diagrams by their relevance. The power counting in effective field theories, especially chiral perturbation theory, was pioneered by Weinberg [165–168], for a more recent discussion we refer to [137,169,170]. We expand the theory in powers of momentum over mass scale, in this case in powers of $\left(\frac{Q}{\Lambda}\right)^{\nu}$, where $\Lambda \simeq 700$ MeV is the QCD scale and p the momentum involved in the process. In general a Feynman diagram will be given by an

expression of the form

$$\delta^{(4)}(p)^C \int \left(d^4q\right)^L \frac{1}{(q^2)^{I_p}} \frac{1}{q_0^{I_n}} \prod_i \left(q^{d_i}\right)^{V_i}, \tag{7.1}$$

where L is the number of loops, I_n (I_p) is the number of internal nucleon (meson) lines, d_i is the number of derivatives or pion mass insertions in the i^{th} vertex, appearing V_i times in the diagram. C counts the number of disconnected diagrams. We can see that such diagrams have a momentum suppression ν of

$$\nu = 4 - 4C + 4L - 2I_p - I_n + \sum_i V_i d_i \tag{7.2}$$

We can use now the identities

$$\begin{aligned} \sum_i V_i n_i &= 2I_n + E_n, \\ \sum_i V_i p_i &= 2I_p + E_p, \end{aligned} \tag{7.3}$$

as well as the topological identity

$$L - C = I_p + I_n - \sum_i V_i, \tag{7.4}$$

to simplify this expression. Here E_n (E_p) is the number of external nucleon (meson) lines in the diagram, n_i (p_i) is the number of nucleon (meson) lines attached to each vertex with index i. We can use Eq. (7.3) to write equation Eq. (7.4) as

$$2(L - C) = -E_n - E_p + \sum_i V_i(n_i + p_i - 2). \tag{7.5}$$

Using this as well as $I_n = \sum_i V_i \frac{n_i}{2} - \frac{E_n}{2}$ we find

$$\nu = 4 + 2(L - C) - \frac{E_n}{2} + \sum_i V_i(d_i + \frac{n_i}{2} - 2). \tag{7.6}$$

As discussed in the references above, due to the different normalization of the multi-particle states,

$$\begin{aligned} 2N: &\quad \langle \boldsymbol{p}_1\boldsymbol{p}_2 \mid \boldsymbol{p}_1'\boldsymbol{p}_2' \rangle = \delta^3\left(\boldsymbol{p}_1' - \boldsymbol{p}_1\right)\delta^3\left(\boldsymbol{p}_2' - \boldsymbol{p}_2\right) \\ 3N: &\quad \langle \boldsymbol{p}_1\boldsymbol{p}_2\boldsymbol{p}_3 \mid \boldsymbol{p}_1'\boldsymbol{p}_2'\boldsymbol{p}_3' \rangle = \delta^3\left(\boldsymbol{p}_1' - \boldsymbol{p}_1\right)\delta^3\left(\boldsymbol{p}_2' - \boldsymbol{p}_2\right)\delta^3\left(\boldsymbol{p}_3' - \boldsymbol{p}_3\right), \end{aligned} \tag{7.7}$$

adding spectator nucleons changes the power counting. This can be circumvented by modifying the counting [170]. We redefine $\nu \to \nu + \frac{3}{2}E_n - 6$ to account for that to find

$$\boxed{\nu = -2 + E_n + 2(L - C) + \sum V_i \Delta_i}, \qquad \Delta_i = d_i + \frac{1}{2}n_i - 2. \tag{7.8}$$

This gives us a consistent power counting in terms of $\left(\frac{p}{\Lambda}\right)^\nu$. However, in HBChPT we simultaneously expand in powers of $\frac{p}{m_N}$. In the following we will use the counting

$$\frac{Q}{m_N} \sim \frac{Q}{\Lambda_\chi}, \tag{7.9}$$

however we also keep in mind that $m_N > \Lambda_\chi$, such that at a given order typically the corrections $\sim \Lambda_\chi^{-1}$ are dominant.

To include the axion in the power counting we first notice that whenever the axion field a appears it comes with a factor of $\frac{1}{f_a}$, where f_a is much larger than all other scales involved. We are interested in processes with one external axion, such that the leading order the amplitude is already $\mathcal{O}\left(\frac{1}{f_a}\right)$. All amplitudes including an additional internal axion are negligible.

We can now compare the pion/nucleon momenta with the one of the axion. Because of the splitting of the nucleon momenta in Eq. (5.32)

$$p^\mu = mv^\mu + k^\mu, \tag{7.10}$$

the residual momentum of the pion and the nucleon will have the relation $v \cdot k \sim \frac{\boldsymbol{k}^2}{2m}$. Since the axion mass is negligible $m_a^2 \simeq 0$, we have

$$(p_a^0)^2 = (\boldsymbol{p}_a)^2. \tag{7.11}$$

This means that it makes no difference in the power counting if the axion couples e.g. like $v \cdot p_a$ or like $S \cdot p_a$:

$$\begin{aligned} v \cdot p_a &\sim p_a^0 \sim \frac{\boldsymbol{p}^2}{2m} \sim \frac{Q}{m} Q, \\ S \cdot p_a &\sim \boldsymbol{\sigma} \cdot \boldsymbol{p}_a \sim |\boldsymbol{p}_a| \sim p_a^0 \sim \frac{Q}{m} Q, \end{aligned} \tag{7.12}$$

where Q is a typical momentum involved.

It is now easy to see now that the leading order axion-nucleon vertex is chiral order $\nu = 0$. There are corrections coming from loops as well as from higher order terms in the Lagrangian at $\nu = 2$.

7.1.2 Finite Density Propagator and Density Loops

Calculations at finite density and temperature are well known, see e.g. [171] for a detailed derivation of propagator in real-time formalism (for a general introduction to finte temperature quantum field theory see e.g. [172]). These techniques have also been applied within ChPT, e.g. in the context of the nucleon potential [173]. In this section we summarize the main points: Following the textbook derivations of the fermion propagator at finite temperature and density, and going to the heavy baryon limit, at leading order we find

$$iG(p,T) = \frac{i}{k^0 + i\epsilon} - 2\pi \left[\delta(k^0 - \frac{\boldsymbol{k}^2}{2m}) \theta(p^0) \frac{1}{e^{\beta(\omega-\mu)} + 1} + \delta(k^0 + 2m)\theta(-p^0) \frac{1}{e^{-\beta(\omega-\mu)} + 1} \right], \tag{7.13}$$

where $\omega \equiv p^0 \simeq m + k^0$ and $\beta = T^{-1}$. Note that we introduced only one chemical potential for the baryons, i.e. for simplicity we looked at mixed matter with an equal amount of protons and neutrons. Conceptually it is also very simple to introduce an asymmetry, as we want when looking at neutron star matter. The momentum k is already the residual momentum of the decomposition (5.32). The first term in equation (7.13) is the normal free-space propagator, while the second term is the so-called "medium insertion" and accounts for the filled Fermi sea of nucleons. In the zero temperature limit, this simplifies to

$$iG(p) = P_+ iG_0(p) P_+ = \frac{i}{k^0 + i\epsilon} - 2\pi\delta(k^0)\theta(p^0)\theta(k_f - |\boldsymbol{k}|). \tag{7.14}$$

It is the medium insertion of this propagator that gives rise to a systematic expansion in $\frac{k_f}{\Lambda_\chi}$. In addition to the usual (vacuum) loop diagrams, for every nucleon momentum in the loop, there is the corresponding term with the density insertion [173]. In Fig. 7.2 we show the leading order ($\nu = 2$) and next-to-leading order ($\nu = 3$) corrections to the nucleon axion vertex with a density insertion. The leading $\nu = 2$ vacuum corrections are already calculated in [174]. Note that to get the $\nu = 3$ density corrections, we need vertices at $\nu = 1$, as the loop adds $\Delta\nu = 2$. To this order, containing at least one axion and one nucleon, the Lagrangian reads as

$$\mathcal{L}^{(0)}_{\pi N} = \bar{N}\left\{iv\cdot D + g_A S\cdot u + g_0 S\cdot \hat{u}\right\} N, \tag{7.15}$$

$$\begin{aligned}\mathcal{L}^{(1)}_{\pi N} = &-\frac{1}{2\mathring{m}_N}\bar{N}\left(D^2 + ig_A\{S\cdot D, v\cdot u\} + ig_0\{S\cdot D, v\cdot\hat{u}\}\right)N + \\ &+\bar{N}\left\{\hat{c}_1\langle\chi_+\rangle + \frac{\hat{c}_2}{2}(v\cdot u)^2 + \hat{c}_3 u^\mu u_\mu + \hat{c}_4\left[S^\mu, S^\nu\right]u_\mu u_\nu + \hat{c}_5\widetilde{\chi}_+ + \right. \\ &\left.+\frac{\hat{c}_8}{4}(v\cdot u)(v\cdot\hat{u}) + \hat{c}_9 u^\mu\hat{u}_\mu\right\}N,\end{aligned} \tag{7.16}$$

and

$$\mathcal{L}^{(1)}_{\pi NN} = \frac{c_D}{2f_\pi^2\Lambda_\chi}(\bar{N}N)\left(\bar{N}S^\mu u_\mu N\right) + \frac{\tilde{c}_D}{2f_\pi^2\Lambda_\chi}(\bar{N}N)\left(\bar{N}S^\mu\hat{u}_\mu N\right). \tag{7.17}$$

The terms $\sim \hat{c}_2$ and $\hat{c}_8$ are suppressed because of the momentum structure and diagrams involving them are one order higher than their formal counting. In the next section, we see how finite density corrections in SN and NS environments, where densities are of the order of nuclear saturation density and higher, can play a large role. Note that the low energy constants that are associated with the isoscalar part of the axion are unknown (as they do not exist in a theory with pions only).

We parametrize the unknown constants according to naturalness similar as in [174]. The large size of $\hat{c}_3$ and $\hat{c}_4$ comes from an enhancement of the Δ resonance going on-shell. Due to isospin selection rules such an enhancement is not there for $\hat{c}_9$. We thus chose a distribution for $\hat{c}^9$ and $\frac{\tilde{c}_D}{\Lambda_\xi}$ that is rather flat around the origin and drops off fast for values $\gg \frac{1}{\Lambda_\chi}$. We parametrize it as a sum of two normal distributions, one around $\frac{0.5}{\Lambda_\chi}$ and one around $-\frac{0.5}{\Lambda_\chi}$, each with a standard-deviation of $\frac{0.5}{\Lambda_\chi}$. In Table 7.2 we summarize the known constants with error bars. Note that for all of the low-energy constants we take the value and error bar from one extraction scheme, however different values quoted by different authors are not necessarily in good agreement.

g_A	g_0	$\mathring{m}_N$
1.25(6)	0.44(6)	872(3)MeV

Table 7.1: Constants in the leading order chiral Lagrangian are taken from [174]. Note that these are the isospin symmetric values at third order and not the physical one.

7.2 The Axion-Nucleon Coupling at Finite Density

We now explicitly evaluate the vertex corrections to the axion mass. This Section is quite technical, as it involves the explicit calculation of all finite density loop diagrams with $\nu \leq 3$. All non-vanishing diagrams are shown in Fig. 7.2. Note that here we evaluate the diagrams at mixed matter, which are conditions similar to a supernova, while for neutron star matter with

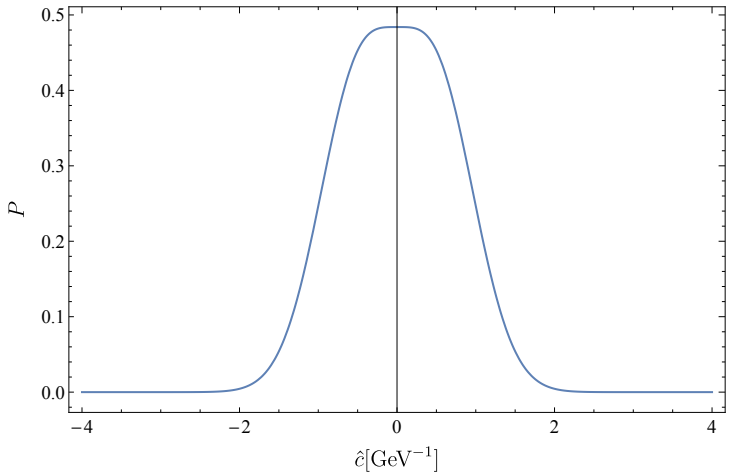

Figure 7.1: The distribution that is used for the unknown constants $\hat{c}_9$ and c_D/Λ_χ in GeV^{-1} as is inspired by dimensional analysis. As discussed in the text, a similar enhancement as for $\hat{c}_{3/4}$ is not expected.

much more neutrons than protons, this can be done in an analogous way. While we only show the calculations for mixed matter, we show the results also for pure neutron matter.

7.2.1 $\nu = 2$ Diagrams

In the first line of Fig. 7.2 we show all non-vanishing diagrams that appear at $\nu = 2$. The are additional ones shown in Fig. 7.3 that evaluate to zero, which can easily be understood: the first diagram gives rise to an in-density mixing of the axion and the pion. We can get rid of this however by a field redefinition. In the limit $m_a \to 0$, this does not generate a new term, and thus these terms have to be $\propto m_a$ and therefore negligible. This can also be checked in an explicit calculation where one finds that they are $\propto (p_a^\mu)^2$. On the other hand, the diagrams cancel each other in pairs, if one plugs in the finite density propagator and evaluates the trivial k^0 integral.

We are thus left with only two different species of diagrams that we need to calculate. The correction coming from the first two diagrams is given by

$$\begin{aligned}\mathbf{V_1} = \int \frac{d^4k}{(2\pi)^4}(-1)\left[-\frac{g_A}{2f_\pi}\boldsymbol{\sigma}\cdot(\boldsymbol{k}-\boldsymbol{p})\tau^a\right]\left[\frac{i}{k^0}-2\pi\delta(k^0)\theta(k_f-|\boldsymbol{k}|)\right]\left[\frac{c_i}{2f_a}\boldsymbol{\sigma}\cdot\boldsymbol{p}_a\right]\times \\ \times\left[\frac{i}{k^0+p_a^0}-2\pi\delta(k^0+p_a^0)\theta(k_f-|\boldsymbol{k}+\boldsymbol{p}_a|)\right]\left[\frac{g_A}{2f_\pi}\boldsymbol{\sigma}\cdot(\boldsymbol{k}-\boldsymbol{p})\tau^b\right]\left[\frac{-i\delta^{ab}}{m_\pi^2-(k-p)^2}\right].\end{aligned} \tag{7.18}$$

We can already see from here that this will only contribute with one higher power of p_a compared to the tree level diagram and is therefore negligible for the typical conditions we consider. Note

$\hat{c}_1$	$\hat{c}_3$	$\hat{c}_4$	$\hat{c}_5$	c_D
$-0.89(6)\text{GeV}^{-1}$	$-4.59(9)\text{GeV}^{-1}$	$3.51(13)\text{GeV}^{-1}$	$-0.09(1)\text{GeV}^{-1}$	0.81(30)

Table 7.2: Low energy constants used in the next section and their errors. The constants $\hat{c}_1$, $\hat{c}_3$, $\hat{c}_4$ are taken from [175], where for c_4 we included an additional term $\frac{\Lambda_\chi}{4\tilde{m}_N}$ (see App. II.A.1), $\hat{c}_5$ is taken from [176], while the central value of c_D is taken from [177].

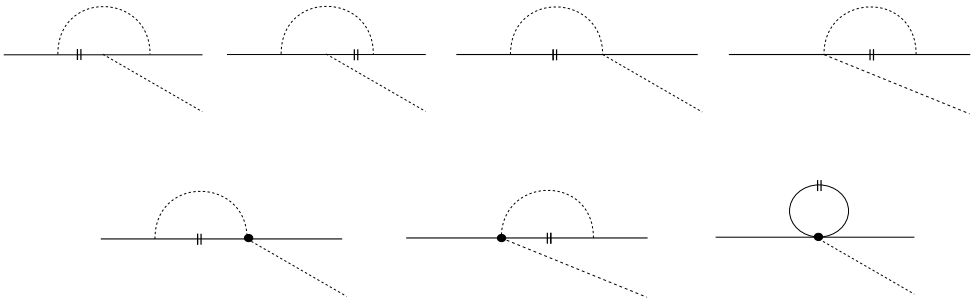

Figure 7.2: First line: all contributing diagrams at $\nu = 2$. Second line: the relevant diagrams at $\nu = 3$. The vertical double line indicates that we used the vertex part of the nucleon propagator. The solid circle indicates that a higher order vertex is used.

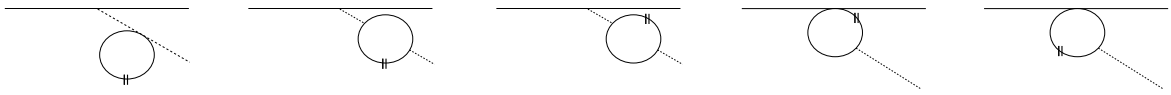

Figure 7.3: Not contributing diagrams at $\nu = 2$. Note that not all diagrams vanish separately, but diagram two and three as well as four and five cancel each other at leading order.

that the above contains the vacuum part along with the finite density contributions. For the density contribution we find (see App. II.A.2 for a sample calculation)

$$\begin{aligned}\mathbf{V_1} = \left(\frac{g_A}{2f_\pi}\right)^2 \frac{1}{p_a^0}\tau^a \frac{c_i}{2f_a}\tau^a \left[2\left(I_1(\tilde{m}_\pi, \boldsymbol{p}, \boldsymbol{p}_a) - I_1(m_\pi, \boldsymbol{p}+\boldsymbol{p}_a, \boldsymbol{p}_a)\right) + \right. \\ \left. - \boldsymbol{\sigma}\cdot\boldsymbol{p}_a \left(I_2(\tilde{m}_\pi, \boldsymbol{p}+\boldsymbol{p}_a) - I_2(m_\pi, \boldsymbol{p})\right)\right].\end{aligned} \tag{7.19}$$

with I_1 and I_2 defined in App. II.A.3. The diagrams three and four in the first line of Fig. 7.2 give

$$\begin{aligned}\mathbf{(1)} = \int \frac{d^4k}{(2\pi)^4}(-1)\left[\frac{c_{u-d}}{2f_\pi f_a} v\cdot p_a \epsilon^{3ab}\tau^b\right]\left[-2\pi\delta(k^0)\theta(k_f - |\boldsymbol{k}|)\right]\times \\ \times\left[\frac{g_A}{2f_\pi}\boldsymbol{\sigma}\cdot(\boldsymbol{k}-\boldsymbol{p}-\boldsymbol{p}_a)\tau^c\right]\left[\frac{-i\delta^{ac}}{m_\pi^2 - (k-p-p_a)^2}\right],\end{aligned} \tag{7.20}$$

$$\begin{aligned}\mathbf{(2)} = \int \frac{d^4k}{(2\pi)^4}(-1)\left[-\frac{g_A}{2f_\pi}\boldsymbol{\sigma}\cdot(\boldsymbol{k}-\boldsymbol{p})\tau^a\right]\left[-2\pi\delta(k^0)\theta(k_f - |\boldsymbol{k}|)\right]\times \\ \times\left[\frac{c_{u-d}}{2f_\pi f_a} v\cdot p_a \epsilon^{3bc}\tau^c\right]\left[\frac{-i\delta^{ab}}{m_\pi^2 - (k-p)^2}\right].\end{aligned} \tag{7.21}$$

We can evaluate the integrals to find (see App. II.A.3 for more details)

$$\mathbf{V_2} = \mathbf{(1)} + \mathbf{(2)} = \frac{c_{u-d} g_A p_a^0}{2f_\pi^2 f_a}\tau^3 \left(I_3(m_\pi, \boldsymbol{p}) + I_3(\tilde{m}_\pi, \boldsymbol{p}+\boldsymbol{p_a})\right). \tag{7.22}$$

At leading order in p_a, this contributes $\propto \frac{m_\pi^2}{(4\pi f_\pi)^2}$. Note that for typical conditions we consider, $k_f \gg m_\pi$, and so the next order diagrams, which scale as $O\left(\frac{k_f^3}{\Lambda_\chi (4\pi f_\pi)^2}\right)$ typically dominate or are of the same size.

7.2.2 Dominant $\nu = 3$ Diagrams

The dominant $\nu = 3$ diagrams are shown in the second row of Fig. 7.2. The vertex (solid dot) can come from multiple terms in the Lagrangian, each with a different structure, and thus we treat them separately. We find

$$\begin{aligned}(\mathbf{1})_1 = \int_{|\boldsymbol{k}|\le k_f} \frac{d^3k}{(2\pi)^3} \left[2i\delta^{3a}\left(\frac{c_{u-d}}{f_\pi f_a}\right)\hat{c}_3\left(k-p-p_a\right)\cdot p_a\right]\left[\frac{-i\delta^{ab}}{m_\pi^2-\left(k-p-p_a\right)^2}\right]\times \\ \times\left[\frac{g_A}{2f_\pi}\boldsymbol{\sigma}\cdot\left(\boldsymbol{k}-\boldsymbol{p}-\boldsymbol{p}_a\right)\tau^b\right]\end{aligned} \tag{7.23}$$

$$\begin{aligned}(\mathbf{1})_2 = \int_{|\boldsymbol{k}|\le k_f} \frac{d^3k}{(2\pi)^3} \left[i\frac{\hat{c}_9 c_{u+d}}{f_\pi f_a}\tau^a\left(k-p-p_a\right)\cdot p_a\right]\left[\frac{-i\delta^{ab}}{m_\pi^2-\left(k-p-p_a\right)^2}\right]\times \\ \times\left[\frac{g_A}{2f_\pi}\boldsymbol{\sigma}\cdot\left(\boldsymbol{k}-\boldsymbol{p}-\boldsymbol{p}_a\right)\tau^b\right]\end{aligned} \tag{7.24}$$

$$\begin{aligned}(\mathbf{1})_3 = \int_{|\boldsymbol{k}|\le k_f} \frac{d^3k}{(2\pi)^3} \left[i\left(\frac{c_{u-d}\hat{c}_4}{f_\pi f_a}\right)\left(\epsilon_{a3b}\tau^b\right)\epsilon_{ijk}\sigma_k\left(k-p-p_a\right)_i p_{aj}\right]\times \\ \times\left[\frac{-i\delta^{ac}}{m_\pi^2-\left(k-p-p_a\right)^2}\right]\left[\frac{g_A}{2f_\pi}\boldsymbol{\sigma}\cdot\left(\boldsymbol{k}-\boldsymbol{p}-\boldsymbol{p}_a\right)\tau^c\right]\end{aligned} \tag{7.25}$$

$$(\mathbf{1})_4 = \int_{|\boldsymbol{k}|\le k_f} \frac{d^3k}{(2\pi)^3} \left[4\hat{c}_5 i\frac{m_a^2 f_a}{f_\pi^3}\tau^a\right]\left[\frac{-i\delta^{ab}}{m_\pi^2-\left(k-p-p_a\right)^2}\right]\left[\frac{g_A}{2f_\pi}\boldsymbol{\sigma}\cdot\left(\boldsymbol{k}-\boldsymbol{p}-\boldsymbol{p}_a\right)\tau^b\right] \tag{7.26}$$

Each of the integrals can be solved and with the help of some manipulations and we find

$$(\mathbf{1})_1 = \left(\frac{g_A c_{u-d}\hat{c}_3}{f_\pi^2 f_a}\right)\tau^3\left(\boldsymbol{p}_a^2 I_3(\tilde{m}_\pi, \boldsymbol{p}+\boldsymbol{p}_a) - I_1\left(\tilde{m}_\pi, \boldsymbol{p}+\boldsymbol{p}_a\right)\right) \tag{7.27}$$

$$(\mathbf{1})_2 = \left(\frac{3g_A\hat{c}_9 c_{u+d}}{2f_\pi^2 f_a}\right)\left(\boldsymbol{p}_a^2 I_3(\tilde{m}_\pi, \boldsymbol{p}+\boldsymbol{p}_a) - I_1\left(\tilde{m}_\pi, \boldsymbol{p}+\boldsymbol{p}_a\right)\right) \tag{7.28}$$

$$(\mathbf{1})_3 = -\left(\frac{g_A c_{u-d}\hat{c}_4}{f_\pi^2 f_a}\right)\tau^3\left[I_1(\tilde{m}_\pi, \boldsymbol{p}+\boldsymbol{p}_a) - \boldsymbol{\sigma}\cdot\boldsymbol{p}_a I_2(\tilde{m}_\pi, \boldsymbol{p}+\boldsymbol{p}_a)\right] \tag{7.29}$$

$$(\mathbf{1})_4 = -\left(\frac{6g_A\hat{c}_5 m_a^2 f_a}{f_\pi^4}\right) I_3(\tilde{m}_\pi, \boldsymbol{p}+\boldsymbol{p}_a), \tag{7.30}$$

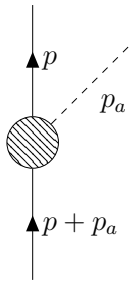

Figure 7.4: Sketch of the effective vertex, where we include all terms up to $\nu = 2$ and the dominant $\nu = 3$ contributions.

where all integrals are again defined in App. II.A.3. We can calculate the second diagrams in an analogous way which we call **(2)**. Summing up all these contributions, we find

$$\begin{aligned}
\mathbf{V_3} &= \mathbf{(1)} + \mathbf{(2)} = \\
&= -\left(\frac{g_A c_{u-d} \hat{c}_3}{f_\pi^2 f_a}\right) \tau^3 \left[-\boldsymbol{p}_a^2 I_3(\tilde{m}_\pi, \boldsymbol{p}+\boldsymbol{p}_a) + I_1\left(\tilde{m}_\pi, \boldsymbol{p}+\boldsymbol{p}_a\right) + I_1\left(m_\pi, \boldsymbol{p}\right)\right] \\
&- \left(\frac{3 g_A \hat{c}_9 c_{u+d}}{2 f_\pi^2 f_a}\right) \left[-\boldsymbol{p}_a^2 I_3\left(\tilde{m}_\pi, \boldsymbol{p}+\boldsymbol{p}_a\right) + I_1\left(\tilde{m}_\pi, \boldsymbol{p}+\boldsymbol{p}_a\right) + I_1\left(m_\pi, \boldsymbol{p}\right)\right] \\
&- \left(\frac{g_A c_{u-d} \hat{c}_4}{f_\pi^2 f_a}\right) \tau^3 \left[I_1\left(\tilde{m}_\pi, \boldsymbol{p}+\boldsymbol{p}_a\right) - \boldsymbol{\sigma}\cdot\boldsymbol{p}_a I_2\left(\tilde{m}_\pi, \boldsymbol{p}+\boldsymbol{p}_a\right) + I_1(m_\pi, \boldsymbol{p}) - \boldsymbol{\sigma}\cdot\boldsymbol{p}_a I_2(m_\pi, \boldsymbol{p})\right] \\
&- \left(\frac{6 g_A \hat{c}_5 m_a^2 f_a}{f_\pi^4}\right) \left[I_3\left(\tilde{m}_\pi, \boldsymbol{p}+\boldsymbol{p}_a\right) - I_3(m_\pi, \boldsymbol{p})\right].
\end{aligned} \tag{7.31}$$

Now there is only one diagram left, with a vertex coming from $\mathcal{L}^{(1)}_{\pi NN}$. Evaluating the loop integral we find

$$\mathbf{V_4} = \frac{\rho}{8 f_\pi^2 f_a \Lambda_\chi} \left(\left(c_D c_{u-d} \tau^3 + \tilde{c}_D c_{u+d}\right) \boldsymbol{\sigma}\cdot\boldsymbol{p}_a\right)_{ij} \tag{7.32}$$

7.2.3 Results

The above calculations give us the leading order density modification of the axion nucleon vertex. Together with the tree level vertex and the vacuum loops [174], we write the effective vertex shown in Fig. 7.4 as

$$\frac{(\boldsymbol{\sigma}\cdot\boldsymbol{p}_a)}{2f_a}\mathcal{A}(p, k_f, p_a, \theta) + \frac{(\boldsymbol{\sigma}\cdot\boldsymbol{p})}{2f_a}\mathcal{B}(p, k_f, p_a, \theta) \tag{7.33}$$

where θ is the angle between the axion momentum $\boldsymbol{p}_a$ and the nucleon momentum $\boldsymbol{p}$ and the isospin structure is hidden inside $\mathcal{A}$ and $\mathcal{B}$. The leading order vertex only contributes to $\mathcal{A}(p, k_f, p_a, \theta)$. In the following we focus on the KSVZ axion, which means we set all $c_q^0 = 0$ in Eq. (5.16). The explicit results for $\mathcal{A}(p, k_f, p_a, \theta)$ and $\mathcal{B}(p, k_f, p_a, \theta)$ can be found in App. II.A.4. To compare the relative sizes, it is beneficial to compare $\mathcal{A}$ wity $\frac{k_f}{|p_a|}\mathcal{B}$, such that the coefficients of both terms have similar size. This is done in Fig. 7.5 and Fig. 7.6 for mixed matter as a function of density (where we recall $k_f = \left(3\pi^2\rho\right)^{1/3}$) using the constants of Table 7.2, making some simplyfing assumptions: As we expect any process at finite density to take place with

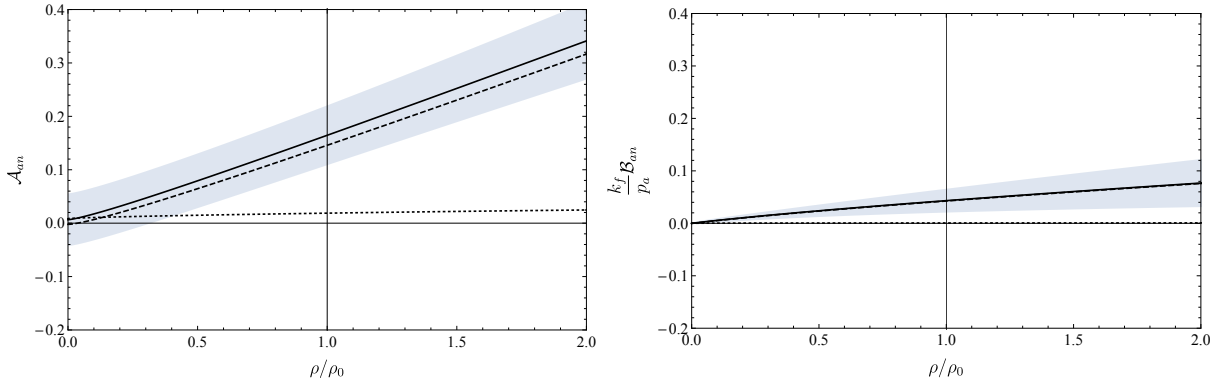

Figure 7.5: The functions $\mathcal{A}$ and $\frac{k_f}{|p_a|}\mathcal{B}$ evaluated for neutrons as a function of density. We show the vacuum loop contribution of [174] (dotted) and the tree level plus density contribution (dashed) together with the full contribution (solid). The one-sigma error bar from the constants chosen in Table 7.1 and Table 7.2 is shown for the full contribution. Note also that higher order terms of ChPT become increasingly important. A ballpark up to where the expansion is under control is one nuclear saturation density $\rho = \rho_0 = 0.16\text{fm}^{-3}$, which we indicate with a vertical line.

momenta given by the Fermi momentum, we set $p \simeq k_f$ and for simplicity we set $\theta = 1/3$. Note that when calculating any specific process, the external momentum will be given or has to be averaged over, both of which actually define p and θ. The dominant error source comes from the uncertainty in the low energy constants of ChPT such as g_0.

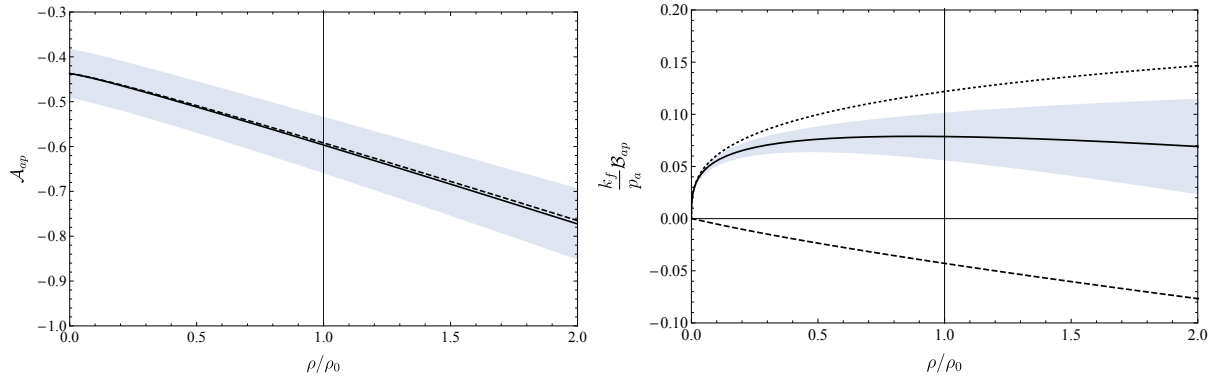

Figure 7.6: The functions $\mathcal{A}$ and $\frac{k_f}{|p_a|}\mathcal{B}$ evaluated for protons as a function of density. The lines the same are as in Fig. 7.5. Note that for $\frac{k_f}{|p_a|}\mathcal{B}$ the dominant contribution comes from the $O\left(\frac{p}{m_N}\right)$ tree level diagrams and not density corrections.

In Fig. 7.7 we show $\mathcal{A}(p, k_f, p_a, \theta)$ and $\mathcal{B}(p, k_f, p_a, \theta)$ for pure neutron matter (see App. II.A.4 for the analytic result as well). In the same appendix we also show that finite temperatures as expected in typical supernova environments, $T \lesssim 50\,\text{MeV}$ have little influence on the results presented here. It is easy to see that the effect of temperature is negligible compared to the density effect. Note that we focussed at the KSVZ axion, where at zero density there was an accidental cancellation in the axion neutron coupling. However we also expect $O(1)$ changes in the couplings for the DFSZ axion.

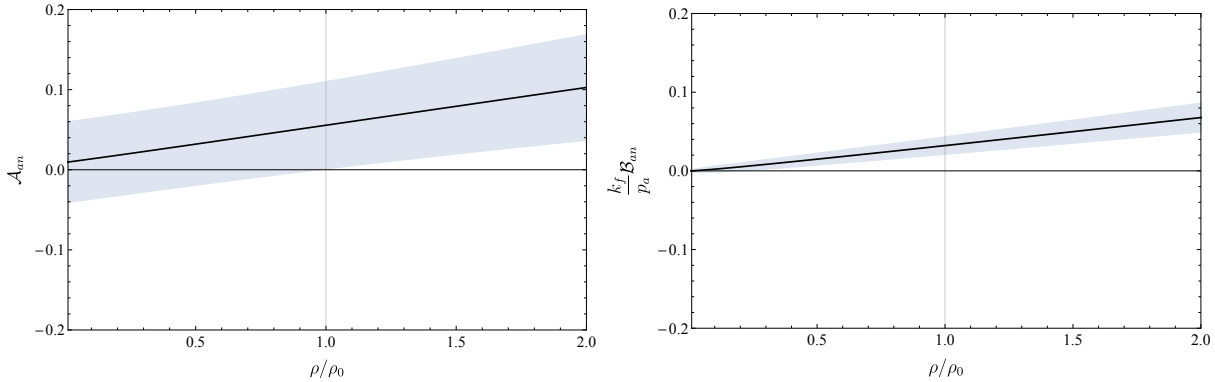

Figure 7.7: The functions $\mathcal{A}$ and $\frac{k_f}{|p_a|}\mathcal{B}$ evaluated for neutrons as a function of density in pure neutron matter. The vacuum contribution of [174] is suppressed compared to the density contribution and not shown explicitly. The one-sigma error bar from the constants chosen in Table 7.1 and Table 7.2 is again shown for the full contribution.

7.3 Implications on Stellar Bounds on Axions

Finite density effects have a large effect on the QCD axion coupling in typical conditions of supernovae and neutron stars. With these at hand we re-asses the bounds on the QCD axion from supernova and neutron star cooling. The common lore is that the dominant process for axion production in these environments is the nucleon Bremsstrahlung process. A crude modelling of this whole process is to take the leading order contribution, the one-pion-exchange, shown in Fig. 7.8. Note that for the full process in total 8 diagrams like this contribute which we get by attaching the axion to different legs and by going from the t-channel to the u-channel. A systematic calculation of the nucleon Bremsstrahlung should go beyond the naive one-pion exchange. While such a systematic calculation at finite density keeping all errors under control is a long term goal, for now we are more modest: we want to calculate the emissivity from the OPE with the density dependent vertex, as shown in Fig. 7.9. The axion emissivity $\dot{\epsilon}_a$ describes the amount of energy emitted by axions per volume of a stellar object (in our case the SN) and time. It is given in units of $\frac{\text{Energy}}{\text{Volume}\times\text{Time}}$ and is defined as [147]

$$\dot{\epsilon}_a = \int d\Pi_1 d\Pi_2 d\Pi_3 d\Pi_4 d\Pi_a (2\pi)^4 S|M|^2 \delta^{(4)}\left(\sum_i p_i\right) E_a f_1 f_2 \left(1-f_3\right)\left(1-f_4\right). \tag{7.34}$$

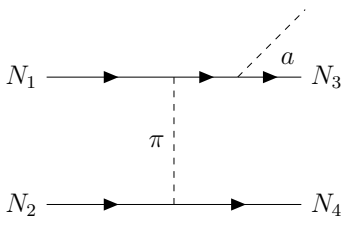

Figure 7.8: The one-pion-exchange diagram with an external axion.

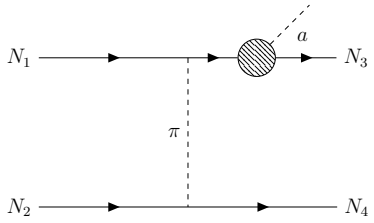

Figure 7.9: The one-pion-exchange diagram with an external axion.

For a systematic expansion of the emissivity we can only expand $|M|^2$ to $O(k_f^3)$. However, as we have seen above, a cancellation of the zero density coupling has been lifted by the finite density contribution. We have no reason to belief that including higher order terms would re-introduce this accidental cancellation. Therefore, to get an idea of the typical size we expect at finite density, we keep also the terms that are formally higher order.

Let us first investigate the supernova bound. For calculation of the density dependent couplings we approximate supernova matter as equal neutrons and protons at zero T. Then numerically calculating the emissivity (Eq. (7.34)) for the KSVZ axion and comparing it to the emissivity using vacuum couplings, at typical densities of a supernova of $\rho \simeq \rho_0 = 0.16/\text{fm}^3$ and $T \simeq 30\,\text{MeV}$, we find

$$\frac{\dot{\epsilon}_a^{\text{full}}}{\dot{\epsilon}_a^{\text{vac}}} \simeq 1.6. \tag{7.35}$$

This gives us a first approximation of the effect that the density dependence of the couplings has on supernova bounds of the QCD axion, while it is ongoing work to use a realistic supernova model [178] to calculate the axion luminosity with density dependent couplings.

While the effect of the density dependence of the couplings on the supernova bound is already $O(1)$, we expect an even more dramatic change of the neutron star cooling bound on axions: At zero density, the KSVZ axion - neutron coupling is compatible with zero. This means that using this coupling, neutron star cooling cannot set a bound on f_a and therefore on the axion mass. However, we found that it is not constant and definitely not compatible with zero at all densities. The exploration of this bound is ongoing work and will also be presented in a future publication.

Chapter 8

Phase Transitions from Stars

In this Chapter we investigate the possibility of detecting a transition between different vacua that is triggered by dense objects such as stars.

To make the discussion of the physics as transparent as possible, in the first Section of this Chapter we work with a simple potential à la Coleman [104], that is a quartic function of a single scalar field ϕ, with a Z_2 symmetry $\phi \to -\phi$, which is explicitly broken by a linear term, and with the scalar field in vacuum sitting at the metastable minimum.

The barrier separating the two minima is argued to decrease with density, thus for sufficiently high densities the metastable minimum disappears, leading to the formation of a non-trivial scalar profile within the dense system. Interestingly, we find that depending on the density profile and evolution of the star, an instability takes place such that the bubble permeates through the entire system, escapes and propagates to infinity, due to the fact that the scalar inside the bubble is in the preferred energy configuration also outside the star. These seeded phase transitions could have catastrophic implications for our universe.

Since our main focus is on transitions to the true vacuum that are classically allowed, they take place as soon as stars that are dense and large enough are formed. Such a late phase transition, at redshifts of around $z \sim 20$, changes the vacuum energy with respect to that inferred from measurements of the CMB. This allows us to place bounds on the parameters of the scalar potential that depend on the type of stars triggering the phase transition. Still, if the energy difference between the two minima is sufficiently small, such phase transitions could be non-lethal and potentially detectable with future cosmological and astrophysical observations.

In the second part of this chapter we apply the results to relaxion models [8], where the scalar potential is a tilted cosine with its magnitude set by the QCD quark condensate or the Higgs VEV, which are sensitive to baryonic densities as those in stars. The formation and escape of such bubbles lead to strong new constraints on the parameter space of these models.

All figures and large parts of the text of this chapter are taken from [11] and [12].

8.1 Density induced Vacuum Instabilities

In Sec. 8.1.1 we present the simple two minimum scalar potential that we take as case study and discuss how it can change at finite density. Sec. 8.1.2 describes the essential properties of the systems of interest, i.e. the stars. Classical bubble formation and dynamical evolution are discussed in Sec. 8.1.3, along with the derivation of the conditions leading to bubble escape. In this section we also comment on quantum bubble formation via tunneling assisted by finite density. In Sec. 8.1.4 we explore the main phenomenological consequences of a late-time phase transition and derive the corresponding constraints on the scalar potential. In App. II.B we

discuss some supplementary approximations and the relevance of ultra-high densities as well of gravitational forces on the bubble dynamics.

8.1.1 General Scalar Potential

The potential we consider is just the familiar quartic potential with a linear tilt,

$$V(\phi) = -\tfrac{1}{3\sqrt{3}}\,\Lambda_{\rm R}^4\,\frac{\phi}{f} + \tfrac{1}{8}\,\Lambda_{\rm B}^4\left(\frac{\phi^2}{f^2}-1\right)^2 . \tag{8.1}$$

$\Lambda_{\rm R}$ and $\Lambda_{\rm B}$ are the scales that control the size of what we denote as linear "rolling" and quartic "barrier" terms respectively (numerical factors are introduced for notational convenience), while f parametrizes the field distance between the two minima. The potential has two minima as long as

$$\delta^2 \equiv 1 - \frac{\Lambda_{\rm R}^4}{\Lambda_{\rm B}^4} > 0\,. \tag{8.2}$$

For $1-\delta^2 \ll 1$ the minima are located at $\phi_\pm \simeq \pm f$, and in particular the metastable minimum ϕ_- is a *deep* minimum. Instead, for $\delta^2 \ll 1$ the minima are at $\phi_- \simeq -f/\sqrt{3}$ and $\phi_+ \simeq 2f/\sqrt{3}$, and ϕ_- is *shallow*. The difference between these two types of metastable minima is evident from the mass of the scalar

$$m_\phi^2 \simeq \begin{cases} \sqrt{\frac{2}{3}}\frac{\Lambda_{\rm B}^4}{f^2}\delta\,, & \text{(shallow)} \\ \frac{\Lambda_{\rm B}^4}{f^2}\,. & \text{(deep)} \end{cases} \tag{8.3}$$

For a shallow minimum ($\delta^2 \ll 1$) the mass is parametrically suppressed with respect to the usual expectation, which is instead reproduced in the case of a deep minimum ($1-\delta^2 \ll 1$). Another quantity of phenomenological interest, which is very different between shallow and deep minima, is the height of the potential barrier,

$$\Delta V_{\rm top} \simeq \begin{cases} \frac{4}{27}\sqrt{\frac{2}{3}}\,\Lambda_{\rm B}^4\,\delta^3\,, & \text{(shallow)} \\ \frac{1}{8}\,\Lambda_{\rm B}^4\,. & \text{(deep)} \end{cases} \tag{8.4}$$

The suppression of the barrier in the case of minima with $\delta^2 \ll 1$ implies that even a small perturbation of the potential can easily destabilize the scalar field.

Let us note that while shallow metastable minima might naively be deemed as tuned, they naturally appear in relaxion models [8], where the barrier term is a periodic function of the scalar field, e.g. $\cos(\phi/f)$, whose amplitude increases very slowly with each ϕ oscillation. There, the first minima of the potential are found when the barriers get just large enough, i.e. $\Lambda_{\rm B}^4 \approx \Lambda_{\rm R}^4$, or in our notation $\delta^2 \ll 1$. The quartic potential we have taken as a case study in Eq. (8.1) is a simplified version of the relaxion case.

Finite density

Finite density can impact a scalar potential in several ways, depending on how the scalar couples to the matter fields that constitute the dense system. In general, density corrections can be encoded as an additional term in the potential that explicitly depends on density, n, and vanishes in vacuum, i.e. $n = 0$. For the sake of concreteness, in this work we focus on the scenario where these corrections can be entirely encoded as a non-trivial density dependence of the parameters

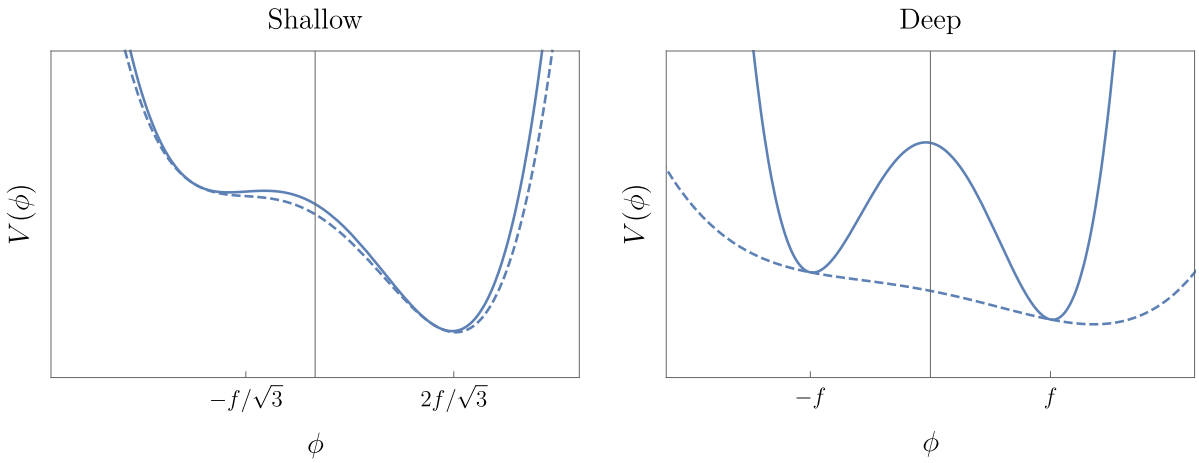

Figure 8.1: Potentials with shallow (left) and deep (right) minima in vacuum (solid) and in medium for a density n slightly larger than critical (dashed).

of the potential Eq. (8.1). In particular, we consider the situation where the barrier $\Lambda_{\rm B}$ depends on density, and define the dimensionless quantity

$$\frac{\Lambda_{\rm B}^4(n)}{\Lambda_{\rm B}^4} \equiv 1 - \zeta(n)\,, \tag{8.5}$$

with $\zeta(n) \geqslant 0$ and $\zeta(0) = 0$.

This scenario is naturally realized when $\Lambda_{\rm B}$ itself is determined by the vacuum expectation value of an operator that is sensitive to finite density corrections. Perhaps the simplest example in the SM is provided by the QCD quark condensate, that is $\Lambda_{\rm B}^4 \propto \langle\bar{q}q\rangle \sim \Lambda_{\rm QCD}^3$, which is well-known to linearly decrease with (small) baryon density $n_b = \langle B^\dagger B\rangle$ [115]. In the notation of Eq. (8.63), this would imply, at leading order in density, that $\zeta(n_b) \propto n_b/\Lambda_{\rm QCD}^4$ in systems with a non-zero nucleon density, such as stars. The case of a $\Lambda_{\rm B}$ proportional to any other QCD condensate that is non-zero in vacuum and changes with baryon density, such as a gluon condensate, belongs to the same class. Within the realm of SM operators, the only other qualitatively different case is given by a barrier set by the Higgs VEV, that is $\Lambda_{\rm B}^4 \propto \langle h^2\rangle = v^2$. There, the coupling of the Higgs field to fermions, $y_\psi h\bar{\psi}\psi$, displaces its expectation value when in a (non-relativistic) ψ background, $\langle\bar{\psi}\psi\rangle \simeq \langle\psi^\dagger\psi\rangle \neq 0$. Considering once again a system with a non-vanishing baryon density, the small displacement in the Higgs would lead, at leading order, to $\zeta(n_b) \propto n_b/m_h^2 v^2$. Let us note that $\Lambda_{\rm B}^4 \propto \langle\bar{q}q\rangle$ is realized by the QCD-axion [118,119], as well as by those models of relaxation of the electroweak scale where the relaxion is identified with the QCD-axion [8]. The case where the leading finite density effects are due to a shift of the Higgs field, $\Lambda_{\rm B}^4 \propto \langle h\rangle^2$, is found in non-QCD relaxion models [8], and it could arise as well in more general Higgs-portal models, e.g. [179]. A detailed discussion of finite density effects in these versions of the relaxion is found below. Going beyond the SM, we could, for instance, entertain the possibility that $\Lambda_{\rm B}$ originates from the confinement of a new QCD-like dynamics decoupled from the SM. Motivated by this case, we should further consider the existence of dark compact objects, a.k.a. dark stars [181–189], whose non-zero density can lead to a change of the scalar potential as in Eq. (8.63).

Because of the smaller barriers at finite density, the metastable minimum in vacuum is no longer a minimum in a dense system as soon as the condition Eq. (8.57), with $\Lambda_{\rm B}^4 \to \Lambda_{\rm B}^4(1-\zeta)$,

is not satisfied. The critical value of ζ above which this destabilization occurs is

$$\zeta_c = 1 - \frac{\Lambda_{\rm R}^4}{\Lambda_{\rm B}^4} = \delta^2 \,. \tag{8.6}$$

It is evident from this expression that a shallow local minimum is more easily destabilized than a deep one, since $\zeta_c \ll 1$ for a shallow minimum while $\zeta_c \approx 1$ for a deep one. This is explicitly shown in Fig. 8.7.

We limit our discussion to $\zeta(n) \leqslant 1$, since otherwise the barrier term changes sign and the scalar potential is no longer bounded from below. This makes the analysis sensitive to higher-order terms in ϕ, which we have implicitly neglected; in other words, the scalar dynamics becomes UV sensitive and therefore no longer predictive. In addition, note that for what concerns the destabilization of the false vacuum, the relevant quantity is the ratio between the rolling and barrier scales. Therefore, we could just as well have considered a density dependent rolling term, $\Lambda_{\rm R}^4(n)$, as the source of the instability. However, as we show in Sec. 8.1.3, the formation of a scalar bubble inside a dense system of finite size, as well as its evolution, strongly depends on the magnitude of the rolling term. For this reason, in this work we keep $\Lambda_{\rm R}$ density independent. Let us also point out that density is treated here a background field that eventually depends on space and time, see Sec. 8.1.2. Although we are phrasing our discussion of the fate of the metastable minimum in terms of a matter density, a priori other space-time dependent background fields could lead to similar effects on the scalar potential. An example where the role of density is played by a background electro-magnetic field will be presented for a relaxion model in Section 8.2.

As discussed above, for densities above the critical one, the scalar potential has a single minimum. We denote this minimum as $(\phi_+)_n$, such that it is clear that it is continuously connected, as the density is taken to zero, to the stable minimum in vacuum, ϕ_+. Let us note that close to criticality, i.e. for $\zeta(n) \simeq \zeta_c$, the in-density potential has the same form as a potential in vacuum with $\delta^2 \ll 1$, thus $\phi_{+\,n\simeq n_c} \simeq 2f/\sqrt{3}$. For the same reason, just before the critical density is reached, the in-medium metastable minimum is shallow and found at $-f/\sqrt{3}$, regardless of its value in vacuum ϕ_-. In contrast, far beyond the critical density, the single minimum of the potential is found at

$$\phi_{+\,n\gg n_c} \sim \left(\frac{1-\zeta_c}{1-\zeta(n)}\right)^{1/3} f \,, \tag{8.7}$$

which can be much larger than f if $\zeta \to 1$. Whenever the scalar potential has two minima, shallow or deep, at zero or non-zero density, the difference in the ground state energy between them is given by

$$\Delta\Lambda \sim -\Lambda_{\rm R}^4 \,, \tag{8.8}$$

up to an irrelevant $O(1)$ factor.

We would like to emphasize that while in this Section we focus on a simple potential of the form Eq. (8.1), the analysis presented here is then applied in Sec. 8.2 to other types of potentials containing local minima separated by a density-dependent barrier. Furthermore, even though we pay particular attention to the fact that at finite density the scalar field can classically move to the true minimum of the potential, this is not the only case of interest; such a change of minimum could be classically forbidden at finite density as well, yet take place anyway due to a much shorter quantum-mechanical lifetime than in vacuum (see Sec. 8.1.3).

Let us comment here on the UV sensitivity of the scalar potential Eq. (8.1) and our assumptions on how it changes at finite density. Indeed, let us consider the case that $\Lambda_{\rm B}^4 = \alpha\langle h\rangle^2$, where

α is just a proportionality factor. By closing the Higgs loop and cutting it off at a scale Λ_h, we obtain a contribution to the barrier term $\Delta\Lambda_{\rm B}^4 \sim \alpha(\Lambda_h/4\pi)^2$. We should then demand that this extra contribution does not erase the instability of the local minimum at finite density, which means $\Delta\Lambda_{\rm B}^4 \ll \Lambda_{\rm B}^4(n_c) \simeq \Lambda_{\rm R}^4$. This conditions translates into an upper bound on the cutoff of the scalar theory, $\Lambda_h \ll 4\pi\langle h\rangle\sqrt{1-\delta^2}$. Note this is larger for potentials with a shallow metastable minimum than for those with a deep minimum. Such a low cutoff does not endanger our analysis of the scalar field dynamics at finite density as long as $\Lambda_h \gg E_{\rm S}$, where $E_{\rm S}$ is the typical energy scale of the dense system. Similar conclusions apply to the other possible cases concerning the density dependence of $\Lambda_{\rm B}$, see the discussion below Eq. (8.63).[1] Besides, already from the quartic scalar interaction in Eq. (8.1), naturalness arguments indicate that new physics should appear at a scale $\Lambda_\phi \sim 4\pi f$ or below. Once again, we should demand that Λ_ϕ is significantly above $E_{\rm S}$.

8.1.2 Spherically Symmetric Dense Systems

We are interested in dense systems of finite size, in particular stars. We model the star as a spherically symmetric (non-rotating) object with a density profile that in general depends on radius and time, i.e. $n(r,t)$. The profile satisfies ($n' = dn/dr$),

$$n'(0,t) = 0\,, \qquad n(R_{\rm S}(t),t) = 0\,, \tag{8.9}$$

such that the density profile is differentiable at the origin, $r = 0$, and that the star ends at a finite radius, $r = R_{\rm S}$, respectively. In addition, we define a transition radius, $r = R_{\rm T}$, where the critical density is reached,

$$n(R_{\rm T}(t),t) = n_c\,. \tag{8.10}$$

We recall that at densities above critical, the local minimum of the potential is lost.

Since the scalar potential at finite density is minimized at a different value than in vacuum, minimization of the action forces the field to acquire a (spherically symmetric) non-trivial profile within and around the star, $\phi(r,t)$. This is determined by the classical EOM ($\dot\phi = d\phi/dt$, $\phi' = d\phi/dr$ and $V_{,\phi} = dV/d\phi$)

$$\ddot\phi - \phi'' - \frac{2}{r}\phi' = -V_{,\phi}\,, \tag{8.11}$$

where $V = V(\phi, n(r,t))$, with the boundary conditions

$$\phi'(0,t) = 0\,, \qquad \lim_{r\to\infty}\phi = \phi_-\,. \tag{8.12}$$

In order to solve Eq. (8.11) one needs to know the density profile of the star, which generically depends on non-trivial and in some cases not well-understood dynamics (e.g. the inner regions of neutron stars). If there is a large separation of scales in the problem, we can however, as a first approximation, be agnostic of the details of the density profile, as we explain in the following. The characteristic scale controlling the classical evolution of the scalar profile, either in time or space, is determined by its potential. For the representative case that we are considering, Eq. (8.1), the EOM for the dimensionless field $\hat\phi \equiv \phi/f$ can be written as

$$\frac{\partial^2\hat\phi}{\partial\hat t^2} - \frac{\partial^2\hat\phi}{\partial\hat r^2} - \frac{2}{\hat r}\frac{\partial\hat\phi}{\partial\hat r} = 1 - \tfrac{3\sqrt{3}}{2}\frac{1-\zeta}{1-\zeta_c}(\hat\phi^2-1)\hat\phi\,, \tag{8.13}$$

[1] $\Lambda_{\rm B}$ is insensitive to the UV if e.g. the barrier term arises from the coupling of the scalar to the QCD topological charge, i.e. $\frac{1}{f}\phi G\tilde G$, which gives rise to a potential sensitive to $\Lambda_{\rm QCD}$ only. For instance, this is the case of the QCD-relaxion, where we recall that the corresponding scalar potential is of the form $\cos(\phi/f)$ instead of the simple quartic function we are considering.

where $\hat{r} = \mu r$, $\hat{t} = \mu t$, and

$$\mu^2 = \tfrac{1}{3\sqrt{3}} \frac{\Lambda_{\rm R}^4}{f^2} \sim \frac{\Lambda_{\rm R}^4}{f^2} \,. \tag{8.14}$$

For densities sufficiently above the critical one, such that $1 - \zeta \ll 1 - \zeta_c$, μ^{-1} sets the typical time and distance required for the scalar to move by $\Delta\hat{\phi} = O(1)$. This is to be compared with the characteristic scales of the dense system.

Let us first discuss time evolution, i.e. the formation of the star. The dimensionless quantity $\mu T_{\rm S}$, where $T_{\rm S}$ is the characteristic time scale of the dense system, gives us a rough idea whether we can treat the evolution of the scalar field as effectively taking place in a nearly static, fixed system, or whether the time dependence of the scalar profile is comparable to (or much slower than) the typical time scale of the star. Indeed, for $\mu T_{\rm S} \gg 1$ the field reacts fast to changes in the background density profile, therefore we can describe the scalar dynamics as a *quasi-static* (or *adiabatic*) process, in which $\dot{\phi}$ and additional time derivatives can be neglected. On the other hand, for $\mu T_{\rm S} \ll 1$ the field reacts slow compared to the evolution of the star, in which case the evolution of the scalar profile can be described in a *sudden* (or *non-adiabatic*) approximation, where the formation of the star can be treated as an instantaneous change from vacuum to $n(r) \neq 0$ and ϕ starts "rolling" down the in-medium potential.

In the adiabatic limit, $\mu T_{\rm S} \gg 1$, the scalar profile can be found at any given time $t = \bar{t}$ during the formation of the star by solving its *time-independent* EOM, within a fixed background density $n(r) = n(r, \bar{t})$.We shall consider simple density profiles that can be parametrized as

$$n(r) = n_o(\bar{t})\, g(r/R_{\rm S}(\bar{t}))\,, \tag{8.15}$$

where the function $g(x)$ fully encodes the radial dependence, with $g(0) = 1$ such that the density at the center is set by n_o, $g(R_{\rm T}R_{\rm S}) = n_c/n_o$, and $g(1) = 0$. While obtaining the specific form of $n(r)$ at a given $\bar{t}$ is generically a complicated problem, the only quantities of qualitative relevance for our analysis are $R_{\rm T}$, the radius below which the critical density is surpassed, that is where the in-vacuo potential barrier disappears and the scalar can potentially be displaced by $O(f)$, and $\Delta R_{\rm T} = R_{\rm S} - R_{\rm T}$, the size of the transition region towards the end of the star, where the potential barrier reappears to its full form. We find that non-trivial dynamics take place when $\mu R_{\rm T} \sim 1$, and additionally when $\mu \Delta R_{\rm T} \sim 1$, see Sec. 8.2.2.A. The value of $R_{\rm T}$ depends on the value of the critical density, which in turn depends on how the scalar potential changes with density. For typical density profiles in which the central density is significantly larger than the critical one, one generically finds $R_{\rm T} \sim R_{\rm S}$ [160, 190]. This then implies that $\Delta R_{\rm T} \sim R_{\rm S}$ as well. In addition, since in practice each class of stars, e.g. neutron stars, white dwarfs, or main-sequence stars like the Sun, covers a range of radii, we also expect to find a range of values for $R_{\rm T}/R_{\rm S}$ and $\Delta R_{\rm T}/R_{\rm S}$, where generically both ratios are $O(1)$.

We only concentrate on the adiabatic limit just described. Since a non-trivial scalar profile develops when $\mu R_{\rm S} \sim 1$, we focus on stellar processes where the relevant time scale is $T_{\rm S} \gg R_{\rm S}$. As an example, let us discuss the interesting case of neutron stars, since they exhibit the largest (baryonic) densities and the fastest dynamics, and assume that densities prior to the birth of the neutron star are below the critical density, which to be concrete we fix at nuclear saturation density, $n_c = n_0 \approx 0.16/\mathrm{fm}^3 \approx (110\,\mathrm{MeV})^3$. The birth of a neutron star follows from the gravitational collapse of the core of a massive star, which leads to a supernova (SN) explosion, see e.g. [191, 192]. While the details of this process are not completely understood, it has been reliably inferred that densities reach and surpass nuclear saturation in a time $T_{\rm S} = T_{\rm NS} \sim 1\,\mathrm{s}$. Within this time, the size of the core of the star in which densities have exceeded n_0 is an $O(1)$ fraction of the total size of the final neutron star, i.e. $R_{\rm T} \sim R_{\rm S} = R_{\rm NS}$. Since the typical radius of a neutron star is $R_{\rm NS} \sim 10\,\mathrm{km}$, we find $R_{\rm NS} \ll T_{\rm S}$, justifying the quasi-static approximation.

Similar conclusions can be reached for other types of stars, for instance white dwarfs, with typical radii $R_{\rm WD} \sim 10^3\,\text{km}$ and densities $n_{\rm WD} \sim$ MeV^3, or the Sun ($R_\odot \approx 7\times10^5\,\text{km}$, $n_\odot \approx 7\times 10^{-9}\,\text{MeV}^3$). In any case, for completeness we briefly discuss the regime $\mu T_{\rm S} \ll 1$ in App. II.B.5.

For the reader's reference, the scale μ^{-1} is of order of the typical size of a neutron star for e.g. the potential parameters

$$\mu R_{\rm S} \sim 5 \left(\frac{R_{\rm S}}{10\,\text{km}}\right)\left(\frac{\Lambda_{\rm R}}{10\,\text{eV}}\right)^2\left(\frac{1\,\text{TeV}}{f}\right) . \tag{8.16}$$

Several additional comments are in order. First, in the special case that the (central) density happens to be very close to n_c, one naturally expects $R_{\rm T} \ll R_{\rm S}$, making the analysis more sensitive to the specifics of the density profile. Second, since the reaction time of the scalar gets suppressed by $\zeta - \zeta_c$, the adiabatic approximation naively fails at some arbitrarily small time interval around the time in which $\zeta \to \zeta_c$. Lastly, our study neglects the effects of temperature altogether. This is a good approximation in most situations, however for e.g. the Sun as well as for SN explosions, temperature could be as important as density, i.e. $T^3 \sim n$. Nevertheless, we note that for the motivated cases in which $\Lambda_{\rm B}^4 \sim \Lambda_{\rm QCD}^3$ or $\Lambda_{\rm B}^4 \sim v^2$, the effect of a finite temperature would generically go in the same destabilizing direction as density, i.e. decreasing the size of the potential barriers, reinforcing our conclusions regarding the formation and escape of a scalar bubble.

Let us conclude this section by briefly discussing our numerical analysis. In order to verify the theoretical results we present in Sec. 8.2.2.A, we have solved the *time-dependent* EOM presented in Eq. (8.13) numerically, assuming simple dependencies, e.g. $\zeta \propto n(r,t)$. The initial conditions for the scalar field are homogenous, i.e. $\phi(r,0) = \dot\phi(r,0) = \phi_-$. We implement a slow evolution of the density profile from $n(r,0) = 0$ to some final configuration Eq. (8.15) at $\bar t = T_{\rm S}$, with $g(x) = 1 - x^2$. Importantly, we fix $\mu T_{\rm S} \gg 1$, in agreement with the adiabatic limit. We verify that the quasi-static solutions we find have negligible amounts of kinetic energy compared to their gradient and potential energies. This quasi-static picture is maintained up until an instability takes place, i.e. until our numerical simulations display an expanding bubble that escapes from the star. Importantly, under our assumptions, the exact details of the star formation do not affect the quantitative scaling we present in the next section for the formation and escape of scalar bubbles.

8.1.3 Bubble Formation and Evolution

The formation of a non-trivial scalar profile induced by a star is effectively described, as justified in Sec. 8.1.2, by the quasi-static spherically-symmetric EOM for the scalar field, with a slowly-varying background density profile. The bubble-like solution $\phi(r)$ can be found numerically given a specific form for the density profile $n(r)$. The simple analytic results presented in this section have been explicitly verified by our numerical simulations.

A few simplifications allow us to analytically understand the dynamics of scalar bubbles at finite density. The field profile minimizes the total energy,

$$E(R) \simeq 4\pi \int_0^R \mathrm{d}r\, r^2 \left[\frac{1}{2}\phi'^2 + \Delta V(\phi, n)\right] , \quad \Delta V(\phi,n) = V(\phi,n) - V(\phi_-,n) , \tag{8.17}$$

where we have cut the integral at a radius R as an approximation to the full infinite space, since the scalar field rapidly converges to its vacuum value ϕ_- for $r \gtrsim R$. Indeed, for radii larger than the transition radius, i.e. $r > R_{\rm T}$, densities are below the critical one and the potential is minimized at approximately the same metastable minimum as outside the star. In the initial

stages of the formation of the dense system, we expect the creation of a scalar *proto-bubble* with $R \simeq R_{\rm T}$, where the scalar field at its center, $\phi(0)$, has not yet reached ϕ_+, the value associated with the stable minimum of the in-vacuum potential, see Sec. 8.1.3. In other words, the field displacement, $\Delta\phi(0) \equiv \phi(0) - \phi_-$, satisfies $\Delta\phi(0) \lesssim \phi_+ - \phi_- \approx 2f$. This is because the star is too small, in particular the (mean) energy density in the field gradient that would correspond to a field displacement $\Delta\phi(0) \sim 2f$, which is $\frac{1}{2}\langle\phi'^2\rangle \sim (2f/R_{\rm T})^2$, is too large compared to the potential energy difference within the proto-bubble, $\epsilon = |\langle\Delta V\rangle|$. Only when the star, by which we mean $R_{\rm T}$, grows large enough, it becomes energetically favorable to reach $\phi(0) \sim \phi_+$. Therefore, only when

$$\left(\frac{2f}{R_{\rm T}}\right)^2 \lesssim \epsilon \tag{8.18}$$

a scalar bubble *fully forms*. Interestingly, once the condition Eq. (8.18) is satisfied, the equilibrium position $R \simeq R_{\rm T}$ can be lost, meaning the bubble can be pushed towards the outer region of the star, see Sec. 8.1.3. If such an instability takes place, the evolution of the bubble is no longer quasi-static, but rather the minimization of the energy of the system becomes a time-dependent problem that can be simply described by a time-dependent bubble radius, $R \to R(t)$, which quickly approaches relativistic speeds. Depending on how fast the potential barrier reappears with radius, the instability cannot be stopped and the bubble expands beyond the star. Specifically, we find that the bubble *escapes* if

$$\frac{\Delta\sigma}{\Delta R_{\rm T}} \lesssim \epsilon\,, \tag{8.19}$$

where $\Delta\sigma$ is the difference between the tension of bubble wall at $R \simeq R_{\rm T}$ and $R \gtrsim R_{\rm S}$. The fact that the wall tension changes as it propagates through the star is one of the unique aspects of the bubble dynamics at finite density. In particular, it gives rise to an extra force that prevents the bubble from escaping the star unless ϵ is large enough. While for a bubble connecting to a shallow metastable minimum the condition Eq. (8.19) is readily satisfied (given Eq. (8.18) is), it is harder in the case of a deep minimum, because of the significant increase of the wall tension, being eventually dominated by the large barriers of the potential in vacuum. A critical bubble that starts to expand for a shallow minimum is much smaller than for a deep minimum. The is visualized in Fig. 8.2.

Formation: Linear Potential Approximation

Let us start by considering the classical formation of a bubble in a star where the critical density is reached. In order not to unnecessarily complicate the discussion, let us assume that the in-density potential can be well approximated by the rolling term only, i.e. that due to the suppression of $\Lambda_{\rm B}^4(n) = \Lambda_{\rm B}^4(1 - \zeta(n))$ we can neglect the barrier term,

$$V(\phi, n > n_{\rm c}) \simeq -\mu^2 f\phi\,, \tag{8.20}$$

where recall that in Eq. (8.14) we have identified $\mu^2 \sim \Lambda_{\rm R}^4/f^2$ as the scale that characterizes the scalar profile. An exact solution to the scalar EOM with a linear potential is

$$\phi(r) = \frac{\mu^2 f}{6}(R_{\rm T}^2 - r^2) + \phi_-\,, \quad r \leqslant R_{\rm T}\,, \qquad \text{(proto-bubble)} \tag{8.21}$$

with boundary conditions $\phi'(0) = 0$ and $\phi(R_{\rm T}) = \phi_-$. We then simply take $\phi(r \geqslant R_{\rm T}) = \phi_-$. We find that the proto-bubble is of size $R = R_{\rm T}$ and the field displacement at its center,

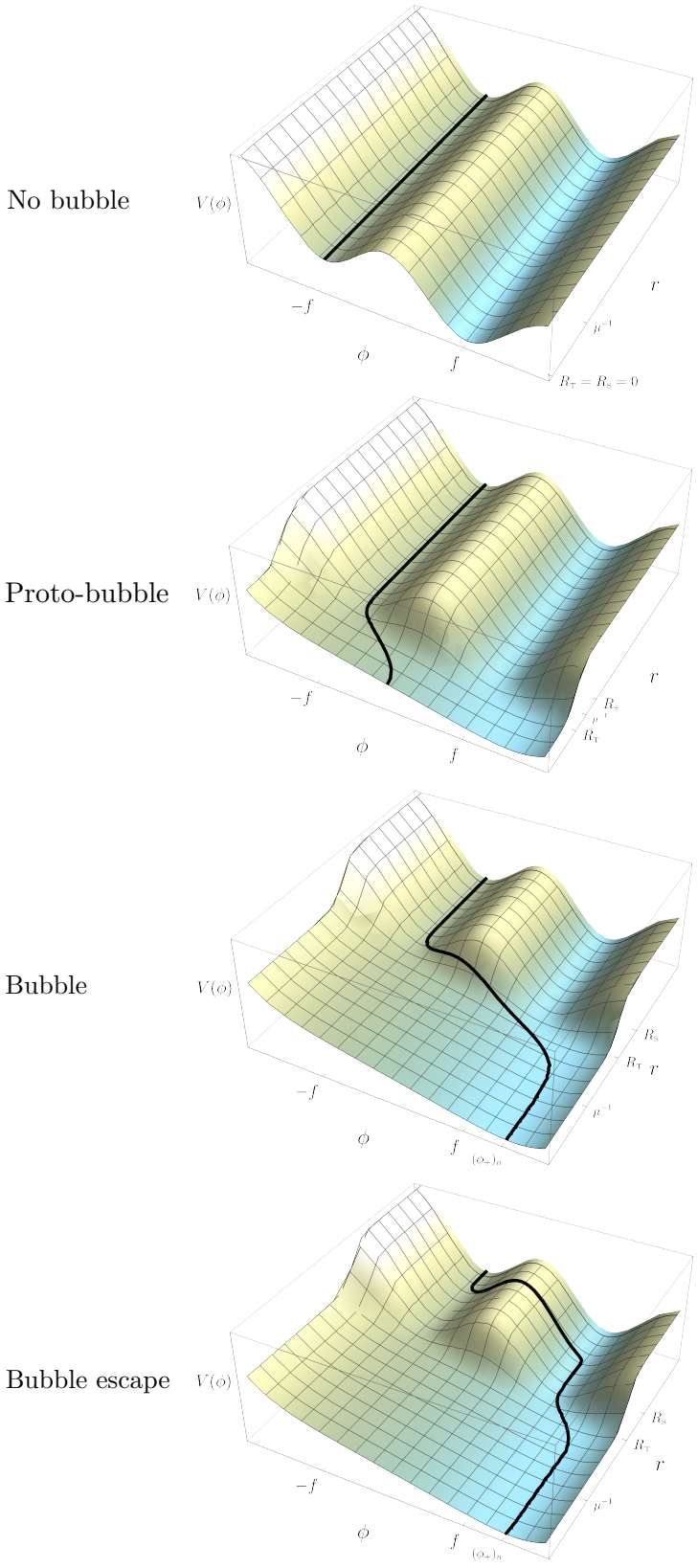

Figure 8.2: Quasi-static evolution of the in-density potential and scalar field profile, from no star to, as the star grows, the formation of the proto-bubble, complete formation of the bubble, and eventual bubble escape.

$\Delta\phi(0) \equiv \phi(0) - \phi_-$, is given by

$$\frac{\Delta\phi(0)}{f} = \frac{(\mu R_{\rm T})^2}{6}\,. \tag{8.22}$$

This situation is explicitly depicted in the second panel of Fig. 8.2. Eq. (8.21) constitutes a good a priori description of the scalar profile as long as the system is small enough that the in-density minimum, $(\phi_+)_n$, is not reached, i.e.

$$\frac{\Delta\phi(0)}{(\phi_+)_n - \phi_-} \lesssim 1\,. \tag{8.23}$$

We recall that in general $(\phi_+)_n > \phi_+$, see the discussion around Eq. (8.7).

It is important to point out here that the quasi-static description of the proto-bubble can break down as soon as $\phi(0) \sim \phi_+$, as we discuss in Sec. 8.1.3. Eq. (8.22) implies that any system, independently of its density profile or maximum density at its core, must have a minimum size in order for $\phi(0) \gtrsim \phi_+$, given by

$$R_{\rm T} \gtrsim \mu^{-1}\,, \tag{8.24}$$

where we have neglected $O(1)$ factors.

The solution Eq. (8.21) can be extended to the situation in which the in-density minimum is reached somewhere inside the star, at $r = R_i < R_{\rm T}$. In that region the potential exhibits a minimum, and consequently the scalar field remains pinned at $(\phi_+)_n$. This is depicted in the third panel of Fig. 8.2, where we have chosen a core density such that $(\phi_+)_n$ is only slightly larger than ϕ_+. The scalar profile is well approximated by

$$\phi(r) = \begin{cases} (\phi_+)_n & r < R_i \\ -\frac{\mu^2 f}{6}(r - R_i)^2 + (\phi_+)_n & R_i < r < R_{\rm T} \\ \phi_- & r > R_{\rm T} \end{cases}, \qquad \text{(bubble)} \tag{8.25}$$

where in the intermediate region, $r \in [R_i, R_{\rm T}]$, we have used the solution of the EOM with the linear potential Eq. (8.20), shifted it by $r \to r - R_i$, and required $\phi'(R_i) = 0$, $\phi(R_i) = (\phi_+)_n$; further matching to $\phi(R_{\rm T}) = \phi_-$ fixes the value of R_i, or equivalently the width of the bubble wall

$$x \equiv \frac{R_{\rm T} - R_i}{R_{\rm T}} \simeq \frac{\sqrt{6}}{\mu R_{\rm T}}\sqrt{\frac{(\phi_+)_n - \phi_-}{f}}\,. \tag{8.26}$$

Of course, in order for $R_i > 0$, $R_{\rm T}$ needs to be large enough as to allow the field to reach the minimum at finite density. In other words, the requirement that $x < 1$ implies

$$R_{\rm T} \gtrsim \frac{\sqrt{6}}{\mu}\sqrt{\frac{(\phi_+)_n - \phi_-}{f}}\,. \tag{8.27}$$

A scalar field profile for which this condition is satisfied is shown in Fig. 8.3, for a choice of central density not much larger than the critical density.

For an increasingly larger system, yet with a core density fixed such that $(\phi_+)_n$ remains constant, the bubble wall becomes thinner, i.e. $x \ll 1$ when $\mu R_{\rm T} \gg 1$. In this thin-wall limit, the energy of the bubble, Eq. (8.17), can be approximated by a volume and a surface term [104],

$$E(R) \simeq -\frac{4\pi}{3}R^3\,\epsilon + 4\pi R^2\,\sigma\,, \tag{8.28}$$

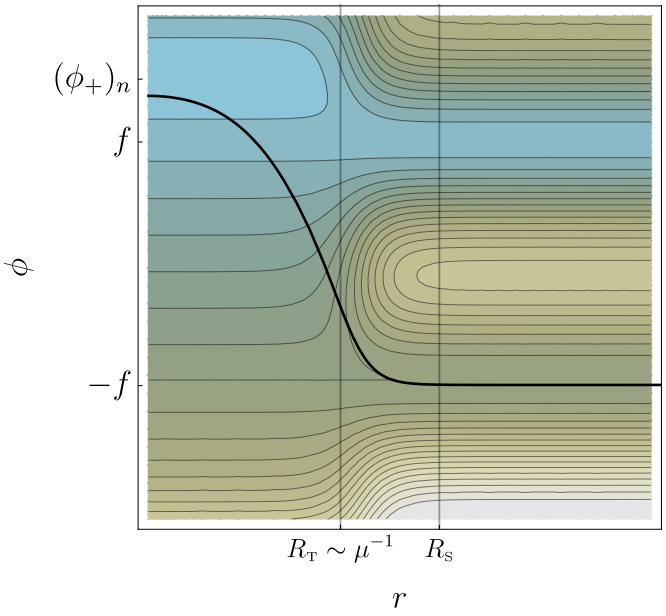

Figure 8.3: Scalar profile for $\mu R_{\rm T} \gtrsim 1$ on top of contours of the scalar potential.

where ϵ is the (potential) energy difference between the in-density and in-vacuo field values, while σ is the bubble-wall tension. For our simple scalar profile these read

$$\epsilon = \mu^2 f((\phi_+)_n - \phi_-) \gtrsim \Lambda_{\rm R}^4 \,, \tag{8.29}$$

$$\sigma = \tfrac{4}{3}\sqrt{\tfrac{2}{3}}((\phi_+)_n - \phi_-)\sqrt{\epsilon} \gtrsim \Lambda_{\rm R}^2 f \,. \tag{8.30}$$

In Eq. (8.28) we have traded $R_{\rm T}$ with R, since we are assuming that during the formation of the bubble its wall sits at $R \simeq R_{\rm T}$; in Sec. 8.1.3 we discuss under which circumstances such an equilibrium is lost, i.e. $R > R_{\rm T}$. Also, we have implicitly assumed that $(\phi_+)_n$ is constant below R_i, i.e. that the density does not significantly change for $r < R_i$. Both the inequalities in Eqs. (8.29), (8.30) follow from $(\phi_+)_n > \phi_+$, after neglecting $O(1)$ factors. These correspond to the minimum values of the potential energy and tension of a fully formed bubble. As expected, we find $\epsilon \gtrsim |\Delta V(\phi_+, n)| = -\Delta\Lambda$, where recall that $\Delta\Lambda$ is the energy difference between the false and true ground states, Eq. (8.8). In addition, let us point out that the condition Eq. (8.27) can be understood from energy considerations, as the requirement that the (mean) field gradient is small enough, $\frac{1}{2}\langle\phi'^2\rangle \sim ((\phi_+)_n - \phi_-)^2/R_{\rm T}^2 \lesssim \epsilon$. Note also that the tension here is dominated by the field displacement, $\sigma \sim ((\phi_+)_n - \phi_-)^2/(xR_{\rm T})$ [193].

In App. II.B.1 we reproduce the above scalings with a simpler linear profile approximation, where we do not need to assume that the potential is well described by a linear slope only. In particular, we can keep the subdominant barrier term and we find that, while leaving ϵ unchanged, it gives a corrections to the tension of the bubble wall that scales as

$$\frac{\Delta\sigma}{\sigma} \sim \frac{\Lambda_{\rm B}^4(n)}{\Lambda_{\rm R}^4} \simeq \frac{1-\zeta(n)}{1-\zeta_c} \,. \tag{8.31}$$

This becomes negligible when $\zeta \to 1$, that is also when $(\phi_+)_n \gg \phi_+$, see Eq. (8.7). On the other hand, when the density is not much above critical, the correction is parametrically $O(1)$. Nevertheless, the most important effect of the potential barriers arises when we consider a bubble whose wall is beyond the transition radius, i.e. $R > R_{\rm T}$, as we discuss in the following.

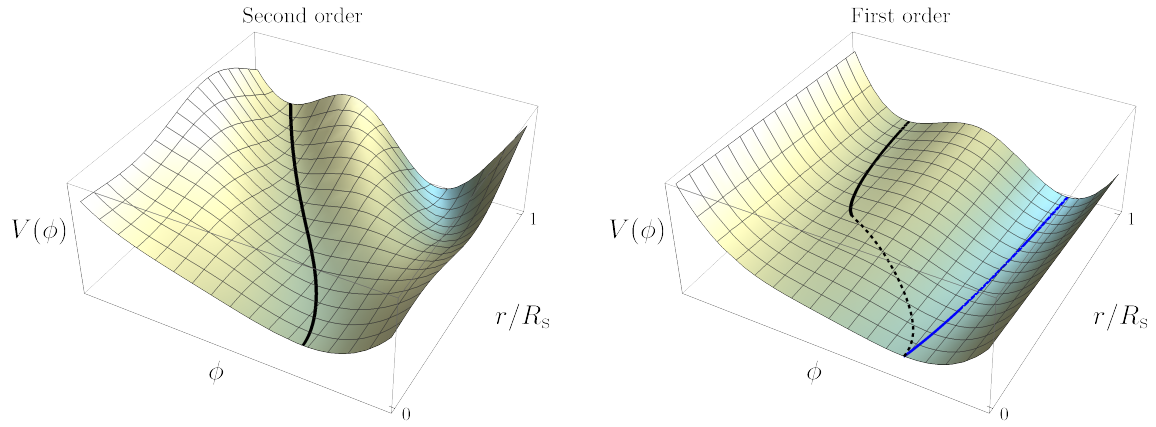

Figure 8.4: Second order (left) versus first order (right) phase transition induced by a dense system (spherically symmetric and of finite size). For both cases the potential is shown as a function of radius, with $r/R_S = 0$ the center of the star. The black solid lines illustrate the scalar profile starting from a given in-vacuo ($r/R_S > 1$) minimum and following it inside the star. For a first-order phase transition, the black line stops where this minimum ceases to exist. The dashed line then illustrates the field profile that connects to the minimum within the star. The profile unavoidably passes through regions where $dV/d\phi \neq 0$, implying there are effective forces acting on the field. These forces give rise to the possibility that the initial scalar profile (black) classically changes to a new minimum in vacuum (blue).

Dynamics: Escape vs Equilibrium

In the previous discussion we worked under the assumption of a nearly-static bubble, which slowly grows with time only due to the increase in size of the transition radius R_T where the critical density is reached. Here we show that in fact this adiabatic description can break down as soon as the star is dense and large enough that the field displacement inside it reaches the position of the true minimum in vacuum.

There are several ways to understand the origin of this instability. Qualitatively, for the potentials we are considering, finite density effects allow for the local minimum in vacuum to be continuously (i.e. classically) connected to the true minimum. This is because the in-vacuo potential barrier between them disappears in some region of the star ($r < R_T$), see the right panel of Fig. 8.4. Once this region is large enough such that $\Delta\phi(0) \gtrsim \phi_+ - \phi_- \approx 2f$, it may become energetically favourable for the tail of the field profile, which extends outside the star, to be pushed over the potential barrier. This effectively leads to a first-order phase transition in the form of a bubble escaping the star. This is in contrast with other types of potentials with metastable minima, such as that shown in the left panel of Fig. 8.4, where even at finite density there is always a potential barrier between the two minima. This class of potentials does not allow for a classical path connecting them, and therefore leads to a smooth cross-over to a different in-density minimum.

Let us note that the discussion is focussed on field displacements that are at least of the order of the field separation between the local and true minimum in vacuum. This is because, at least qualitatively, a bubble with $(\phi_+)_n \sim \phi_+$ captures all the non-trivial dynamics of the phase transition. In the following we focus on such a case, which corresponds to maximal densities of the order of the critical density. A discussion of the bubble dynamics for $(\phi_+)_n \gg \phi_+$, is deferred to App. II.B.4.

In order to quantitatively understand the dynamics of induced first-order phase transitions,

we resort to the description of the scalar bubble wall as a particle in $d = 1 + 1$ dimensions. While this is a standard treatment when studying the dynamics of bubbles in vacuum or at finite temperature (see e.g. [194]), here we adapt it to the finite density environment, crucially including a position-dependent tension, $\sigma(R)$. The Lagrangian for the time-dependent bubble-wall position $R(t)$ is given by

$$\mathcal{L} = -\mathcal{M}(R)/\gamma - \mathcal{V}(R)\,, \tag{8.32}$$

where $\gamma = 1/\sqrt{1-\dot{R}^2}$. In the thin-wall approximation, $x \ll 1$, where the particle description best applies, we have

$$\mathcal{M}(R) = 4\pi \int_{R(1-x)}^{R} \mathrm{d}r\, r^2 \left[\frac{1}{2}\phi'^2 + \Delta V(\phi, n(r))\right] \equiv 4\pi R^2 \sigma(R)\,, \tag{8.33}$$

$$\mathcal{V}(R) = -\frac{4\pi}{3} R^3 \Delta\Lambda \equiv -\frac{4\pi}{3} R^3 \epsilon\,. \tag{8.34}$$

Several comment are in order regarding the bubble mass and potential at finite density. First, the bubble's energy given in Eq. (8.28) is precisely the Hamiltonian associated with Eq. (8.32) in the static limit $\dot{R} = 0$. Second, from the integral expression of $\mathcal{M}(R)$, it is clear that in the thin-wall limit the bubble wall is only sensitive to the density at $r = R$. Therefore, as the bubble moves through the star, its tension changes due to the changing density.[2] Since the bubble is born with $R \simeq R_{\rm T}$, from Eq. (8.30) with $(\phi_+)_n \sim \phi_+$ we have

$$\sigma(R \simeq R_{\rm T}) \sim \Lambda_{\rm R}^2 f\,. \tag{8.35}$$

Recall that for the bubble to have been fully formed, $R_{\rm T}$ needs to satisfy Eq. (8.27), which for $(\phi_+)_n \sim \phi_+$ reads $R_{\rm T} \gtrsim \mu^{-1}$. Finally, $\mathcal{V}(R)$ is controlled by the potential energy difference between the two sides of the bubble wall, which from Eq. (8.29) with $(\phi_+)_n \sim \phi_+$ is given by

$$\epsilon \sim \Lambda_{\rm R}^4\,. \tag{8.36}$$

The equation motion of the bubble wall reads

$$\sigma \ddot{R} \gamma^3 = \epsilon - \gamma \left(\frac{2\sigma}{R} + \sigma'\right)\,, \qquad \sigma' = \frac{d\sigma}{dR}\,. \tag{8.37}$$

Since we are mainly interest in the dynamics of the bubble right after its formation, we concentrate on the non-relativistic limit, i.e. we set $\gamma = 1$. The right hand side of Eq. (8.37) is the sum of forces acting on the bubble wall. The potential energy difference between the two sides of the wall pushes it outwards. The second and third terms are associated with the tension of the wall, both pushing it inwards. In particular, the change in tension σ' is positive, since densities decrease with R and in turn the potential barriers, controlled by $\Lambda_{\rm B}^4(n)$, reappear and increase towards its vacuum value outside the star.

In order to understand the behaviour of $\sigma(R)$, let us first recall that when the bubble is just formed, the tension is dominated by the field displacement, see Eq. (8.30). This implies that only the contribution to the tension from the barrier, estimated in Eq. (8.31), leads to an increasing tension with R. For bubbles connecting shallow minima, $\delta^2 \ll 1$, this increase is small between $R_{\rm T}$ and $R_{\rm S}$,

$$\sigma(R_{\rm S}) - \sigma(R_{\rm T}) \sim f \Lambda_{\rm R}^2 \delta^2\,. \qquad \text{(shallow)} \tag{8.38}$$

[2] We are implicitly assuming that the width of the wall is the smallest scale in the system. If this were not the case, we would expect finite-size effects in the form of e.g. deformations of the bubble. However, these would lead to at most $O(1)$ corrections to our already approximate analytical results, leaving our qualitative conclusions unchanged.

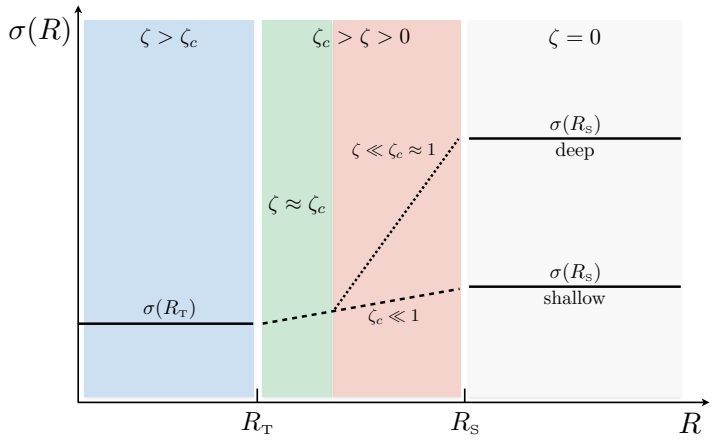

Figure 8.5: Sketch of the relevant regions of star for what concerns the bubble-wall tension. Dashed and dotted lines do not necessarily represent the functional form of $\sigma(R)$. In the green region the tension is dominated by the field displacement, while in the red region the barriers come to dominate. Note that for $\zeta_c = \delta^2 \ll 1$ (i.e. shallow minimum), there is in fact no red region.

In contrast, for deep minima, $\delta^2 \approx 1$, the tension goes from being displacement-dominated at $R \simeq R_{\rm T}$, to barrier-dominated towards the end as well as outside of the star $R \simeq R_{\rm S}$. There we can use the standard thin-wall approximation to compute the tension [104],

$$\sigma(r \simeq R_{\rm S}) \simeq \int_{-f}^{f} {\rm d}\phi \sqrt{2V(\phi)} \simeq \frac{2}{3}\Lambda_{\rm B}^2 f\,, \qquad \text{(deep)} \tag{8.39}$$

and $\sigma(R_{\rm S}) - \sigma(R_{\rm T}) \simeq \sigma(R_{\rm S})$. In addition, let us note that the bubble gets thinner when the barrier term dominates the tension. The bubble wall tension, as a function of its location, is schematically summarized in Fig. 8.5 for both the shallow and deep minimum cases.

Before moving to the detailed discussion of how the changing tension affects the dynamics of the bubble wall, let us note that in Eq. (8.37) we have ignored the effect of the gravitational force of the star on the bubble wall. In App. II.B.2 we discuss such a force, showing that while for neutron stars it could be quantitatively relevant at some stage during the expansion, it does not qualitatively change the picture presented here.

Having established the behaviour of the tension from $R_{\rm T}$ to $R_{\rm S}$, let us understand the dynamics of the bubble wall. Right after the formation of a thin-wall bubble at $R \simeq R_{\rm T} \gtrsim \mu^{-1}$, the particle description Eq. (8.37) applies. One then automatically finds $\ddot{R} > 0$ right before the transition region, since we can simply assume that σ' vanishes for $R < R_{\rm T}$, that is $\sigma'(R_{\rm T}^-) = 0$. The acceleration would remain positive in the limit that the force due to the change in tension vanished for any R, $\sigma' \to 0$; in this limit the bubble would expand indefinitely, in particular beyond the star. In the opposite limit, in which σ' is very large just past the edge of the transition region, that is $\sigma'(R_{\rm T}^+) \to \infty$, the wall could not expand and therefore it would remain at an equilibrium radius $R = R_{\rm eq} = R_{\rm T}$ (and the bubble would only grows if $R_{\rm T}$ kept increasing). Clearly, a realistic situation lies in between these two limits, and it depends on how fast the density profile and thus the tension changes from $R_{\rm T}$ to the end of the star. This discussion gives us a qualitative understanding of why the bubble might generically be found in an equilibrium position at $R_{\rm S} > R > R_{\rm T}$. In a similar fashion, we can understand under which conditions the bubble escapes from the star. In the limit that the star has grown so large that the transition

region starts at a radius much larger than the one needed to form the bubble, i.e. $R_{\rm T} \gg \mu^{-1}$, we have $\epsilon \gg 2\sigma(R_{\rm T})/R_{\rm T}$. Then, it follows from the equation of motion that the bubble wall would continue to accelerate for $R > R_{\rm T}$ as long as $\epsilon > \sigma'$. In the opposite limit, in which $R_{\rm T} \simeq \mu^{-1}$, we have $\epsilon \to 2\sigma(R_{\rm T})/R_{\rm T}$ and the additional force due to σ' would be enough to forbid its expansion. These different limits lead us to the conclusion that for a sufficiently large star, satisfying $R_{\rm T} \gtrsim \sigma(R_{\rm T})/[\epsilon - \sigma'(R_{\rm T})]$, the system is unstable and the bubble escapes if

$$\epsilon \gtrsim \kappa\, \sigma'_{\rm max}\,, \tag{8.40}$$

where $\sigma'_{\rm max}$ is the maximum value of σ' and $\kappa = O(1)$. This condition is explicitly verified by our numerical simulations as well as in App. II.B.3, where we investigate Eq. (8.37) in the simplest case of a constant σ', finding $\kappa = 3$. Note that up to order 1 factors, this condition is the same as for a critical bubble outside the star to exist. Once again, (a version of) this condition can be expected to hold in general, on the basis that the standard force due to the surface tension becomes irrelevant at large R, leaving the variation of the tension as the only relevant force to determine if the bubble does or does not escape from the star.

Summary: Formation and Escape Conditions

Given that the change in the wall tension is very different for a bubble connecting shallow or deep minima in vacuum, let us explicitly summarize for each case the conditions under which the bubble forms and escapes from the star.

For a shallow bubble, $\delta^2 \ll 1$, we find as formation and escape conditions, respectively

$$R_{\rm T} \gtrsim \frac{f}{\Lambda_{\rm R}^2} \quad \text{and} \quad \Delta R_{\rm T} \gtrsim \frac{f}{\Lambda_{\rm R}^2}\delta^2\,, \qquad \text{(shallow)} \tag{8.41}$$

up to irrelevant $O(1)$ factors. Note that since σ' is suppressed by δ^2, as shown in Eq. (8.38), the escape condition is easier to satisfy than the condition for formation. This is unless, contrary to the expectation from generic density profiles, $\Delta R_{\rm T}$ is anomalously small. In terms of the mass of the scalar in vacuum, Eq. (8.59), these two conditions read as $m_\phi R_{\rm T} \gtrsim \sqrt{\delta}$ and $m_\phi \Delta R_{\rm T} \gtrsim \delta^{5/2}$.

For a bubble connecting deep minima, $\delta^2 \approx 1$, the rate of change of the tension is determined by the tension in vacuum, $\sigma' \sim \sigma(R_{\rm S})/\Delta R_{\rm T}$, as shown in Eq. (8.39). Therefore, we find the following conditions for the formation and escape of a deep bubble, respectively

$$R_{\rm T} \gtrsim \frac{f}{\Lambda_{\rm R}^2} \quad \text{and} \quad \Delta R_{\rm T} \gtrsim \frac{f}{\Lambda_{\rm R}^2}\frac{1}{\sqrt{1-\delta^2}}\,, \qquad \text{(deep)} \tag{8.42}$$

up to $O(1)$ factors. As expected, it is generically much more difficult for a bubble connecting deep minima to transverse the transition region and expand beyond the star. Besides, while the condition for formation is formally the same as for shallow minima, let us recall that $\zeta_c = \delta^2 \approx 1$ generically implies that much larger densities are needed in this case. In terms of the mass of the scalar in vacuum, Eq. (8.59), the two conditions in Eq. (8.42) read as $m_\phi R_{\rm T} \gtrsim 1/\sqrt{1-\delta^2}$ and $m_\phi \Delta R_{\rm T} \gtrsim 1/(1-\delta^2)$.

Classical vs quantum

To conclude this section, we wish to investigate the possibility that, even when the system is not dense enough as to allow for a classical transition between the local and true minimum, finite density could still lead to a much shorter quantum-mechanical lifetime of the metastable minimum compared to the one in vacuum. This is reminiscent of the idea that black holes or

compact objects can act as seeds for false vacuum decay, due to their strong gravitational fields, see e.g. [195–199].

Indeed, up until this point we did not care about the lifetime of the false vacuum, implicitly assuming that it was sufficiently large. The decay rate per unit volume is determined by the bounce action, $\Gamma/\mathcal{V} = Ae^{-S_{\rm B}}$ [104, 105]. In the case where the metastable minimum is deep, the thin-wall approximation holds and the action is well approximated by $S_{\rm B} \simeq (27/2)\pi^2\sigma^4/\epsilon^3$, which given the in-vacuo tension Eq. (8.39) and $\epsilon = -\Delta\Lambda \simeq \frac{2}{3\sqrt{3}}\Lambda_{\rm R}^4$, results in

$$S_{\rm B} \simeq 27\sqrt{3}\pi^2 \left(\frac{f}{\Lambda_{\rm B}}\right)^4 \frac{1}{(1-\delta^2)^3}\,. \qquad \text{(deep)} \tag{8.43}$$

Since $\delta^2 \approx 1$ for a deep minimum, the bounce action is generically large and the decay rate extremely suppressed. For a shallow minimum, we can estimate the action by considering $\sigma \sim \Delta\phi^2/\Delta R$ with $\Delta R \sim \Delta\phi/\sqrt{\epsilon}$, which leads to $S_{\rm B} \sim \pi^2\Delta\phi^4/\epsilon$. We therefore find,[3]

$$S_{\rm B} \sim 24\pi^2 \left(\frac{f}{\Lambda_{\rm B}}\right)^4 . \qquad \text{(shallow)} \tag{8.44}$$

While for the same value of the ratio $f/\Lambda_{\rm B}$ the bounce action is smaller in the shallow than in the deep case, this is not the comparison we really care about. Instead, let us assume that the local minimum is, for all practical purposes, stable in vacuum. This fact can dramatically change in a dense system only in the case of a deep minimum (even before a classical transition is allowed). This is clear since for a shallow minimum $S_{\rm B}(n < n_c) \simeq S_{\rm B}(0)$, while for a deep one

$$\frac{S_{\rm B}(n<n_c)}{S_{\rm B}(0)} \simeq [1-\zeta(n)]^2\,, \qquad \text{(deep)} \tag{8.45}$$

which is much smaller than one if $\zeta \approx 1$ (yet $\zeta < \zeta_c = \delta^2$). Certainly, the bounce action at finite density can only be sufficiently small in absolute terms if $(f/\Lambda_{\rm B})^4 = 1/\lambda$ is small, which drives us to the non-perturbative regime for the scalar quartic coupling λ. Nevertheless, this issue could well be specific to the type of false vacua we are taking as case study, thus one could imagine other scalar potentials where, being sensitive to finite density (either of SM degrees of freedom or beyond, e.g. dark matter), their local minima have much smaller lifetimes in a dense system. Additionally, let us note that the corresponding seeded nucleation of bubbles of the true ground state would generically not take place during the formation of the star. On the contrary, one would expect $T_{\rm B} = 1/\Gamma \gg T_{\rm S}$, while still being shorter than the typical lifetime of the star. This raises the possibility of a latent phase transition that could take place at any time.

Finally, let us point out that in the computation of the bounce action at finite density, we have assumed the system is large and homogeneous enough as for the effects of a non-trivial density profile or a spatial boundary to be negligible. We can phrase this as the requirement that $R_0 \ll R_{\rm S}$, where $R_0 = 3\sigma/\epsilon$ is the radius of the nucleated bubble. For a deep minimum, this translates into $m_\phi R_{\rm S} \gg 1/(1-\delta^2)$, which coincides with the condition for the escape of a deep, classically formed, bubble, see Eq. (8.42). It would be interesting to further study, beyond these simple approximations, the process of quantum bubble nucleation in finite-size dense systems [201, 202].

[3] More refined estimates can be easily derived for potentials where the barrier is negligible, see e.g. [200]. Nevertheless, our conclusions will not depend on such a refinement.

8.1.4 Phenomenological Implications

In this section we discuss the phenomenological consequences of the expansion, beyond the dense object, of a bubble of the true vacuum. The main model-independent signature of such a seeded phase transition is a change of the vacuum energy of the universe, Λ, or equivalently a change of the cosmological dark energy density, ρ_Λ (with equation of state parameter $\omega = -1$).[4]

A particularly interesting trademark of these phase transitions is that they take place relatively late in the history of the universe. As explained in the previous section, the bubble forms, expands and eventually escapes along with the formation of the star. Therefore, if a phase transition of this sort can happen, it took place at the onset of star formation. The first stars were born around the epoch of galaxy formation, thus at redshifts $z = z_{\rm S} \sim 30$ [203]. This then implies that the universe underwent a change of ρ_Λ between recombination, $z \sim 10^3$, and the late universe, $z \lesssim 1$. Note that we are assuming that at redshifts $z \sim 1$ (associated with late-time cosmological measurements) the universe already transitioned successfully to the true ground state. The change in the dark energy content of the universe can thus best be probed by comparing CMB measurements versus local measurements (SNe, baryon acoustic oscillations or large-scale structure) of the expansion rate of the universe. Such a comparison depends on the fate of the bubbles, for instance if the phase transition proceeds via a single bubble or instead many bubbles are formed all over the universe (from as many stars) that subsequently collide and transfer at least an $O(1)$ fraction of the kinetic energy of their walls into radiation. Providing a precise answer to this question is beyond the scope of this work. Instead, below we work out simple cosmological constraints on how much the energy budget of the universe can vary due to a late ($z \sim 10$) phase transition, to confirm our intuition that a change in the vacuum energy much larger than the current one is experimentally ruled out.

A too large change in vacuum energy leads to constraints on the parameters of the scalar potential. To make this point clear, let us note that the change in vacuum energy is given by $\Delta\Lambda = -\epsilon \sim -\Lambda_{\rm R}^4$, and the rolling scale enters both the conditions for formation and escape of a bubble of the true vacuum, see Eqs. (8.41), (8.42). Then, assuming the existence of stars with densities above critical, $n > n_c$, the condition for formation of a bubble with $R_{\rm T} \sim R_{\rm S}$, as expected for most stellar profiles, implies

$$-\Delta\Lambda \gtrsim \left(\frac{f}{R_{\rm S}}\right)^2 \approx \Lambda_0 \times 10^{15} \left(\frac{f}{10\,\text{TeV}}\right)^2 \left(\frac{10\,\text{km}}{R_{\rm S}}\right)^2 , \tag{8.46}$$

where $\Lambda_0 \approx (2.3\,\text{meV})^4$ is the value of the vacuum energy inferred from ΛCDM, and we have fixed $R_{\rm S}$ to the typical radius of a neutron star as an example. If such type of bubbles could have escaped from neutron stars, the corresponding change in the vacuum energy would be in gross contradiction with experimental data.

However, for much smaller values of f, or if we were to consider much larger astrophysical bodies (the largest stars known have $R_{\rm S} \sim 10^3 R_\odot$), astronomical structures, or even dense objects beyond the SM (such as dark stars), the change in the dark energy density could be much smaller. The corresponding nucleation of bubbles of the true vacuum and subsequent phase transition could then be an experimentally viable and very interesting phenomenon, which could be detected in the near future given the expected increase in precision of many current and planned cosmological observatories.

Amusingly, if the phase transition proceeds via quantum tunneling, as we have argued in Sec. 8.1.3, a recent creation of a true vacuum bubble could lead to other, more direct, experimental signatures: since the bubble interacts with SM matter, gravitationally at the very

[4] In the following we exclude the possibility of an adjustment mechanism for the cosmological constant. Such a mechanism could interfere with the formation or escape of the bubble.

least, the effects of a (non-percolated) bubble wall passing through Earth could potentially be detected [204, 205].

Let us finally point out that seeded phase transitions with $\Delta\Lambda \lesssim \Lambda_0$ could impact our understanding of the landscape solution to the cosmological constant problem. Originally connected with the requirement for galaxies and stars to form [108], the cosmological constant was predicted to lie within a range a couple of orders of magnitude larger than the value actually observed as dark energy. In light of our late-time phase transitions, taking place precisely because structures form, this discrepancy could well be an accident associated with the sensitivity to finite density effects of a scalar potential with metastable minima (potentially many of them as in [206]).

Cosmological Constraints

While it is beyond the scope of this work to examine in detail the cosmological and astrophysical constraints arising from a phase transition at the dawn of galaxy/star formation, let us briefly comment on simple arguments why a large change in the energy content of the universe is not experimentally viable.

From local measurements of the (accelerated) expansion of the universe, we know it is dark energy dominated, and in particular $\rho_r \ll \rho_\Lambda$ at $z \lesssim 1$, where ρ_r is the energy density in radiation. If we assume that, at redshifts $z_{\rm S} \sim 30$, an $O(1)$ fraction of the kinetic energy of the bubbles goes into radiation after they collide and percolate, then we find $\epsilon = \Delta\rho_r(z_{\rm S}) \ll (1+z_{\rm S})^4\rho_{\Lambda_0} \approx 10^6\rho_{\Lambda_0}$, which is inconsistent with e.g. Eq. (8.46).

Still, it would be preferable to proceed with minimal assumptions regarding the fate of the bubble. One relatively robust assumption is that today our Hubble patch is in the true vacuum, while it was not prior to star formation, that is $\rho_\Lambda(z > z_{\rm S}) \neq \rho_{\Lambda_0}$. In this case, the most reliable test is to contrast late versus early universe measurements, something that has been actively pursued in recent years in light of the Hubble tension, the disparity between CMB and local determinations of the Hubble constant (see [207, 208] for recent discussions). Of particular relevance is the study in [209], where constraints on the size of an early dark energy content of the universe at the time of recombination are derived. The bounds are given as a function of the critical redshift z_c where the dark energy starts to decay quickly, as $1/a^6$ (thus faster than radiation). Such a behaviour decreases the impact of this non-standard energy component at later times $z < z_c$, which we take as a good approximation towards independence from the fate of the bubble(s). Identifying $z_c = z_{\rm S}$, the bound $\rho_\Lambda(z > z_{\rm S}) \gtrsim 10^3\rho_{\Lambda_0}$ is derived, three order of magnitude stronger than the crude bound we derived before. Although we expect that a proper analysis of the fate of the bubbles and its impact on cosmological observables would yield even stronger bounds, for now we take

$$-\Delta\Lambda \lesssim 10^3 \times \Lambda_0 \tag{8.47}$$

to set constraints on the parameters of the scalar potential Eq. (8.1).

For the bound Eq. (8.47) to apply, the conditions for a bubble of the true ground state to form and escape from the dense system must be satisfied. Let us recall that the first of these conditions is that densities need to be above the critical density, i.e. $n > n_c$, or more specifically

$$\zeta(n) > 1 - \frac{\Lambda_{\rm R}^4}{\Lambda_{\rm B}^4}\,, \tag{8.48}$$

see Eqs. (8.57), (8.64). Since in this work we do not focus on any specific scenario for the function $\zeta(n)$,[5] we simply assume that stars exist with $n > n_c$, and note that denser stars

[5] Constraints on relaxion models, where $\zeta(n)$ can be explicitly computed, will be presented in [180].

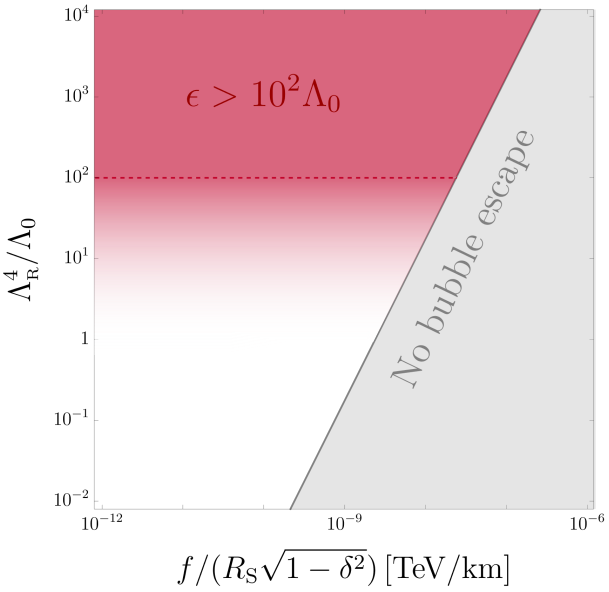

Figure 8.6: Region excluded by a density induced vacuum instability if it happens at redshifts $z \lesssim 10$ (shaded red) in the plane $(f/R_S\sqrt{1-\delta^2}, \Lambda_R^4/\Lambda_0)$, where R_S is the typical radius of the (type of) star triggering the phase transition, i.e. where densities above critical are realized, $n > n_c$.

are typically smaller. The other conditions concern the formation and escape of the bubble, which are different for a shallow metastable minimum than for a deep one, see Eq. (8.41) and Eq. (8.42), respectively. These depend on either R_T or $\Delta R_T = R_S - R_T$, which in turn depend on the density profile of the star. We will take $R_T \sim \Delta R_T \sim R_S$ as a generic expectation for stars where the core density is not very close to the critical one, as discussed in Sec. 8.1.2. Under this assumption, the strongest of the formation and escape conditions, for both shallow and deep minima, can be written as

$$\Lambda_R^4 \gtrsim \frac{f^2}{R_S^2}\frac{1}{1-\delta^2}\,. \tag{8.49}$$

We show the region of parameter space where this condition is satisfied in Fig. 8.6. Since a phase transition seeded by stars takes place in this region, the bound Eq. (8.47) applies, ruling out the corresponding part of it. Note that for a bubble connecting deep minima, Eq. (8.49) can be rewritten as $\Lambda_R^4 \gtrsim \Lambda_B^2 f/R_S$.

8.2 Bounds on Relaxion Models from Density Induced Phase Transitions

Both the conditions for a scalar bubble to escape from a star and the experimental constraints on the associated phase transition have been discussed above in the context of a simple quartic potential with a tilt, i.e. with two non-degenerate minima. In this section we extend them to the case of the relaxion potential, which we review in Sec. 8.1.1. Since by construction the relaxion potential depends on the QCD quark condensate (QCD-relaxion) or the Higgs VEV squared (non-QCD relaxion), its landscape of minima changes in a dense environment of SM matter. We show in Sec. 8.2.2 that at sufficiently high densities and for large enough stars, the in-vacuo relaxion minimum can be destabilized and a bubble of a lower energy minimum can expand

indefinitely. This fact allows us to set new constraints on the relaxion mechanism, which we present in Sec. 8.2.3. The most relevant ones are found in the case of the non-QCD relaxion (Sec. 8.2.3.B), where the minima are typically very shallow and the small change in the Higgs VEV induced by a finite baryon density is enough to trigger the transition. We also find that the large electric and magnetic fields generated by pulsars/magnetars can lead to analogous phase transitions for relaxions with large couplings to photons (Sec. 8.2.3.C). Finally, we show that if the vacuum instability is seeded by the largest stars in the universe (with radii thousand times that of the Sun), or if dark astrophysical objects exist (Sec. 8.2.3.D), a change of minimum in the relaxion landscape can take place with the corresponding change in vacuum energy being very small. A priori, such a phase transition is phenomenologically viable and an interesting target for future exploration.

8.2.1 The Relaxion Potential

The relaxion potential [8] is characterized by a washboard-like shape where after integrating out the Higgs, the amplitude of the wiggles depends on the relaxion field ϕ itself,

$$V(\phi) = -\Lambda_{\rm R}^4 \frac{\phi}{f} - \tilde{\Lambda}_{\rm B}^4 F(\phi) \cos\frac{\phi}{f} \,. \tag{8.50}$$

$\Lambda_{\rm R}$ and $\tilde{\Lambda}_{\rm B}$ are the scales that control the size of the linear rolling and periodic back-reaction terms respectively, while $2\pi f$ parametrizes the field distance between adjacent minima. The monotonically increasing function $F(\phi)$ is of the form

$$F(\phi) = \left(\frac{\phi}{\phi_c} - 1\right)^{k/2} \Theta(\phi - \phi_{\rm c}) \,, \tag{8.51}$$

with $k = 1, 2$ and where ϕ_c is the field value where the periodic barriers turn on. This is taken such that the change in the size of the wiggles after a $2\pi f$ period is small, i.e. $\phi_c \gg f$, and therefore the landscape is densely populated over field ranges of order ϕ_c. The case $k = 0$ corresponds to Abbott's potential [206], where the size of the potential barriers is constant. The non-trivial behavior for $k = 1, 2$ arises from the dependence of the periodic term on the Higgs VEV, h, which in turn is determined by the scalar field ϕ.

Indeed, the Higgs potential, in particular the mass term, depends on the value of the relaxion,

$$V(h) = \tfrac{1}{2}(M^2 - g\phi M)h^2 + \tfrac{1}{4}\lambda h^4 \,, \tag{8.52}$$

where M is the cutoff and g is a small coupling that breaks the shift-symmetry associated with ϕ. Note that the periodic term in the relaxion potential, while breaking the continuous shift-symmetry, is still invariant under the discrete shift $\phi \to \phi + 2\pi f n$, $n \in \mathbb{Z}$. The coupling to the Higgs, as well as the linear term in the potential, break it completely, thus we expect

$$\frac{\Lambda_{\rm R}^4}{f} = c\, g M^3 \,, \tag{8.53}$$

where c is a parameter with the dimensions of an inverse coupling squared, therefore $c \sim 1/(4\pi)^2$ in a strongly coupled UV completion; for simplicity we take $c = 1$. Likewise, naive dimensional analysis yields $M \sim 4\pi f$; here we keep M and f independent and require that $f > M/4\pi$ ($f \gg M$ would correspond to a weakly coupled UV completion). As soon as the Higgs mass parameter turns negative, h acquires a VEV, given by

$$h^2 = \frac{M^2}{\lambda}\left(\frac{\phi}{\phi_c} - 1\right) \,, \quad \phi_c \equiv M/g \,, \tag{8.54}$$

where we have identified ϕ_c as given in Eq. (8.51).

One must now specify how the amplitude of the relaxion periodic term depends on the Higgs VEV. In Sec. 8.2.3 we discuss specific realizations of the relaxion, where such a dependence is either linear (QCD-relaxion), $\tilde{\Lambda}_{\rm B}^4 F(\phi) \equiv \Lambda_{\rm QCD}^4 h/v$ with $v \approx 246$GeV and $\Lambda_{\rm QCD}$ the QCD quark condensate, or quadratic (non-QCD-relaxion), $\tilde{\Lambda}_{\rm B}^4 F(\phi) \equiv \Lambda_{\rm C}^4 (h/v)^2$, where $\Lambda_{\rm C}$ is the analogous of $\Lambda_{\rm QCD}$ for a new QCD-like confining dynamics. These two cases therefore correspond to $k = 1, 2$ in Eq. (8.51), respectively. More complicated functions, beyond Eq. (8.51), arise in the presence of extra light scanning scalars [153]. In any case, the change in the Higgs field between adjacent minima is

$$\Delta h^2 = \frac{2\pi}{\lambda} \frac{\Lambda_{\rm R}^4}{M^2} \,. \tag{8.55}$$

The requirement that $\phi_c \gg f$, which is correlated with the fact that the rolling term is hierarchically smaller than the cutoff of the theory, $\Lambda_{\rm R} \ll M$, see Eq. (8.53), ensures that the Higgs VEV varies slowly with every period of the potential.

Recall that in the relaxion mechanism, ϕ goes through a period of dynamical evolution, originally assumed to happen during a phase of cosmological inflation [8], where it rolls towards the minima of the landscape, generically stopping at one of the first (see below for a characterization of the minima). The parameters of the potential are adjusted, in a technically natural fashion, such that the Higgs VEV is of the right size at the minimum where the relaxion stops its evolution, that is $h = v$. Other proposals regarding the aforementioned time evolution of the relaxion have been put forward in e.g. [154–156] and [157]. In addition, already in [8] and subsequently in e.g. [153,158], the potential itself was made to evolve during inflation, eventually leading to the relaxion resting in a minimum many periods beyond the first. We will however not be concerned with the early cosmological dynamics of the relaxion. Instead, our analysis generally applies to whichever minimum the relaxion eventually stopped at, i.e. to the minimum where the relaxion is found when structures in the universe, in particular stars, start to form.

To ease the analysis of the landscape of relaxion minima, it is useful to redefine the scalar field as

$$\phi \equiv \phi_\ell(\theta) = (2\pi\ell + \theta)\, f \quad \text{with} \quad \ell \in \mathbb{N} \,, \quad \theta \in [0, 2\pi) \,, \tag{8.56}$$

where ℓ labels the period of the field. The local (metastable) minima of the potential are then denoted by $\phi_{\ell_*}(\theta_*)$, where the precise value of θ_* depends on the period ℓ_*. Minima are found as soon as the (ℓ_*-dependent) effective back-reaction grows large enough,

$$\Lambda_{\rm B}^4 \equiv \tilde{\Lambda}_{\rm B}^4 F(\phi_{\ell_*}(\pi/2)) > \Lambda_{\rm R}^4 \,. \tag{8.57}$$

In addition, we can conveniently choose to shift the origin of field space such that the minima start with $\ell_* = 1$, $\phi_\ell \to \phi_\ell + 2\pi f(\bar{\ell} - 1)$ with $\bar{\ell} = (\phi_c/2\pi f)\big[(\Lambda_{\rm R}^4/\tilde{\Lambda}_{\rm B}^4)^{2/k} + 1\big] + \xi$, where $\xi \in [0, 1)$ such that $\bar{\ell} \in \mathbb{N}$.

The relaxion landscape in Eq. (8.50) has two qualitatively different types of minima, depending on the relative size of the rolling and back-reaction terms, see Fig. 8.7. In analogy to Eq. (8.2), these can be parametrized by the variable δ

$$f V'(\phi_{\ell_*}(\pi/2)) \simeq -\Lambda_{\rm R}^4 + \Lambda_{\rm B}^4 \equiv \delta_{\ell_*}^2 \Lambda_{\rm B}^4 \,, \tag{8.58}$$

where V' is the derivative of the potential, here evaluated at the period ℓ_*. We note that δ_{ℓ_*} depends on the period, although to ease the notation we shall henceforth omit the subscript whenever unnecessary. For the first periods of the potential in which a minimum is present, the parameter δ is small. This implies that these minima are *shallow* [159]. Indeed, for $\delta^2 \ll 1$ the minimization condition $0 = f V'(\phi_{\ell_*}(\theta_*)) \simeq -\Lambda_{\rm R}^4 + \Lambda_{\rm B}^4 \sin(\theta_*)$ is satisfied at $\theta_* \simeq \pi/2 - \sqrt{2}\delta$,

which is very close to the local maximum (found at $\theta \simeq \pi/2 + \sqrt{2}\delta$), see the lower-left panel of Fig. 8.7. The mass of the relaxion in these minima is given by

$$m_\phi^2 \simeq \frac{\Lambda_{\rm B}^4}{f^2}\sqrt{2}\delta\,, \qquad \text{(shallow)} \tag{8.59}$$

parametrically suppressed with respect to the usual expectation $m_\phi^2 \simeq \Lambda_{\rm B}^4/f^2$. In subsequent minima one finds $m^2_{\phi_{\ell_*}} = \sqrt{\ell_*}\, m^2_{\phi_1}$, where the value of δ^2 corresponding to $\ell_* = 1$ is

$$\delta^2_{\ell_*=1} \simeq \frac{k\pi f}{\phi_c}\left(\frac{\tilde{\Lambda}_{\rm B}^4}{\Lambda_{\rm R}^4}\right)^{2/k}\left(\tfrac{1}{4}+\xi\right)\,. \tag{8.60}$$

The other type of minima we are interested in corresponds to $\delta^2 \approx 1$. As discussed above for the simplified potential, these are *deep* minima, since $\Lambda_{\rm B} \gg \Lambda_{\rm R}$, see the lower-right panel of Fig. 8.7. The minimization condition yields $\theta_* \simeq 1 - \delta^2 \ll 1$, and the relaxion mass is simply

$$m_\phi^2 \simeq \frac{\Lambda_{\rm B}^4}{f^2}\,. \qquad \text{(deep)} \tag{8.61}$$

Another quantity of phenomenological interest, which is markedly different between shallow and deep minima, is the height of the potential barrier,

$$\Delta V_{\rm top} \simeq \begin{cases} 4\sqrt{2}\Lambda_{\rm B}^4\delta^3\,, & \text{(shallow)} \\ 2\Lambda_{\rm B}^4\,. & \text{(deep)} \end{cases} \tag{8.62}$$

The suppression of the barrier in the case of minima with $\delta^2 \ll 1$ implies that even a small perturbation of the potential can easily destabilize the relaxion, displacing it towards lower energy minima.

8.2.2 The Relaxion at Finite Density

As we have seen above, similar to temperature, finite density effects can have a strong impact on potentials of the sort of Eq. (8.50). While a priori these corrections could modify the landscape in several ways, here we mainly focus on a decrease of the back-reaction term, since for the relaxion this constitutes the leading deformation in most circumstances.[6] Indeed, in QCD-relaxion models, the size of the potential barriers is controlled by $\Lambda_{\rm QCD}$, which is known to linearly decreases with (small) baryon density [115, 116], a fact that has already been shown to affect the QCD axion [118, 119]. Alternatively, for non-QCD-relaxion models, we show in Sec. 8.2.3.B that it is the change of the Higgs VEV with density that leads to a reduction of the potential barriers. In addition, in Sec. 8.2.3.D we speculate about the possibility of dense systems made of the dark baryons, where the back-reaction term would decrease in a similar fashion as in QCD.

Just as in the previous section we introduce the dimensionless quantity ζ to parametrize the relative change in the back-reaction term at finite density

$$\zeta(n) \equiv 1 - \frac{\tilde{\Lambda}_{\rm B}^4(n)}{\tilde{\Lambda}_{\rm B}^4}\,, \tag{8.63}$$

[6] In Sec. 8.2.3.C we discuss a relaxion model in which the rolling term changes due to an electromagnetic background, as well as the modifications that this possibility introduces w.r.t. what we present in this section.

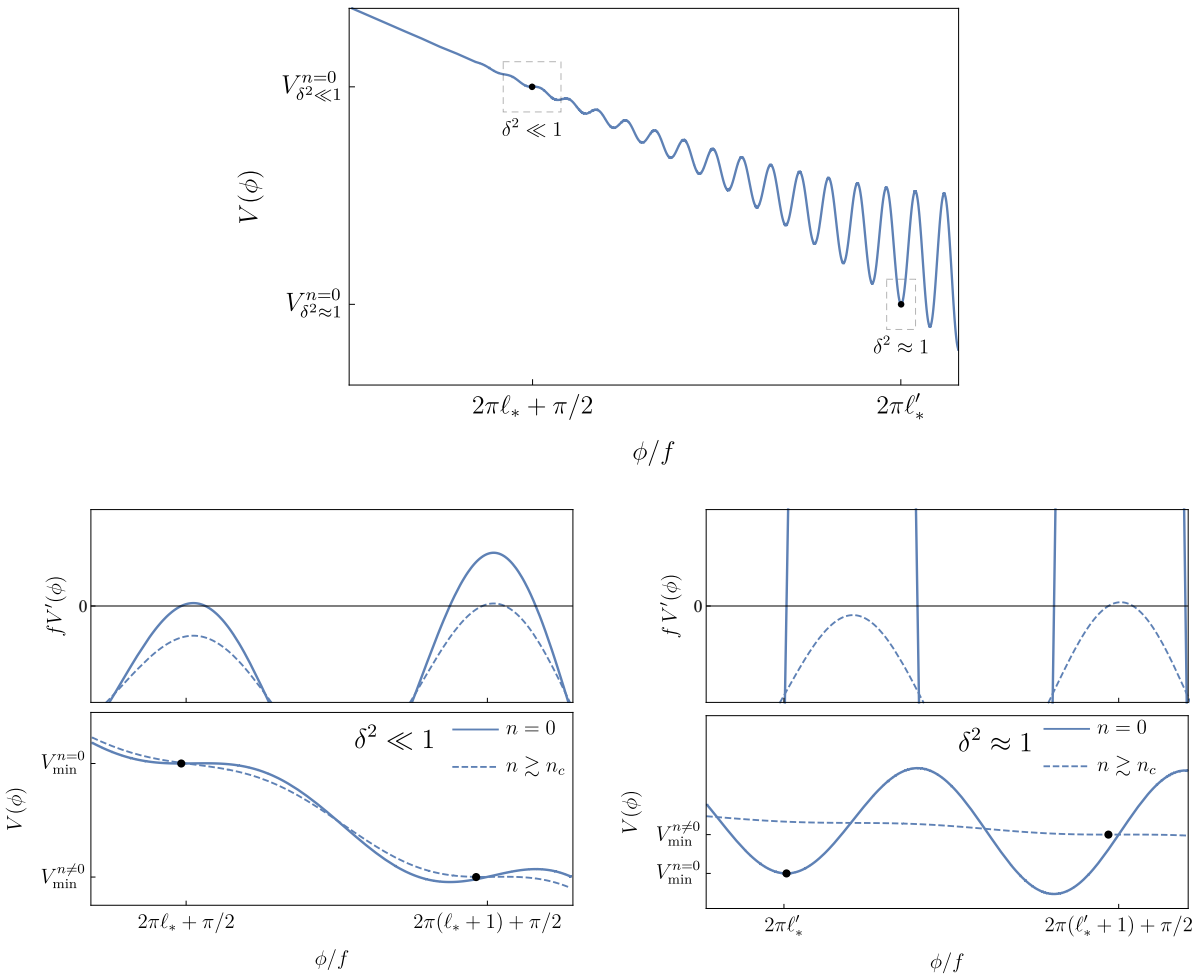

Figure 8.7: Global view of the relaxion potential (upper panel) and zoomed in regions with shallow (lower left) and deep (lower right) minima. Also plotted in the lower panels the in-density potential for n slightly larger than critical (dashed). The upper sub-panels show the derivative of the potential, both for $n = 0$ and $n \gtrsim n_c$. The first minima at finite density are always shallow.

with $\zeta(n) \geqslant 0$ and $\zeta(0) = 0$. Let us now consider that in vacuum the relaxion sits at the minimum corresponding to some fixed period ℓ_*. One can then define a critical density, n_c, above which the effective back-reaction $\Lambda_{\rm B}$ at this minimum is no longer larger than the rolling term. This is implicitly given by

$$\zeta_c \equiv \zeta(n_c) = \delta^2_{\ell_*} \,, \tag{8.64}$$

where we recall that $\delta^2_{\ell_*} = 1 - \Lambda_{\rm R}^4/\Lambda_{\rm B}^4$. When the critical density is reached, the local minimum associated with $\Lambda_{\rm B}$ ceases to exist. In other words, the relaxion minimum corresponding to the period ℓ_* (and obviously all the previous minima) is destabilized when $\zeta(n) > \delta^2_{\ell_*}$. Shallow minima, where $\delta^2 \ll 1$, are easily destabilized by density corrections, since $\zeta_c \ll 1$, while deep minima require $\zeta_c \approx 1$ in order to disappear, see Fig. 8.7. In the following we restrict our discussion to $\zeta(n) \leq 1$, leaving the discussion of the case where the barriers change sign to App. II.B.7.

Hence at densities $n > n_c$ the minimum in which the relaxion resides in vacuum disappears. The number of periods between such a minimum and the first minimum of the in-medium

potential is given by

$$N \equiv \ell_{*n} - \ell_* = \frac{\phi_c}{2\pi f}\left[\left(\frac{1-\zeta_c}{1-\zeta}\right)^{2/k} - 1\right]\left(\frac{\Lambda_{\rm R}^4/\tilde{\Lambda}_{\rm B}^4}{1-\zeta_c}\right)^{2/k} + \xi\,, \tag{8.65}$$

where $\xi \in [0,1)$ such that $N \in \mathbb{N}$. Independently of k ($k \neq 0$), N scales with the difference $\zeta - \zeta_c$. In addition, N scales with $\phi_c/f \gg 1$, thus as soon as ζ is above the critical value, the first in-density minimum is generically many periods beyond the one in vacuum. Additionally, the first minimum at finite density is always shallow: it lies at $\theta_{*n} \simeq \pi/2$, and the mass of the scalar as well as the potential barrier are suppressed beyond the naive expectations, much like for the shallow minima in vacuum.

The change in the ground state energy between consecutive minima, be these shallow or deep, at zero or non-zero density, is always

$$\Delta\Lambda \simeq -2\pi\Lambda_{\rm R}^4\,. \tag{8.66}$$

A Formation and Escape of a Bubble

The disappearance of the in-vacuo minimum at supercritical densities leads to a non-trivial scalar profile, $\phi(r)$, developing within finite size systems such as stars. The characteristic scale of such a relaxion bubble is set by $\mu = \Lambda_{\rm R}^2/f$. This implies that for stars whose core, defined as where $n(r) > n_c$, is larger than μ^{-1}, the field is displaced from its value in vacuum by an amount $\Delta\phi(0) \gtrsim 2\pi f$. Note that this means that inside the bubble, the relaxion has surpassed the field distance corresponding to one period of the potential in vacuum. This gives rise to the possibility that a relaxion bubble, originally confined to dense system, expands beyond the core of the star, given that such a value of relaxion corresponds to a lower energy configuration also in vacuum. In fact, if the gain in energy density is large enough to compensate for the increase of the surface tension of the bubble between the core and outside of the star, the relaxion bubble expands indefinitely.

The conditions for the formation and escape of a scalar bubble interpolating between two adjacent minima of the potential have been recently derived above (Sec. 8.1), for a quartic scalar potential with a tilt. In the neighbourhood of a given minimum of the relaxion potential, the same analysis applies. Intuitively, this is to be expected because the conditions for formation and escape simply follow from energy considerations. First, a scalar bubble associated with a field displacement of one period, that is $2\pi f$, forms when the associated gain in energy density, $\epsilon = -\langle\Delta\Lambda\rangle \sim 2\pi\Lambda_{\rm R}^4$ (see Eq. (8.66)) is enough to compensate for the field gradient $\frac{1}{2}\langle\phi'^2\rangle \sim (2\pi f/R_{\rm T})^2$, where $R_{\rm T}$ is the radius of the star's core. Second, in a finite-size dense system there is an additional contracting force acting on a bubble wall (of radius R), besides the usual expanding force associated with ϵ and the contracting force associated with its surface tension $2\sigma/R$. This additional force is due to the increase of σ with R from the core to the outer edge of the star, $\sigma' = d\sigma/dR \sim \Delta\sigma/\Delta R_{\rm T}$, where $\Delta R_{\rm T}$ is the size of the transition region from the core to the end of the star. Since for a sufficiently large bubble the surface-tension force becomes small, a scalar bubble can expand beyond the confines of the star if $\epsilon \gtrsim \sigma'$.

For a shallow relaxion minimum ($\delta^2 \ll 1$), the change in the wall's tension is negligible, since already in vacuum the potential barrier separating the two adjacent minima is very small, Eq. (8.62). Therefore, when a shallow relaxion bubble forms, it generically escapes from the star as well. The condition for this to happen is

$$R_{\rm T} \gtrsim \frac{f}{\Lambda_{\rm R}^2}\,. \qquad \text{(shallow)} \tag{8.67}$$

Instead, for a deep relaxion minimum ($\delta^2 \approx 1$), the change in the wall's tension is significant, going from being dominated by the gradient energy at the core, to being dominated by the large potential barrier in vacuum. This implies that the escape condition is stronger than the condition for formation. The former reads

$$\Delta R_{\rm T} \gtrsim \frac{f}{\Lambda_{\rm R}^2}\frac{1}{\sqrt{1-\delta^2}} = \frac{f\Lambda_{\rm B}^2}{\Lambda_{\rm R}^4}\,. \qquad \text{(deep)} \tag{8.68}$$

As expected, it is generically much more difficult for a bubble connecting deep minima to escape from the star than for a shallow bubble. Furthermore, recall that in order to destabilize a deep minimum much larger densities are needed than in the shallow case.

In practice, we take both the size of the core $R_{\rm T}$, and the size of the transition region from the core to the end of the star $\Delta R_{\rm T}$, to be of the same order as the whole size of the star, $R_{\rm S} \sim R_{\rm T} \sim \Delta R_{\rm T}$. This is justified for density profiles where the core density is not accidentally close to the critical one. In this regard, notice that different types of stars span not only a range of radii but a range of core densities as well, so cases in which $R_{\rm T}$, $\Delta R_{\rm T} \ll R_{\rm S}$ are not generic.

In the following we consider main-sequence stars like the Sun, white dwarfs (WD), or neutron stars (NS). We take the following as typical radii

$$\begin{aligned} R_{\rm NS} &\equiv \sqrt{8\pi} M_{\rm P}/m_p^2 \approx 2.7\,{\rm km}\,, \\ R_{\rm WD} &\equiv R_{\rm NS}(m_p/m_e) \approx 5\times 10^3\,{\rm km}\,, \\ R_\odot &\approx 7\times 10^5\,{\rm km}\,. \end{aligned} \tag{8.69}$$

For the baryonic densities of these types of stars, which are the most relevant for relaxions, we take as typical values

$$\begin{aligned} n_{\rm NS} &\equiv n_0 \approx 0.16/{\rm fm}^3 \approx 1.3\times 10^6\,{\rm MeV}^3\,, \\ n_{\rm WD} &\equiv 2.8\times 10^7\,{\rm g/cm}^3 \times 1/m_p \approx 0.13\,{\rm MeV}^3\,, \\ n_\odot &\approx 1.5\,{\rm g/cm}^3 \times 1/m_p \approx 7\times 10^{-9}\,{\rm MeV}^3\,, \end{aligned} \tag{8.70}$$

where n_0 is the nuclear saturation density. Note that for white dwarfs we have in fact taken $n_{\rm WD} = m_e^3$, as determined by Fermi degeneracy, since this matches their mean density well [160, 190].

Before moving to the phenomenological consequences of escaping bubbles for specific relaxion models, several additional comments are in order:

As we have seen, the conditions in Eqs. (8.41), (8.68) hold under the assumption that the typical reaction time of the relaxion field (set by $\mu^{-1} = f/\Lambda_{\rm R}^2$) is much faster than the time it takes for a forming star to develop a core (in which $n > n_c$) of size $R_{\rm T} \gtrsim \mu^{-1}$. For stellar processes where this is not the case, the formation of a scalar bubble takes place suddenly instead of in the nearly static fashion we have assumed (for more details on the sudden case, see Sec. II.B.5).

Irrespective of the time evolution, if the stars grows very large compared to μ^{-1}, very large field displacements (w.r.t. to where the relaxion resides in vacuum) are energetically allowed inside the bubble. Indeed, at a fixed core density such that ζ is not accidentally close to criticality, a very large core $R_{\rm T} \sim \sqrt{N}\mu^{-1} \gg \mu^{-1}$ allows for the relaxion to move by many periods $N \gg 1$, see Eq. (8.65). As explained in App. II.B.6, such a large relaxion bubble has the effect of helping the standard bubble connecting two adjacent minima (i.e. for which $\Delta\phi(0) \sim 2\pi f$) to escape from the star. In fact, such a bubble escapes independently of the density profile, regardless of how fast density decreases towards the outer edge of the star. In

this case the conditions Eqs. (8.41), (8.68) read the same, only with $R_{\rm S}$ instead of $R_{\rm T}$ and $\Delta R_{\rm T}$; they simply encode the requirement for a standard relaxion bubble to expand once it is outside of the star, see Eqs. (II.B.24), (II.B.25). If one bubble is able to escape, the new relaxion minimum in vacuum becomes the one associated with the next period, i.e. $\ell_* + 1$. Interestingly, since $N = \ell_{*\,n} - \ell_* \gg 1$, such a new minimum is also unstable inside the dense system. This then implies that another bubble, within which this time the relaxion sits at the minimum $\ell_* + 2$, will generically be able to escape as well, and so on until the escape condition is no longer satisfied.

Finally, let us note that our whole discussion relies on the assumption that the density profile is treated as a background field that does not receive a large back-reaction from the formation and expansion of a relaxion bubble. In App. II.B.8 we discuss the interactions of the relaxion (non-trivial configurations) with the density profile, thereby justifying this treatment.

8.2.3 Bounds on Relaxions

The relaxion bubbles discussed above are born along with the stars that seed them. Therefore, if the conditions for the bubble to expand beyond the dense system are met, a phase transition in the universe to a new relaxion vacuum can take place whenever the right type of stars are formed. A rough experimental bound on such a change was derived in (8.47). The possibility of such most phase transitions in relaxion models is therefore ruled out by cosmological data. Still, it is interesting to note that if we were to consider bubbles nucleated by the largest stars observed so far, with radii $R_{\rm S} \sim 10^3 R_\odot$, or by large non-standard astrophysical objects, associated for instance with some beyond the SM relic species, e.g. dark matter (see Sec. 8.2.3.D), then a phenomenologically viable late-time phase transition could have taken place. In this regard, it would be interesting to perform a detailed assessment of the associated cosmological and astrophysical signatures.

Besides, in relaxion models the change of minimum also implies a change in the Higgs VEV, for which there exist cosmological (and astrophysical) constraints as well. However, let us note right away that the relative change of the electroweak scale between minima is much smaller than the change in the vacuum energy: $(\Delta h^2/v^2)/(|\Delta\Lambda|/\Lambda_0) = \Lambda_0/\lambda c v^2 M^2 \ll 1$, where we have used Eq. (8.55). Nevertheless, since this is one of the trademarks of relaxion models compared to other landscapes, let us briefly review the bounds. There are significant constraints on a different value of the Higgs VEV during BBN, $|\Delta h/v| \lesssim 10^{-2}$ where $\Delta h = h - v$ [210]. In addition, it has been recently argued that SN explosions can only happen if h is below a factor of a few away from v [211]. While these constraints (the one from BBN in particular) could be violated if the universe underwent a change of relaxion minimum at star formation, as shown above the associated change in vacuum energy always yields a more or equally stringent constraint.

In the remainder of this section, we work out the specifics of how a non-vanishing SM matter density (or an electromagnetic background) affects the potential of some benchmark relaxion models, and re-express the conditions for the formation and escape of bubbles in terms of their parameters.

A QCD Relaxion

The most economic origin of the relaxion periodic term is low-energy QCD dynamics, in which case we identify the relaxion with the QCD axion. The dependence on the Higgs VEV arises from the well-known dependence of the axion potential on the quark masses. This leads us to identify $\tilde{\Lambda}_{\rm B}$ in Eq. (8.50) as well as $\Lambda_{\rm B}$, the effective size of the periodic term at the minimum

where the relaxion sits in vacuum, as

$$\tilde{\Lambda}_{\rm B}^4 = \Lambda_{\rm QCD}^4 \frac{M}{v\sqrt{\lambda}}\,, \quad \Lambda_{\rm B}^4 = \Lambda_{\rm QCD}^4 \frac{h}{v}\,. \tag{8.71}$$

Note that if a seeded phase transition took place, the relaxion would not sit at the same minimum today than right before star formation. Nevertheless, in the following we conservatively fix $h = v \approx 246\text{GeV}$, since any minimum prior to star formation with a smaller h would necessarily be shallower than the present one, making it easier for the transition to take place. The exponent of the function $F(\phi)$ in Eq. (8.51) is determined as well, $k = 1$, since the dependence of the back-reaction term on the Higgs VEV is linear. Note that the QCD(-axion) scale is $\Lambda_{\rm QCD}^4 \simeq m_\pi^2 f_\pi^2/4$. Finally, the value of δ, which determines if the relaxion minimum is shallow or deep, depends on the relative size of the rolling term, $\Lambda_{\rm R}^4 = gM^3 f$, according to Eq. (8.58),

$$\delta^2 = 1 - g\frac{M^3 f}{\Lambda_{\rm QCD}^4}\,. \tag{8.72}$$

In this regard, let us note that, as advanced, for the first minima of the potential δ is always a small parameter as long as the scanning of the Higgs VEV is sufficiently precise. At the first minimum,

$$\delta_{\ell_*=1}^2 \simeq \frac{\pi\Lambda_{\rm QCD}^4}{\lambda v^2 M^2}\left(\tfrac{1}{4} + \xi\right) \ll 1\,, \quad \xi \in [0,1)\,, \tag{8.73}$$

while for all the subsequent minima $\delta_{\ell_*}^2 = \ell_* \delta_1^2$. Since it has no actual significance, from now on we set $\xi = 0$.

Once all the relevant parameters of our potential have been identified, let us consider the fate of the relaxion bubbles, starting with shallow minima, $\delta^2 \ll 1$. This case should be mostly considered as illustrative, since the value of the relaxion at the minimum is displaced from a multiple of $2\pi f$ by approximately $\pi/2$, thus the strong CP angle is also $\theta_{\rm QCD} \simeq \pi/2$, which is experimentally ruled out. Keeping this in mind, we can compute the dependence of the back-reaction term, or equivalently ζ in Eq. (8.63), on the baryon density n_b by means of the Feynman-Hellmann theorem, as explained in e.g. [118],

$$\zeta(n_b) \simeq \frac{\sigma_{\pi N} n_b}{m_\pi^2 f_\pi^2}\,. \tag{8.74}$$

This holds for densities below a few times nuclear saturation, and where $\sigma_{\pi N} \approx 45\,\text{MeV}$ is known as the pion-nucleon sigma term. In turn, since the critical value of ζ for which the relaxion can classically move is given by $\zeta_c = \delta^2$, we find that a proto-bubble can start forming if

$$n_b > \frac{\ell_*}{M^2}\frac{\pi\Lambda_{\rm QCD}^8}{\sigma_{\pi N}\lambda v^2} \approx 1\times 10^{-8}\,\text{MeV}^3\left(\frac{1\,\text{TeV}}{M/\sqrt{\ell_*}}\right)^2\,, \tag{8.75}$$

that is if densities are larger than $3\,\text{g/cm}^3 \times 1/m_p$. This is a very low critical density, found not only in neutron stars and white dwarfs, but in the Sun as well. The densities reached in these systems then set the minimum value of $M/\sqrt{\ell_*}$ that is excluded if the bubble eventually fully forms and escapes the star. The corresponding condition is given in Eq. (8.41), which for the QCD-relaxion reads

$$R_{\rm S} \gtrsim \frac{f}{\Lambda_{\rm QCD}^2}\,, \tag{8.76}$$

where we have taken $R_{\rm T} \sim R_{\rm S}$ as argued in Sec. 8.2.2.A, and traded $\Lambda_{\rm R}$ with $\Lambda_{\rm QCD}$ given that $\delta^2 \ll 1$. Using the reference radii and densities quoted in Eqs. (8.69), (8.70), we arrive at the following excluded values for the relaxion decay constant and cutoff

$$\begin{aligned} \text{NS}: &\quad f \lesssim 3\times 10^{-2} M_{\rm P}\,, &\quad M/\sqrt{\ell_*} \gtrsim 1\times 10^{-4}\text{GeV}\,, & \\ \text{WD}: &\quad f \lesssim 63\, M_{\rm P}\,, &\quad M/\sqrt{\ell_*} \gtrsim 0.3\text{GeV}\,, & \quad \text{(QCD; shallow)} \\ \odot: &\quad f \lesssim 9\times 10^{3} M_{\rm P}\,, &\quad M/\sqrt{\ell_*} \gtrsim 1.4\,\text{TeV}\,. & \end{aligned} \tag{8.77}$$

Therefore, while recalling that the shallow QCD relaxion is already ruled out by a too large $\theta_{\rm QCD}$, we find that classical rolling and escape would happen for nearly all values of f and $M/\sqrt{\ell_*}$. Note in fact that for both white dwarfs and main-sequence stars the upper bounds on f are above $M_{\rm P}$, and that for neutron stars and white dwarfs the lower bound on M is not larger than the electroweak scale.

The situation is markedly different for deep minima, in particular since we must require $\theta_{\rm QCD} \lesssim 10^{-10}$, which then fixes $1-\delta^2$ to be as small at the minimum in question. Since $\zeta_c = \delta^2$, this implies that the QCD barriers at finite density, $\Lambda^4_{\rm QCD}(1-\zeta(n))$, would need to nearly disappear for the relaxion to be able to classical move to the next minimum. Such large densities, if attainable at all inside neutron stars, are certainly beyond perturbative control and thus the linear approximation used to derive Eq. (8.74) is not applicable. However, since in the cores of neutron stars densities could be higher than ten times nuclear saturation density [191], it has been long been hypothesised that new phases of QCD, such as kaon condensation or color-superconductivity, could take place there, see e.g. [118] and references therein. As shown in that work, this raises the possibility that, while remaining finite, the periodic potential flips sign. As explained in App. II.B.7 (see also [212]), this would lead to relaxion condensation with $\Delta\phi(0) = \pi$, assuming a small rolling region. Such a type of bubble would remain confined inside the dense system.

Still, an interesting option remains that such a change of phase of strongly interacting matter, being controlled by QCD dynamics, happens very fast compared to the reaction time of the relaxion. In the case of a deep minimum this reaction time is prolonged compared to a shallow one, $\mu^{-1} = f/\Lambda^2_{\rm R} = \theta_{\rm QCD}^{-1/2} f/\Lambda^2_{\rm QCD}$. Then, as discussed in [12], the kinetic energy that the field acquires after the sudden change of its potential could be enough to overcome the (flipped) barriers and to create a relaxion bubble with $\Delta\phi(0) \gg 2\pi f$. This facilitates the escape of a standard $2\pi f$ bubble, as discussed above (see also App. II.B.6). With our current knowledge of QCD at such extreme densities we cannot assert whether this is the right picture. Nevertheless, if it were, a phase transition would take place if the condition Eq. (II.B.25) is satisfied

$$f < \sqrt{\theta_{\rm QCD}}\Lambda^2_{\rm QCD} R_{\rm NS} \approx 8\times 10^{11}\text{GeV}\left(\frac{\theta_{\rm QCD}}{10^{-10}}\right)^{1/2}\,. \qquad \text{(QCD; deep)} \tag{8.78}$$

B Non-QCD Relaxion

The correlation between the relaxion selection of the electroweak scale and of $\theta_{\rm QCD}$, i.e. between the electroweak hierarchy and the strong CP-problem, can be broken by positing that dynamics other than QCD is responsible for the generation of the periodic back-reaction term [8]. Such a non-QCD strong sector must still couple to the relaxion in such a way as for the amplitude of the barriers to depend on the Higgs VEV. Experimental constraints on new electroweak-charged degrees of freedom that get mass from electroweak symmetry breaking motivates that such a dependence is quadratic, instead of the linear dependence of the QCD scale (see however

Sec. 8.2.3.C). Therefore, we identify our potential parameters in Eq. (8.50) as

$$\tilde{\Lambda}_{\rm B}^4 = \Lambda_{\rm C}^4 \frac{M^2}{\lambda v^2}\,, \quad \Lambda_{\rm B}^4 = \Lambda_{\rm C}^4 \frac{h^2}{v^2}\,, \quad k = 2\,, \tag{8.79}$$

where $\Lambda_{\rm C}$ is the new confinement scale, analogous to $\Lambda_{\rm QCD}$ in Eq. (8.71). In order for the size of the barriers to be naturally dominated by the Higgs VEV squared, the condition $\Lambda_{\rm C}^2 \lesssim 4\pi v^2$ must be required [8, 153, 157, 213]. In parallel with the QCD-relaxion, the value of δ at a given minimum is determined by the relative size of the rolling term and $\Lambda_{\rm C}^4$, i.e. Eq. (8.72) with $\Lambda_{\rm QCD} \to \Lambda_{\rm C}$. The first minima of the landscape are always shallow, since $\delta_1^2 \simeq \pi\Lambda_{\rm C}^4/2\lambda v^2 M^2 \ll 1$ for $\Lambda_{\rm C}^2 \lesssim 4\pi v^2$ and $M \gg 4\pi v$.

The dependence of the back-reaction term on the (SM) matter density in this case is indirect, stemming from a change in the Higgs VEV. This is due to the coupling of the Higgs field to fermions, $\mathcal{L} \supset -\frac{1}{\sqrt{2}}\, y_\psi h \bar{\psi}\psi$, which in a (non-relativistic) ψ background, $\langle\bar{\psi}\psi\rangle \simeq \langle\bar{\psi}\gamma_0\psi\rangle = n_\psi$, displaces its VEV from its value in vacuum. The small relative displacement with respect to Eq. (8.54) is given, at leading order in n_ψ, by

$$\delta h^2(n_\psi) = \frac{y_\psi}{\sqrt{2}} \frac{n_\psi}{\lambda v^3}\,, \tag{8.80}$$

where we have evaluated $h = v$. The change $h^2 \to h^2(1 + \delta h^2)$ is then responsible for the density dependence of the relaxion potential. In this regard, note that both the rolling and back-reaction terms are affected, since both of them are in fact quadratic in the Higgs, see Eq. (8.52) and Eq. (8.79) respectively. Nevertheless, it is easy to see that the leading effect is associated with the latter since, while the Higgs contribution to the barriers is the leading piece, it is a subleading one for the linear slope as long as $v^2/M^2 \ll 1$.

The most relevant densities to consider, as in the case of the QCD-relaxion, are baryonic, since these are usually the largest (in particular in the cores of neutron stars) and the coupling of nucleons to the Higgs is significant $y_N = \sigma_{\pi N}/v$, where $N = n, p$. In neutron stars, besides neutrons and protons, leptons are present as well. Charge neutrality implies $n_p + n_e + n_\mu = 0$, where note that due to the highly energetic Fermi surface of the electron, β-equilibrium not only implies $\mu_n = \mu_p + \mu_e$ but $\mu_e = \mu_\mu$ as well, implying a non-vanishing muon density (for $\mu_\mu > m_\mu$). This is interesting since the coupling of muons to the Higgs, $y_\mu = m_\mu/v$, is twice as large as to nucleons. In the outer layers of neutron stars, in white dwarfs and main-sequence stars, baryon densities become once again the most important, given the small coupling of electrons to the Higgs. We therefore focus on the effects of a non-vanishing n_b. Still working in the linear approximation, the decrease of the non-QCD barriers is encoded as

$$\zeta(n_b) \simeq \sqrt{2}\frac{\sigma_{\pi N} n_b}{m_h^2 v^2}\,, \tag{8.81}$$

where we have written it in terms of the physical Higgs mass, $m_h^2 = 2\lambda v^2$, to make apparent the similarity with Eq. (8.74). A relaxion bubble can then classically form if densities satisfy the following condition

$$n_b > \frac{\ell_* \Lambda_{\rm C}^4}{M^2} \frac{\pi v^2}{\sqrt{2}\sigma_{\pi N}} \approx 3 \times 10^{-3}\,{\rm MeV}^3 \left(\frac{1\,{\rm TeV}}{M/\sqrt{\ell_*}}\right)^2 \left(\frac{\Lambda_{\rm C} \simeq \Lambda_{\rm R}}{1\,{\rm MeV}}\right)^4 . \tag{8.82}$$

Even though finite density effects are relatively suppressed in the case of the non-QCD relaxion, the required critical densities are sufficiently small, for large cutoffs or small back-reactions, that

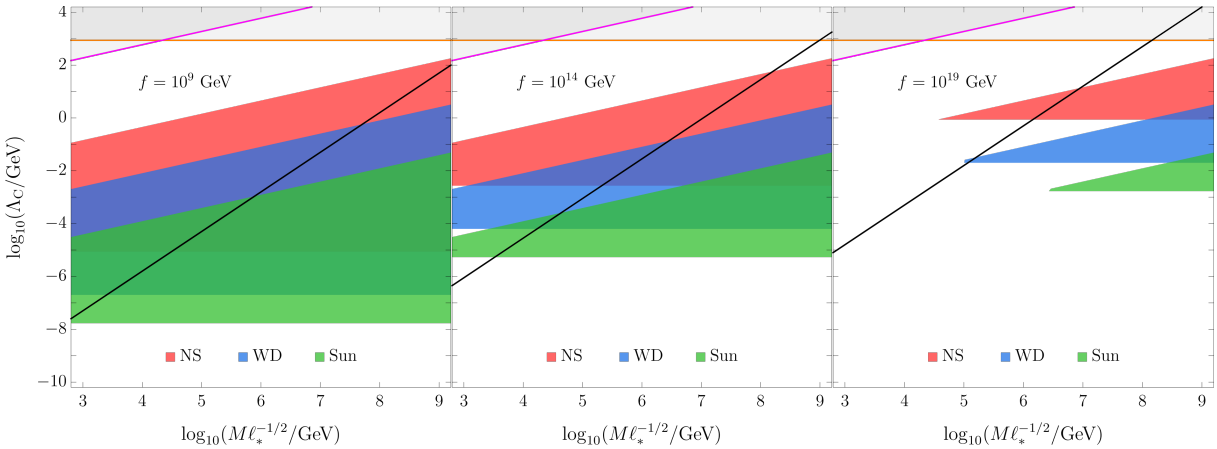

Figure 8.8: $(M/\sqrt{\ell_*}, \Lambda_C)$-regions excluded by the formation and escape of a non-QCD relaxion bubble induced by neutron stars (red), white dwarfs (blue), and the Sun (green), in the case of shallow minima, $\delta^2 \ll 1$ or equivalently $\Lambda_R \simeq \Lambda_C$, and for $f = 10^9$, 10^{14}, 10^{19}GeV (left, middle, right panel, respectively). The grey, shaded region is excluded by the requirements $\Lambda_C^2 \lesssim 4\pi v^2$ (orange line) and $\Delta h^2 < v^2$ (magenta line), while the region of parameter space preferred by relaxation during inflation lies above the diagonal black line. Note that the latter line depends on a model-dependent period of dynamical evolution, which our constraints are independent of. The three lines are drawn taking $\ell_* = 1$.

they can be found from neutron stars to the Sun. Furthermore, relaxion bubbles will only form for shallow minima, $\zeta_c = \delta^2 \ll 1$, since values of $\zeta(n_b)$ close to unity, which are required to destabilize deep minima, can never be achieved (this would require exorbitant densities, of order $m_h^2 v^2/\sigma_{\pi N} \sim 10^{19}\,\mathrm{MeV}^3$).

The condition for a shallow bubble to fully form and escape the star simply reads

$$R_S \gtrsim \frac{f}{\Lambda_C^2}\,, \qquad \text{(non-QCD; shallow)} \tag{8.83}$$

where recall that for $\delta^2 \ll 1$ we have $\Lambda_R \simeq \Lambda_C$. The conditions in Eqs. (8.82), (8.83), which if satisfied imply a late-time phase transition at odds with experiment, give rise to non-trivial constraints on the parameter space of the non-QCD relaxion. These are qualitatively different and generically stronger than those dependent on the period of dynamical evolution; namely $\Lambda_R^4 > M^6 f/\sqrt{12}\pi M_P^3$ for relaxation during inflation, associated with the requirement of classical evolution of the field along with the energy density associated with the relaxion being a subdominant component [8,153,157,213]. A related but different discussion of chameleon effects relevant for dark matter direct detection experiments have been recently presented in [214]. We show our constraints in Figs. 8.8 and 8.9, in the planes $(M/\sqrt{\ell_*}, \Lambda_C)$, and (M, g) for $\ell_* = 1$, respectively. These are for three different values of the relaxion decay constant, $f = 10^9$, 10^{14}, 10^{19}GeV. In both planes, it is evident that the lower boundary of the excluded (shaded) regions extends to smaller values of either $\Lambda_C \simeq \Lambda_R$ or g as f is taken smaller, since it is easier for the relaxion bubble to fit inside a given type of star, Eq. (8.83). In turn, as f is taken larger, either Λ_C or g must be larger for the bubble to be able to form, which then requires higher densities, Eq. (8.82); this is why the constrains from less dense stars become comparatively weaker. Note that although the plots are cut at $M = 10^9$GeV, the constraints actually extend up to $M \lesssim 4\pi f$ in each case. Let us also point out that if the theoretical expectation that $f < M_P$ is accepted, the constraints for $f = 10^{19}\mathrm{GeV} \approx M_P$ can be considered as absolute, meaning the corresponding

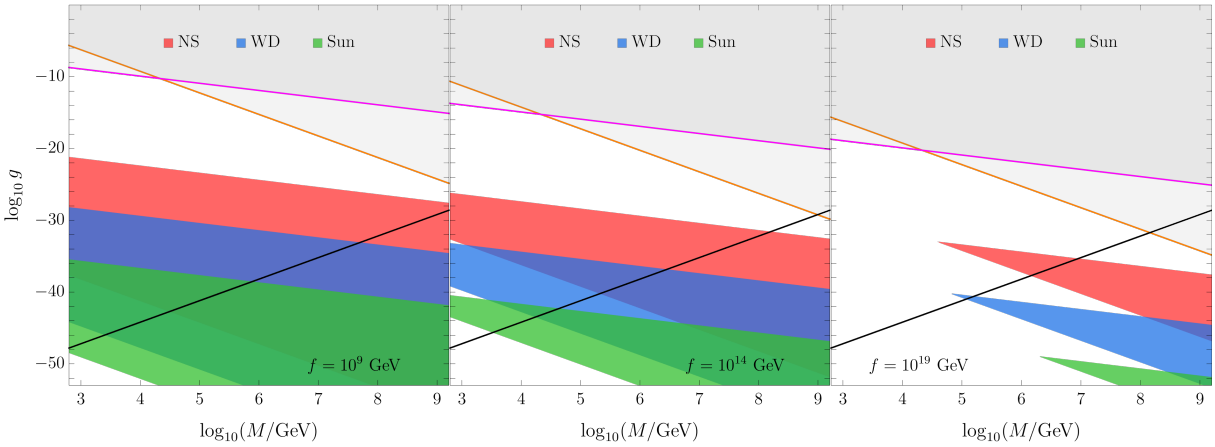

Figure 8.9: (M, g)-regions excluded by the formation and escape of a non-QCD relaxion bubble induced by neutron stars (red), white dwarfs (blue), and the Sun (green), in the case of shallow minima, $\delta^2 \ll 1$ or equivalently $\Lambda_{\rm R} \simeq \Lambda_{\rm C}$, and for $f = 10^9, 10^{14}, 10^{19}$GeV (left, middle, right panel). The grey, shaded region is excluded by the requirements $\Lambda_{\rm C}^2 \lesssim 4\pi v^2$ (orange line) and $\Delta h^2 < v^2$ (magenta line), while the region of parameter space preferred by relaxation during inflation lies above the diagonal black line. Note that the latter line depends on a model-dependent period of dynamical evolution, which our constraints are independent of. Recall that $g = \Lambda_{\rm R}^4/M^3 f$ and we have taken $\ell_* = 1$ in Eq. (8.82).

parameter space is excluded for any (possible) value of the axion decay constant. Finally, considering larger stars with enough density would enlarge the excluded regions. In the case of the (green) region associated with main-sequence stars, once the inequality Eq. (8.47) is saturated, more refined experimental constraints on changes in the energy budget of the universe or from other observables, would be needed. The investigation of these detailed bounds is beyond the scope of this work.

C Technicolored Relaxion

For the QCD and non-QCD relaxion models, the most important density deformation of their respective landscapes is in the form of a smaller back-reaction term. Now we wish to point out that in general this is not the only possibility. In this section we present a scenario in which the leading effect is due to a change in the rolling term. Furthermore, this change is induced not by background matter but by the electromagnetic fields surrounding a spinning neutron star.

Another variant of the relaxion model involves a technicolor-like sector which provides an additional source of electroweak symmetry breaking on top of the elementary Higgs. While this sector, irrespective of the relaxion, is severely constrained experimentally (by electroweak precision data, Higgs coupling measurements and resonance searches at the LHC), it is not yet ruled out [215, 216]. Exactly like for the QCD axion, the coupling of the relaxion to the topological charge of this new confining sector gives rise to the periodic potential term [213], with the analogue of $\Lambda_{\rm QCD}$ given by

$$\Lambda_{\rm TC}^4 \simeq 4\pi v'^3 m_U \,, \tag{8.84}$$

where v' is the electroweak-breaking order parameter of the technicolor (TC) sector. The electroweak scale is given by $v^2 = v'^2 + h^2$ and $m_U = y_U h/\sqrt{2}$ is the lightest techniquark mass, linearly proportional to the elementary Higgs VEV. The parameters of the relaxion potential

are then identified as $\Lambda_{\rm R}^4 = gM^3 f$ (like in all the previous models), while $\tilde{\Lambda}_{\rm B}$ and $\Lambda_{\rm B}$ are similar to the QCD relaxion, Eq. (8.71), with the following replacements

$$\Lambda_{\rm QCD} \to \Lambda_{\rm TC}\,, \quad v \to \sqrt{v^2 - v'^2}\,. \tag{8.85}$$

Due to the aforementioned experimental constraints, v' cannot be large, $v' \lesssim 70$GeV, nor very small either, since the masses of the TC resonances are expected below $4\pi v'$ [215].

It is crucial for our analysis that the relaxion in this model has a large coupling to photons. Just like for the QCD axion, this coupling is a consequence of the (model-independent) coupling to the technigluons as well as the (model-dependent) electromagnetic anomaly,

$$\frac{g_{\phi\gamma\gamma}}{4}\frac{\phi}{f}F_{\mu\nu}\tilde{F}^{\mu\nu}\,, \quad g_{\phi\gamma\gamma} = c\left(\frac{\alpha}{2\pi}\right)\,, \tag{8.86}$$

where c is a model-dependent constant. Such an interaction, which is not suppressed by the small shift-symmetry breaking parameter g, has significant implications for the fate of this relaxion model, in particular because of the existence of strong electromagnetic fields surrounding rapidly rotating neutron stars (magnetars/pulsars).[7] Indeed, in such an environment the linear term in the relaxion potential receives an additional contribution, $\Lambda_{\rm R}^4 \to \Lambda_{\rm R}^4(1+\eta)$, where

$$\eta = \frac{g_{\phi\gamma\gamma}\boldsymbol{E}\cdot\boldsymbol{B}}{\Lambda_{\rm R}^4}\,. \tag{8.87}$$

The critical value of η at which the minimum in vacuum ceases to be a minimum in the electromagnetic background is given by $\eta_c = \delta^2/(1-\delta^2)$. This statement can be translated to a transition radius, $R_{\rm T}^{\rm EM}$, which is the maximal radius for which classical rolling is allowed (equivalent to the radius of the dense star core $R_{\rm T}$, see Sec. 8.2.2.A), and given by the solutions of $\eta(R_{\rm T}^{\rm EM}) = \eta_c$. It is also the position of the bubble wall at formation. The value of δ^2 at the ℓ_*-th shallow minimum is given, as in the QCD relaxion, by $\delta^2_{\ell_*} = \ell_*\delta_1^2$, where $\delta^2_{\ell_*=1}$ is as in Eq. (8.73) with $\Lambda_{\rm QCD} \to \Lambda_{\rm TC}$. The electric and magnetic fields depend on the intrinsic properties of the star as well as on space-time, in a similar fashion as the (baryonic) density profiles that were considered in our previous examples. However, in contrast to the case of a dense system of finite size, here the electromagnetic background extends to infinity (i.e. much beyond the surface of the star). This implies, for instance, that the radius at which classical rolling is allowed is potentially much larger than $R_{\rm S}$. As explained in Sec. 8.2.2.A (see [12] for a more detailed discussion) it is the size of this region compared to μ^{-1}, the typical length scale of the relaxion, that determines whether a bubble is formed or not. For a technicolored relaxion μ^{-1} is r-dependent,

$$\mu^{-1}(r) = \frac{f}{\Lambda_{\rm R}^2}\frac{1}{\sqrt{1+\eta(r)}}\,. \tag{8.88}$$

Let us then consider a simple model of the magnetosphere, in particular a rotating dipole in vacuum (see e.g. [217]),

$$\boldsymbol{E}\cdot\boldsymbol{B} = \frac{R_{\rm S}^6 B_{\rm S}^2 \Omega_{\rm S}}{4r^5}\sin\alpha\big(\cos\theta\sin\alpha + \sin\theta\cos\alpha\left[r\Omega_{\rm S}\cos\left(\lambda + r\Omega_{\rm S}\right) - \sin\left(\lambda + r\Omega_{\rm S}\right)\right]\big)\,, \tag{8.89}$$

with $B_{\rm S}$ the magnetic field at the stellar surface, $\Omega_{\rm S}$ the rotation frequency of the star, α the inclination angle of the dipole w.r.t. the rotation axis, and $\lambda = \phi - \Omega_{\rm S} t$ the co-rotating azimuthal

[7] By considering a rotating star we are departing from our main assumptions concerning the characteristics of the system, as described in [12], in particular spherical symmetry and (near) time-independence. However, we expect such departures to neither have a large impact on our qualitative description, nor to change the order of magnitude results we derive.

angle. From here on we take $\alpha = \pi/4$ for simplicity. In addition, we average the dipole over one quadrant, that is $\theta \in [0, \pi/2]$ and $\phi \in [0, \pi]$, as well as over the relaxion time scale μ^{-1}. We identify two distinct limits, the first where the field reacts fast compared to the rotation frequency, $\mu \gg \Omega_{\rm S}$, and the second where it reacts slowly, $\mu \ll \Omega_{\rm S}$. Since the bubble dynamics, in particular if the bubble escapes or stays confined to the star, is a local statement governed by the position of the bubble wall at its formation, we take $\mu^{-1}(R_{\rm T}^{\rm EM})$ as the relevant time scale in both limits. Within the fast limit, in order to analytically determine $R_{\rm T}^{\rm EM}$ we perform an expansion both in $\Omega_{\rm S}/\mu \ll 1$ and $\Omega_{\rm S} r \ll 1$. For critical bubbles connecting shallow minima, the validity of the second approximation follows from the first along with Eq. (8.92). For critical bubbles connecting deep minima such an approximation is not valid in general, yet we verified a posteriori that it holds in the region of interest, i.e. where the bounds lie, see Fig. 8.10. In the limit where the field reacts slowly, we just perform an expansion in $\mu/\Omega_{\rm S} \ll 1$. After the dust settles, we end up with

$$\left\langle \boldsymbol{E} \cdot \boldsymbol{B} \right\rangle \simeq \frac{B_{\rm S}^2 R_{\rm S}^6 \Omega_{\rm S}}{4\pi^2 r^5} \begin{cases} (\pi - 2)\,, & \mu \gg \Omega_{\rm S}\,, \\ \pi\,, & \mu \ll \Omega_{\rm S}\,, \end{cases} \tag{8.90}$$

where we only kept the leading order terms. Note that the difference between the fast and slow limits is due to the time-dependent piece of the dipole, which is relevant only in the first case. For such a leading order averaged dipole, the transition radius is given by

$$R_{\rm T}^{\rm EM} = \left(\frac{\alpha}{8\pi^3} \frac{B_{\rm S}^2 R_{\rm S}^6 \Omega_{\rm S}}{\Lambda_{\rm TC}^4 \delta^2} \right)^{1/5} \begin{cases} (\pi - 2)^{1/5}\,, & \mu \gg \Omega_{\rm S}\,, \\ \pi^{1/5}\,, & \mu \ll \Omega_{\rm S}\,, \end{cases} \tag{8.91}$$

where we chose $c = 1$. Clearly, $R_{\rm T}^{\rm EM}$ is much larger for shallow minima ($\delta^2 \ll 1$) than for deep ones ($\delta^2 \approx 1$), since the size of the critical electromagnetic field is much smaller for the former than for the latter. The condition that $R_{\rm T}^{\rm EM} > R_{\rm S}$, which is equivalent to the statement that the critical value of η is reached somewhere before the surface of the star, is certainly necessary for a bubble to form (equivalent to the condition $\zeta(n_b) > \zeta_c$ in the relaxion models previously discussed). However, since $\boldsymbol{E} \cdot \boldsymbol{B} = 0$ for $r < R_{\rm S}$, the conditions for the formation and expansion to infinity of the bubble sets a lower bound on the size of the region $R_{\rm T}^{\rm EM} - R_{\rm S}$ which is always more stringent than just $\eta(R_{\rm S}) > \eta_c$. For shallow minima, the condition for the formation of a $2\pi f$ bubble is roughly given by

$$R_{\rm T}^{\rm EM} - R_{\rm S} \gtrsim \frac{f}{\Lambda_{\rm R}^2} \simeq \frac{f}{\Lambda_{\rm TC}^2}\,. \qquad \text{(technicolor; shallow)} \tag{8.92}$$

This is the same condition leading to the escape of a bubble to infinity, since when $\delta^2 \ll 1$ the change in the potential from the inside to the outside of the transition region $r \sim R_{\rm T}^{\rm EM}$ is barely appreciable. We can explicitly verify that this is the case by considering the equation of motion of the bubble wall within the background electromagnetic field (see [12] for the equivalent in the case of a bubble wall within a star),

$$\sigma \ddot{R} = \epsilon - \frac{2\sigma}{R} - \sigma'\,, \qquad \epsilon(R) = 2\pi \Lambda_{\rm R}^4 \left[1 + \frac{\delta^2}{1 - \delta^2} \left(\frac{R_{\rm T}^{\rm EM}}{R} \right)^5 \right], \tag{8.93}$$

where ϵ is the energy density inside the bubble. Its R-dependence is due to the R-dependence of η. It is then clear that for a shallow minimum, where $\delta^2 \ll 1$ and therefore $\sigma' = d\sigma/dR \simeq 0$, the condition for the bubble to escape is, to good approximation, given by Eq. (8.92). Note that we

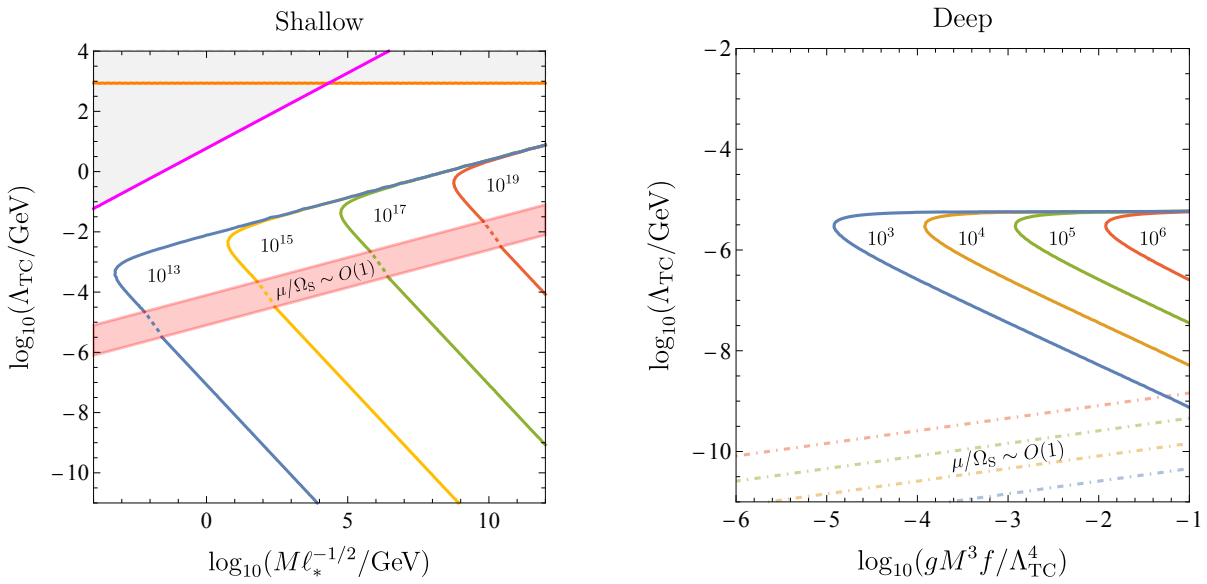

Figure 8.10: Regions excluded (inside labelled lines for several values of f[GeV]) by the formation and escape of a TC relaxion bubble induced by the electromagnetic fields generated by rotating neutron stars. Left panel: for a bubble connecting shallow minima, $\delta^2 \ll 1$ or equivalently $\Lambda_{\rm R} \simeq \Lambda_{\rm TC}$. The red band shows $\mu \sim \Omega_{\rm S}$ for a critical bubble. Right panel: for a bubble connecting deep minima, the depth parametrized by $gM^3 f/\Lambda_{\rm TC}^4 = 1-\delta^2$. Dot-dashed lines show $\mu \sim \Omega_{\rm S}$ for the corresponding decay constant. Note the different range for $\Lambda_{\rm TC}$ (recall for shallow minima $\Lambda_{\rm TC} \simeq \Lambda_{\rm R}$) between the two plots.

have neglected $O(1)$ factors as we did in Eqs. (8.41), (8.68), yet we expect them to be different here due to the non-spherical morphology of the system.

When the condition in Eq. (8.92) is satisfied, the phase transition implies a change in vacuum energy that is experimentally too large for $2\pi\Lambda_{\rm R}^4 \gtrsim 10^2\Lambda_0$, see Eq. (8.47). This allows us to exclude large regions of parameter space of the technicolored relaxion, as shown in the left panel of Fig. 8.10. To evaluate such a condition, we have taken as rotating neutron star properties, $R_{\rm S} = R_{\rm NS}$ in Eq. (8.69), and typical values for the surface angular velocity and magnetic fields of neutron stars,

$$\Omega_{\rm NS} \approx 10\,{\rm Hz}\,, \quad B_{\rm NS} \approx 10^{10}\,{\rm T}\,, \tag{8.94}$$

see e.g. [218]. The relaxion coupling to photons is given in Eq. (8.86), where we set $c = 1$ (and $\alpha \approx 1/137$); note that only if $c > 0$ the rolling term is larger than in vacuum ($c < 0$ would instead make the minimum deeper in the electromagnetic background). In Fig. 8.10 (left panel), the region to the right of a given labelled line is excluded, where each line corresponds to a different value of the relaxion decay constant (from $f = 10^{13}$ to 10^{19}GeV). Therefore, for a given f, large values of $M/\sqrt{\ell_*}$ are excluded depending on $\Lambda_{\rm R} \simeq \Lambda_{\rm TC}$. As $\Lambda_{\rm TC}$ increases, a certain critical value is reached where the size of the critical region quickly decreases and becomes smaller than $R_{\rm NS}$. The condition $R_{\rm T}^{\rm EM} \gtrsim R_{\rm NS}$ is independent of f, which is why all the excluded regions share the same upper boundary. The red band marks the region where the field neither reacts fast nor slowly compared to the rotation frequency, i.e. $\mu(R_{\rm T}^{\rm EM}) \sim \Omega_{\rm S}$. Given that $R_{\rm T}^{\rm EM}$ in Eq. (8.91) does not depend explicitly on f, the red band does not either. Within the band we expect $O(1)$ deviations from the naive interpolation, shown as dashed lines in Fig. 8.10.

Interestingly, the presence of large electromagnetic fields around neutron stars would also lead to non-trivial constraints in the case of a bubble which connects deep minima. If the

condition $\eta > \eta_c$ is satisfied, the condition for formation of a deep bubble is easily satisfied. This is because since $\eta_c \gg 1$, the slope of the potential is much larger in the region $r \lesssim R_{\rm T}^{\rm EM}$ than in vacuum. The relevant condition that leads to a phase transition is then the one concerning the escape of the bubble. We derive such a condition under the conservative simplification that past the transition radius the relaxion potential approximately returns to its in-vacuo form, i.e. $\eta(r > R_{\rm T}^{\rm EM}) = 0$. This is justified by the rapid decrease of $\boldsymbol{E}\cdot\boldsymbol{B}$, and therefore of η, with R, see Eq. (8.90). Then, our escape condition follows from requiring that $\ddot{R} > 0$ in Eq. (8.93), taking the minimal value of ϵ, that is $2\pi\Lambda_{\rm R}^4$, and the value of the tension force at the transition radius, that is $2\sigma/R_{\rm T}^{\rm EM}$, where note that due to our simplification we have $\sigma'(r > R_{\rm T}^{\rm EM}) = 0$. Then, a deep bubble escapes to infinity if

$$R_{\rm T}^{\rm EM} - R_{\rm S} \gtrsim \frac{f}{\Lambda_{\rm R}^2}\frac{1}{\sqrt{1-\delta^2}} \simeq \frac{\Lambda_{\rm TC}^2}{gM^3}\,, \qquad \text{(technicolor; deep)} \tag{8.95}$$

where we recall that $1-\delta^2 = \Lambda_{\rm R}^4/\Lambda_{\rm TC}^4 \ll 1$ and $\Lambda_{\rm R}^4 = gM^3 f$. As in the case of relaxion bubbles seeded by baryon density, this condition implies that it is more difficult for a deep bubble to escape than a shallow one. The underlying reason is the same as well, in vacuum the bubble-wall tension is dominated by large potential barriers. Nevertheless, as shown in the right panel of Fig. 8.10, for not too small values of $\Lambda_{\rm R}^4/\Lambda_{\rm TC}^4$, a phase transition could still be induced between deep minima of the technicolored relaxion. As expected, the excluded regions, to the right of a given line, correspond to small values of the relaxion decay constant (up to $f \sim 10^6$GeV) and of the technicolor confinement scale. Dot-dashed lines show $\mu \sim \Omega_{\rm S}$ for a given f, and as can be seen the fast approximation holds where in the region of parameter space where the bounds lie. We checked explicitly that the expansion $\Omega_{\rm S} r \ll 1$ yields the correct results since $\Omega_{\rm S} R_{\rm T}^{\rm EM} \ll 1$ for the region of interest. We note that in this case of deep minima, the region we have excluded due to a phase transition with a too large change of the vacuum energy, is also ruled out from both CAST [219] and laboratory experiments, e.g. [220]. Still, for the allowed values $f \gtrsim 1.7\times 10^7$GeV and $c = 1$, there would still be a non-trivial axion configuration around the neutron star, similar to [217].

Finally, we note that the lower bounds we derived on $\Lambda_{\rm TC}$ can be rephrased, given the collider constraints on v', as a lower bound on m_U in Eq. (8.84).

D Dark Compact Objects

In this section we entertain the possibility that there are dark compact objects [181–189] in the universe. These dark stars, similar to standard stars, can induce the instability of a metastable vacuum. This would be particularly relevant when the periodic term in the landscape potential Eq. (8.50) arises from dark dynamics, as in the case of the non-QCD relaxion (especially if the scalar is sitting in a deep minimum, as in e.g. [153]) or in models where the barriers are Higgs independent [155, 156]. In addition, we show that this possibility opens the door to late-time phase transitions for which the associated change in vacuum energy is a priori experimentally allowed. As shown in Eq. (8.46), in the case of standard stars this can only happen for quite low values of f and if the bubbles are seeded solely by the largest stars known to date, with $R_{\rm S} \sim 10^3 R_\odot$.

Let us assume then a new species of fermion, which we refer to as dark baryon, whose relic abundance is non-negligible and which constitutes the main component of the dark stars (yet not necessarily making up all of the dark matter). Let us note right away that the existence of these stars requires non-trivial dynamics by which the dark fermion can dissipate their kinetic energy, accumulate and eventually form a compact object. If this is the case, the smaller dark

stars will only be sustained by the Fermi degeneracy pressure associated with the dark baryon, thus with typical radii and densities

$$R_{\tilde{\mathrm{S}}} \sim \sqrt{8\pi}\frac{M_{\mathrm{P}}}{m_{\tilde{b}}^2}\,, \quad n_{\tilde{b}} \sim m_{\tilde{b}}^3\,, \tag{8.96}$$

where $m_{\tilde{b}}$ is the mass of the dark baryon.

Before moving on, we note that such a dark baryon is in fact motivated by the non-QCD relaxion, whose simplest UV realization crucially involves $N_{\tilde{f}}$ flavours of SM-neutral fermions, N, charged under a new confining $SU(N_{\tilde{\mathrm{C}}})$ gauge group. The associated IR scale, which controls the size of the relaxion barriers, is given by $\Lambda_{\mathrm{C}}^4 \simeq 4\pi f_{\tilde{\pi}}^3 m_N$ where $m_N = m_N(h^2) \ll 4\pi f_{\tilde{\pi}}$ is the mass of the dark quarks (taken degenerate for simplicity), whose dominant contribution is proportional to the square of the Higgs VEV, Eq. (8.54). The mass of the dark baryons, analogous to the QCD baryons, receives two contributions,

$$m_{\tilde{b}} = \tilde{m}_0 + \tilde{\sigma}(m_N)\,, \tag{8.97}$$

where $\tilde{m}_0$ is purely due to the dark strong dynamics while $\tilde{\sigma}$ is the analogue of the pion-nucleon sigma term of QCD. Likewise, at finite dark density, the barriers decrease according to $\Lambda_{\mathrm{C}}^4 \to \Lambda_{\mathrm{C}}^4(1-\zeta)$, where in the linear approximation,

$$\zeta(n_{\tilde{b}}) \simeq \frac{\tilde{\sigma} n_{\tilde{b}}}{\Lambda_{\mathrm{C}}^4} \sim \frac{m_{\tilde{b}}^3}{4\pi f_{\tilde{\pi}}^3}\,. \tag{8.98}$$

where in the last equality we have used Eq. (8.96) and the fact that $\tilde{\sigma} \simeq a m_N$ if $m_N \ll f_{\tilde{\pi}}$, where $a = \mathcal{O}(1)$ (yet note that in QCD the analogous coefficient is rather ≈ 10). Therefore, for a sufficiently large dark baryon mass, yet small enough to retain perturbative control, densities can be enough to seed the formation of a bubble. Finally, the condition that the system is large enough for the bubble to escape, assuming for simplicity that $\delta \sim 1$, and given that the size of the dark neutron star is controlled by $m_{\tilde{b}}$, yields the condition

$$m_{\tilde{b}} \lesssim \Lambda_{\mathrm{C}} \sqrt{\frac{M_{\mathrm{P}}}{f}}\,. \tag{8.99}$$

Interestingly, the change in vacuum energy Eq. (8.66) associated with such a relaxion bubble is controlled by $m_{\tilde{b}}$ as well. Considering again for simplicity the case $\Lambda_{\mathrm{R}} \sim \Lambda_{\mathrm{C}}$,

$$-\Delta\Lambda \gtrsim m_{\tilde{b}}^4 \left(\frac{f}{M_{\mathrm{P}}}\right)^2 \approx 6\times 10^{-3}\,\Lambda_0 \left(\frac{m_{\tilde{b}}}{10\,\mathrm{keV}}\right)^4 \left(\frac{f}{10\,\mathrm{TeV}}\right)^2\,, \tag{8.100}$$

where the values of the dark mass and decay constant have been taken to illustrate that the change can be small enough as to avoid any trivial experimental inconsistency between the early and late universe. This gives rise to the exciting possibility that the change in the relaxion minimum could be detected with future cosmological measurements. In addition, if $m_{\tilde{b}}$ or f are small enough and the dark stars are dense and large enough to destabilize many relaxion minima (i.e. $N \gg 1$, see Eq. (8.65) and App. II.B.6), the effects of the continued phase transitions originating from the ongoing creation of relaxion bubbles interpolating between lower and lower pairs of consecutive minima could resemble the time evolution of a quintessence field as dark energy [204][8].

[8] We expect these continued phase transitions to take place as well due to bubble collisions, since these could in principle trigger the field to further jump to the next-to-next minimum, thereby triggering a cascade of phase transitions. The exploration of these collision-triggered cascades is ongoing work. Note that this might lead to a stronger bound than just $2\pi N\Lambda_R \lesssim 10^2\Lambda_0$ (recall that for the bounds on the relaxion from standard stars, $N=1$ was enough to lead to an exclusion).

Finally, we note that the in-vacuo relaxion mass, for the range of relaxion parameters where the change in vacuum energy is smaller than its current value, is

$$m_\phi \lesssim \frac{1}{f}\sqrt{\frac{\Lambda_0}{2\pi}} \approx 2\times 10^{-16}\,\mathrm{meV}\left(\frac{10\,\mathrm{TeV}}{f}\right)\,, \tag{8.101}$$

which is, as expected, extremely small. Accordingly, the size of the dark compact object, $R_{\tilde{\mathrm{S}}} \sim 1/m_\phi$, is very large

$$R_{\tilde{\mathrm{S}}} \gtrsim f\sqrt{\frac{2\pi}{\Lambda_0}} \approx 1\times 10^{9}\,\mathrm{km}\left(\frac{f}{10\,\mathrm{TeV}}\right)\,, \tag{8.102}$$

which for this value of f is roughly the size of the solar system.

8.3 Discussion and Conclusions

Could a phase transition have taken place in the universe due to the formation of stars? In this chapter we explored this question by studying how false vacua change at finite density. Similar to the interactions with a thermal bath, the coupling of a scalar field to background matter can give rise to significant deformations of the scalar potential, to the point that a metastable minimum present in vacuum disappears at finite density. This leads to the formation of a non-trivial scalar profile, a.k.a. a scalar bubble, where the maximum field displacement within is controlled by the size of the dense system relative to the characteristic scale of the in-density potential; if the star gets large enough, a classical path to a deeper minimum of the potential becomes accessible.

Interestingly, we found that when this occurs, the bubble, originally confined within the star, can become unstable and expand beyond the star and extend to infinity! By means of simple analytic arguments, we have shown that the bubble cannot be contained within the star if the energy difference between the minima is large compared to how fast the potential barrier between them reappears towards the surface of the star. In other words, we have shown that if certain conditions regarding the properties of the metastable minimum and of the density profile are satisfied, stars can indeed act as seeds for a phase transition in the universe.

Our analysis of the fate of a false vacuum at finite density has first been based on a tilted quartic potential, as in the classic work by Coleman [104]. This potential is characterized by the energy difference between the local and true minimum, the height of the potential barrier between them, and their separation in field space. Such a simple potential encodes the main features of local minima present in many scenarios beyond the SM. Specifically, we then applied the results found in this general potential to the relaxion [8], a mechanism to explain the smallness of the electroweak scale that relies on a closely-packed landscape of local minima, with barriers between that depend on the value of Higgs field thus sensitive to SM matter densities.

Phase transitions triggered by dense systems such as stars must confront the experimental constraints that arise from the change in the energy of the vacuum at late cosmological times, $z \sim 30$, when star formation begins. Indeed, on the one hand the change in the ground state energy between the local and true vacuum is the key parameter that determines if a scalar bubble formed in a dense and large enough star is able to escape and propagate to infinity. On the other hand, early versus late cosmological measurements of the dark content of the universe constrain such a change. Detailed cosmological and astrophysical constraints on these types of transitions, beyond the simple and likely too conservative bounds we have derived, deserves further investigation, in particular because of the relevance of scalar potentials with (many) false vacua for the electroweak hierarchy or the cosmological constant problems.

We showed that the connection of the relaxion with the Higgs is precisely what is behind the sensitivity of the relaxion vacua to finite density effects. In particular, in realizations where the potential barriers are generated by QCD dynamics, baryonic densities decrease the chiral symmetry breaking scale, leading to the possibility of QCD-relaxion bubbles. In realizations where instead new confining dynamics is responsible for the barriers, the change in the Higgs VEV due to the background nucleons and muons, although small, is sufficient in some regions of parameter space to induce the formation of bubbles. Generically, we found that these bubbles easily escape from the stars where they are formed: neutron stars, white dwarfs, or main-sequence stars, depending on how small the overall scale of the non-QCD relaxion potential is. Once the bubble escapes, the associated change in the vacuum energy of the universe is too large to conform with early versus late cosmological measurements of the energy budget of our universe. Therefore, we set new bounds on relaxion models, ruling out those regions of parameter space where expanding relaxion bubbles could have been generated during star formation. As a result, we were able to place new bounds on various relaxion models, ruling out regions of parameter space where such forbidden phase transitions would take place once stars are formed.

Notably, we discovered that not only matter density but an electromagnetic background can destabilize a metastable vacuum. This possibility is motivated by some constrained yet still viable realizations of the relaxion, those in which the scalar field has large couplings to photons. We found that the large electric and magnetic fields of magnetars/pulsars destabilize the metastable minimum and lead to a phase transition that cannot be confined. Moreover, in this scenario, the transition can occur not only for shallow minima, but also for metastable vacua in which there is a hierarchical separation between the energy difference and the potential barrier between the minima.

In general, relaxion phase transitions leading to a very small change in vacuum energy compared to its measured value could in fact have been induced by the formation of large dense objects in the universe. This is the case for very low relaxion decay constants and for the largest stars in the universe acting as seeds. We also considered the possibility that these naively harmless phase transitions may be the result of the formation of very large dark stars. Such stars would be sustained by the Fermi degeneracy pressure associated with the light stable dark baryons motivated by the non-QCD relaxion.

Even though we focussed on classical transitions between minima, we have also shown how stars could act as a catalyzer where the tunneling probability of a false vacuum can be greatly enhanced. Although of a different, quantum-mechanical origin, once formed the dynamics of the corresponding scalar bubble would be described along similar lines as those presented here. The possibility of a seeded vacuum decay leaves us with another question: is it likely that a phase transition in the universe due to the formation of stars is soon to take place?

Finally, the new type of bound derived in this work for the relaxion landscape, namely vacuum instability induced by dense objects, could be relevant for other landscapes if subject to finite density deformations. These deformations are generically expected if the vacua are tied to the electroweak scale or relying on the Higgs-portal e.g. [113, 114, 179, 221, 222] and should be investigated in the light of our findings

Chapter 9

Structure of Stellar Remnants in the Presence of Light Scalars

In this Chapter we focus on the potential observable effects of a shift-symmetry breaking coupling of an ALP on the properties of stellar remnants. Such effects may result from a formation of a new phase inside the dense star, where the scalar field assumes a different value than in the zero-density vacuum. This new phase can be thought of as a bubble confined to the dense star, or equivalently the star can be described as sourcing the scalar field. Such a possibility was first considered in [119] for a *light* QCD axion whose mass is below the expected value of $\sim \Lambda_{\rm QCD}^2/f_a$ (cf. Sec. 5.3). This light mass results in scalar profiles with long tails extending far beyond the edge of the NS, leading to effective long range forces which can be potentially observed in NS-NS inspirals detected by gravitational waves (GWs). Although the bona fide QCD axion might also be sourced by NSs [118], such long range forces are generically not expected to exist in the minimal scenario.
In these previous studies, the back-reaction of the sourced scalar field (i.e. the bubble) on the matter fluid has largely been neglected. The goal of this chapter is to study this back-reaction and its effect on perhaps the most easily-observable properties of NSs and WDs, namely its mass and radii. In Sec. 9.1 we explore the back-reaction effects on the structure of NSs for different couplings of the light scalar field, while in Sec. 9.2 we use the observational data of WDs together with the change in structure that a new light scalar implies to set new bounds on *light* QCD axions.

The content of this chapter is based on work in progress, [14] and [15].

9.1 Heavy Neutron Stars from Lights Scalars

The maximal mass of NSs has been used for decades as a key observable to constrain the properties of matter at high densities. The recent detection of GWs by the LIGO collaboration and the advancement of multi-messenger astronomy would undoubtedly shed more light on the properties of NSs. For example, the merger event GW190814 [223] has measured one of the progenitors to be a stellar remnant of $2.6M_\odot$, which might be the heaviest NS discovered to date (or the lightest blackhole). Bounds on the maximal mass of NSs [224–226] were also deduced from GW190814 and the first observed NS-NS merger GW170817 [227]. The observation of a NS whose mass violates the robust causal bounds would be extremely hard to explain using SM physics alone. Interestingly, we found that, if observed, the violation of the causal bounds could be interpreted as evidence for light BSM scalars.

Importantly, this new ground state is accessible only in large enough systems due to the

gradient energy required for the formation of a bubble [119] (cf. Sec. 8.1.3). Small or dilute systems (like nuclei, regular stars and planets) are in this case meta-stable and long-lived while large and dense system (like NSs) can exist in a new ground state and have very different properties as we will see below. Importantly, they can have a mass heavier than the maximal mass predicted by the causal bounds [228, 229]. The causal bounds assume certain low-density behavior consistent with the properties of dilute matter, an assumption which is not valid in case a new ground is present. We find that, in some parts of the parameter space, large $\mathcal{O}(10)$ enhancements of the maximal mass of NSs are possible.

The section is organized as follows: In Sec. 9.1.1, we start by presenting our toy model and the equations governing the full coupled system. All of our results are qualitatively described in this section in a somewhat model-independent fashion. Then, in Sec. 9.1.1.A, we discuss the limit where the gradient energy can be neglected, in which case in this sensible to define an EOS. After going over the two qualitatively different types of EOS we expect, we discuss the effects of finite gradient energy in Sec. 9.1.1.B. A more quantitative case study in presented in Sec. 9.1.2 for three type of scalar-matter couplings, namely ALP-like (Sec. 9.1.2.A), quadratic (Sec. 9.1.2.B) and linear (Sec. 9.1.2.C). A detailed discussion regarding the limit of negligible gradient energy, which is used extensively throughout this work, is presented in App. II.C.1.

9.1.1 Free Fermi Gas and a Light Scalar

Degenerate stars are well-described at leading order by a non-interacting Fermi gas coupled to gravity. In order to study the effects of a scalar field coupled to fermions, we consider the following model containing a single massive spin 1/2 fermion ψ and a single real scalar ϕ coupled to the gravitational field $g_{\mu\nu}$ with the following Lagrangian

$$\mathcal{L}_{\psi\phi} = \sqrt{-g}\left[\bar{\psi}\left(ig^{\mu\nu}\gamma_\mu D_\nu - m_*(\phi)\right)\psi + \frac{1}{2}g^{\mu\nu}(\partial_\mu\phi)(\partial_\nu\phi) - V(\phi)\right], \tag{9.1}$$

where D_μ is the covariant derivative of a fermion field in curved space. ψ and ϕ are coupled via the term $m_*(\phi)\bar{\psi}\psi$, while the self interactions of ϕ are encoded in the function $V(\phi)$. For convenience, we shall henceforth work with the dimensionless field $\theta \equiv \phi/f$, where we introduce the scale f as the typical scale of the scalar field. We further assume that at zero density (i.e. in the absence of the Fermi gas), the potential $V(\theta)$ is minimized at θ_0 such that [1]

$$\left.\frac{\partial V}{\partial\theta}\right|_{\theta=\theta_0} = 0\,, \quad V(\theta_0) = 0 \quad \text{and} \quad m(\theta_0) \equiv m \quad \text{(at zero density)}\,. \tag{9.2}$$

Throughout this work, it should be understood that our fermion field ψ plays the role of nuclear matter in its simple form: pure neutrons, which are believed to be the central components in neutron stars. Clearly, our toy model does not include important ingredients such as additional particles (protons, electrons) and interactions, namely the electric and nuclear interactions. The latter in particular plays a critical role, as nuclear interactions become increasingly important at high densities. All of these, however, generate $O(1)$ corrections to the main predictions (e.g. maximal mass of the bound object), which rely on the degeneracy pressure of neutrons balancing the crushing force of gravity. The same statement can be said about the various models of dense matter and different approaches to the construction of equations of state. This toy model is

[1] For models with $\partial m_*(\theta)/\partial\theta\big|_{\theta=\theta_0} \neq 0$, some of the parameter space may be ruled out by terrestrial fifth force experiments due to single particle exchange. Higher-order non-vanishing derivatives may induce an effective quantum force (see e.g. [230]), for which fifth force constraints are generically weaker.

therefore still useful when trying to identify large effects which can be a result of beyond the standard model physics.

Let us now derive the static (coupled) equations of motion for the fermion, scalar and gravitational fields. We assume radial symmetry, which allows us the parametrize the metric in radial coordinates as

$$g_{00} = e^{2\nu(r)}\,, \quad g_{rr} = -e^{2\lambda(r)} \quad g_{\Theta\Theta} = -r^2\,, \quad g_{\varphi\varphi} = -r^2\sin^2\Theta\,, \tag{9.3}$$

following the mostly-minus flat metric convention $\eta_{\mu\nu} = \mathrm{Diag}[1, -1, -r^2, -r^2\sin^2\Theta]$ (in radial coordinates). The gravitational field is sourced by an energy-momentum tensor, which can be described as a sum of two terms,

$$T^{\mu}{}_{\nu} = (T_{\rm ideal})^{\mu}{}_{\nu} + (T_{\rm grad})^{\mu}{}_{\nu}\,. \tag{9.4}$$

The first term contains the contributions of the Fermi gas *and* the scalar potential, $V(\theta)$. The second term is proportional to f^2 and contains of the contribution gradient energy of the scalar field, to be discussed below. $T_{\rm ideal}$ has the form of an ideal fluid, i.e. $(T_{\rm ideal})^{\mu}{}_{\nu} = \mathrm{Diag}[\varepsilon, -p, -p, -p]$, where the *total* energy density ε and pressure p are given by

$$\varepsilon(\theta,\rho) = \varepsilon_\psi(\theta,\rho) + V(\theta) \qquad \text{with} \qquad \varepsilon_\psi(\theta,\rho) \equiv 2\int^{k_f(\rho)} \frac{\mathrm{d}^3k}{(2\pi)^3}\sqrt{\mathbf{k}^2 + m_*^2(\theta)}\,, \tag{9.5a}$$

$$p(\theta,\rho) = p_\psi(\theta,\rho) - V(\theta) \qquad \text{with} \qquad p_\psi(\theta,\rho) \equiv \frac{2}{3}\int^{k_f(\rho)} \frac{\mathrm{d}^3k}{(2\pi)^3}\frac{k^2}{\sqrt{\mathbf{k}^2 + m_*^2(\theta)}}\,. \tag{9.5b}$$

Note that we are switching notation and now use ρ for the nucleon number density to follow the NS literature, e.g. [160]. The Fermi momentum k_f and the number density ρ are related as usual by $k_f(\rho) = (3\pi^2\rho)^{1/3}$. The total pressure of the system p as defined above can become negative in regions where the contribution from the potential $V(\theta)$ dominates over the strictly positive pressure of the Fermi gas. The derivation of the standard expression for the energy density ε_ψ and pressure p_ψ of a free Fermi gas can be found in many textbooks, *e.g.* see [160]. Note that while we are using the expressions for a *free* Fermi gas, we actually take into account the scalar interactions by allowing the fermion mass to be θ-dependent. In this mean field approximation, we treat θ as an r-dependent background field[2]. In later stages it would prove useful to change variables to the chemical potential μ, which must be a continuous parameter in any static solution where chemical equilibrium is assumed. This change of variables is simply done by identifying the Fermi energy with the chemical potential, namely $k_f(\mu) = \sqrt{\mu^2 - m_*^2(\theta)}\Theta(\mu - m_*(\theta))$. From this definition it should be understood that, for a given θ, for values of μ below the mass threshold $m_*(\theta)$, the total energy and pressure of the system are μ-independent and originate only from the scalar field, i.e. $\varepsilon \to V(\theta)$ and $p \to -V(\theta)$.

In addition to the ideal-fluid-like contribution, the gradient of the scalar field also contributes to the energy-momentum tensor

$$(T_{\rm grad})^{\mu}{}_{\nu} = f^2 e^{-2\lambda(r)}(\partial_r\theta)^2\left(\frac{1}{2}\delta^\mu_\nu - \delta^\mu_r\delta^r_\nu\right)\,. \tag{9.6}$$

[2]By using the mean field approach, we neglect *e.g.* single particle exchanges, which are possible for background values of θ for which $\partial m_*(\theta)/\partial\theta \neq 0$. However, we expect this additional force (which may be effectively long range for light scalar masses) to be suppressed by the small effective coupling $\sim m/f \ll 1$.

The first term in the parenthesis describes the gradient energy of the field[3]. The second term deviates from the perfect fluid behavior in the form of additional pressure in the radial direction. Both terms are proportional to f, therefore we expect them to become negligible when f is much smaller than other scales appearing in the equations of motion, see App. II.C.1 for a detailed discussion.

Using the standard procedure, we derive three independent equations of motion by minimizing the action defined by the Lagrangian $\mathcal{L} = (M_{\rm pl}^2/2)\sqrt{-g}R + \mathcal{L}_{\psi\phi}$ to find

$$p' = -\frac{(p+\varepsilon)e^{2\lambda}}{2r}\left(\frac{r^2 p + \frac{1}{2}f^2 r^2 e^{-2\lambda}\theta'^2}{M_{\rm pl}^2} + 1 - e^{-2\lambda}\right) - \theta'\left(\frac{\partial V}{\partial\theta} + \rho_s\frac{\partial m_*}{\partial\theta}\right), \tag{9.7a}$$

$$\left(re^{-2\lambda}\right)' = 1 - \frac{r^2\varepsilon + \frac{1}{2}f^2 r^2 e^{-2\lambda}\theta'^2}{M_{\rm pl}^2}, \tag{9.7b}$$

$$e^{-2\lambda}\theta'' + \frac{1}{r}\theta'\left(1 + e^{-2\lambda} - \frac{r^2}{2M_{\rm pl}^2}(\varepsilon - p)\right) = \frac{1}{f^2}\left(\frac{\partial V}{\partial\theta} + \rho_s\frac{\partial m_*(\theta)}{\partial\theta}\right), \tag{9.7c}$$

where all derivatives are with respect to the radial coordinate. Here we introduced a new quantity, the fermion scalar density $\rho_s(\theta,\rho) \equiv \langle\bar{\psi}\psi\rangle$, which can be calculated in a similar fashion to the energy density and pressure of a free Fermi gas. It is simply given by $\rho_s(\theta,\rho) = (\varepsilon_\psi(\theta,\rho) - 3p_\psi(\theta,\rho))/m_*(\theta)$.

The first two equations are the generalized Tolman–Oppenheimer–Volkoff (TOV) equations [231, 232]. Eq. (9.7a) dictates how the total pressure is balanced by the gravitational force (first term) and an additional *new* scalar force (second term). Eq. (9.7b), for the spatial component of the metric $\lambda(r)$, is associated with the enclosed mass, defined as

$$M(r) \equiv 4\pi r M_{\rm pl} 2(1 - e^{-2\lambda(r)}). \tag{9.8}$$

Lastly, Eq. (9.7c) is the generalized form of the scalar equation of motion. It contains the coupling to gravity, which deforms the derivatives on the LHS. The scalar self interactions are encoded in the first term in parenthesis on the RHS. Finally, the scalar interaction with the fermions is given by the second term in parenthesis on the RHS. There are in principle two additional equations of motion which we do not present; the equation of motion for the fermion field is implicitly used in the expression for the energy and pressure of the Fermi gas[4]. The equation of motion for the temporal component of the metric $\nu(r)$ can be solved separately, since $\nu(r)$ and its derivatives do not appear in any of the other equations. The combination of all equations of motion imply by construction energy-momentum conservation, i.e. $\partial_{;\mu}T^{\mu\nu} = 0$, sometimes known in this context as the hydrostatic equilibrium condition [233].

The coupled system of Eq. (9.7) can in principle be numerically solved by specifying the initial conditions $p(0)$ and $\theta(0)$, with the remaining initial conditions $\theta'(0) = \lambda'(0) = 0$ dictated by radial symmetry. In practice, however, finding valid static solutions for Eq. (9.7c) is challenging. This can be understood by the classic intuition provided by Coleman [234]. Static solutions of the scalar EOM are analogous to classical one-dimensional trajectories in an inverted potential, where the radial direction plays the role of time. In this picture, a valid static solution is one

[3]In principle, one could redefine $\varepsilon(\theta,\rho)$ and $p(\theta,\rho)$ to include this piece, since both the gradient energy and the potential term $V(\theta)$ originate from the same contribution to the stress-energy tensor, i.e. $-\delta^\mu{}_\nu\mathcal{L}$.

[4]Note we are using the fermion EOM in flat space, since the microscopic properties of the Fermi gas are independent on the gravitational field; we can always choose reference frame which is flat at small scales.

which connects one maximum of the potential to another, with the tail of the scalar profile staying exponentially close to θ_0 for arbitrarily large values of r. These type of trajectories are inherently chaotic; small variations to the initial condition would cause either an over- or an undershoot[5]. Thus, viable static solutions of Eq. (9.7c) typically require tuning the initial condition $\theta(0)$. This issue can be avoided in case Eq. (9.7c) is solved in isolation by adding a fictitious friction term [119]. This requires neglecting the back-reaction of the scalar field on the density profile, which is precisely the effect we are looking for. Therefore, our numerical solutions for Eq. (9.7) are based on an automatized shooting method, which tunes the value $\theta(0)$ for a fixed $p(0)$ until a viable static solution is found.

A Equation of State: the Negligible Gradient Approximation

Finding a solution for the coupled system of Eq. (9.7) is significantly simpler when the LHS of Eq. (9.7c) can be neglected. We refer to this particularly simple limit of this theory as the **negligible gradient energy limit**. Before discussing the physical justification of this limit, let us first discuss the solution predicted by the scalar EOM in this limit. The value of the scalar field at a given number density ρ or chemical potential μ is determined either by minimizing w.r.t θ the total energy $\varepsilon(\theta,\rho)$ or the grand canonical potential $\Omega(\theta,\mu) \equiv \varepsilon - \mu\rho = -p(\theta,\mu)$

$$\left.\frac{\partial\varepsilon(\theta,\rho)}{\partial\theta}\right|_{\rho=\text{const.}} = \left.\frac{\partial\Omega(\theta,\mu)}{\partial\theta}\right|_{\mu=\text{const.}} = \frac{\partial V}{\partial\theta} + \rho_s\frac{\partial m_*(\theta)}{\partial\theta} = 0\,, \tag{9.9}$$

where ρ_s depends on the chosen free variable, namely either ρ or μ. Eq. (9.9) defines the *microscopic equation of state*. Unsurprisingly, this is nothing more than the scalar EOM in the limit where the scalar derivatives are negligible, i.e. Eq. (9.7c) with its LHS set to zero. Importantly, in order for Eq. (9.9) to have non-trivial solutions, there must be a region where the two terms appearing in it are comparable. Otherwise, if the equation is always dominated by the potential term $|\rho_s\partial m_*/\partial\theta| \ll |\partial V/\partial\theta|$, the scalar field would remain close to its zero density value θ_0 and the system becomes trivial. The condition $\rho_s\partial m_*/\partial\theta \sim \partial V/\partial\theta$ implies that the bound object must be dense enough in order for non trivial solutions to exist. This denseness condition, along with the largeness condition of Eq. (9.12) discussed below, are essentially the same conditions discussed in the context of scalar bubble formation at finite density [12,212].

Eq. (9.9) allows us to calculate $\theta(\mu)$ (or $\theta(\rho)$). It would generically connect the zero density value of $\theta(\mu=0)=\theta_0$ to some other (potentially density dependent) value at higher density. This mapping allows us to express the total energy and pressure of the system in terms of a single independent variable, *e.g.* the chemical potential μ

$$\varepsilon(\theta,\mu) \to \varepsilon(\mu) = \varepsilon(\theta(\mu),\mu) \quad \text{and} \quad p(\theta,\mu) \to p(\mu) = p(\theta(\mu),\mu)\,. \tag{9.10}$$

By constructing the equation of state using μ as the free parameter, the preferred phase (with maximal pressure) is always selected and the procedure outlined above produces the stable branch of the EOS. This insures the continuity of μ and p across a phase transition boundary, required for chemical and mechanical stability[6]. At this point one can readily construct the

[5] One important difference in our scenario is the explicit radial dependence of the scalar potential through the pressure dependence of $\rho_s(\theta(r),p(r))$, which translates to a time-dependent potential in the classical trajectory analogy. This leads to a violation of energy conservation which could complicate the over/undershooting argument. However, since pressure is always continuous, this dependence can be neglected in small regions where p can be treated as constant.

[6] In some situations an unstable, but potentially long lived, branch of the EOS may exist, which can be found by using ρ as the free parameter.

effective (and non-trivial) equation of state, i.e. $\varepsilon(p)$, and numerically solve the usual TOV equations

$$p' = -\frac{(p+\varepsilon)}{8\pi r^2 M_{\rm pl}2}\left(1-\frac{M}{4\pi r M_{\rm pl}2}\right)^{-1}\left(4\pi r^3 p + M\right)\,, \tag{9.11a}$$

$$M' = 4\pi r^2 \varepsilon\,, \tag{9.11b}$$

given the initial condition $M(0)=0$ and some internal pressure $p(0)$. Note that in Eq. (9.11) we neglected the terms $\propto f^2\theta'^2$, which are $\mathcal{O}(f/M_{\rm pl})$ corrections. See discussion below and App. II.C.1 for further details.

We are now in the position to discuss the origin of the negligible gradient energy limit. The solutions of Eq. (9.11) imply a non-trivial profile $\theta(r)$ which connects the θ_0 zero-density value outside the object to some other value inside the object, denoted by θ_∞. While the continuity of μ and p across a phase transition boundary is insured, other quantities, like energy and number density, are typically discontinuous across a phase boundary. Crucial to our discussion, θ may also be discontinuous across the phase boundary. This jump in θ can be thought of as a thin-bubble wall, which is infinitesimally thin in the negligible gradient energy limit. However, the formation of such bubble wall requires some energy, which we refer to as the gradient energy. This energy is negligibly small compared to the gain in potential energy in the limit where the effective wavelength of the scalar field, λ_ϕ, is much smaller than the typical size of the star R

$$\lambda_\phi \ll R\,. \tag{9.12}$$

The effective wavelength scales linearly with f, $\lambda_\phi = f/\Lambda_{\rm eff}^2$, where $\Lambda_{\rm eff}^2$ is a scale typically associated with either the potential term $\sqrt{\partial V(\theta)/\partial\theta}$ or the Fermi gas term $\sqrt{\rho_s(\partial m_*(\theta)/\partial\theta)}$ in Eq. (9.9). The detailed derivation of this limit from a dimensional analysis of Eq. (9.7c) is presented in App. II.C.1. We note that in some solutions of Eq. (9.11), the angle profile $\theta(r)$ may also include finite regions where θ varies by $\mathcal{O}(1)$, which we do not associate with a bubble wall, but nevertheless require some finite energy in order to displace the scalar field. Since the energy needed for such smooth variation of θ is $\mathcal{O}(\lambda_\phi/R)$ smaller than that required for the thin-bubble wall, it typically represents a weaker constraint on f compared to Eq. (9.12), and therefore can be neglected as long as Eq. (9.12) holds. We note that it is in these finite regions, in which varies θ smoothly, where small $\mathcal{O}(f/M_{\rm pl})$ corrections to the energy density and pressure are neglected in Eq. (9.11), see App. II.C.1 for further details.

Let us get a qualitative understanding of how the effective mass of the fermion $m_*(\theta)$ would change at increased densities in light of Eq. (9.9). As we make an infinitesimal change in density (i.e. increasing $\rho \approx \rho_s$ in the non-relativistic limit), Eq. (9.9) can only be satisfied if $\partial m_*/\partial\theta < 0$, namely if the mass of the fermion decreases. In other words, the increase in $V(\theta)$ due to the deviation from θ_0 would be compensated by the decrease in the energy of the Fermi gas[7]. Indeed, for a fixed number density ρ, a Fermi gas has less energy when the mass of the fermion is decreased. Thus, we find that solutions of Eq. (9.9) always satisfy the upper bound $m_*(\theta) \leq m_*(\theta_0) \equiv m$ at all densities. It is also useful to consider the opposite regime of very high densities, where we identify two types of solutions for Eq. (9.9). The first type is relevant if there exists a θ_∞ for which $m_*(\theta_\infty) = 0$. Then, Eq. (9.9) is solved at arbitrary high densities along a curve in the

[7]For concreteness, we use $\epsilon(\theta,\rho)$ as the relevant quantity for this particular discussion, but similar arguments can be made using $\Omega(\theta,\mu)$.

$\{\theta, \rho\}$ plane defined by

$$\rho_s(\theta,\rho) = \left|\frac{\partial V/\partial\theta}{\partial m_*(\theta)/\partial\theta}\right|_{\theta=\theta_\infty} \equiv \rho_{s,\infty} = \text{const.} \tag{9.13}$$

In the ultra-relativistic approximation $\rho_s(\theta,\rho) \approx \frac{1}{2}(\frac{3}{\pi})^{2/3}\rho^{2/3}m_*(\theta)$, therefore the condition above is satisfied by $m_*(\theta) \propto \rho_{s,\infty}/\rho^{2/3}$, which is achieved by taking θ close enough to θ_∞ for $\rho \gg \rho_{s,\infty}$, namely

$$\theta(\rho) \approx \theta_\infty + \left(\frac{\rho_{s,\infty}}{\frac{1}{2}(\frac{3}{\pi})^{2/3}\rho^{2/3}(\partial m_*(\theta)/\partial\theta)|_{\theta=\theta_\infty}}\right) \tag{9.14}$$

Therefore, in this type of solution, $m_*(\theta)$ remains positive and approaches 0 from above as the density is increased. This implies that the effective mass of the fermion can be much smaller than its zero density value m at high enough densities.

If $m_*(\theta)$ is bounded from below and does not cross 0, we find the second type of solution: the asymptotic value of θ at high densities would then be θ_∞ for which the first derivative vanishes, namely $(\partial m_*(\theta)/\partial\theta)|_{\theta=\theta_\infty} = 0$. This could be easily understood as the solution of Eq. (9.9) in the limit where the contribution from $\partial V(\theta)/\partial\theta$ is negligible and $\rho_s \neq 0$. The approximate solution in this case is

$$\theta(\rho) \approx \theta_\infty - \left(\frac{\partial V/\partial\theta}{\rho_s(\theta,\rho)\partial^2 m_*(\theta)/\partial\theta^2 + \partial^2 V/\partial\theta^2}\right)\Bigg|_{\theta=\theta_\infty}. \tag{9.15}$$

In this type of solution, $m_*(\theta)$ remains positive and approaches $m_*(\theta_\infty)$ from above as the density is increased. Depending on the function $m_*(\theta)$, both $m_*(\theta_\infty) \lesssim m$ and $m_*(\theta_\infty) \ll m$ are possible. The scalar density ρ_s increases as ρ increases while the mass is fixed, which implies that $\theta(\rho) \to \theta_\infty$ at high densities, making this solution self-consistent. In both cases discussed above, we find that any solution of Eq. (9.9) satisfies also the lower bound $m_*(\theta) > 0$ at all densities.

What kind of equation of state can we expect? In order to answer this question, let us first consider the qualitative effects of the scalar field. The first effect comes from the *reduction of the mass* of the fermion ψ. This has the generic effect of stiffening the equation of state, which can be seen easily *e.g.* in the non-relativistic approximation (neglecting $V(\theta)$),

$$p_\psi^{\text{n.r}} \propto \varepsilon_\psi^{\text{n.r}}\left(\frac{\varepsilon_\psi^{\text{n.r}}}{m_*^4(\theta)}\right)^{2/3} \quad\to\quad \frac{\partial p_\psi^{\text{n.r}}}{\partial m_*(\theta)} < 0\,. \tag{9.16}$$

A reduction of mass leads to a larger pressure for a fixed energy density, therefore to a *stiffer* equation of state. On the other hand, the additional contribution of $V(\theta)$ would generically lead to a softening in the equation of state, since again in the non-relativistic approximation,

$$p^{\text{n.r}} \approx c\, m_*^4(\theta)\left(\frac{\varepsilon^{\text{n.r}} - V(\theta)}{m_*^4(\theta)}\right)^{5/3} - V(\theta) \quad\to\quad \frac{\partial p^{\text{n.r}}}{\partial V(\theta)} < 0\,, \tag{9.17}$$

where c is a numerical constant. An *increase* in $V(\theta)$ leads to smaller pressure for a fixed energy density, therefore to a *softer* equation of state.

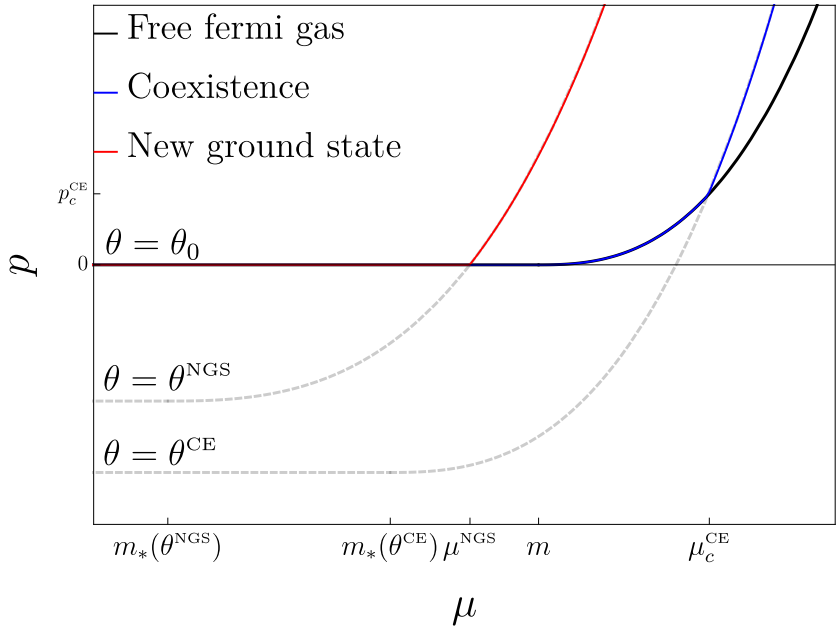

Figure 9.1: Pressure as a function of chemical potential. The black curve describes a free Fermi gas. The blue curve describes a first-order phase transition from θ_0 to some $\theta^{\rm CE}$, typical in the CE region of parameter space. The phase transition occurs at a critical chemical potential $\mu_c^{\rm CE}$ where the pressure of both phase is equal, denoted here by $p_c^{\rm CE}$. The red curve describes a new ground state at $\theta^{\rm NGS}$. The new ground state is located at the $p = 0$ point at non-zero $\mu^{\rm NGS} < m$. This plot demonstrates how the intersection point between the $\theta \neq \theta_0$ curves and the black curve, which is controlled by the properties of $m_*(\theta)$ and $V(\theta)$, determine whether a certain parameter point belongs to the CE or the NGS region.

These two competing effects split the parameter space of any model to two qualitatively different regions. First, a **coexistence** (CE) region, in which another phase of matter is accessible above a certain critical pressure. In this case, for internal pressures above the critical pressure, the bound object can be described as a hybrid star; with a core in one phase and a crust in another. Below that critical pressure, only the low density phase is present. It is known that such phase transitions typically soften the equation of state, and the resulting hybrid stars are less massive in comparison to stars made of matter in its low density phase.

We dub the rest of the parameter space the **new ground state** (NGS) region. As the name suggests, at high enough densities matter can transition to a new, stable ground state. Stars could be totally stable only in this new phase, while dilute stars can be long-lived until a fluctuation causes them to transition to the stable phase. Importantly, the equation of state for the new ground state could be stiffer in comparison to the low density (meta-stable) phase, and therefore may support bound objects with larger masses. The NGS region shares some similarities with strange stars, made out of the hypothetical deconfined ground state dubbed strange matter [235].

In order to better define these two regions, let us denote our parameter space as $\{\alpha_i\}$, namely the space of parameters (couplings and scales) which fix the $m_*(\theta)$ and $V(\theta)$ functions. The two regions can be easily defined in terms of preferred phases. In this case, it is useful to pick μ as the independent variable, where the preferred phase is simply the one with maximal pressure.

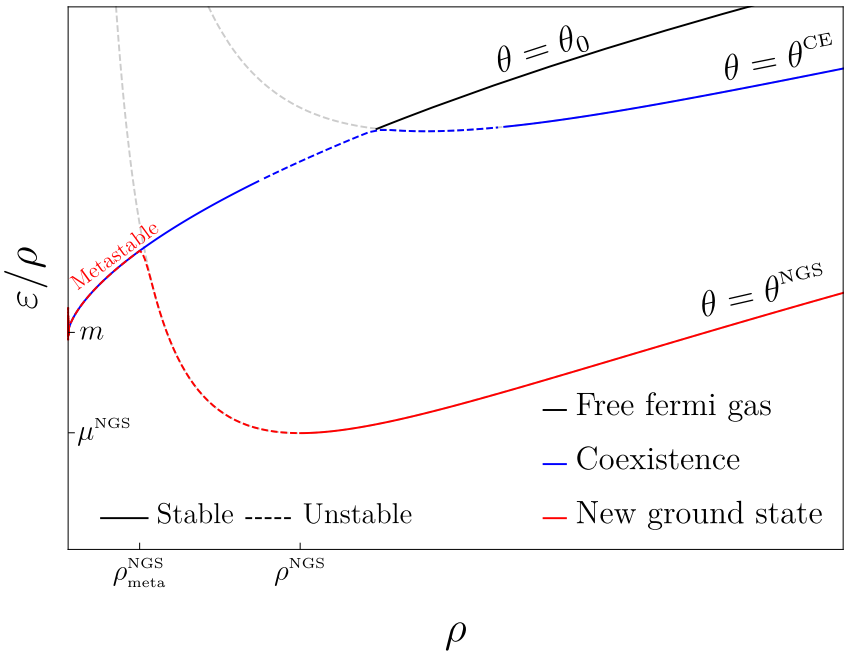

Figure 9.2: The binding energy ε/ρ as a function of number density ρ. The black curve describes a free Fermi gas. The blue curve describes a first-order phase transition typical in the CE region of parameter space. The phase transition is accompanied by a discontinuity in ε and ρ, in the region plotted here as the dashed blue line. The phases at the edges of the dashed blue line have the same pressure. Both the black and the blue curve share the same ground state at $\rho \to 0$, where the binding energy is simply the rest mass m. The red curve described the binding energy of a new ground state. An absolutely stable branch is defined for $\rho \geq \rho^{\mathrm{NGS}}$, with the new ground state located at ρ^{NGS}. A meta-stable branch equivalent to a free Fermi gas in found at $\rho < \rho^{\mathrm{NGS}}_{\mathrm{meta}}$. The region $\rho^{\mathrm{NGS}}_{\mathrm{meta}} < \rho < \rho^{\mathrm{NGS}}$ is completely unstable.

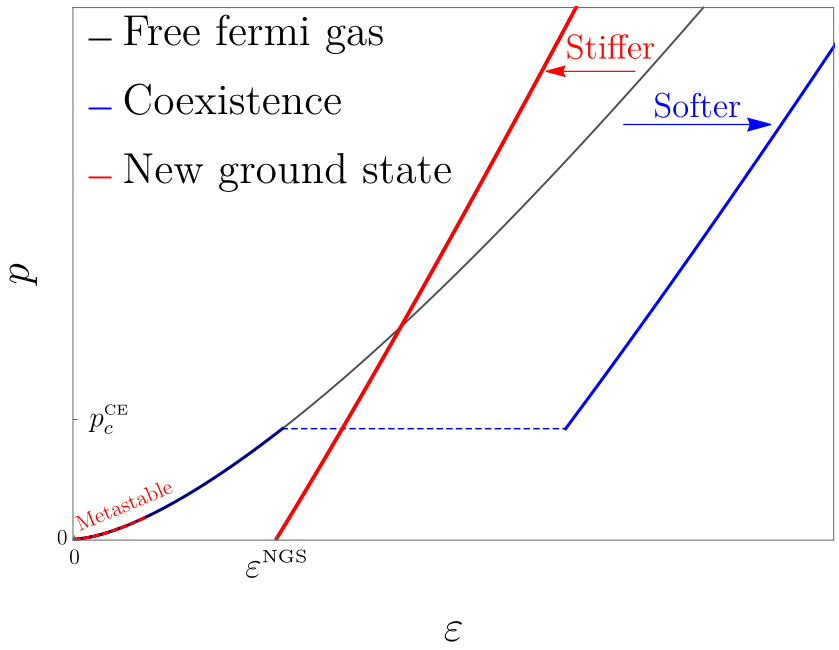

Figure 9.3: Pressure as a function of energy density, also know as the equation of state, for the various cases discussed in the text. The black curve describes a free Fermi gas. The blue curve describes a first-order phase transition, typical in the CE region of parameter space. While the pressure is continuous across the phase transition, the energy density is discontinuous, shown as the dashed blue line. Such a jump leads to a softer EOS, at least in some finite region. The red curve describes a new ground state, characterized by vanishing pressure at some finite energy density $\varepsilon^{\mathrm{NGS}}$. This EOS can be stiffer than the θ_0 phase at high densities. There is typically also a meta-stable branch at low energy densities, equivalent to the free Fermi gas, shown here as the dashed red curve.

Coexistence Region

This region in parameters space is defined by $p(\theta, \mu; \{\alpha_i\}) < 0$ for all values of θ and for $0 < \mu < m$. This means that the θ_0 phase is preferred around the $\mu \gtrsim m$ threshold (since by definition $p(\theta_0, \mu) = 0$ in the region $0 < \mu < m$), and a phase transition may occur at some critical $\mu_c^{\rm CE} > m$, see blue curve in Fig. 9.1. Although this transition is always continuous in (p, μ), it could either be smooth or first-order in (ε, ρ). In the latter case there is a discontinuity (i.e. "jump"), like the one shown in Fig. 9.2. Phase transitions typically lead to a *softening* of the equation of state, see Fig. 9.3. We also note that one can classify three types of possible phase transition, depending on whether the low- and high-density phases are non-relativistic (NR) or ultra-relativistic (UR). A noticeable effect arises only when at least one of the phases is NR (where the mass still plays a role), therefore only in NR $\to$ NR and NR $\to$ UR transitions. The third possible transition, UR $\to$ UR, occurs when the mass is irrelevant and therefore changing its value does not effect the EOS. Note that the UR $\to$ NR transition is not possible; as argued above, the mass of the fermion in the high-density phase is never larger.

New Ground State Region

The rest of the parameter space is the new ground state region, also defined by demanding that $p(\theta^{\rm NGS}, \mu^{\rm NGS}, \{\alpha_i\}) = 0$ for some value $\theta^{\rm NGS}$ and for some value $\mu^{\rm NGS}$, with the latter satisfying $m_*(\theta^{\rm NGS}) < \mu^{\rm NGS} < m$, see red curve in Fig. 9.1. This implies the existence of a new ground state of the system. In order to see that, it is useful to switch and use the number density ρ as a free parameter. We therefore define $\rho^{\rm NGS} \equiv ((\mu^{\rm NGS})^2 - m_*^2(\theta^{\rm NGS}))^{3/2}/(3\pi^2)$. The condition above implies

$$p(\theta^{\rm NGS}, \rho^{\rm NGS}) = (\rho^{\rm NGS})^2 \frac{\partial(\varepsilon/\rho)}{\partial\rho}\bigg|_{\theta=\theta^{\rm NGS}, \rho=\rho^{\rm NGS}} = \mu^{\rm NGS}\rho^{\rm NGS} - \varepsilon^{\rm NGS} = 0\,, \tag{9.18}$$

where $\varepsilon^{\rm NGS} \equiv \varepsilon(\theta^{\rm NGS}, \rho^{\rm NGS})$. From this condition we learn two things,

1. There is a minimum of the function ε/ρ at $\rho = \rho_c$.
2. The value the function at that minimum is $\frac{\varepsilon^{\rm NGS}}{\rho^{\rm NGS}} = \mu^{\rm NGS} < m$.

This new and deeper minimum is shown in Fig. 9.2. We find that the function describing the energy-per-particle or binding energy, namely ε/ρ, has a global minimum at $\{\theta^{\rm NGS}, \rho^{\rm NGS}\}$, which is lower than the minimum at $\rho = 0$, since $\lim_{\rho\to 0} \varepsilon(\theta_0, \rho)/\rho = m$. This implies the existence of a new ground state for matter at $\theta = \theta^{\rm NGS}$. This is analogous to the effect of the nuclear force in nuclear matter. The short-distance repulsion and long-distance attraction are balanced at nuclear saturation density, i.e. the density of nuclei, which are the ground states of nuclear matter. In the presence of a new ground state, the equation of state has a stable branch which reaches $p = 0$ at some non-vanishing number density $\rho^{\rm NGS}$, see Fig. 9.3. Importantly for our discussion, the equation of state of this new phase could be *stiffer* than the θ_0 phase, and therefore can potentially support bound object of larger mass. Since the new ground state is not continuously connected to the θ_0 phase, matter below some critical density $\rho < \rho_{\rm meta}^{\rm NGS}$ is meta-stable and follows a meta-stable branch in the equation of state, see Fig. 9.3. Given a system in sub-critical density, any density fluctuation large enough to overcome the potential barrier can cause a phase transition, even fluctuations which are small in their spatial extent compared to the size of the system (due to the $f \to 0$ limit formulated as the condition in Eq. (9.12)). The region $\rho_{\rm meta}^{\rm NGS} < \rho < \rho^{\rm NGS}$ is completely unstable.

Let us consider the simple case of a new ground state, where the contribution coming from the scalar self interactions, i.e. from $V(\theta)$, is negligible. Furthermore, let us assume that the effective fermion mass remains approximately in the new ground state; this would be the case in models where $m_*(\theta)$ is positive and bounded from below at some $\theta = \theta_\infty$ (see discussion below Eq. (9.13)). Thus, if the total effect of the scalar interactions can be described as simply reducing the mass of the fermion to some density-independent value $m_*(\theta_\infty) < m$, the maximal mass of a star composed of matter in this new phase and its radius can be easily calculated using the standard TOV equations, to find

$$M_{\max} = (0.7\ M_\odot)\left(\frac{m_N}{m_*(\theta_\infty)}\right)^2 \quad \text{with} \quad R(M_{\max}) = (9.4\ \text{km})\left(\frac{m_N}{m_*(\theta_\infty)}\right)^2 , \tag{9.19}$$

where $m_N \approx 1$ GeV is the neutron mass. Clearly, this reduction in fermion mass has a strong effect on the maximal mass of the bound object. This effect is potentially much larger than the usual $O(1)$ effect one gets by using different EOSs, which model dense matter using different approaches (*e.g.* see [236]). Note, however, that the effect of the scalar self interactions encoded in $V(\theta)$ would generically have the opposite effect and would drive the maximal mass to lower values compared to this simple case [237]. Another simple prediction regarding the mass-radius ratio can be given for objects in the ground state with densities of order $\rho^{\rm NGS}$; this is the region in the EOS where the energy density becomes almost constant as $p \to 0$, and the energy density approaches the critical value $\varepsilon \to \varepsilon^{\rm NGS}$. The mass of these almost-constant-density objects is than given simply by the product of the energy density times the volume, and the M-R curve is dictated from the simple relation

$$M/R^3 \approx 4\pi\varepsilon^{\rm NGS}/3\,. \tag{9.20}$$

As a consequence, similarly to strange stars [238], stars made of matter in the NGS has the potential to rotate faster than usual neutron stars. The minimal period depends on the maximal mass and the corresponding radius and is given by [239–241]

$$P_{\min} \approx 0.87\ \text{ms}\left(\frac{(R(M_{\max})/10\ \text{km})^3}{M_{\max}/M_\odot}\right)^{1/2} . \tag{9.21}$$

Therefore, for a star described by pure Fermi gas has $P_{\min} \approx 0.95\ \text{ms}\,(m_N/m_*(\theta_\infty))^2$, which is also the typical minimal period expected for realistic neutron stars. Plugging Eq. (9.20) in Eq. (9.21), we find that for star in the NGS the minimal period depends only on the energy density

$$P_{\min} \approx 1\ \text{ms}\left(\frac{(0.2\ \text{GeV})^4}{\varepsilon^{\rm NGS}}\right)^{1/2} . \tag{9.22}$$

B Finite Gradient Effects

Meta-stability

The negligible gradient energy (or $f \to 0$) limit is useful when discussing bound objects that are large enough, such that the effective wavelength of the scalar field is much smaller than the size of the bound object (see Eq. (9.12)). For much smaller objects, whose size R satisfies the opposite condition

$$R \ll \lambda_\phi\,, \tag{9.23}$$

the gradient energy needed to move the field from its zero density position θ_0 is too large, the field is "stuck" and the system becomes trivial. This decoupling limit ($f \to \infty$), valid for small systems, has an important implication: the new phase of matter *is not accessible* in small systems (assuming they are dense enough). Even for a very low value of $f = 10^3$ GeV, taking a conservative estimation $\Lambda_{\rm eff}^2 \sim (1\ {\rm GeV})^2$ (which is relevant for neutrons), we find that the effective wavelength is $\lambda_\phi \sim 200$ fm, two orders of magnitude larger than nuclear radii $\sim 1\ {\rm fm} \times A^{1/3}$, with mass number A. Since most nuclei with $A \sim \mathcal{O}(200)$ are already short-lived, it is extremely unlikely that a nucleus with $A \sim 10^6$ is spontaneously formed in small systems. In practice, the lower bound of f due to astrophysical bounds is typically much higher and is around $(10^7 - 10^8)$ GeV [242], making λ_ϕ much larger and the new phase even less accessible in small systems.

The (meta)stability of nuclei w.r.t the new phase induced by the scalar field is therefore ensured due to the gradient energy required to displace the scalar field. It is therefore consistent with the fact that some nuclei are very long lived, and in fact stable in cosmological scales. Only fluctuations whose spatial extent is of the order of λ_ϕ (which, as discussed above, is typically many orders of magnitude larger than nuclei), can lead to a phase transition. These type of large and dense regions are expected in violent events such as supernova collapse and NS mergers, which, similarly to strange matter, are expected to be the main production mechanisms of matter in its new ground state. Note that in our toy example, every time a new ground state nugget comes in contact with matter in its low density phase, it would convert it to the new ground state. Therefore, we would expect to find the entire universe in this new ground state, which does not seem to be consistent with the presence of nuclear matter in the universe. Like for strange matter, this can be avoided by some repulsive force that would prevent NGS nuggets from coming in contact with matter. This can be achieved, for example, by adding protons to our toy model. In this case our NGS would be positively charged and the coulomb barrier would prevent them from converting other nuclei to the NGS.

Since, as argued above, terrestrial experiments are too small for the field to be sourced, terrestrial fifth force experiments cannot probe the long distance force one expects to find in the sourced phase [119]. Another important consequence of finite f regards the so called causal bounds on neutron star masses [243, 244]. By assuming that the EOS is known at low densities and extrapolating it at high densities using the stiffest (yet causal) EOS, namely $p = \varepsilon$, one finds typically that neutron stars cannot be heavier than $\sim 4M_\odot$. This seems to be in contradiction, for example, with our simple estimate in Eq. (9.19). However, these causal bounds are derived based on our understanding of nuclear matter in nuclei. But nuclear matter as we know it in nuclei may be only *metastable*. Thus, if the EOS is actually stiffer on the stable branch, the usual causal bounds on the neutron star maximal mass can be evaded.

Self-bound Objects

Another interesting implication of finite f is the existence of self-bound objects (SBOs), which are composed of matter in its new ground state, held together by the gradient pressure of the scalar field at the boundary of the object, where the scalar field transitions from one value to the other. These are typically the smallest objects in which the scalar field can be sourced, namely as small as $R \gtrsim \lambda_\phi$, and they are held together not by the gravitational force (which might be negligibly small), but rather by the new force induced by the scalar field. These bound objects are typically not compact $M/R \ll M_{\rm pl}2$, and their pressure profiles can be computed by solving

the $M_{\rm pl} \to \infty$ limit of the coupled TOV equations,

$$p' = -\theta' \left(\frac{\partial V}{\partial \theta} + \rho_s \frac{\partial m_*}{\partial \theta} \right) = -f^2 \theta' \left(\theta'' + \frac{2}{r} \theta' \right) , \tag{9.24a}$$

$$\theta'' + \frac{2}{r} \theta' = \frac{1}{f^2} \left(\frac{\partial V}{\partial \theta} + \rho_s \frac{\partial m_*(\theta)}{\partial \theta} \right) . \tag{9.24b}$$

The pressure profile is non trivial in regions where $\theta' \neq 0$ and the condition in Eq. (9.9), which defined our microscopic EOS, is not satisfied. Therefore, as appose to the negligible gradient energy limit, for these objects all the interesting physics occurs in the phase boundary.

Let us discuss the characteristics of these bound objects described by the solutions of Eq. (9.24). They are well-described by spherical, constant density objects with radius $R \gg \lambda_\phi$, with constant internal pressure and energy density. The values of the scalar field θ is also constant inside the object. Without any additional forces, such object would reduce its pressure (and energy) by expanding. The object is however held together by the gradient pressure exerted at the edge of the object, where the scalar field transitions from its value inside the object to its value outside the object. This transition happen in a small region of size $\lambda_\phi \ll R$. This bubble wall "traps" the matter inside and prevents it from expanding.

The internal (outwards) pressure and energy density of the SBOs can be written as a function of their density[8]

$$p_{\rm in}^{\rm SBO}(\rho) = p_\psi(\rho) - p_\psi(\rho^{\rm NGS}) , \qquad \varepsilon^{\rm SBO}(\rho) = \varepsilon_\psi(\rho) - \varepsilon_\psi(\rho^{\rm NGS}) + \varepsilon^{\rm NGS} . \tag{9.25}$$

The self-bound objects are denser than the NGS density $\rho^{\rm NGS}$, and as $\rho \to \rho^{\rm NGS}$ the pressure inside vanishes $p_{\rm in}^{\rm SBO} \to 0$ and the energy goes to a constant $\varepsilon^{\rm SBO} \to \varepsilon^{\rm NGS}$. The NGS density $\rho^{\rm NGS}$ is proportional to $V(\theta^{\rm NGS})$, and can be analytically estimated given a specific model (*e.g.* for the ALP model of Sec. 9.1.2.A, see Eq. (9.40) and Eq. (9.41)). The mass of the this constant-density object is given simply by $M = 4\pi R^3 \varepsilon^{\rm SBO}/3$.

The inwards pressure of the bubble wall at the edge of the star can be deduced from Eq. (9.24), where we approximate the field profile as a linear transition s.t $\theta' \approx \Delta\theta/\lambda_\phi = \text{constant}$[9]. Integrating Eq. (9.24) over the small transition region, we find

$$p_{\rm grad}(\rho, R) \approx \frac{2 f^2 (\Delta\theta)^2 \lambda_\phi^{-1}}{R} = \frac{c f \sqrt{g m \rho_s(\rho)}}{R}, \tag{9.27}$$

where in the second step we used the definition of the effective (density-dependent) wave length defined in Eq. (II.C.10), where we parametrized $\partial m_*(\theta)/\partial\theta \sim g m$, with g some coupling. We also absorbed all the $\mathcal{O}(1)$ uncertainties in the constant $c \sim \mathcal{O}(1)$[10]. By equating the two

[8] In the following expressions we assume the fermion mass inside the object is (1) fixed **or** (2) density-dependent but negligibly small. Assumption (1) is relevant for the case of $m_*(\theta)$ bounded from below, while assumption (2) is relevant when $m_*(\theta)$ crosses the value zero.

[9] We neglect the θ'' term in the EOM, which is actually dominate at large radii over the r-suppressed θ'/r. However, the θ'' term does not contribute to the pressure since

$$\int_R^{R+\lambda_\phi} (\theta'\theta'') \, {\rm d}r = \frac{1}{2} \int_R^{R+\lambda_\phi} (\theta'^2)' \, {\rm d}r = (\theta'^2)\Big|_R^{R+\lambda_\phi} \approx 0 , \tag{9.26}$$

where we used the fact that the field becomes approximately constant on either side of the transition region.

[10] Note that $\Delta\theta$ can always be redefined away by rescaling $f \to f/\Delta\theta$.

pressures of Eq. (9.25) and Eq. (9.27), we can find the relation between the density of the object and its radius,

$$R^{-1}(\rho) = \frac{p_\psi(\rho) - p_\psi(\rho^{\rm NGS})}{cf\sqrt{gm\rho_s(\rho)}} = \frac{1}{cf\sqrt{gm\rho_s(\rho^{\rm NGS})}} \frac{(\rho^{\rm NGS})^{5/3}}{E_f(\rho^{\rm NGS})} \left(\rho/\rho^{\rm NGS} - 1\right) + \dots , \tag{9.28}$$

with $E_f(\rho) \equiv \sqrt{(m_*^{\rm NGS})^2 + (3\pi^2\rho)^{2/3}}$. In the second step we expanded to leading order in $\rho/\rho^{\rm NGS} - 1 \ll 1$ and (re)absorbed all the $\mathcal{O}(1)$ factors in the constant $c \sim \mathcal{O}(1)$. From Eq. (9.28), it is clear that these bound objects become smaller (larger) as the central density and pressure increase (decrease). The $f \to 0$ limit permits only one solution, namely an infinitely large, zero-pressure object $R \to \infty$ at the NGS density $\rho \to \rho^{\rm NGS}$. For finite f, the SBOs are bounded in size both from above and from below. The smallest object possible would have

$$R_{\rm min}^{\rm SBO} \approx \lambda_\phi \,, \tag{9.29}$$

where the approximation $R \gg \lambda_\phi$ breaks down. This also implicitly defines the maximal possible density of the self bound object, above which Eq. (9.24) does not admit non-trivial solutions. On the other hand, for very low densities the object becomes large, reaching the point where gravity can no longer be neglected. This occurs when the drop in the pressure inside the object due to gravity is comparable to the internal pressure. This drop in pressure can be calculated directly from Eq. (9.7a), assuming constant energy density, to find

$$\Delta p_{\rm gravity}(\rho) = -\frac{(\varepsilon^{\rm SBO})^2 R^2}{12 M_{\rm pl} 2} \,. \tag{9.30}$$

As expected, $\Delta p_{\rm gravity}$ vanishes in the $M_{\rm pl} \to \infty$ limit. The maximal radius of an SBO is found by setting $|\Delta p_{\rm gravity}(\rho)| = p_{\rm in}^{\rm SBO}(\rho) = p_{\rm grad}(\rho)$, which can be solved to find the maximal SBO density (remember R is not an independent variable but rather depends on ρ, see Eq. (9.28)). In practice, the large and low pressure SBOs have number density close to $\rho^{\rm NGS}$, which allows us to more simply approximate the largest radius as

$$R_{\rm max}^{\rm SBO} \approx \left(\frac{12 M_{\rm pl} 2 f \sqrt{gm\rho_s}}{(\varepsilon^{\rm NGS})^2} \right)^{1/3} \Bigg|_{\rho=\rho^{\rm NGS}} . \tag{9.31}$$

where both ρ_s and $\varepsilon^{\rm SBO}$ should be evaluated at $\rho = \rho^{\rm NGS}$, which is the typical density of the largest SBOs. To get an idea of how large these objects can be, we plug in some numbers to find

$$R_{\rm max}^{\rm SBO} \approx (8.9 \text{ km}) \left(\frac{f}{10^{17} \text{ GeV}} \right)^{1/3} \left(\frac{gm}{m_N} \right)^{1/6} \left(\frac{\rho_s}{\rho_{\rm sat}} \right)^{1/6} \left(\frac{(200 \text{ MeV})^4}{\varepsilon^{\rm NGS}} \right)^{2/3} , \tag{9.32}$$

where we used for reference an SBO energy of the order of the QCD scale and scalar density similar to nuclear saturation density $\rho_{\rm sat} = 0.16 \text{ fm}^{-3}$. Using the same numerical values, the maximal mass is given by

$$M_{\rm max}^{\rm SBO} = \frac{4\pi (R_{\rm max}^{\rm SBO})^3 \varepsilon^{\rm SBO}}{3} \approx 0.54 \, M_\odot \,. \tag{9.33}$$

We note that the existence of the SBO solutions is ensured only if $R_{\rm max}^{\rm SBO} > R_{\rm min}^{\rm SBO}$, a condition which generally depends on the model parameters and can be expressed as an upper bound on f

$$f < \left(\frac{\sqrt{12} gm\rho_s}{\varepsilon^{\rm NGS} \Delta\theta} \right) \Bigg|_{\rho=\rho^{\rm NGS}} M_{\rm pl} \,. \tag{9.34}$$

For objects of size $R \gtrsim R_{\rm max}^{\rm SBO}$, where the gravitational force is non-negligible, the full coupled set of equations of Eq. (9.7) must be solved, as discussed just above Sec. 9.1.1.A. There is a smooth transition between SBOs (where gravity is negligibly small) and the usual gravitationally-bound stars (where the gradient pressure is typically negligible and the $f \to 0$ limit may be used).

For the general discussions above, we made minimal assumptions regarding the form of $m_*(\theta)$ and $V(\theta)$. In the following sections we study in detail three models, motivated by various BSM scenarios involving scalars.

9.1.2 Case Studies

A Axion-like Particle

The first model we consider assumes the scalar field $\phi \equiv f\theta$ is an axion-like particle (ALP). The coupling to matter and the self-coupling(s) are given by

$$m_*^{\rm ALP}(\theta) = m\left[1 + \frac{g}{2}\left(\cos\theta - 1\right)\right], \quad V^{\rm ALP}(\theta) = -\Lambda^4(\cos\theta - 1)\,, \tag{9.35}$$

where we introduced a dimensionless coupling g which controls the interaction strength between the scalar and the fermion, and a mass scale Λ, which sets the scale of the scalar self-interactions. In particular, it can be related to the scalar mass at zero density, namely $m_\phi = \Lambda^2/f$. The couplings are symmetric under a discrete shift symmetry $\theta \to \theta + 2\pi$, which is a common feature of ALP models. It is important to note that in a natural theory (i.e. without fine-tuning) one expects Λ^4 to be at least $\mathcal{O}(g^2 m^2 \Lambda_{\rm QCD}^2)$, where in a more general setup $\Lambda_{\rm QCD}$ should be replaced with the cutoff scale of the theory. As we discussed above, the existence of a new ground state typically requires small values of Λ/m, which means some degree of fine-tuning. However, a seemingly fine-tuned ALP can be realized using symmetry-based mechanisms, see *e.g.* [123,124]. This general statement is relevant also for the other models consider in this work, namely the quadratic coupling considered in Sec. 9.1.2.B and the linear coupling considered in Sec. 9.1.2.C.

As in the previous section, it is useful to first consider the negligible gradient ($f \to 0$) limit where we can define the microscopic EOS, and postpone the discussion on finite f effects to a later stage.

Equation of State

Plugging the function defined in Eq. (9.35) in Eq. (9.9), we find the scalar EOM in the negligible gradient limit,

$$\left.\frac{\partial\Omega}{\partial\theta}\right|_{\mu=\text{const.}} = \left(-\frac{gm}{2}\rho_s(\theta,\mu) + \Lambda^4\right)\sin\theta = 0\,. \tag{9.36}$$

From this equation we compute $\theta(\mu)$, which connects the zero-density value, in this case $\theta_0 = 0$, to its value at high density $\theta_\infty \equiv \lim_{\mu\to\infty}\theta(\mu)$,

$$\theta_\infty^{\rm ALP} = \begin{cases} \cos^{-1}\left(1 - \frac{2}{g}\right) & g \geq 1 \\ \pi & 0 < g < 1 \\ 0 & g \leq 0 \end{cases}\,. \tag{9.37}$$

These two cases represent to two general types of solution discussed above (see Eq. (9.9)). In the first case ($g \geq 1$), Eq. (9.36) is satisfied by taking $m_*(\theta) \to 0$ such that the scalar density remains fixed as $\mu \to \infty$, i.e. $\rho_s(\theta, \mu) \to \rho_c^{\rm ALP}$, where

$$\rho_c^{\rm ALP} \equiv \frac{2\Lambda^4}{gm} \,. \tag{9.38}$$

In these solutions the mass becomes arbitrarily small at high densities and the scalar density ρ_s is fixed. In the second case ($g < 1$), the mass function $m_*(\theta)$ does not cross zero and is bounded from below. Eq. (9.36) is satisfied by taking $\theta \to \pi$ where $\partial m_*(\theta)/\partial\theta \to 0$[11]. As the density increases and the mass stays fixed at $m_*(\theta_\infty) = m(1-g)$, the scalar density ρ_s increases. Lastly, if g is negative, $\theta(\mu) = 0$ for all values of μ since a phase with a heavier fermion is never preferred. We shall henceforth assume that $g > 0$.

The parameter space of this model is two-dimensional and is spanned by the dimensionless parameters g and Λ/m, see Fig. 9.4 (for concreteness we chose $m = m_N$). The boundary between the CE region and the NGS region in the $\{g, \Lambda/m\}$ plane is given by[12]

$$p(0, m; g, \Lambda/m) = p(\theta_\infty^{\rm ALP}, m; g, \Lambda/m) \quad \text{(CE-NGS boundary)} \,. \tag{9.39}$$

The NGS region is plotted in green in Fig. 9.4, below the black curve defined by Eq. (9.39). The NGS region can be further divided into two sub-regions. In the light-green region, the new ground state the NGS is non-relativistic. In the dark-green region, the mass in the NGS is typically much smaller and the NGS is ultra-relativistic. Above the black dashed line the NGS has a large energy density, $\varepsilon^{\rm NGS} \geq (0.2\ {\rm GeV})^4$ for $m = m_N$, which implies sub-millisecond rotation periods of bound objects in the NGS, see Eq. (9.22). Above the solid black line, we find the coexistence region, plotted in red in Fig. 9.4. As discussed above, this region is characterized by a first-order phase transition which softens the equation of state. This region can also be further divided into two sub-regions. In the light-red region, both phases are NR around the phase transition point. In the dark-red region, the high density phase is already ultra-relativistic around the transition point. For even larger values of Λ/m, both phase are ultra-relativistic when the transition occurs, which does not influence the EOS. Only a small part of the UR→UR region appears in Fig. 9.4, namely the gray region in the upper-left corner.

NGS Region

The EOS in the NGS region consists of two branches; a meta-stable branch at low densities and the stable branch of the new ground state. It is therefore easier to describe the EOS using the number density ρ[13]. The meta-stable branch is found at low densities $\rho < \rho_{\rm meta}^{\rm NGS}$, where $\rho_{\rm meta}^{\rm NGS}$ is defined by $\rho_s(0, \rho_{\rm meta}^{\rm NGS}) \equiv \rho_c^{\rm ALP}$. The stable branch of the EOS, describing matter in its new ground state, begins at some density $\rho^{\rm NGS}$ and $\theta^{\rm NGS}$, defined by $p(\theta^{\rm NGS}, \rho^{\rm NGS}) = 0$. First let us focus on the case $g < 1$ shown in Fig. 9.4. In this region, we verified numerically that $\theta^{\rm NGS} \approx \theta_\infty^{\rm ALP} \approx \pi$ in

[11] For this special choice of $m_*^{\rm ALP}(\theta)$ and $V^{\rm ALP}(\theta)$, $\theta = \pi$ is an exact solution since it is also a maximum of the potential. In general, the first derivative of the potential does not necessarily vanish at θ_∞.

[12] This approximation relies on the assumption that the transition between 0 and $\theta_\infty^{\rm ALP}$ is instantaneous, in the sense that if the transition from 0 to $\theta_\infty^{\rm ALP}$ occurs in some interval $[\mu_-, \mu_+]$, then $\frac{\mu_+ - \mu_-}{\mu_+ + \mu_-} \ll 1$. We verified numerically that this is indeed a good approximation in the relevant part of parameter space.

[13] The meta-stable branch can be calculated by using ρ as the free parameter, since using μ gives, by construction, only the stable branche of the EOS.

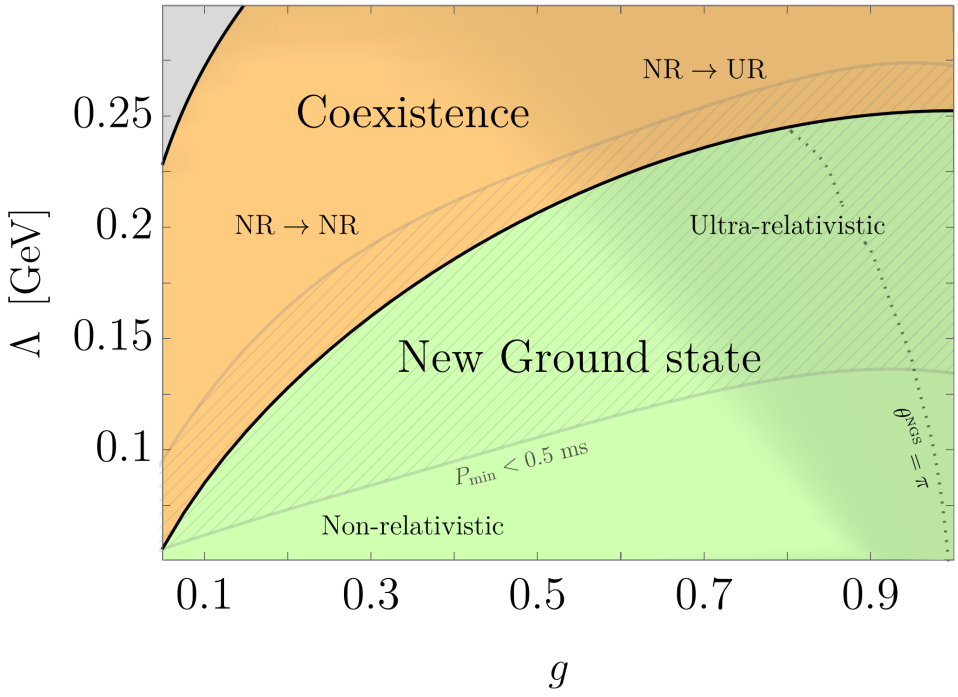

Figure 9.4: The $\{g, \Lambda/m\}$ parameter space of the ALP model, where we chose for concreteness $m = m_N$. The black line, defined by Eq. (9.39), separates between the CE region (in red) and the NGS region (in green). The EOS in the CE region describes a first-order phase transition, where the low-density phase is non-relativistic and the high-density can either be non-relativistic (light-red region) or ultra-relativistic (dark-red region). The EOS in the NGS region describes anew ground states, which is either non-relativistic (light-green region) or ultra-relativistic (dark-green region). Above the blue curve, $\varepsilon^{\rm NGS} > (200\ {\rm GeV})^4$ which implies sub-millisecond rotation periods, see Eq. (9.22). On the right of the dashed vertical curve, the NGS phase is characterized by some $\theta^{\rm NGS} < \theta_\infty = \pi$ with scalar density fixed at $\rho_c^{\rm ALP}$.

most of the parameter space[14] and θ remains approximately density-independent for $\rho > \rho^{\rm NGS}$. Thus, by solving $p(\pi, \rho^{\rm NGS}) = 0$, approximate analytical expressions for $\rho^{\rm NGS}$ and $\rho_s^{\rm NGS}$ can be calculated. In the NR limit,

$$\rho^{\rm NGS} \approx \rho_s^{\rm NGS} \approx \left(\frac{10^3}{3^2\pi^4}\right)^{1/5} \left((1-g)m\,\Lambda^4\right)^{3/5} \qquad \text{(NR NGS)}\,, \tag{9.40}$$

which is relevant in the light-green region of Fig. 9.4. In the UR limit,

$$\begin{aligned} \rho^{\rm NGS} &\approx \frac{m^3}{6\sqrt{2}\pi^2}\left((1-g)^2 + \sqrt{(g-1)^4 + 96\pi^2(\Lambda/m)^4}\right)^{3/2}\,, \\ \rho_s^{\rm NGS} &\approx \frac{(1-g)^3 m^3}{4\pi^2}\left(1 + \sqrt{(g-1)^4 + 96\pi^2(\Lambda/m)^4}\right)\,, \end{aligned} \tag{9.41}$$

which is relevant in the dark-green region of Fig. 9.4 where $\theta^{\rm NGS} = \pi$, left of the dashed horizontal curve. Note in the derivation of Eq. (9.41) one has to expand $p(\pi, \rho^{\rm NGS})$ to next-to-leading order in density, i.e. up to the $(1-g)^2 m^2 (\rho^{\rm NGS})^{2/3}$ term, in order to find this g-dependent result. The energy densities can be estimated using the number densities above,

$$\varepsilon^{\rm NGS} \approx 2\Lambda^4 + m^4 \begin{cases} \left(\frac{10^3}{3^2\pi^4}\right)^{1/5} \left(\frac{\Lambda}{m}\right)^{12/5} (1-g)^{8/5} & \text{NR NGS} \\ \left(\frac{\sqrt{(g-1)^4 + 96\pi^2(\Lambda/m)^4} + (g-1)^2}{4\pi}\right)^2 & \text{UR NGS} \end{cases}\,. \tag{9.42}$$

The UR approximation of $\rho_s^{\rm NGS}$ breaks down as $g \to 1$ where $\theta^{\rm NGS}$ starts to deviates from π. In this region

$$\rho_s^{\rm NGS}(\theta^{\rm NGS}, \rho^{\rm NGS}) = \frac{2\Lambda^4}{gm} \quad (\text{UR}, \quad g \lesssim 1)\,, \tag{9.43}$$

which as we argued above, can be a solution for the EOM for $\theta^{\rm NGS} < \pi$. For $g > 1$, Eq. (9.43) is always satisfied in the NGS at all densities. The equation $p(\theta^{\rm NGS}, \rho^{\rm NGS}) = 0$ can be solved under the constraint Eq. (9.43), which is used to express $\theta^{\rm NGS}$ in terms of $\rho^{\rm NGS}$, to find the NGS number density in the $g > 1$ region

$$\rho^{\rm NGS} \approx \frac{4\Lambda^3 (2/3)^{1/4}}{\sqrt{\pi} g^{3/4}}\left(1 + \mathcal{O}\left(\frac{\Lambda}{m\sqrt{g}}\right)\right) \quad (\text{NR}, \quad g > 1)\,, \tag{9.44}$$

with the energy density

$$\varepsilon^{\rm NGS} \approx \frac{8\Lambda^4}{gm} \quad (\text{NR}, \quad g > 1)\,. \tag{9.45}$$

Lastly, the region $\rho_{\rm meta}^{\rm NGS} < \rho < \rho^{\rm NGS}$ is strictly unstable, since $\partial(\varepsilon/\rho)/\partial\rho \propto p < 0$ in this region. In Table 9.1 we summarize the energy density and pressure in the relevant interval of ρ, from which the equation of state in the NGS region can be easily deduced.

[14] The smallest values of $\theta^{\rm NGS}$ are found in the upper-right corner of the dark-green region of Fig. 9.4, where $\theta^{\rm NGS} \gtrsim 0.7\pi$.

	$p(\rho)$	$\varepsilon(\rho)$	range of ρ
Meta-stable	$p_\psi(0,\rho)$	$\varepsilon_\psi(0,\rho)$	$\rho < \rho^{\rm NGS}_{\rm meta}$
Unstable	-	-	$\rho^{\rm NGS}_{\rm meta} < \rho < \rho^{\rm NGS}$
Stable	$p_\psi(\theta^{\rm ALP}_\infty,\rho) - p_\psi(\theta^{\rm ALP}_\infty,\rho^{\rm NGS})$	$\varepsilon_\psi(\theta^{\rm ALP}_\infty,\rho) + \frac{2\Lambda^4}{\max[1,g]}$	$\rho^{\rm NGS} < \rho$

Table 9.1: The energy density and pressure for the NGS EOS including the meta-stable region at low densities and the stable region at high densities, where we neglected the small deviations from $\theta^{\rm ALP}_\infty$. Note that $p_\psi(\theta^{\rm ALP}_\infty,\rho^{\rm NGS}) \equiv \frac{2\Lambda^4}{\max[1,g]}$.

CE Region

In the rest of the parameter space, above the curved defined by Eq. (9.39) in the $\{g, \Lambda/m\}$ plane, the two phases of matter coexist and the EOS consists of a single, stable branch describing a phase transition. It is therefore easier to describe using the chemical potential and the angle θ. While the chemical potential and the total pressure are insured to be continuous across the phase transition, θ may jump from zero to some value at some critical chemical potential which we denote by $\mu_c^{\rm CE}$. This jump in θ implies a jump in the fermion mass, which leads to a jump in other quantities like number and energy densities. There are two types of qualitatively different transitions which may occur depending on the position in the $\{g, \Lambda/m\}$ plane.

In the light-red region of Fig. 9.4, the phase transition is first order, characterized by a jump from a non-relativistic $\theta = 0$ phase to a non-relativistic $\theta = \pi$ phase at a critical chemical potential $\mu_c^{\rm CE}$. It can be calculated in the NR approximation from the condition $p(0,\mu_c^{\rm CE}) = p(\pi,\mu_c^{\rm CE})$. Knowing the chemical potential $\mu_c^{\rm CE}$ and θ on both sides of the transition, we can use the relation between the number density and chemical potential to calculate the number density before and after the transition. Due to the Maxwell construction, the jump typically occurs from some value of ρ below the critical $\rho_c^{\rm ALP}$ to some value above it. A similar jump occurs in the scalar density ρ_s.

The second type of transition occurs in the dark-red region of Fig. 9.4. For now, let us limit the discussion to the case $g < 1$. First, there is a jump from a non-relativistic $\theta = 0$ phase to an ultra-relativistic $\theta = \theta_c^{\rm CE}$ phase at a critical chemical potential $\mu_c^{\rm CE}$. Right after this jump, the equation of motion is satisfied due to the fact that $\rho_s(\theta_c^{\rm CE},\mu_c^{\rm CE}) = \rho_c^{\rm ALP}$. By solving this equation, along with $p(0,\mu_c^{\rm CE}) = p(\theta_c^{\rm CE},\mu_c^{\rm CE})$, one can find the two unknowns $\{\theta_c^{\rm CE},\mu_c^{\rm CE}\}$. This can be done either numerically, or analytically using the proper approximations (the NR limit for the low density phase and the UR limit for the high density phase). In the interval $\mu_c^{\rm CE} < \mu < \mu_\infty^{\rm CE}$, θ continues to increase and the equation of motion is satisfied due to $\rho_s(\theta(\mu),\mu) = \rho_c^{\rm ALP}$, until finally reaching its final value $\theta = \pi$ at $\mu_\infty^{\rm CE}$. The chemical potential $\mu_\infty^{\rm CE}$ can be analytically calculated by solving $\rho_s(\pi,\mu_\infty^{\rm CE}) = \rho_c^{\rm ALP}$ in the appropriate UR limit, giving

$$\mu_\infty^{\rm CE} = \frac{2\pi m(\Lambda/m)^2}{\sqrt{(1-g)g}}\,. \tag{9.46}$$

For $\mu > \mu_\infty^{\rm CE}$, the EOM is satisfied by the fact that $\theta = \pi$ and the scalar density begins to increase above the critical value $\rho_c^{\rm ALP}$. A similar transition occurs when $g > 1$, with the main difference being that $\mu_\infty^{\rm CE} \to \infty$. Therefore, $\theta_\infty^{\rm ALP}$ is only reached asymptotically and $\rho_s(\theta,\mu)$ is fixed at $\rho_c^{\rm ALP}$ for all values of $\mu > \mu_c^{\rm CE}$.

Finite Gradient Effects

After discussing the general features of the EOS in the ALP model, we proceed to discuss the deviations from the microscopic EOS picture due to finite gradient energy effects. Below we present our numerical results of the full coupled system given by Eq. (9.7), which demonstrate the finite gradient energy effects discussed in previous sections. For this section we fix m to be the nucleon mass $m_N \approx 0.939$ GeV and focus on two illustrative benchmark points in our parameter space. The first benchmark point,

$$\text{BM1} : g = 0.025 \qquad\qquad \Lambda/m = 0.075 \text{ GeV}/m_N \approx 0.08\,, \tag{9.47}$$

is inspired by the values expected for the QCD axion (see e.g [118])

$$\begin{aligned} g &= \frac{1}{2}\frac{\sigma_N}{m_N} \approx 0.025 \left(\frac{\sigma_N}{50 \text{ MeV}}\right)\,, \\ \Lambda^4 &= m_a^2 f_a^2 = \frac{m_u m_d}{(m_u+m_d)^2} m_\pi^2 f_\pi^2 \approx (0.075 \text{ GeV})^4\,, \end{aligned} \tag{9.48}$$

where we used $m_\pi = 135$ MeV, $f_\pi = 92$ MeV and $m_u/m_d \approx 0.5$. This point lies in the CE region of parameter space. We expect a phase transition of the NR $\to$ NR type around the critical density

$$\rho_c^{\text{ALP}} \approx 0.35 \text{ fm}^{-3} \approx 2.1 \rho_{\text{sat}} \quad \text{(BM1)}\,. \tag{9.49}$$

The resulting mass-radius curves are shown in Fig. 9.5 for $f = \{5\times 10^{16}, 10^{16}, 10^{15}\}$ GeV. As expected, the phase transition leads to a softening of the EOS, and therefore less massive bound objects. The objects occupying on the branch on the right are made only of the low density phase, which is essentially just the pure Fermi gas. The branch on the left is describes hybrid stars, composed of a core in the high-density ($\theta = \pi$) phase and an exterior region in the low-density ($\theta = 0$) phase.

In fact, the phase transition appearing in Fig. 9.5 occurs due to the same mechanism which lead Migdal to consider the possibility of pion condensation in the early 1970s [245], namely the naive reduction of the π_0 mass by the baryonic background. In our simple setup, the ALP undergoes a similar reduction in mass, leading to the phase transition appearing in Fig. 9.5. However, for the parameters chosen in the above example, this transition happens at baryon densities where we do not trust the theory any more. A detailed study of the ALP chiral Lagrangian, in particular the QCD axion, at finite density shows that the axion condensation might still be triggered by Kaon condensation [118]. Such axion condensation would lead to qualitatively similar effects, namely softening of the EOS and less-massive stars.

The effect of the gradient energy/pressure can be seen in two features in the mass-radius curves of Fig. 9.5. First, the inner core of the homogenous stars (on the right branch) can in fact have a region which is above the critical density, as long as this region is smaller than the effective in-medium wavelength of the scalar field. Higher values of f trace the pure Fermi gas line until smaller radii and larger masses, at which point a large enough central region is created and it is energetically favorable for the high-density phase to form inside. Second, for higher values of f the start of the hybrid branch consists of configurations where the ALP is not fully sourced, i.e. the value of the field does not reach π at the core due to the resistance of the gradient energy. These type of so-called thick-wall bubbles are an indication that the gradient energy still plays a significant role. In such configurations, the transition region of the scalar inside the hybrid star is large and occupies a more significant portion of the whole object, and the gradient pressure plays a more important role in the equilibrium configuration. This explains the visible

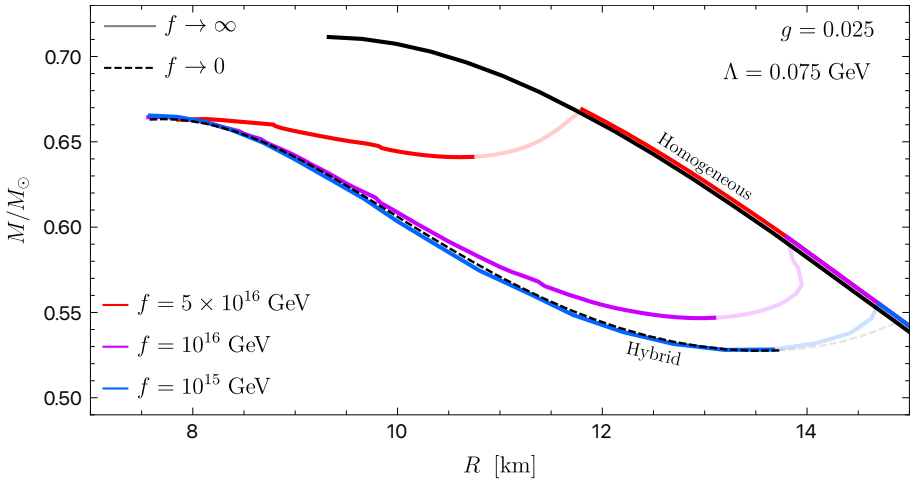

Figure 9.5: The mass-radius curve of the BM1 point (QCD axion-like) in the ALP model. The black solid line is mass-radius curve of a pure Fermi gas, equivalent to the ALP decoupling limit ($f \to \infty$). The black dashed line is the numerical result obtained in the negligible gradient energy limit ($f \to 0$) using the effective microscopic EOS. The red, purple and blue curves are the result of numerically solving the full coupled system for $f = \{5 \times 10^{16}, 10^{16}, 10^{15}\}$ GeV, respectively. Finite f curves tracking the pure-Fermi lines consist of homogenous configurations made of the low-density phase. The second branches appearing on the left consist of hybrid stars, with a core in the high-density phase and a crust in the low-density phase. The light-colored curves are the unstable configurations.

deviations of the finite f hybrid branches compared to the $f \to 0$ limit hybrid branch. However at high-enough internal pressures, once the ALP is fully sourced and a thin-wall bubble forms, all the curves converge to a similar curve in the $\{M, R\}$ plane, and in particular to a similar maximal mass configuration. This is not a surprise, since the existence of a thin-bubble wall is by itself an indication that the gradient energy is negligible.

The second benchmark point,

$$\text{BM2} : g = 0.5 \qquad \Lambda/m = 0.075 \text{ GeV}/m_N \approx 0.08\,, \tag{9.50}$$

was chosen to illustrate the effects of the existence of the NGS. As discussed above, we expect to find meta-stable configurations with central densities which are at most of the order of the critical density, in this case

$$\rho_c^{\text{ALP}} \approx 0.017 \text{ fm}^{-3} \approx 0.1\rho_{\text{sat}} \quad \text{(BM2)}\,. \tag{9.51}$$

The absolutely stable configurations are composed purely of the NGS phase, characterized by number and energy densities similar to those at nuclei

$$\rho^{\text{NGS}} \approx 0.17 \text{ fm}^{-3} \approx \rho_{\text{sat}}\,, \quad \varepsilon^{\text{NGS}} \approx m_N \rho^{\text{NGS}} \approx \varepsilon_{\text{sat}} = 2.5 \times 10^{14} \text{gr/cm}^3 \tag{9.52}$$

where we used Eq. (9.40), which is within 10% of the value obtained numerically. The smallest stable objects can be described as self-bound, and their minimal and maximal radii (as a function of f) are given by

$$R_{\text{min}}^{\text{SBO}} \approx 25 \text{ m} \left(\frac{f}{10^{15} \text{ GeV}}\right)\,, \quad R_{\text{max}}^{\text{SBO}} \approx 2.3 \text{ km} \left(\frac{f}{10^{15} \text{ GeV}}\right)^{1/3}\,. \tag{9.53}$$

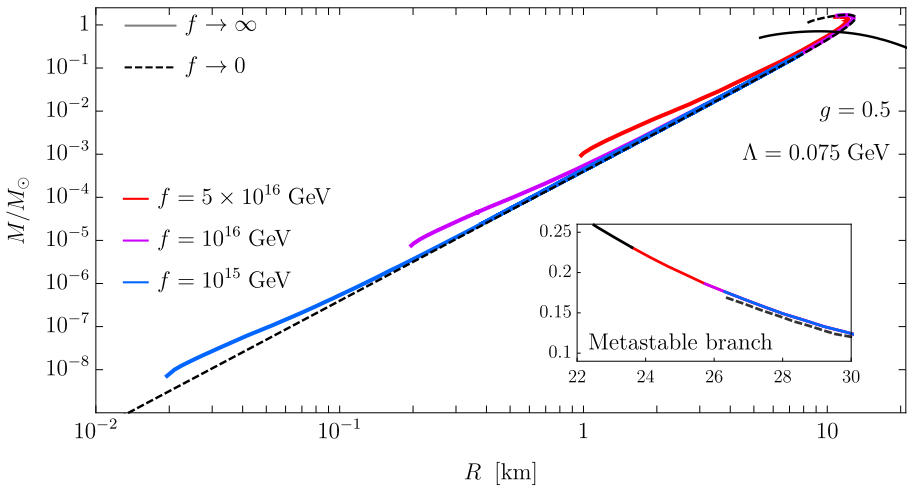

Figure 9.6: The mass-radius curve of the BM2 point in the ALP model. The black solid line is mass-radius curve of a pure Fermi gas, equivalent to the ALP decoupling limit ($f \to \infty$). The black dashed line is the numerical result obtained in the negligible gradient energy limit ($f \to 0$) using the effective microscopic EOS. The red, purple and blue curves are the result of numerically solving the full coupled system for $f = \{5 \times 10^{16}, 10^{16}, 10^{15}\}$ GeV, respectively. Finite f curves tracking the pure-Fermi lines, shown in the sub-plot at large radii, consist of the homogenous meta-stable configurations made of the low-density phase. The second branches appearing on the left consist of NGS stars, consisting purely of the high-density phase.

For objects with radii larger than $R^{\rm SBO}_{\rm max}$, gravity becomes comparable and eventually dominant over the scalar force. However, as long as the energy density of the object is approximately constant (which stays true even for low-density gravitationally-bound objects), the mass and radius are related by Eq. (9.20), in this case

$$M \approx 5 \times 10^{-4} M_\odot \left(\frac{R}{1\ \text{km}}\right)^3 , \tag{9.54}$$

which is independent of f.

In Fig. 9.6 we plot the mass-radius curves for BM2 for $f = \{5 \times 10^{16}, 10^{16}, 10^{15}\}$ GeV. At large radii we find the low-density meta-stable branch, which corresponding to the meta-stable states of pure Fermi gas. Similarly to BM1, higher values of f trace the pure Fermi gas line to lower radii until a large enough central region is formed, which would induce a collapse to the stable phase. At small radii we find the stable branch. The objects can only be as small as the (f-dependent) in-medium effective wavelength of the field. Our numerical results agree with our estimation for $R^{\rm SBO}_{\rm min}$ given in Eq. (9.53) and are indeed well-described at lower pressures by the curve defined by Eq. (9.54) independently of f. The visible deviations from the line at lower radii is a finite gradient energy effect explained by our model of the SBOs given in Sec. 9.1.1.B. The smallest SBOs can have a central number and energy densities which can be a few times larger than of $\rho^{\rm NGS}$ and $\varepsilon^{\rm NGS}$, respectively. Thus, the energy density can be larger than $\varepsilon^{\rm NGS}$, leading to configurations which lie above the curve defined by Eq. (9.54). For the smallest objects for which $R \approx R^{\rm SBO}_{\rm min}$, the size of the transition region becomes comparable to the size of the object and the assumptions of constant pressure and number density, on which our description depends on, are no longer valid. For BM2, the *average* energy density of the smallest solution

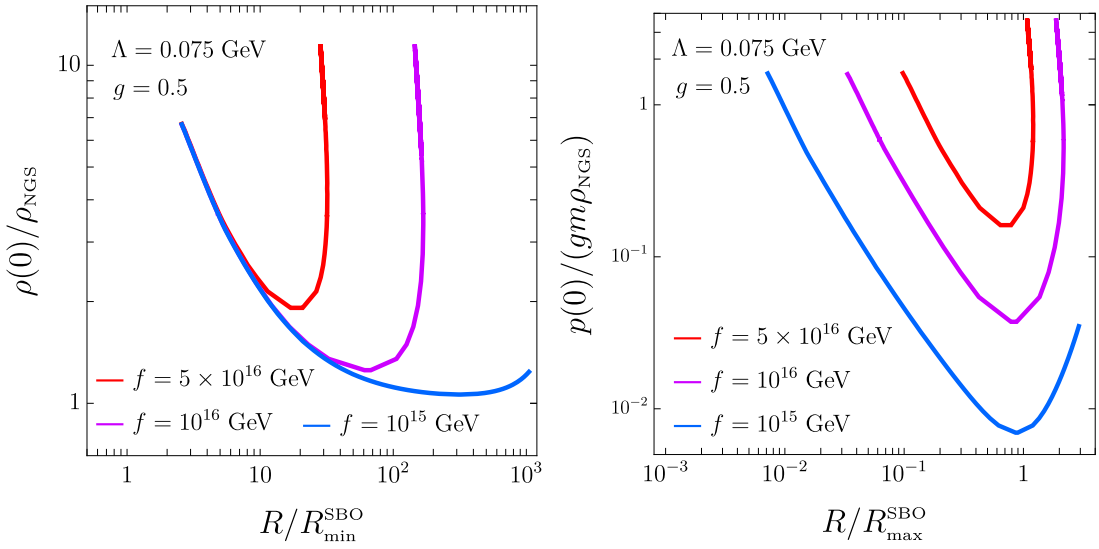

Figure 9.7: Left panel : The NGS configurations in the $\{\rho(0), R\}$ plane, where $\rho(0)$ is the central number density. $\rho(0)$ is plotted in units of the (f-independent) NGS number density given in Eq. (9.52), while the radius is given in units of the (f-dependent) minimal radius expected for the SBOs, given in Eq. (9.53) . The numerical results agree with the analytical estimation of the minimal size up to $\mathcal{O}(1)$ factors. The smallest SBOs are also the densest, with the size increasing as their density decreases. Right panel : The NGS configurations in the $\{p(0), R\}$ plane, where $p(0)$ is the central pressure. $p(0)$ is plotted in units of the estimate (f-independent) maximal pressure given in Eq. (9.55), while the radius is given in units of the (f-dependent) maximal radius expected for the SBOs, given in Eq. (9.53). The numerical results agree with the analytical estimation of the maximal pressure and size up to $\mathcal{O}(1)$ factors. The largest SBOs are the most low-pressure, dilute configurations. For larger objects gravity becomes increasingly important, and the configuration behave like typical gravitationally-bound stars.

is larger than $\varepsilon^{\rm NGS}$. Therefore, the stable branch begins above the line and approaches it as the objects become larger[15]. Note that the negligible gradient energy ($f \to 0$) line in Fig. 9.6 always describes *gravitationally-bound* objects, since gravity is the only remaining force in this limit. However, as long as the object is dilute enough, i.e. $\rho \approx \rho^{\rm NGS}$, it has constant energy density $\varepsilon^{\rm NGS}$ and Eq. (9.54) is valid, regardless of whether it is a self- or gravitationally-bound object. Note that for the most massive NGS stars, the effects of the gradient pressure at the edge of the star is increasingly negligible, making the properties of the gravitationally-bound stars essentially f-independent.

As shown in Fig. 9.7, the numerical solutions agree with our simple modelling of the SBOs given in Sec. 9.1.1.B. The smallest SBOs are the densest and exhibit the highest internal pressure. These properties are in fact f-independent, *e.g.* the maximal pressure is given in this case by

$$p^{\rm SBO}_{\rm max} \approx g m_N \rho^{\rm NGS} \approx \varepsilon_{\rm sat} \,, \tag{9.55}$$

which can be found by plugging in $R = (\pi f)/\sqrt{gm\rho^{\rm NGS}}$ in Eq. (9.27) and evaluating it at $\rho = \rho^{\rm NGS}$. The maximal density can be found by solving $p^{\rm SBO}_{\rm in}(\rho) = p^{\rm SBO}_{\rm max}$ (see Eq. (9.25))

[15] In other parts of parameter space, we found that the average density can be smaller, producing curves which approach the line from below.

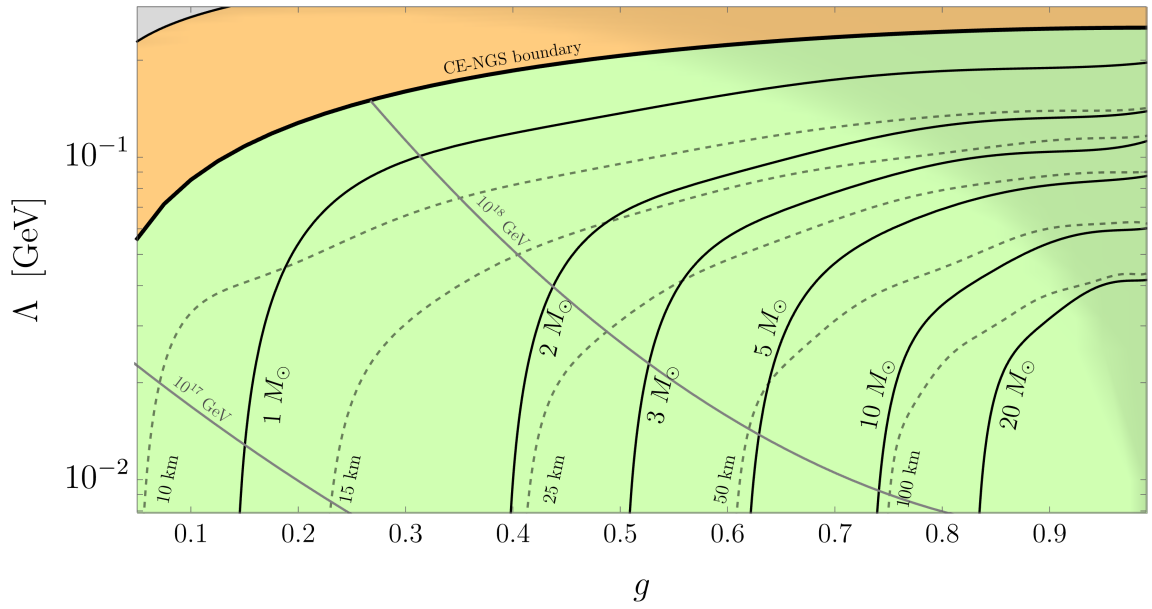

Figure 9.8: The $\{g, \Lambda/m\}$ parameter space of the ALP model, where we chose for concreteness $m = m_N$. The thick black line, defined by Eq. (9.39), separates between the CE region (in orange) and the NGS region (in green). The solid lines are contours of constant mass of the heaviest star calculated in the negligible gradient energy limit, while the dashed lines are contours of the corresponding radii. The gray contours represent the line where the effective in-medium wavelength associated with the labeled f value is the size of the heaviest star, i.e. the upper bound on f, beyond which the gradient energy cannot be neglected. For most of the parameter space, the negligible gradient energy limit is valid as long as $f \ll 10^{17}$ GeV.

numerically, which results in $\rho_{\max} \approx 10\rho^{\rm NGS}$ for BM2. These results match up to $\mathcal{O}(1)$ factors with the numerical results shown in Fig. 9.7, confirming the f-independent behavior of the smallest SBOs in number density (left panel) and pressure (right panel). Note that the smallest SBOs are the least compatible with the underlying assumptions of our SBO model, namely constant density and small transition region. Fig. 9.7 also confirms our f-dependent predictions, i.e. the minimal and maximal size of the SBOs. The qualitative behavior of the curves follows the description given in Sec. 9.1.1.B; the smallest SBOs with $R \approx R^{\rm SBO}_{\rm min}$ are the densest and have the highest pressures. As the number density decreases and ρ approaches $\rho^{\rm NGS}$, the object becomes larger, more dilute and the internal pressure decreases. This continues until $R \approx R^{\rm SBO}_{\rm max}$, where gravity becomes important and matter must be added inside in order to counter the crushing pressure of gravity. From this point onwards the the mass and radius increases as the central number density and pressure increase.

Negligible Gradient Results

We conclude the discussion on the ALP model by presenting a global view on the phase space in the negligible gradient energy ($f \to 0$) limit, plotted in Fig. 9.8. We performed a scan of the parameter space and calculated at each point the microscopic EOS, which can than be used to calculated the mass-radius curve by solving Eq. (9.11) numerically. From the mass-radius curve, we extract the maximal mass of a stable bound object and its radius. In Fig. 9.8 we plot

the contours of constant mass and radii for the heaviest bound objects in the NGS region. As demonstrated above in Sec. 9.1.2.A, the properties of objects in which thin-wall bubbles have formed are essentially f-independent, in particular the largest and most massive stars in the NGS region. Therefore, Fig. 9.8 is valid for all values of f up to the values plotted in the red contours; e.g in the region above the $f = 10^{18}$ GeV contour, if $f \gg 10^{18}$ GeV, bubbles are not formed and the scalar is effectively decoupled since the effective in-medium wavelength is much larger than the size of the most massive object. Values of $f \gtrsim 10^{18}$GeV cannot be neglected, since the effective in-medium wavelength is comparable to the size of the most massive object. This is the threshold of bubble formation where a numerical solution of the full system is needed. Since finite gradient energy effect tend to make the mass-radius curve more similar to the ideal Fermi gas curve, the negligible gradient energy limit results of Fig. 9.8 represent the maximal effect one can expect from the scalar interactions.

We identify two qualitatively different regions. For small values of Λ, the constant mass and radius contour are approximately Λ-independent. The increase in mass and radius of the NGS stars are solely due to the decrease in the fermion mass. We recover the same scaling as in Eq. (9.19), in particular in the ALP model

$$M_{\rm max} = (0.7\ M_\odot)\left(\frac{m_N}{m(1-g)}\right)^2 \quad \text{with} \quad R(M_{\rm max}) = (9.4\ \text{km})\left(\frac{m_N}{m(1-g)}\right)^2 . \tag{9.56}$$

On the other hand, in the dark-green region of Fig. 9.8, the NGS is ultra-relativistic, and therefore the mass of the fermion plays a small role in the EOS. Instead, the only dimensionful parameter in the system is $V(\theta)$, which can be approximated as a constant $\approx V(\theta_\infty)$ in regions far enough below the CE-NGS boundary. For an ultra-relativistic Fermi gas, the EOS branch of the NGS takes a particularly simple form

$$\epsilon(\rho) = 3p(\rho) + 4V(\theta_\infty)\,, \tag{9.57}$$

where $p(\rho) = p_\psi^{\rm u.r}(\rho) - V(\theta_\infty)$. Since $V(\theta_\infty)$ is the only scale appearing in the problem, the mass-radius curve implied by Eq. (9.57) can be calculated once in units of $V(\theta_\infty)$, leading to the analog of Eq. (9.19) for the maximal mass star

$$M_{\rm max} \approx 1.05 M_\odot \left(\frac{(0.2\ \text{GeV})^4}{V(\theta_\infty)}\right)^{1/2} \quad \text{and} \quad R \approx 5.83\ \text{km}\left(\frac{(0.2\ \text{GeV})^4}{V(\theta_\infty)}\right)^{1/2} . \tag{9.58}$$

As expected, larger values of $V(\theta_\infty)$ make the EOS softer, resulting in lighter stars. In particular for the ALP model, $V(\theta_\infty) \approx 2\Lambda^4/g$ in the dark-green region as well as for $g > 1$. Thus, we find that

$$M_{\rm max} \approx (0.74 M_\odot)\sqrt{g}\left(\frac{0.2\ \text{GeV}}{\Lambda}\right)^2 \quad \text{and} \quad R \approx (4.1\ \text{km})\sqrt{g}\left(\frac{0.2\ \text{GeV}}{\Lambda}\right)^2 . \tag{9.59}$$

B Quadratic Coupling to Fermions

The next model we consider is a scalar field with a quadratic coupling to fermions [16],

$$m_*^{\rm Quad}(\phi) = m - \frac{1}{M}\phi^2\ , \quad V^{\rm Quad}(\phi) = \frac{1}{2}m_\phi^2\phi^2 + \frac{\lambda}{4}\phi^4. \tag{9.60}$$

[16] Note that in the $g \gg 1$ limit of the ALP model, the field excursion of θ are small ($\theta \ll 1$), the ALP model can be mapped to quadratic model with $m_\phi^2 = \Lambda^4/f^2$, $\lambda = -(\Lambda/f)^4/6$ and $M = 4f^2/(mg)$.

As appose to the ALP model where the scale f originates from the discrete shift symmetry of ϕ, in this model we have to freedom to choose f. One convenient choice is $f = \sqrt{mM}$, such that the mass and potential terms can be rewritten as

$$m_*^{\text{Quad}}(\theta) = m\left(1-\theta^2\right) \ , \quad V^{\text{Quad}}(\theta) = \frac{\Lambda^4}{g^2}\left(g\theta^2+\theta^4\right). \tag{9.61}$$

where

$$\Lambda \equiv \frac{m_\phi^4}{\lambda}, \qquad g \equiv \frac{2m_\phi^2}{\lambda m M}. \tag{9.62}$$

The microscopic EOS is determined by the EOM in the negligible gradient limit (see Eq. (9.9)), which in the quadratic model is given by

$$\left.\frac{\partial\Omega}{\partial\theta}\right|_{\mu=\text{const.}} = \frac{2\Lambda^4}{g^2}\left(g\theta+2\theta^3\right) - 2m\rho_s(\theta,\mu)\theta = 0\,. \tag{9.63}$$

As discussed in Sec. 9.1.1.A, in the high-density phase, θ asymptotically approaches the value θ_∞ for which $m_*(\theta_\infty)=0$, in this case $\theta_\infty = 1$ (due to our choice of f). The high-density phase is characterized by an approximately constant scalar density, see Eq. (9.13),

$$\rho_{s,\infty}^{\text{Quad}} = \frac{\Lambda^4}{g^2 m}(g+2) = \frac{1}{2}M(m_\phi^2+\lambda m M). \tag{9.64}$$

Focusing at this point on the effect of the scalar field on the heaviest stars, we proceed our analysis in the negligible gradient energy limit. As discussed in Sec. 9.1.2.A, this would allow us to find the maximal potential effect of the scalar field on the heaviest stars, since finite f effects would only tend to make the system more similar to a free Fermi gas.

Similar to the ALP model, the parameter space of this model is two dimensional and spanned by $\{g, \Lambda/m\}$. It can again be split into a CE region as well as a NGS region. In the NGS region, similar as in the ALP case, there is a metastable branch of normal matter and a stable branch of the new ground state. As oppose to the ALP case, it is more difficult in this model to provide an analytic equation which defines the NGS/CE regions (like Eq. (9.39)), therefore it must be calculated numerically. The problem is simpler in two parts of parameter space, which we dub the **mass domination** region ($g \gg 1$ or equivalently $\lambda \ll m_\phi^2/(mM)$) and the **quartic domination** region ($g \ll 1$ or equivalently $\lambda \gg m_\phi^2/(mM)$).

In each of these regions, the parameter space collapses to an effectively one-dimensional space, since only one combination of g and Λ/m appear in the theory, namely

$$c_{m_\phi}^{\text{Quad}} \equiv \frac{\Lambda^4}{g m^4} = \frac{M m_\phi^2}{2m^3} \quad \text{and} \quad c_\lambda^{\text{Quad}} \equiv \frac{\Lambda^4}{g^2 m^4} = \frac{\lambda M^2}{4m^2} \tag{9.65}$$

for the mass domination region and quartic domination region, respectively. $c_{m_\phi}^{\text{Quad}}$ and c_λ^{Quad} have a clear physical interpretation as the contribution of the scalar self-interactions $V(\theta_\infty)$ (in units of m^4) to ε and p in the high-density phase. The critical values, which separate the CE and NGS regions, were calculated numerically and are given by

$$c_{m_\phi}^{\text{Quad}} \lesssim 0.0093 \quad \text{and } c_\lambda^{\text{Quad}} \lesssim 0.015\,. \tag{9.66}$$

These upper bounds define the NGS region of parameter space for the mass domination region and quartic domination region, respectively, shown as dotted lines in Fig. 9.9. In the region $0.1 \lesssim g \lesssim 10$, the parameter space is two dimensional. The NGS-CE boundary was calculated numerically and is well-described by the following approximate expression

$$\log_{10}(\Lambda/m) = -0.05\log_{10}^2(g) + 0.35\log_{10}(g) - 0.6\,. \tag{9.67}$$

This is shown in Fig 9.9 as a dashed line.

NGS Region

Far enough from the CE-NGS boundary, the *entire* NGS parameter space (even the region where $g \sim O(1)$), can be reduced to an effective one-dimensional space. As oppose to the ALP model, in the quadratic model the NGS is always ultra-relativistic with an approximately-constant $\theta \approx \theta_\infty$[17]. As discussed in Sec. 9.1.2.A in the context of the ALP model, this means that the only dimensionful parameter appearing in the problem is the approximately constant $V(\theta_\infty)$. Therefore, the scaling of Eq. (9.58) can be used to determined the heaviest star mass and radius with

$$V^{\rm Quad}(\theta_\infty) = \frac{\Lambda^4}{g^2}\,(g+1) = m^4(c_{m_\phi}^{\rm Quad} + c_\lambda^{\rm Quad})\,, \tag{9.68}$$

which is shown in the right panel of Fig. 9.9. In this same region of parameter space, namely sufficiently far away from the CE-NGS boundary line, one can also find analytic expressions for $\rho^{\rm NGS}$ and $\varepsilon^{\rm NGS}$,

$$\rho^{\rm NGS} \approx \left(\frac{64}{3\pi}\right)^{1/4} (V^{\rm Quad}(\theta_\infty))^{3/4}\,, \quad \varepsilon^{\rm NGS} \approx 4V^{\rm Quad}(\theta_\infty). \tag{9.69}$$

CE Region

In the rest of the parameter space, the CE region, the EOS has one stable branch describing a phase transition. As before, analytic approximations for θ_c and μ_c can be found assuming the transition is from a non-relativistic $\theta = 0$ phase to a relativistic $\theta = \theta_c^{\rm CE}$ phase. This is done by solving $\rho_s(\theta_c^{\rm CE}, \mu_c^{\rm CE}) = \left.\frac{\frac{\partial V}{\partial\theta}}{\frac{\partial m}{\partial\theta}}\right|_{\theta_c^{\rm CE}}$ and $p(0,\mu_c^{\rm CE}) = p(\theta_c^{\rm CE}, \mu_c^{\rm CE})$ with the appropriate analytical approximations.

C Linear Coupling to Fermions

The last model we investigate is a scalar which couples linearly to fermions,

$$m^{\rm Lin}(\phi) = m - g_S\phi\ , \quad V^{\rm Lin}(\phi) = \frac{1}{2}m_\phi^2\phi^2 + \frac{\lambda}{4}\phi^4. \tag{9.70}$$

This gives us after rescaling $\phi \to \theta f$

$$\theta_\infty^{\rm LIN} = \frac{m}{f g_S}. \tag{9.71}$$

Due to fifth force bounds it is enough to go to the limit of mass domination to conclude that this model does not have an interesting phenomenology with O(1) changes in the structure of

[17] There are $O(1)$ deviations from this approximation near the CE-NGS boundary, but the approximation is valid away from the boundary.

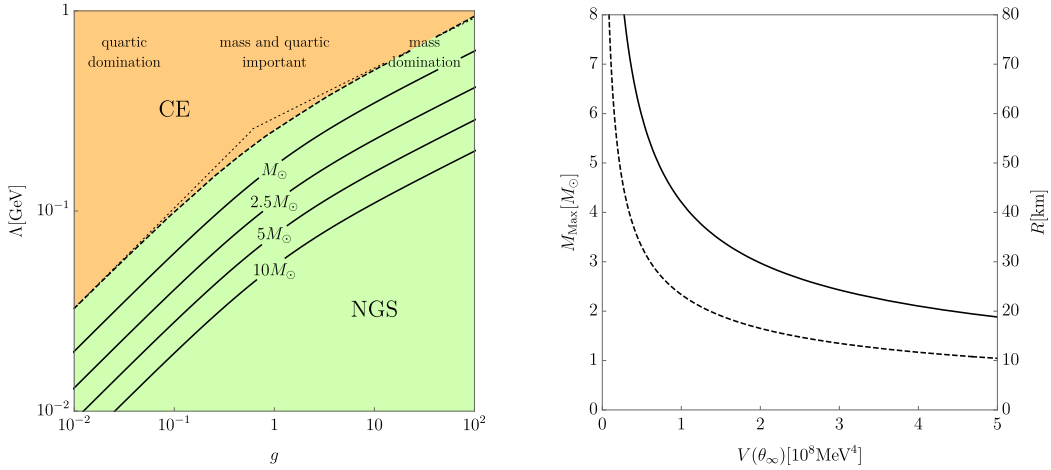

Figure 9.9: Left: Parameter space of the quadratic model. CE region in orange vs NGS region in green (from full numerical analysis). Black-dashed: the transition between NGS and CE assuming mass and quartic domination. Black: contours of maximal mass, for clarity only up to $10M_\odot$. Right: Maximal mass (solid) and radius of the maximal mass star (dashed) over $V(\theta_\infty)$.

dense stars. To show this, let us remind ourselves that for a fixed mass having a sizeable quartic can only soften the equation of state, see Eqs. (9.17), (9.57). Therefore, from now on we set $\lambda = 0$, to see the effects of the stiffest EOS that is possible consistent with fifth force bounds. The stellar structure of this model with $\lambda = 0$ was recently investigated [247]. In the following we re-derive some of the results and apply fifth force bounds on them.
We again take the limit of negligible gradient, which corresponds to

$$R \gg \frac{f}{\sqrt{\rho_s \frac{\partial m_*(\theta)}{\partial \theta}}} \approx \frac{1}{m_\phi}, \tag{9.72}$$

where we used that in medium $\rho_s \approx \rho_{s,\infty}$. As the rescaling constant f is arbitrary, we find that the parameter space is again one dimensional and given by

$$c^{\rm LIN} = \frac{1}{2}\frac{m_\phi^2}{m^2 g_S^2}. \tag{9.73}$$

Determining numerically the value of $c^{\rm LIN}$ at which the transition from the CE region to the NGS takes place gives $c^{\rm LIN}_{\rm crit} \approx 0.014$. In Fig. 9.10, we show this transition between the NGS and the CE region in black in comparison with current fifth force bounds taken from [248].

Close to the transition between CE and NGS, we expect $R \sim R_{NS}$. In contrast, deep inside the NGS, the EOS is again leading to $R_{\rm max} \approx \sqrt{\frac{c_{\rm crit}}{c}} R_{c_{\rm crit}} \sim O(1)\sqrt{\frac{c_{\rm crit}}{c}} R_{\rm NS}$. Together with (9.72) and the parametric estimate $R_{NS} \sim \frac{M_p}{m^2}$, this implies that the negligible gradient approximation is valid for $g_S \gg O(10)\frac{m}{M_p}$. The region where approximation becomes worse is shown in yellow, while in the red region for the gradient is too strong s.t. the field cannot move far and the new scalar has negligible effect on the structure of neutron stars. The fact that a non-negligible λ generically softens the EOS and therefore needs larger couplings g_S to be at the boundary between NGS and CE is indicated by a black arrow. All of the NGS parameter space is excluded from fifth force bounds. Assuming that these fifth force bounds somehow can be circumvented, the details of the EOS and stellar structure in this model have recently been worked out in [247].

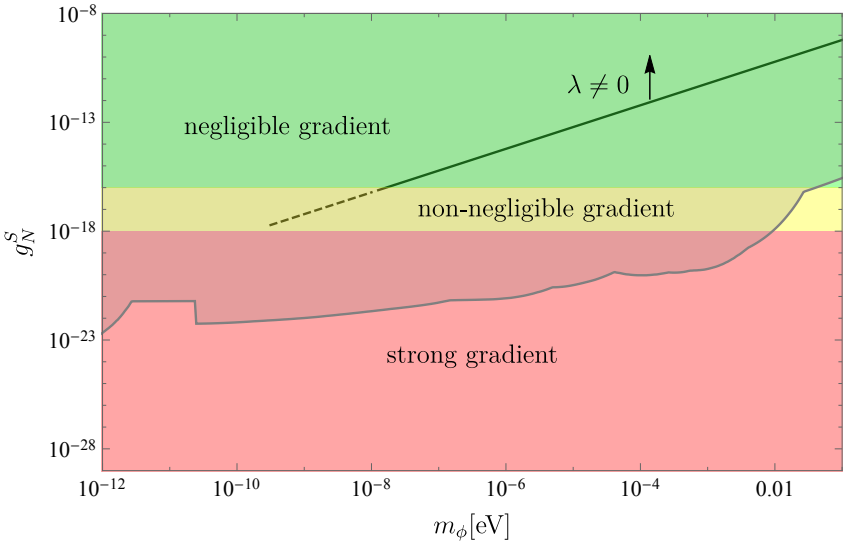

Figure 9.10: Parameter space of the linear model. In black the transition between the NGS (above) and the CE region (below). The little arrow indicates that this lines move above for non-zero λ. In the green region, the negligible gradient approximation is valid, while in yellow we should take the gradient into account and in red the field barely moves because of the strong gradient. The shaded region is excluded by fifth force experiment, taken from [248], leading to the conclusion that all interesting parameter space is excluded.

9.1.3 Conclusions

In the above section we demonstrated a novel mechanism to increase the mass of neutron stars. The mechanism relies on a new scalar field that is coupled to the mass of neutrons. We showed that if the scalar is coupled linearly, the interesting parameter space is ruled out by fifth force experiments, however if coupled quadratically, or, like the QCD axion, with a cosine, this coupling is poorly constrained. This leads to the freedom to enhance the mass of neutron stars by up to an order of magnitude. This is an especially interesting in light of future NS mergers expected to be seen in LIGO and the increasingly larger stellar remnant catalog [120–122].

9.2 White Dwarfs as a Probe of Light QCD Axions

So far in this Chapter due to their high density, we have focussed on how light scalars can affect neutrons stars and their structure. A particularly clean and well studied example of stellar remnants however are white dwarfs. The modifications of the white dwarf M - R relationship allow us to directly probe large regions in the light QCD axion parameter space. The reasoning is the following: While a free Fermi gas of electrons with nuclei following them due to charge neutrality describes WDs reasonably well, large deviations thereof are not consistent with astrophysical data. We have reviewed the free Fermi gas EOS for a white dwarf in Sec. 6.

9.2.1 New Ground State: The Axion WD System

In the presence of the axion the complete system as above is described by the Lagrangian

$$\mathcal{L} = \sqrt{-g}\left(\frac{1}{16\pi G}R + \mathcal{L}_{\psi\phi} + \mathcal{L}_{\phi}\right), \tag{9.74}$$

where $R = R^{\mu}{}_{\mu}$ is the trace over the Ricci tensor, and $\mathcal{L}_{\psi\phi}$ and $\mathcal{L}_{\phi}$ are the Lagrangians describing the interaction of nuclei with the axion and the axion self-interaction respectively, given by

$$\mathcal{L}_{\psi\phi} = \bar{\psi}\left[ig^{\mu\nu}\gamma_{\mu}D_{\nu} - m^{*}_{\psi}(\phi)\right]\psi, \tag{9.75}$$

$$\mathcal{L}_{\phi} = \frac{1}{2}g^{\mu\nu}(\partial_{\mu}\phi)(\partial_{\nu}\phi) - V(\phi). \tag{9.76}$$

Here the axion potential is given by

$$V(\phi) = -\epsilon\, m_{\pi}^{2} f_{\pi}^{2}\left(\sqrt{1 - \frac{4m_u m_d}{(m_u+m_d)^2}\sin^2\left(\frac{\phi}{2f}\right)} - 1\right), \tag{9.77}$$

and we consider the scenario that the axion couples isospin symmetric, such that the effective mass of the nuclei is related to the effective nucleon mass $m^{*}_{\psi}(\phi) = 2m^{*}_{N}(\phi)$ and we have

$$m^{*}_{N}(\phi) = m_N - \sigma_N\left(1 - \sqrt{1 - \frac{4m_u m_d}{(m_u+m_d)^2}}\right). \tag{9.78}$$

As above, the gravitational field is sourced by an energy-stress tensor, consisting of two terms

$$T_{\mu\nu} = T^{\psi\phi}_{\mu\nu} + T^{\mathrm{grad}}_{\mu\nu}. \tag{9.79}$$

The first term contains the gas of charged nuclei with ϕ-dependent effective mass, the Fermi gas of electrons, the axion self-interaction and takes the form of an ideal fluid, $T^{\psi\phi}_{\mu\nu} = \mathrm{diag}\,(p, \varepsilon, \varepsilon, \varepsilon)$, with

$$p(\phi,\rho) = \frac{2}{3}\int_0^{k_F(\rho)} \frac{\mathrm{d}^3k}{(2\pi)^3}\frac{k^2}{\sqrt{k^2+m_e^2}} - V(\phi), \tag{9.80}$$

$$\varepsilon(\phi,\rho) = 2\int_0^{k_F(\rho)} \frac{\mathrm{d}^3k}{(2\pi)^3}\sqrt{k^2 + (m^{*}_{\psi}(\phi))^2} + V(\phi), \tag{9.81}$$

where we neglected the sub-leading contributions for pressure and energy density, $\varepsilon_e(\rho) \simeq 0 \simeq p_{\psi}(\phi,\rho)$, respectively. The second term in Eq. (9.79) contains the contribution of the axion gradient

$$(T^{\mathrm{grad}})^{\mu}{}_{\nu} = \frac{(\phi')^2}{2}\left[1 - \frac{2GM}{r}\right](\delta^{\mu}_{\nu} - 2\delta^{\mu}_{r}\delta^{r}_{\nu}). \tag{9.82}$$

Minimizing the action, we find the following set of coupled first- and second order differential equations

$$\phi''\left[1 - \frac{2GM}{r}\right] + \frac{2}{r}\phi'\left[1 - \frac{GM}{r} - 2\pi G r^2(\varepsilon - p)\right] = \frac{\partial V}{\partial\phi} + \rho\frac{\partial m^{*}_{\psi}(\phi)}{\partial\phi} \equiv U(\phi,\rho), \tag{9.83a}$$

$$p' = -\frac{GM\varepsilon}{r^2}\left[1 + \frac{p}{\varepsilon}\right]\left[1 - \frac{2GM}{r}\right]^{-1}\left[1 + \frac{4\pi r^3}{M}\left(p + \frac{(\phi')^2}{2}\left[1 - \frac{2GM}{r}\right]\right)\right] - \phi' U(\phi,\rho), \tag{9.83b}$$

$$M' = 4\pi r^2\left[\varepsilon + \frac{1}{2}\left[1 - \frac{2GM}{r}\right](\phi')^2\right]. \tag{9.83c}$$

Eq. (9.83a) is the static axion equation of motion coupled to gravity, while Eq. (9.83b) and Eq. (9.83c) are the TOV equations in the presence of an axion. Since the nuclei are, even at the highest densities accessible in white dwarfs, non-relativistic, we set $\langle\bar{\psi}\psi\rangle \simeq \rho$.

Note that, in the limit $\phi = 0$ we recover the ordinary TOV equations, see Eq. (6.1). This set of equations can be integrated numerically using the shooting method. Although this is the way we solve the system at very high f, we can again go to the limit in which these equations simplify dramatically.

The displacement of the axion at sufficiently high densities costs gradient energy and can only occur if the gain in potential energy pays up for it. This leads to the typical scale on which the axion is displaced

$$\lambda_\phi \simeq \frac{\pi f}{\sqrt{2\delta m_N \rho - V(\pi f)}}, \tag{9.84}$$

and is to be evaluated at typical white dwarf densities. Importantly, if we have $R_{\rm WD} \gg \lambda_\phi$, the field essentially tracks the minimum of the effective in density potential on stellar scales and is given by the solution to

$$U(\phi, \rho) = 0. \tag{9.85}$$

At the same time, the gradient terms in Eq. (9.83b) and Eq. (9.83c) are confined to a small transition shell, where the field does not follow its minimum. Therefore, if we consider large systems we can neglect the axion gradient $\phi' \simeq 0$. As a result, the set of equations, Eq. (9.83), decouples to give the regular TOV equations, Eq. (6.1), in addition to Eq. (9.85). Note that the latter is the same condition as the minimization of the energy density $\varepsilon(\phi, \rho)$ with respect to ϕ. Solutions, $\phi(\rho)$, to this equation give thermodynamic stable EOS which we eventually use to solve the regular TOV equations.

Most interestingly, we find that if the axion is destabilized in a white dwarf, the energy per particle of the light nuclei $E^n_\psi(\rho) = \varepsilon(\rho)/\rho$ is not anymore minimized when the nuclei are infinitely separated, but at the new ground state density ρ^*, which can be found numerically.

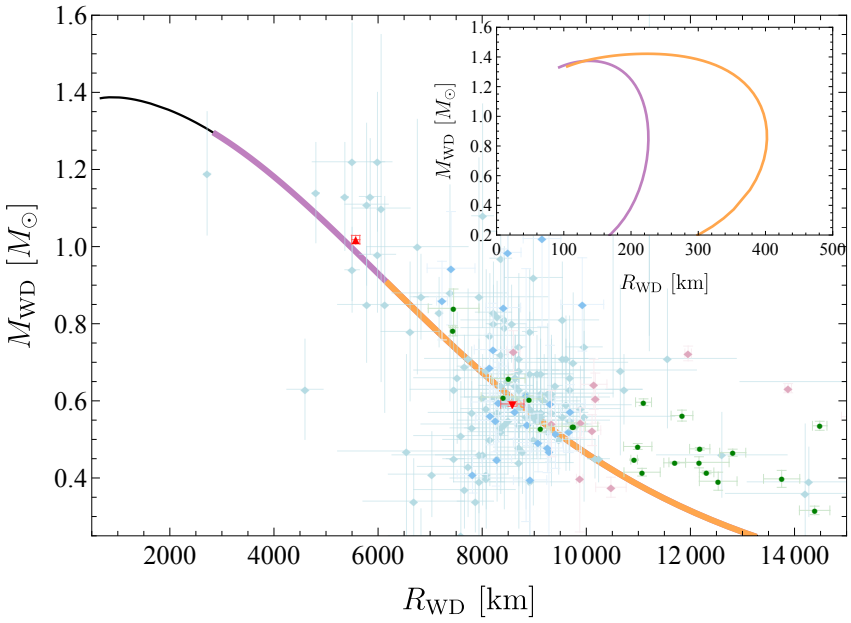

Figure 9.11: White dwarf M-R relation with light axions. Free Fermi gas electrons with nuclei as a source of mass (black) and meta-stable branches following the white dwarf line, for $\epsilon = 10^{-6}$ (purple) and $\epsilon = 10^{-7}$ (orange). Corresponding new ground state phases have much smaller radii and are shown in the inset. Data points are taken from [249] (turquoise), [250] (blue), [251, 252] (red) and [253] (green).

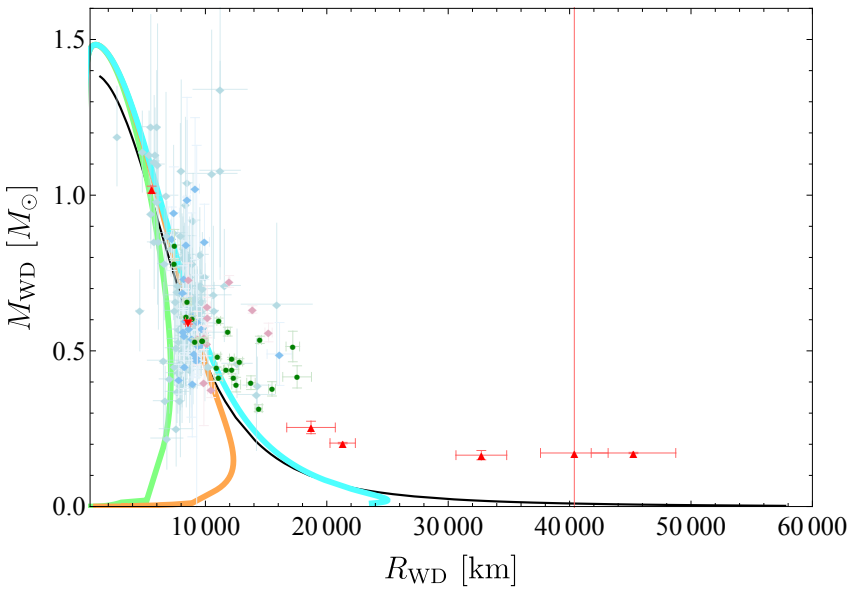

Figure 9.12: The lowest ε that can still be excluded from the existence of extremely low mass white dwarfs. In cyan is $\varepsilon = 10^{-18}$, in orange $\varepsilon = 10^{-15}$, in green $\varepsilon = 10^{-13}$. The black line is again the free Fermi gas.

In contrast to neutron stars, for light axions in white dwarfs there is no coexistence region. Note that the density of the new ground state is always larger than the density at which the destabilisation happens, $\rho^* > \rho_c \equiv \epsilon\, m_\pi^2 f_\pi^2 / 2\sigma_N$.

Again, for low densities $\rho < \rho_c$, nuclear matter is in a meta-stable state where the classical sourcing of the axion is not accessible. Once the axion is sourced there exists a range $\rho_c < \rho < \rho^*$, where the energy per particle decreases $\partial_\rho E^n_\psi(\rho) < 0$, implying a negative pressure, which can be understood as a completely unstable phase in which the system is contracting until it stabilizes in the phase of the new ground state.

Note that the above discussion is only valid for $R_{\rm WD} \gg \lambda_\phi$. For $R_{\rm WD} \sim \lambda_\phi$ we solve the full coupled system numerically. However, in the opposite limit, $R_{\rm WD} \ll \lambda_\phi$, the behaviour can again easily be qualitatively understood: the gradient is so strong that the field cannot move away from it's in-vacuum minimum any more and therefore has no influence on the structure of white dwarfs.

9.2.2 Confrontation with Observational Data

There exist large data-sets containing masses and radii of white dwarfs (see e.g. [249–260]). However, not all of these data-sets can be used to probe the M - R relationship: in many catalogs, (see [254–258]), the M - R relation is in fact used as an input to significantly reduce observational error. On the other hand there exist sets (e.g. [249–253, 259, 260]) that systematically test the M - R relation using observational data.

Note, that there is a slight difference in model dependence: while in [253] the determination of the mass and radius is completely independent of white dwarf models, most other works use an atmosphere model to determine the radius. Nevertheless, we combine the data-sets [249–253] and show them in Fig. 9.11. Since the most massive white dwarfs set the most stringent limits on the axion, we exclude all points in the axion parameter space that cannot predict a white dwarf with masses higher than around $\sim 0.9\, M_\odot$ on the meta-stable branch. For $R_{\rm WD} \gg \lambda_\phi$,

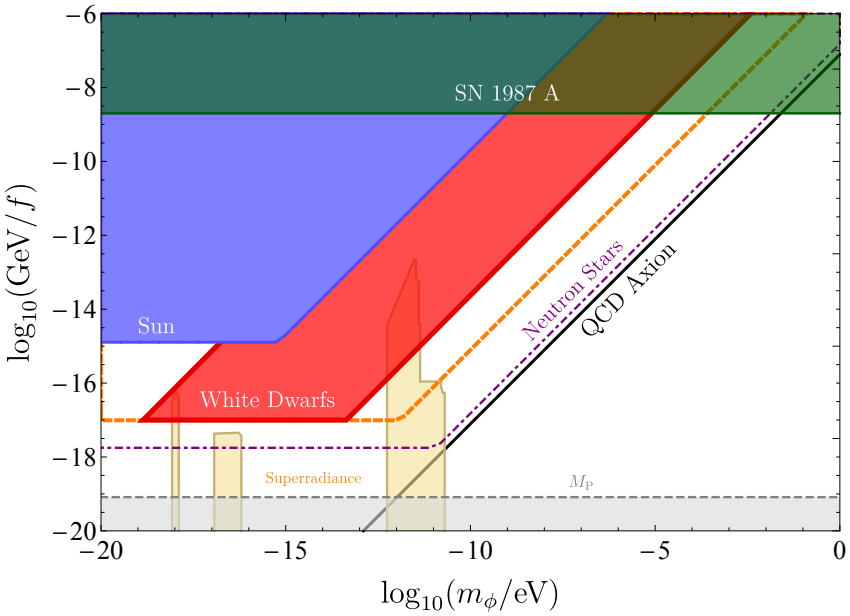

Figure 9.13: Constraints and future projections on the axion parameter space. Exclusions from modifications of the white dwarf M - R relation are shown in red. More precise measurements thereof can further probe the parameter space until the orange dashed line. The solid black line shows the QCD axion with $m_\phi f = m_\pi f_\pi$. Gravity suggests $f \lesssim M_\mathrm{P}$ (gray). Further bounds originate from the sourcing in the Sun [119] (blue), the supernova 1987A (green) and BH superradiance [264] (yellow). Finally, we show which parameters lead to a new ground state accessible in neutron stars (dot-dashed purple).

this translates to an exclusion of all $\epsilon \lesssim 10^{-7}$, as shown inFig. 9.13. For larger f, i.e. larger λ_ϕ, we use solutions of the coupled system, Eq. 9.83, to place the corresponding bounds. This is still ongoing work and the exclusion limit presented here is based on the $f \to 0$ limit. The robustness of this bound against the influence of finite temperature modification of the EOS is discussed in Appendix II.C.2. Note that for very small $\varepsilon \lesssim 10^{-13}$, the metastable branch follows the free Fermi gas for most of the data-points in Fig. 9.12. However, there also exist measurements of extremely low mass white dwarfs [261–263], which exclude all $\varepsilon \gtrsim 10^{-18}$. For even smaller ε, while the axion is sourced in white dwarfs, the structure of with dwarfs in the region where we measured then only has small modifications.

9.2.3 Conclusions

The mass-radius relation of white dwarfs is well understood and has been tested with increasing accuracy in the last years. We have shown how light QCD axions change the structure of white dwarfs. We used existing data of white dwarf masses and radii to place novel bounds on light QCD axions.

The QCD axion generically predicts a non-derivative coupling to nucleons. At finite baryon density this coupling can lead to a destabilization of the axion from its in-vacuum minimum. If sourced, the non-zero axion expectation value changes the mass of nucleons. For a large region of the parameter space, this leads to a new ground state of nuclear matter, which has less energy per particle than infinitely separated nucleons. If accessible in white dwarfs, this drastically changes their mass-radius relation.

More precise tests of the white dwarf mass-radius relation using the recent Gaia DR3 are expected in the near future and will further probe the parameter space of light QCD axions.

Appendices part II

II.A Axion Couplings at Finite Density

In this appendix we first construct the necessary Lagrangian used above and then explicitly calculate some of the integrals of Sec. 7.2 analytically and investigate numerically the effect of finite temperature on the axion nucleon couplings.

II.A.1 Construction of the Lagrangian

As we have seen in the main text, we need the Lagrangian up to $\nu = 1$ in order to calculate the leading density contributions. For the explicit construction we closely follow [265]. In general every term in the πN Lagrangian can be written as

$$\bar{\mathcal{N}} A^{\mu\nu\cdots} \Theta_{\mu\nu\ldots} \mathcal{N} + \text{ h.c.}, \tag{II.A.1}$$

where $A^{\mu\nu\cdots}$ describes the fields and covariant derivatives acting on them, $\Theta_{\mu\nu\ldots}$ is an element of the Clifford algebra times a symmetrized product of covariant derivatives of the form

$$\Theta_{\mu\nu\ldots\alpha\beta\ldots} = \Gamma_{\mu\nu\ldots} D^n_{\alpha\beta\ldots}, \tag{II.A.2}$$

with $D^n_{\alpha\beta\ldots\omega} = \{D_\alpha, \{D_\beta, \{\ldots, D_\omega\}\}\}$. The fields that act as our building block have been defined above. They are

$$u_\mu,\ \hat{u}_\mu,\ \chi_\pm, \tag{II.A.3}$$

as well as combinations and derivatives thereof. In addition to the chiral symmetry, we require all the terms in the Lagrangian to be hermitian and invariant under parity (P) and charge conjugation (C). Thus we have to figure out first the fields $A^{\mu\nu\cdots}$ and the algebra element $\Theta_{\mu\nu\ldots}$ transform under those transformation. We define the constant h_A, h_Γ, c_A and c_Γ according to

$$A^\dagger = (-1)^{h_A} A, \quad A^c = (-1)^{c_A} A^T, \tag{II.A.4}$$

$$\Gamma^\dagger = (-1)^{h_\Gamma} \gamma^0 \Gamma \gamma^0, \quad \Gamma^c = (-1)^{c_\Gamma} \Gamma^T. \tag{II.A.5}$$

Taking a general term of the πN Lagrangian plus its hermitian conjugate we thus find

$$\bar{\mathcal{N}} A^{\mu\nu\ldots\alpha\beta\ldots} \Gamma_{\mu\nu\ldots} D^n_{\alpha\beta\ldots} \mathcal{N} + (-1)^{h_A + h_\Gamma} \bar{\mathcal{N}} \overleftarrow{D}^n_{\alpha\beta\ldots} \Gamma_{\mu\nu\ldots} A^{\mu\nu\ldots\alpha\beta} \mathcal{N}. \tag{II.A.6}$$

After partial integration this gives up to higher order terms

$$\bar{\mathcal{N}} A^{\mu\nu\ldots\alpha\beta\ldots} \Gamma_{\mu\nu\ldots} D^n_{\alpha\beta\ldots} \mathcal{N} + (-1)^{h_A + h_\Gamma + n} \bar{\mathcal{N}} A^{\mu\nu\ldots\alpha\beta\ldots} \Gamma_{\mu\nu\ldots} D^n_{\alpha\beta\ldots} \mathcal{N}. \tag{II.A.7}$$

The same can be shown for charge conjugation up to higher order terms

$$\bar{\mathcal{N}} A^{\mu\nu\ldots\alpha\beta\ldots} \Gamma_{\mu\nu\ldots} D^n_{\alpha\beta\ldots} \mathcal{N} + (-1)^{c_A + c_\Gamma + n} \bar{\mathcal{N}} A^{\mu\nu\ldots\alpha\beta\ldots} \Gamma_{\mu\nu\ldots} D^n_{\alpha\beta\ldots} \mathcal{N}. \tag{II.A.8}$$

Defining $h_\Theta = h_\Gamma + n$, $c_\Theta = c_\Gamma + n$, we see that for the terms invariant under (C) and hermitian conjugation the constants fulfil

$$(-1)^{h_A+h_\Theta} = 1, \quad (-1)^{c_A+c_\Theta} = 1. \tag{II.A.9}$$

Further one can use the equations of motion at leading order and make the substitution

$$\not{D}\mathcal{N} \to -im\mathcal{N} \tag{II.A.10}$$

This is used in [265] to eliminate many of the possible Clifford algebra elements. We will not do this here in detail, we just give a brief example and the main results needed for our construction. Using the equations of motion we find for example

$$\bar{\mathcal{N}} A^\mu i D_\mu \mathcal{N} + \text{h.c.} \doteq 2m\bar{\mathcal{N}}\gamma_\mu A^\mu \mathcal{N}, \tag{II.A.11}$$

where $\doteq$ means up to higher order terms. Therefore we do not need to take the structure $\gamma_\mu A^\mu$ into account, just $A^\mu D_\mu$ has to be included. Similar relations can be derived for all the other terms too. In [265] the following set of $\Theta_{\mu\nu\ldots}$ has been found to be sufficient to generate the complete chiral Lagrangian up to fourth order:

$$\begin{aligned}
&1;\\
&\gamma_5\gamma_\mu,\ D_\mu;\\
&g_{\mu\nu},\ \sigma_{\mu\nu},\ \gamma_5\gamma_\mu D_\nu,\ D_{\mu\nu};\\
&g_{\mu\nu}\gamma_5\gamma_\rho,\ g_{\mu\nu}D_\rho,\ \sigma_{\mu\nu}D_\rho,\ \varepsilon^\lambda_{\mu\nu\rho}D_\lambda,\ \gamma_5\gamma_\mu D_{\nu\rho}, D_{\mu\nu\rho};\\
&g_{\mu\nu}g_{\rho\tau},\ \varepsilon_{\mu\nu\rho\tau},\ g_{\mu\nu}\sigma_{\rho\tau},\ g_{\mu\nu}\gamma_5\gamma_\rho D_\tau,\ g_{\mu\nu}D_{\rho\tau},\ \sigma_{\mu\nu}D_{\rho\tau},\ \varepsilon^\lambda_{\mu\nu\rho}D_{\lambda\tau},\ \gamma_5\gamma_\mu D_{\nu\rho\tau},\ D_{\mu\nu\rho\tau}.
\end{aligned} \tag{II.A.12}$$

We aim to derive the Lagrangian up to $\mathcal{O}(p^2)$. Since our building blocks u_μ and $\hat{u}_\mu$ have chiral dimension one, we need them up to quadratic order contracted with the building blocks in (II.A.12) up to two indices. For those the transformation properties are listed in table II.A.1. One can also derive the transformation properties under C and P symmetry for u_μ and $\hat{u}_\mu$. One has to use that under charge conjugation $u \to u^\top$ and under parity transformation $u \to u^\dagger$. This is obvious if we reinstate the pions: for charge conjugation the π^+ and the π^- field are exchanged, which is exactly what the transpose of the isospin matrices does [18]. The axion field is invariant under charge conjugation and under parity it behaves like $a \to -a$ [19]. From these properties it is straightforward to derive the transformation of u_μ and $\hat{u}_\mu$ and combinations of them. In the same way one can calculate the transformation properties of $\chi_\pm$. One has to be careful when it comes to the building blocks: we have to treat isovector and isoscalar fields differently. For u_μ and $\hat{u}_\mu$ this is taken care of by the fact that u_μ just contains isovector and

[18] This can also be seen by using the covariant derivative with the photon field acting in the pion field defined by $D_\mu U = \partial_\mu U - \frac{ie}{2f_\pi} A_\mu [\tau_3, U] = \partial_\mu U + \frac{e}{f_\pi} A_\mu \tau_a \epsilon_{a3b} \pi_b$. The EOM's for the pion fields under the exchange of $e \to -e$ are exactly satisfied by $U^\top$.

[19] In general one can determine the transformation properties of the external fields by requiring the invariance of equation (5.18) under C and P symmetry. Doing so one finds

$$v_\mu \overset{P}{\mapsto} v_\mu, \quad v_\mu^{(s)} \overset{P}{\mapsto} v_\mu^{(s)}, \quad a_\mu \overset{P}{\mapsto} -a_\mu, \quad a_\mu^{(s)} \overset{P}{\mapsto} -a_\mu^{(s)}, \quad s \overset{P}{\mapsto} s, \quad p \overset{P}{\mapsto} -p, \tag{II.A.13}$$

$$v_\mu \overset{C}{\to} -v_\mu^T, \quad v_\mu^{(s)} \overset{C}{\to} -v_\mu^{(s)T}, \quad a_\mu \overset{C}{\to} a_\mu^T, \quad a_\mu^{(s)} \overset{C}{\to} a_\mu^{(s)T}, \quad s, p \overset{C}{\to} s^T, p^T, \tag{II.A.14}$$

up to transformations of the space-time indices for P symmetry with a matrix P^μ_ν which are irrelevant for us since we will always contract them in order for the Lagrangian to be Lorentz invariant.

$\hat{u}_\mu$ just isoscalar fields. For $\chi_\pm$ and all other (composite) fields we have to take care about this manually. We do so by defining

$$\widetilde{X} = X - \frac{1}{2}\langle X\rangle, \tag{II.A.15}$$

where $\langle\ldots\rangle$ stand for the trace in flavour space. Using this definition for example the anticommutator of two u_μ's can be written as

$$\{u_\mu, u_\nu\} = \langle u_\mu u_\nu\rangle \mathbf{1}. \tag{II.A.16}$$

More importantly the fields $\chi_\pm$ can be decomposed into $\tilde{\chi}_\pm$ and $\langle\chi_\pm\rangle$, where in $\tilde{\chi}_\pm$ the isoscalar part of $\chi_\pm$. The fields decomposed in isoscalar and vector part are the ones we consider as building blocks for the chiral Lagrangian.

The nucleon field $\mathcal{N}$ and its adjoint transform under charge and parity according to

$$\begin{aligned} &\mathcal{N} \xrightarrow{\mathrm{C}} C\bar{\mathcal{N}}^\top, \quad \bar{\mathcal{N}} \xrightarrow{\mathrm{C}} \mathcal{N}^\top C, \quad C = i\gamma^2\gamma^0, \\ &\mathcal{N} \xrightarrow{\mathrm{P}} i\gamma^0\mathcal{N}, \quad \bar{\mathcal{N}} \xrightarrow{\mathrm{P}} -i\bar{\mathcal{N}}\gamma^0. \end{aligned} \tag{II.A.17}$$

The resulting properties are listed in table II.A.2 The signs in table II.A.1 and table II.A.2 are define by the prefactors after transformation i.e.

$$\begin{aligned} &\bar{\mathcal{N}}\Theta_{\mu\nu\ldots}\mathcal{N} \xrightarrow{\mathrm{P}} (\pm 1) P^\alpha_\mu P^\beta_\nu \ldots \bar{\mathcal{N}}\Theta_{\alpha\beta\ldots}\mathcal{N}, \\ &\bar{\mathcal{N}}\Theta_{\mu\nu\ldots}\mathcal{N} \xrightarrow{\mathrm{C}} (\pm 1)\left(\bar{\mathcal{N}}\Theta_{\mu\nu\ldots}\mathcal{N}\right)^\top = (\pm 1)\bar{\mathcal{N}}\Theta_{\mu\nu\ldots}\mathcal{N}, \\ &A^{\mu\nu\ldots} \xrightarrow{\mathrm{P}} (\pm 1) P^\mu_\alpha P^\nu_\beta A^{\alpha\beta\ldots}, \\ &A^{\mu\nu\ldots} \xrightarrow{\mathrm{C}} (\pm 1)\left(A^{\mu\nu\ldots}\right)^\top, \end{aligned} \tag{II.A.18}$$

with $P^\mu_\nu = diag(1,-1,-1,-1)$. Since all Lorentz indices are contracted in the Lagrangian, the P^μ_ν's will drop out anyway. Note that the gamma matrices and all other objects that are not fields do not transform under charge or parity transformation, the only thing that transforms are their space-time indices. The signs of table II.A.1 are induced by the transformations of the fields according to equations (II.A.17) and (II.A.18). For table II.A.2 we need to take into account the transformation properties of all the operators they contain. Note that the signs we write in tables II.A.1 and II.A.2 for parity are given in terms of the definitions (II.A.4) and (II.A.5) by $(-1)^{c_\Theta}$ and $(-1)^{c_A}$. The chiral dimension of the fields and operators can also be

$\Theta_{\mu\nu\ldots}$	1	γ_5	γ_μ	$\gamma_\mu\gamma_5$	$\sigma_{\mu\nu}$	$g_{\mu\nu}$	$\varepsilon_{\lambda\mu\nu\rho}$	D_μ	$\gamma_5\gamma_\mu D_\nu$	$D_{\mu\nu}$
chiral dimension	0	1	0	0	0	0	0	0	0	0
parity	+	−	+	−	+	+	−	+	−	+
charge conjugation	+	+	−	+	−	+	+	−	−	+

Table II.A.1: Transformation properties of different operators $\Theta_{\mu\nu\ldots}$.

found in table II.A.1 and II.A.2. They are given by the number of derivatives acting on the fields (except the nucleon fields) and pion mass insertions. The chiral dimension of γ^5 is special. It is one because the projection to ChPT does not give a leading order (chiral dimension 0) term, but instead the lowest order term generated by it is of chiral dimension 1.

$A^{\mu\nu\ldots}$	u_μ	$\hat{u}_\mu$	$[u_\mu, u_\nu]$	$\{u_\mu, u_\nu\}$	$u_\mu \hat{u}_\nu$	$\tilde{\chi}_+$	$\tilde{\chi}_-$	$\langle \chi_+ \rangle$	$\langle \chi_- \rangle$
chiral dimension	1	1	2	2	2	2	2	2	2
parity	$-$	$-$	$+$	$+$	$+$	$+$	$-$	$+$	$-$
charge conjugation	$+$	$+$	$-$	$+$	$+$	$+$	$+$	$+$	$+$

Table II.A.2: Transformation properties of different fields $A^{\mu\nu\cdots}$ needed for the construction.

We pick one example from each table and show it explicitly here. Let us take $\gamma_\mu\gamma_5$ and find

$$\begin{aligned}
\bar{\mathcal{N}}\gamma_\mu\gamma_5\mathcal{N} &\xrightarrow{\mathrm{P}} -i\bar{\mathcal{N}}\gamma^0\gamma_\mu\gamma_5 i\gamma^0\mathcal{N} \\
&= \bar{\mathcal{N}}\gamma^0\gamma_\mu\gamma_5\gamma^0\mathcal{N} \\
&= -\bar{\mathcal{N}}\gamma^0\gamma_\mu\gamma^0\gamma_5\mathcal{N} \\
&= -\bar{\mathcal{N}}\gamma_\mu^\dagger\gamma_5\mathcal{N} \\
&= -P_\mu^\alpha\bar{\mathcal{N}}\gamma_\alpha\gamma_5\mathcal{N},
\end{aligned} \tag{II.A.19}$$

thus it has $(-)$ parity. For the charge conjugation we find

$$\begin{aligned}
\bar{\mathcal{N}}\gamma_\mu\gamma_5\mathcal{N} &\xrightarrow{\mathrm{C}} \mathcal{N}^\top C\gamma_\mu\gamma_5 C\bar{\mathcal{N}}^\top \\
&= -\mathcal{N}^\top C\gamma_\mu\gamma_5 C^{-1}\bar{\mathcal{N}}^\top \\
&= -\mathcal{N}^\top C\gamma_\mu C^{-1}C\gamma_5 C^{-1}\bar{\mathcal{N}}^\top \\
&= \mathcal{N}^\top(\gamma_\mu)^\top(\gamma_5)^\top\bar{\mathcal{N}}^\top \\
&= -(\bar{\mathcal{N}}\gamma_5\gamma_\mu\mathcal{N})^\top \\
&= (\bar{\mathcal{N}}\gamma_\mu\gamma_5\mathcal{N})^\top \\
&= \bar{\mathcal{N}}\gamma_\mu\gamma_5\mathcal{N},
\end{aligned} \tag{II.A.20}$$

where the minus sign in the penultimate lines comes from the fact that we have to commute the fermion fields,which are antisymmetric. Next we show the transformation properties of u_μ.

$$\begin{aligned}
u_\mu &= iu^\dagger\partial_\mu u - iu\partial_\mu u^\dagger + u^\dagger a_\mu u + ua_\mu u^\dagger \\
&\xrightarrow{\mathrm{P}} P_\mu^\alpha\left(iu\partial_\alpha u^\dagger - iu^\dagger\partial_\alpha u - ua_\alpha u^\dagger - u^\dagger a_\alpha u\right) \\
&= -P_\mu^\alpha u_\alpha
\end{aligned} \tag{II.A.21}$$

$$\begin{aligned}
u_\mu &= iu^\dagger\partial_\mu u - iu\partial_\mu u^\dagger + u^\dagger a_\mu u + ua_\mu u^\dagger \\
&\xrightarrow{\mathrm{C}} iu^\star\partial_\mu u^\top - iu^\top\partial_\mu u^\star + u^\star a_\mu u^\top + u^\top a_\mu u^\star \\
&= \left(iu^\dagger\partial_\mu u - iu\partial_\mu u^\dagger + u^\dagger a_\mu u + ua_\mu u^\dagger\right)^\top \\
&= (u_\mu)^\top.
\end{aligned} \tag{II.A.22}$$

From the terms in table II.A.1 and II.A.2 we can now isolate the combinations that are invariant under C and P symmetry. Additionally requiring that the Lagrangian is invariant under chiral transformation and that all the operators are hermitian, we find for the most

general form of the chiral Lagrangian up to $\mathcal{O}(p^2)$

$$\begin{aligned}\mathcal{L}_{\pi N} &= \mathcal{L}^{(1)}_{\pi N} + \mathcal{L}^{(2)}_{\pi N},\\ \mathcal{L}^{(1)}_{\pi N} &= \bar{\mathcal{N}}\left(i\not{D} - m + \frac{g_A}{2}\not{u}\gamma_5 + \frac{g_0}{2}\not{u}\gamma_5\right)\mathcal{N},\\ \mathcal{L}^{(2)}_{\pi N} &= \sum_{i=1}^{9} c_i \bar{\mathcal{N}}\mathcal{O}^{(2)}_i\mathcal{N},\end{aligned} \tag{II.A.23}$$

with the operators $\mathcal{O}^{(2)}_i$ given in Table II.A.3. The non-relativistic reduction of this Lagrangian following e.g. [137] then leads to the Lagrangian in Eq. (7.16). We summarize the differences in Table II.A.3, where the $\hat{O}_i$ are the HBChPT operators and the $\hat{c}_i$ the corresponding constants.

i	$\mathcal{O}^{(2)}_i$	$\hat{\mathcal{O}}^{(2)}_i$	$2m\,(\hat{c}_i - c_i)$
1	$\langle\chi_+\rangle$	$\langle\chi_+\rangle$	0
2	$-\frac{1}{8m^2}\left\{u_\mu, u_\nu\right\} D^{\mu\nu} +$ h.c.	$\frac{1}{2}(v\cdot u)^2$	$-\frac{1}{4}g_A^2$
3	$u^\mu u_\mu$	$u^\mu u_\mu$	0
4	$\frac{i}{4}\left[u_\mu, u_\nu\right]\sigma^{\mu\nu}$	$\frac{1}{2}\left[S^\mu, S^\nu\right]\left[u_\mu, u_\nu\right]$	$\frac{1}{2}$
5	$\widetilde{\chi}_+$	$\widetilde{\chi}_+$	0
8	$-\frac{1}{8m^2}u_\mu\hat{u}_\nu D^{\mu\nu} +$ h.c.	$\frac{1}{4}(v\cdot u)(v\cdot\hat{u})$	
9	$u^\mu\hat{u}_\mu$	$u^\mu\hat{u}_\mu$	0

Table II.A.3: Operators and differences between the constants of the ChPT and HBChPT Lagrangian. The terms with $i = 6, 7$ are not listed here. They contain $F_{\mu\nu}$ and thus would vanish as described above. Note that we extended table 3 of [265] by the terms involving the axion.

Now we also discuss the contact terms of nucleons. The pure nucleon contact terms are collectively denoted by $\mathcal{L}_{NN}$ and $\mathcal{L}_{NNN}$, the ones including a pion or a axion are denoted by $\mathcal{L}_{\pi NN}$. While the pure nucleon terms are well known (e.g. [266]), due to the inclusion of the axion, there are new terms in $\mathcal{L}_{\pi NN}$. Instead of constructing them as above (writing down the most general chiral Lagrangian and then projecting to the HB Lagrangian) we aim to directly construct the HBChPT Lagrangian by symmetry arguments as done for the chiral Lagrangian above. In HBChPT our basic operator building blocks are v^μ, S^μ, the identity matrix in spin and isospin space, the isospin matrices τ^a, combinations of them and spatial derivatives (the latter one are just relevant for higher order terms). Under charge and parity our building blocks transform as given in table II.A.4. The transformation of the isospin matrix τ^a under charge

$\Theta_{\mu\nu\ldots}$	1	v^μ	$\varepsilon_{\lambda\mu\nu\rho}$	τ^a	S^μ	$[S^\mu, S^\nu] = i\epsilon^{\mu\nu\rho\sigma}v_\rho S_\sigma$
parity	+	+	−	+	−	+
charge conjugation	+	−	+	$\star$	+	−

Table II.A.4: Transformation properties of different operators $\Theta_{\mu\nu\ldots}$ in ChPT.

are marked with a $\star$, because they are special in the sense that they can not simply be given by a simple sign in this table.

We construct pure nucleon contact terms as well as contact terms with one external axion field in the following way: Using the operators from table II.A.4 and the chiral dimension one fields from table II.A.2 we construct all the two nucleon bilinears with maximum one spacetime and one isospin index. The reason why we just use bilinears is the following. One could contract

Operator	Parity (P)	Charge (C)
$\bar{N}N$	$+$	$+$
$\bar{N}\tau^a N$	$+$	$\bar{N}(\tau^a)^\top N$
$\bar{N}S^\mu N$	$-$	$+$
$\bar{N}S^\mu\tau^a N$	$-$	$\bar{N}S^\mu(\tau^a)^\top N$
$\bar{N}u_\mu N$	$-$	$+$
$\bar{N}u_\mu\tau^a N$	$-$	$\bar{N}(\tau^a)^\top u_\mu N$
$\bar{N}S^\mu u_\mu N$	$+$	$+$
$\bar{N}S^\mu u_\mu\tau^a N$	$+$	$\bar{N}S^\mu(\tau^a)^\top u_\mu N$
$\bar{N}S_\nu u_\rho N\epsilon^{\mu\nu\rho\sigma}v_\sigma$	$-$	$-$
$\bar{N}S_\nu u_\rho\tau^a N\epsilon^{\mu\nu\rho\sigma}v_\sigma$	$-$	$-\bar{N}S_\nu(\tau^a)^\top u_\rho N\epsilon^{\mu\nu\rho\sigma}v_\sigma$
$\bar{N}\hat{u}_\mu N$	$-$	$+$
$\bar{N}\hat{u}_\mu\tau^a N$	$-$	$\bar{N}\hat{u}_\mu(\tau^a)^\top N$
$\bar{N}S^\mu\hat{u}_\mu N$	$+$	$+$
$\bar{N}S^\mu\hat{u}_\mu\tau^a N$	$+$	$\bar{N}S^\mu\hat{u}_\mu(\tau^a)^\top N$
$\bar{N}S_\nu\hat{u}_\rho N\epsilon^{\mu\nu\rho\sigma}v_\sigma$	$-$	$-$
$\bar{N}S_\nu\hat{u}_\rho\tau^a N\epsilon^{\mu\nu\rho\sigma}v_\sigma$	$-$	$-\bar{N}S_\nu\hat{u}_\rho(\tau^a)^\top N\epsilon^{\mu\nu\rho\sigma}v_\sigma$

Table II.A.5: Transformation properties of the Lagrangian building block in HBChPT. If the operator just picks up a sign we just write $\pm$ in the table. If it changes non-trivial we write the term explicitly. The transformation of spacetime indices is neglected because they will be contracted in the final Lagrangian.

the spin index of a nucleon field with another nucleon than the isospin index contrary to what is done for bilinear fields. However, by applying Fierz identity for spin and isospin matrices

$$\tau^a_{ij}\tau^a_{kl} = 2\delta_{il}\delta_{kj} - \delta_{ij}\delta_{kl} \tag{II.A.24}$$

$$\sigma^i_{ab}\sigma^i_{cd} = 2\delta_{ad}\delta_{cb} - \delta_{ab}\delta_{ab} \tag{II.A.25}$$

all such terms reduce again to bilinear terms. Now lets justify why we restrict our self to just terms with one spacetime and one isospin index. After all we could write down terms which have the same operator twice between the same nucleons e.g. $\bar{N}S^\mu S^\nu\tau^a N\bar{N}S_\mu S_\nu\tau^a N$ or $\bar{N}S^\mu\tau^a\tau^b N\bar{N}S_\mu\tau^a\tau^b N$ or terms with an ϵ^{abc} where two indices are contracted with two indices from the other bilinear such as $\bar{N}S^\mu\tau^a\tau^b N\bar{N}S_\mu\tau^c N\epsilon^{abc}$ and analogous for the spacetime indices. However, all the terms that include more then one operator S^μ or τ^a in between the same nucleons can be reduced to a combination of zero and one operator of type S^μ or τ^a by the relations

$$S^\mu S^\nu = \frac{1}{2}\{S^\mu, S^\nu\} + \frac{1}{2}[S^\mu, S^\nu], \tag{II.A.26}$$

$$\tau^a\tau^b = \frac{1}{2}\{\tau^a, \tau^b\} + \frac{1}{2}[\tau^a, \tau^b], \tag{II.A.27}$$

with

$$\{S^\mu, S^\nu\} = \frac{1}{2}\left(v^\mu v^\nu - g^{\mu\nu}\right), \quad [S^\mu, S^\nu] = i\epsilon^{\mu\nu\rho\sigma}v_\rho S_\sigma, \tag{II.A.28}$$

$$\{\tau^a, \tau^b\} = 2\delta^{ab}, \quad [\tau^a, \tau^b] = 2i\epsilon^{abc}\tau^c. \tag{II.A.29}$$

Various other combinations involving additionally combinations with $\epsilon^{\mu\nu\rho\sigma}$ and v^μ can be reduced (or are equal to zero) by the relations

$$v^2 = 1 \quad S^2 = -\frac{3}{4}, \quad v\cdot S = 0. \tag{II.A.30}$$

Additionally the epsilon tensor in isospin space with two open indices have to be contracted with two indices from the other bilinear. But these two indices can just cone from a δ^{ab} which gives zero or from $\tau^a\tau^b$ or another epsilon tensor. Terms of the form $\tau^a\tau^b$ as well as the contraction of two epsilon tensor can be reduced by the relations given above. Thus bilinears with more then one isospin index do not generate new terms because they can always be reduced. The same is true for the spacetime indices and $\epsilon^{\mu\nu\rho\sigma}$.

Let us first write down all such term that transform invariant under charge and parity. Theses are then reduced to a minimal set of terms by using basic identities. The bilinears we consider are all given in table II.A.5.

$$\begin{aligned} u_\mu\tau^a &= \frac{1}{2}\{u_\mu,\tau^a\} + \frac{1}{2}[u_\mu,\tau^a] \\ &= u_\mu^a + i\epsilon^{abc}\tau^b u_\mu^c. \end{aligned} \tag{II.A.31}$$

It is more useful to split $u_\mu\tau^a$ in a commuting and anti commuting part which both have a more straighforward transformation behaviour for our construction which can be found in table II.A.6. The symmetric part does not lead to any new terms so we omit them there. While the pure

Operator	Parity (P)	Charge (C)
$\frac{1}{2}\bar{N}[u_\mu,\tau^a]N$	$-$	$-\frac{1}{2}\bar{N}[u_\mu,(\tau^a)^\top]N = -i\epsilon^{abc}\bar{N}(\tau^b)^\top u_\mu^c N$
$\frac{1}{2}\bar{N}S^\mu[u_\mu,\tau^a]N$	$+$	$-\frac{1}{2}\bar{N}S^\mu[u_\mu,(\tau^a)^\top]N = -i\epsilon^{abc}\bar{N}S^\mu(\tau^b)^\top u_\mu^c N$
$\frac{1}{2}\bar{N}S_\nu[u_\rho,\tau^a]N\epsilon^{\mu\nu\rho\sigma}v_\sigma$	$-$	$\frac{1}{2}\bar{N}S_\nu[u_\rho,(\tau^a)^\top]N\epsilon^{\mu\nu\rho\sigma}v_\sigma = i\epsilon^{abc}\bar{N}S_\nu(\tau^b)^\top u_\rho^c N\epsilon^{\mu\nu\rho\sigma}v_\sigma$

Table II.A.6: Transformation properties of the Lagrangian building block in HBChPT. The notation is the same as in table II.A.5.

nucleon contact terms are well known, we now aim to construct all possible 2-nucleon contact terms which include either the field u_μ or $\hat{u}_\mu$. Those are the only fields with chiral dimension one from table II.A.2. We start with the ones including u_μ. From table II.A.5 and II.A.6 the only terms one can construct to fulfil the right transformation properties are

$$\bar{N}S^\mu N\bar{N}u_\mu N, \quad \bar{N}N\bar{N}S^\mu u_\mu N, \quad \epsilon^{abc}\epsilon^{\mu\nu\rho\sigma}v_\sigma\bar{N}S_\nu\tau^b N\bar{N}S_\rho\tau^c N u_\mu^a. \tag{II.A.32}$$

It can easily be shown that taking the non-relativistic limit and applying Fierz and other basic identities these are in fact not independent of each other. The explicit relations are $\bar{N}S^\mu N\bar{N}u_\mu N = -\bar{N}N\bar{N}S^\mu u_\mu N$ and $8\bar{N}S^\mu N\bar{N}u_\mu N = \epsilon^{abc}\epsilon^{\mu\nu\rho\sigma}v_\sigma\bar{N}S_\nu\tau^b N\bar{N}S_\rho\tau^c N u_\mu^a$. Therefore we only need one of them in the Lagrangian which following the literature (e.g. [266]) we write as

$$\mathcal{L}_{\pi NN} \supset \frac{c_D}{2f_\pi^2\Lambda_\chi}(\bar{N}N)\left(\bar{N}S^\mu u_\mu N\right). \tag{II.A.33}$$

For the terms involving $\hat{u}_\mu$ things are even simpler because $\hat{u}_\mu$ is proportional to the identity matrix in isospin space. There are only two possible combinations satisfying the transformation properties given by

$$\bar{N}N\bar{N}S^\mu\hat{u}_\mu N, \quad \bar{N}\tau^a N\bar{N}S^\mu\hat{u}_\mu\tau^a N. \tag{II.A.34}$$

Again, it can easily be seen that $\bar{N}\tau^a N\bar{N}S^\mu\hat{u}_\mu\tau^a N = -3\bar{N}N\bar{N}S^\mu\hat{u}_\mu N$ and so we find for the Lagrangian

$$\mathcal{L}_{\pi NN} \supset \frac{\tilde{c}_D}{2f_\pi^2\Lambda_\chi}(\bar{N}N)\left(\bar{N}S^\mu\hat{u}_\mu N\right). \tag{II.A.35}$$

This concludes the construction of all terms of the Lagrangian necessary to calculate the corrections to the axion-nucleon coupling.

II.A.2 Sample Calculation of V_1

In this part of the Appendix, we want to show an explicit finite density loop calculation. We focus on the vertex correction $\mathbf{V_1}$. The two different contributions are

$$\begin{aligned}\mathbf{V_1} = \int \frac{d^4k}{(2\pi)^4}(-1)\left[-\frac{g_A}{2f_\pi}\boldsymbol{\sigma}\cdot(\boldsymbol{k}-\boldsymbol{p})\tau^a\right]\left[\frac{i}{k^0}-2\pi\delta(k^0)\theta(k_f-|\boldsymbol{k}|)\right]\left[\frac{c_i}{2f_a}\boldsymbol{\sigma}\cdot\boldsymbol{p}_a\right]\times\\ \times\left[\frac{i}{k^0+p_a^0}-2\pi\delta(k^0+p_a^0)\theta(k_f-|\boldsymbol{k}+\boldsymbol{p}_a|)\right]\left[\frac{g_A}{2f_\pi}\boldsymbol{\sigma}\cdot(\boldsymbol{k}-\boldsymbol{p})\tau^b\right]\left[\frac{-i\delta^{ab}}{m_\pi^2-(k-p)^2}\right].\end{aligned} \tag{II.A.36}$$

Note that for any diagram, we need to take care of the spin and isospin structure separately. Only then we can evaluate the full integration. We only consider the density dependent part. Due to the δ functions, the dk^0 are trivial and we get after cancelling some minus signs

$$\begin{aligned}\mathbf{V_1} = \int \frac{d^3k}{(2\pi)^3}\Bigg\{&\left[\frac{g_A}{2f_\pi}\boldsymbol{\sigma}\cdot(\boldsymbol{k}-\boldsymbol{p})\tau^a\right]\left[\frac{c_i}{2f_a}\boldsymbol{\sigma}\cdot\boldsymbol{p}_a\right]\left[\frac{g_A}{2f_\pi}\boldsymbol{\sigma}\cdot(\boldsymbol{k}-\boldsymbol{p})\tau^a\right]\times\\ &\times\frac{1}{p_a^0}\theta(k_f-|\boldsymbol{k}+\boldsymbol{p}_a|)\left[\frac{1}{m_\pi^2-(k-p)^2}\right]-\left[\frac{g_A}{2f_\pi}\boldsymbol{\sigma}\cdot(\boldsymbol{k}-\boldsymbol{p})\tau^a\right]\left[\frac{c_i}{2f_a}\boldsymbol{\sigma}\cdot\boldsymbol{p}_a\right]\times\\ &\times\frac{1}{p_a^0}\theta(k_f-|\boldsymbol{k}|)\left[\frac{g_A}{2f_\pi}\boldsymbol{\sigma}\cdot(\boldsymbol{k}-\boldsymbol{p})\tau^a\right]\left[\frac{1}{m_\pi^2-(k-p)^2}\right]\Bigg\}.\end{aligned} \tag{II.A.37}$$

We now simple properties of the pauli matrices to find

$$\begin{aligned}[\boldsymbol{\sigma}\cdot(\boldsymbol{k}-\boldsymbol{p})]\,[\boldsymbol{\sigma}\cdot\boldsymbol{p}_a]\,[\boldsymbol{\sigma}\cdot(\boldsymbol{k}-\boldsymbol{p})] &= \frac{1}{2}\left(\sigma_i\sigma_j\sigma_k+\sigma_k\sigma_j\sigma_i\right)(k-p)_i(p_a)_j(k-p)_k = \\ &= 2\,[\boldsymbol{p}_a\cdot(\boldsymbol{k}-\boldsymbol{p})]\,[\boldsymbol{\sigma}\cdot(\boldsymbol{k}-\boldsymbol{p})]-[\boldsymbol{\sigma}\cdot\boldsymbol{p}_a]\,(\boldsymbol{k}-\boldsymbol{p})^2\end{aligned} \tag{II.A.38}$$

Now plugging this back in, we find

$$\begin{aligned}\mathbf{V_1} = &\left(\frac{g_A}{2f_\pi}\right)^2\frac{1}{p_a^0}\tau^a\frac{c_i}{2f_a}\tau^a\times\\ &\int\frac{d^3k}{(2\pi)^3}\left\{\theta(k_f-|\boldsymbol{k}+\boldsymbol{p}_a|)\frac{2\,[\boldsymbol{p}_a\cdot(\boldsymbol{k}-\boldsymbol{p})]\,[\boldsymbol{\sigma}\cdot(\boldsymbol{k}-\boldsymbol{p})]-[\boldsymbol{\sigma}\cdot\boldsymbol{p}_a]\,(\boldsymbol{k}-\boldsymbol{p})^2}{\tilde{m}_\pi^2+(\boldsymbol{k}-\boldsymbol{p})^2}+\right.\\ &\left.-\,\theta(k_f-|\boldsymbol{k}|)\frac{2\,[\boldsymbol{p}_a\cdot(\boldsymbol{k}-\boldsymbol{p})]\,[\boldsymbol{\sigma}\cdot(\boldsymbol{k}-\boldsymbol{p})]-[\boldsymbol{\sigma}\cdot\boldsymbol{p}_a]\,(\boldsymbol{k}-\boldsymbol{p})^2}{m_\pi^2+(\boldsymbol{k}-\boldsymbol{p})^2}\right\},\end{aligned} \tag{II.A.39}$$

where we used $m_\pi^2-(k-p_a)^2=m_\pi^2-(k_0^2+2k_0p_a^0+p_{a0}^2)+(\boldsymbol{k}-\boldsymbol{p}_a)^2=\tilde{m}_\pi^2+(\boldsymbol{k}-\boldsymbol{p}_a)^2$ with $k_0\sim\frac{Q^2}{2m}\ll Q$ negligible and we called $\tilde{m}_\pi^2=m_\pi^2-p_a^2$. Now we shift one of the integrals by $-\boldsymbol{p}_a$, such that we find

$$\begin{aligned}\mathbf{V_1} = &\left(\frac{g_A}{2f_\pi}\right)^2\frac{1}{p_a^0}\tau^a\frac{c_i}{2f_a}\tau^a\times\\ &\int_{|k|<k_f}\frac{d^3k}{(2\pi)^3}\left\{\frac{2\,[\boldsymbol{p}_a\cdot(\boldsymbol{k}-\boldsymbol{p}-\boldsymbol{p}_a)]\,[\boldsymbol{\sigma}\cdot(\boldsymbol{k}-\boldsymbol{p}-\boldsymbol{p}_a)]-[\boldsymbol{\sigma}\cdot\boldsymbol{p}_a]\,(\boldsymbol{k}-\boldsymbol{p}-\boldsymbol{p}_a)^2}{\tilde{m}_\pi^2+(\boldsymbol{k}-\boldsymbol{p}-\boldsymbol{p}_a)^2}+\right.\\ &\left.-\,\frac{2\,[\boldsymbol{p}_a\cdot(\boldsymbol{k}-\boldsymbol{p})]\,[\boldsymbol{\sigma}\cdot(\boldsymbol{k}-\boldsymbol{p})]-[\boldsymbol{\sigma}\cdot\boldsymbol{p}_a]\,(\boldsymbol{k}-\boldsymbol{p})^2}{m_\pi^2+(\boldsymbol{k}-\boldsymbol{p})^2}\right\}.\end{aligned} \tag{II.A.40}$$

We can now write this in term of integrals defined below as

$$\begin{aligned}\mathbf{V_1} = &\left(\frac{g_A}{2f_\pi}\right)^2\frac{1}{p_a^0}\tau^a\frac{c_i}{2f_a}\tau^a\left[2\left(I_1(\tilde{m}_\pi,\boldsymbol{p},\boldsymbol{p}_a)-I_1(m_\pi,\boldsymbol{p}+\boldsymbol{p}_a,\boldsymbol{p}_a)\right)+\right.\\ &\left.-\,\boldsymbol{\sigma}\cdot\boldsymbol{p}_a\left(I_2(\tilde{m}_\pi,\boldsymbol{p}+\boldsymbol{p}_a)-I_2(m_\pi,\boldsymbol{p})\right)\right].\end{aligned} \tag{II.A.41}$$

II.A.3 Helpful Integrals

Let us calculate a few integrals which will be useful later. First we define

$$\begin{aligned}
\Gamma_0(m,p) &= \int_0^{k_f} dk \int_{-1}^{1} dx \frac{k^2}{m^2+p^2+k^2+2pkx}, \\
\Gamma_1(m,p) &= \int_0^{k_f} dk \int_{-1}^{1} dx \frac{k^3 x/p}{m^2+p^2+k^2+2pkx}, \\
\Gamma_2(m,p) &= \int_0^{k_f} dk \int_{-1}^{1} dx \frac{k^4\left(1-x^2\right)/2}{m^2+p^2+k^2+2pkx}, \\
\Gamma_3(m,p) &= \int_0^{k_f} dk \int_{-1}^{1} dx \frac{k^4\left(3x^2-1\right)/\left(2p^2\right)}{m^2+p^2+k^2+2pkx}.
\end{aligned} \tag{II.A.42}$$

As we have seen already above in Sec. II.A.2, typically for m can either have m_π or $\tilde{m}_\pi$ with

$$\tilde{m}_\pi^2 = m_\pi^2 - (p_a^0)^2. \tag{II.A.43}$$

The gamma functions defined here have the following dimensions (in terms of k_f)

$$[\Gamma_0] = \mathcal{O}(k_f^1), \quad [\Gamma_1] = \mathcal{O}(k_f^1), \quad [\Gamma_2] = \mathcal{O}(k_f^3), \quad [\Gamma_3] = \mathcal{O}(k_f^1). \tag{II.A.44}$$

To make them dimensionless we can also define the functions K_i as

$$K_0(p) = \frac{\Gamma_0(p)}{k_f}, \quad K_1(p) = \frac{\Gamma_1(p)}{k_f}, \quad K_2(p) = \frac{\Gamma_2(p)}{k_f^3}, \quad K_3(p) = \frac{\Gamma_3(p)}{k_f}. \tag{II.A.45}$$

An integral that very often appears is

$$\begin{aligned}
I_1(m,\boldsymbol{p}) &= \int_{|\boldsymbol{k}|<k_f} \frac{d^3k}{(2\pi)^3} \frac{\boldsymbol{\sigma}\cdot(\boldsymbol{k}+\boldsymbol{p})\boldsymbol{q}\cdot(\boldsymbol{k}+\boldsymbol{p})}{m^2+(\boldsymbol{k}+\boldsymbol{p})^2} \\
&= \frac{1}{(2\pi)^3}\int_0^{k_f}\int_{-1}^{1}\int_0^{2\pi} dk\, dx\, d\phi\, k^2 \times \\
&\times \frac{(\boldsymbol{\sigma}\cdot\boldsymbol{k})(\boldsymbol{q}\cdot\boldsymbol{k}) + (\boldsymbol{\sigma}\cdot\boldsymbol{k})(\boldsymbol{q}\cdot\boldsymbol{p}) + (\boldsymbol{\sigma}\cdot\boldsymbol{p})(\boldsymbol{q}\cdot\boldsymbol{k}) + (\boldsymbol{\sigma}\cdot\boldsymbol{p})(\boldsymbol{q}\cdot\boldsymbol{p})}{m^2+p^2+k^2+2pkx}.
\end{aligned} \tag{II.A.46}$$

Choosing coordinates and noting that some of the $d\phi$ integrals vanish we can simplify the numerator

$$\begin{aligned}
&\int_0^{2\pi} d\phi\,(\boldsymbol{\sigma}\cdot\boldsymbol{k})(\boldsymbol{q}\cdot\boldsymbol{k}) = \int_0^{2\pi} d\phi\left[(\sigma_x k_x)(q_x k_x) + (\sigma_y k_y)(q_y k_y) + (\sigma_z k_z)(q_z k_z)\right] \\
&= \int_0^{2\pi} d\phi\left[\sigma_x q_x k^2(1-x^2)\cos^2\phi + \sigma_x q_x k^2(1-x^2)\sin^2\phi + \sigma_z q_z k^2 x^2\right] \\
&= \sigma_x q_x k^2(1-x^2)\pi + \sigma_y q_y k^2(1-x^2)\pi + \sigma_z q_z k^2 x^2 2\pi \\
&= \boldsymbol{\sigma}\cdot\boldsymbol{q}\, k^2(1-x^2)\pi + \boldsymbol{\sigma}\cdot(\boldsymbol{p}+\boldsymbol{q})\boldsymbol{q}\cdot(\boldsymbol{p}+\boldsymbol{q})\frac{k^2\pi(3x^2-1)}{p^2},
\end{aligned} \tag{II.A.47}$$

and

$$\begin{aligned}
\int_0^{2\pi} d\phi\left[(\boldsymbol{\sigma}\cdot\boldsymbol{k})(\boldsymbol{q}\cdot\boldsymbol{p}) + (\boldsymbol{\sigma}\cdot\boldsymbol{p})(\boldsymbol{q}\cdot\boldsymbol{k})\right] &= \int_0^{2\pi} d\phi\, kx \frac{(\boldsymbol{\sigma}\cdot\boldsymbol{p})(\boldsymbol{q}\cdot\boldsymbol{p}) + (\boldsymbol{\sigma}\cdot\boldsymbol{p})(\boldsymbol{q}\cdot\boldsymbol{p})}{p} \\
&= \int_0^{2\pi} d\phi\, 2kx \frac{(\boldsymbol{\sigma}\cdot\boldsymbol{p})(\boldsymbol{q}\cdot\boldsymbol{p})}{p} \\
&= 4\pi kx \frac{(\boldsymbol{\sigma}\cdot\boldsymbol{p})(\boldsymbol{q}\cdot\boldsymbol{p})}{p}.
\end{aligned} \tag{II.A.48}$$

With this and the definitions in Eq. (II.A.42) we can simplify the integral to

$$\boxed{I_1(m,\boldsymbol{p}) = \frac{1}{4\pi^2}\left[(\boldsymbol{\sigma}\cdot\boldsymbol{q})\,\Gamma_2(m,p) + (\boldsymbol{\sigma}\cdot\boldsymbol{p})\,(\boldsymbol{q}\cdot\boldsymbol{p})\,(\Gamma_0(m,p) + 2\Gamma_1(m,p) + \Gamma_3(m,p))\right]}, \tag{II.A.49}$$

Next we have a look at the following integral

$$\begin{aligned} I_2(m,\boldsymbol{p}) &= \int_{|\boldsymbol{k}|<k_f} \frac{d^3k}{(2\pi)^3}\frac{(\boldsymbol{k}+\boldsymbol{p})\cdot(\boldsymbol{k}+\boldsymbol{p})}{m^2+(\boldsymbol{k}+\boldsymbol{p})^2} \\ &= \int_{|\boldsymbol{k}|<k_f} \frac{d^3k}{(2\pi)^3}\left[\frac{m^2+(\boldsymbol{k}+\boldsymbol{p})^2}{m^2+(\boldsymbol{k}+\boldsymbol{p})^2} - \frac{m^2}{m^2+(\boldsymbol{k}+\boldsymbol{p})^2}\right] \\ &= \frac{1}{(2\pi)^3}\frac{k_f^3}{3}4\pi - m^2\Gamma_0(m,p)\frac{1}{4\pi^2} \\ &= \frac{1}{4\pi^2}\left(\frac{2k_f^3}{3} - m^2\Gamma_0(m,p)\right). \end{aligned} \tag{II.A.50}$$

So

$$\boxed{I_2(m,\boldsymbol{p}) = \frac{1}{4\pi^2}\left(\frac{2k_f^3}{3} - m^2\Gamma_0(m,p)\right)}. \tag{II.A.51}$$

The last important integral used in the main text is

$$I_3(m,\boldsymbol{p}) = \int_{|\boldsymbol{k}|<k_f} \frac{d^3k}{(2\pi)^3}\frac{\boldsymbol{\sigma}\cdot(\boldsymbol{k}+\boldsymbol{p})}{m^2+(\boldsymbol{k}+\boldsymbol{p})^2}, \tag{II.A.52}$$

which evaluates to

$$\boxed{I_3(m,\boldsymbol{p}) = \boldsymbol{\sigma}\cdot\boldsymbol{p}\frac{1}{4\pi^2}\left(\Gamma_1(m,p) + \Gamma_0(m,p)\right)}. \tag{II.A.53}$$

II.A.4 The Full Analytic Results at Zero Temperature

We summarize here the full result in the case of mixed matter at zero temperature. Summing up the contributions, we find

$$\begin{aligned}
\mathbf{V} &= \mathbf{V_1} + \mathbf{V_2} + \mathbf{V_3} + \mathbf{V_4} = \\
&= +\frac{c_{u-d} g_A p_a^0}{2 f_\pi^2 f_a} \tau^3 \left(I_3(m_\pi, \boldsymbol{p}) + I_3(\tilde{m}_\pi, \boldsymbol{p} + \boldsymbol{p}_a)\right) \\
&+ \left(\frac{g_A}{2 f_\pi}\right)^2 \frac{1}{p_a^0} \tau^a \frac{c_i}{2 f_a} \tau^a \left[2\left(I_1(\tilde{m}_\pi, \boldsymbol{p}, \boldsymbol{p}_a) - I_1(m_\pi, \boldsymbol{p} + \boldsymbol{p}_a, \boldsymbol{p}_a)\right)\right] \\
&- \left(\frac{g_A}{2 f_\pi}\right)^2 \frac{1}{p_a^0} \tau^a \frac{c_i}{2 f_a} \tau^a \boldsymbol{\sigma} \cdot \boldsymbol{p}_a \left[\left(I_2(\tilde{m}_\pi, \boldsymbol{p} + \boldsymbol{p}_a) - I_2(m_\pi, \boldsymbol{p})\right)\right] \\
&- \left(\frac{g_A c_{u-d} \hat{c}_3}{f_\pi^2 f_a}\right) \tau^3 \left[-\boldsymbol{p}_a^2 I_3(\tilde{m}_\pi, \boldsymbol{p} + \boldsymbol{p}_a) + I_1\left(\tilde{m}_\pi, \boldsymbol{p} + \boldsymbol{p}_a\right) + I_1\left(m_\pi, \boldsymbol{p}\right)\right] \\
&- \left(\frac{3 g_A \hat{c}_9 c_{u+d}}{2 f_\pi^2 f_a}\right) \left[-\boldsymbol{p}_a^2 I_3(\tilde{m}_\pi, \boldsymbol{p} + \boldsymbol{p}_a) + I_1\left(\tilde{m}_\pi, \boldsymbol{p} + \boldsymbol{p}_a\right) + I_1\left(m_\pi, \boldsymbol{p}\right)\right] \\
&- \left(\frac{g_A c_{u-d} \hat{c}_4}{f_\pi^2 f_a}\right) \tau^3 \left[I_1(\tilde{m}_\pi, \boldsymbol{p} + \boldsymbol{p}_a) - \boldsymbol{\sigma} \cdot \boldsymbol{p}_a I_2(\tilde{m}_\pi, \boldsymbol{p} + \boldsymbol{p}_a) + I_1(m_\pi, \boldsymbol{p}) - \boldsymbol{\sigma} \cdot \boldsymbol{p}_a I_2(m_\pi, \boldsymbol{p})\right] \\
&- \left(\frac{6 g_A \hat{c}_5 m_a^2 f_a}{f_\pi^4}\right) \left[I_3(\tilde{m}_\pi, \boldsymbol{p} + \boldsymbol{p}_a) - I_3(m_\pi, \boldsymbol{p})\right] \\
&+ \frac{\rho}{8 f_\pi^2 f_a \Lambda_\chi} \left(\left(c_D c_{u-d} \tau^3 + \tilde{c}_D c_{u+d}\right) \boldsymbol{\sigma} \cdot \boldsymbol{p}_a\right).
\end{aligned} \tag{II.A.54}$$

Note that some of the spin structure is hidden in the integrals. A similar expression can be written down for pure neutron matter. The propagator in pure neutron matter is given by

$$G\left(k_0, \boldsymbol{k}\right) = \frac{i}{k_0 + i\epsilon} - 2\pi\delta\left(k_0\right)\theta\left(k_f - |\boldsymbol{k}|\right)\frac{1 - \tau^3}{2}. \tag{II.A.55}$$

With this, we can evaluate all loops again to find for the full density correction of the vertex

$$\begin{aligned}
\mathbf{V} &= \mathbf{V_1} + \mathbf{V_2} + \mathbf{V_3} + \mathbf{V_4} = \\
&= \frac{g_A^2}{8 f_\pi^2 f_a} \frac{\boldsymbol{\sigma} \cdot \boldsymbol{p}_a}{p_a^0} \left(\frac{\hat{g}_a - \tilde{g}_a}{2}\right) \left(I_2(\tilde{m}_\pi, \boldsymbol{p} + \boldsymbol{p}_a) - I_2(m_\pi, \boldsymbol{p})\right) \\
&+ \left(\frac{g_A c_{u-d} \hat{c}_3}{f_\pi^2 f_a}\right) \left(\frac{\tau^3 - \mathbf{1}}{2}\right) \left(\boldsymbol{p}_a^2 I_3(\tilde{m}_\pi, \boldsymbol{p} + \boldsymbol{p}_a) - I_1\left(\tilde{m}_\pi, \boldsymbol{p} + \boldsymbol{p}_a\right) - I_1\left(m_\pi, \boldsymbol{p}\right)\right) \\
&+ \left(\frac{g_A \hat{c}_9 c_{u+d}}{2 f_\pi^2 f_a}\right) \left(\frac{3 + \tau^3}{2}\right) \left(\boldsymbol{p}_a^2 I_3(\tilde{m}_\pi, \boldsymbol{p} + \boldsymbol{p}_a) - I_1\left(\tilde{m}_\pi, \boldsymbol{p} + \boldsymbol{p}_a\right) - I_1\left(m_\pi, \boldsymbol{p}\right)\right) \\
&- \left(\frac{g_A c_{u-d} \hat{c}_4}{f_\pi^2 f_a}\right) \left(\frac{\tau^3 + \mathbf{1}}{2}\right) \left[I_1(\tilde{m}_\pi, \boldsymbol{p} + \boldsymbol{p}_a) - \boldsymbol{\sigma} \cdot \boldsymbol{p}_a I_2(\tilde{m}_\pi, \boldsymbol{p} + \boldsymbol{p}_a)\right] \\
&- \left(\frac{g_A c_{u-d} \hat{c}_4}{f_\pi^2 f_a}\right) \left(\frac{\tau^3 + \mathbf{1}}{2}\right) \left[I_1(m_\pi, \boldsymbol{p}) - \boldsymbol{\sigma} \cdot \boldsymbol{p}_a I_2(m_\pi, \boldsymbol{p})\right]. \\
&+ \frac{\rho}{8 f_\pi^2 f_a \Lambda_\chi} \left(\left(c_D c_{u-d} \left(\frac{\tau^3 - \mathbf{1}}{2}\right) + \tilde{c}_D c_{u+d} \left(\frac{\mathbf{1} - \tau^3}{2}\right)\right) \boldsymbol{\sigma} \cdot \boldsymbol{p}_a\right)_{ij}.
\end{aligned} \tag{II.A.56}$$

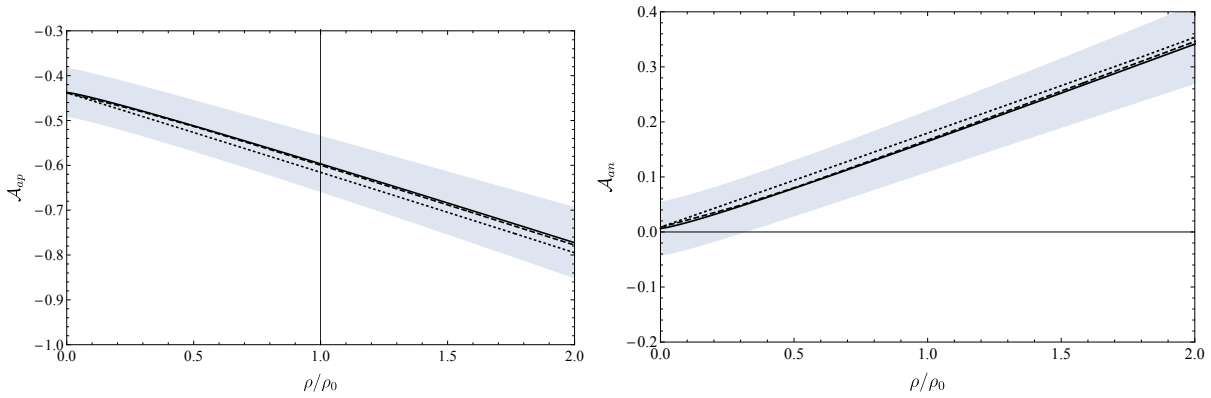

Figure II.A.1: The function $\mathcal{A}$ evaluated for protons and neutrons as a function of density. In solid the zero temperature limit, in dashed $T = 10\,\mathrm{MeV}$, dotted $T = 50\,\mathrm{MeV}$.

II.A.5 The Influence of (small) Temperature

The temperature of supernovae and proto-neutron stars can be $T \gtrsim 30\,\mathrm{MeV}$. It is not a priori obvious that our description of density loops without including temperature is a good approximation in these systems. However, as we see in this subsection, including temperature has little effect and does not affect our conclusions. We include finte T by using the propagator of Eq. (7.13) instead of the pure density one. The temperature and density integrals are now not cut off by a Heaviside function any more, but still decay fast for high momenta. Solving these integrals analytically is not possible any more, however we present in Fig. II.A.1 a numerical study, where we show the above couplings for temperatures below $\sim 50\,\mathrm{MeV}$. It can clearly be seen that the effect of these temperatures is small. The result is still within the error bar of the finite density calculation. Note that this comes from the fact that $\frac{T}{\mu} \ll 1$ for all temperatures that we considered.

II.B Density induced Instabilities

In this appendix we give some additional analytic estimates that back up some of the approximations used in Sec. 8.

II.B.1 Linear Profile Approximation

The parametric dependence of the results in Sec. 8.1.3 can be reproduced by considering a simpler, linear approximation for the scalar profile (recall $\Delta\phi(0) \equiv \phi(0) - \phi_-$)

$$\phi(r) = \begin{cases} \phi(0) & r < R_i \\ \phi(0) - \frac{\Delta\phi(0)}{R_\mathrm{T} - R_i}(r - R_i) & R_i < r < R_\mathrm{T} \\ \phi_- & r > R_\mathrm{T} \end{cases}, \qquad \text{(bubble; linear)} \tag{II.B.1}$$

and treating both $\phi(0)$ and R_i as variational parameters determined by the minimization of the energy of the bubble $E(\phi(0), R_i)$, i.e. Eq. (8.17) with $R = R_\mathrm{T}$. Expressing it in terms of $\Delta\phi(0)$ and the width $x = 1 - R_i/R_\mathrm{T}$, the energy is given by

$$E(\Delta\phi(0), x) = -E_0 \frac{\Delta\phi(0)}{f}\left[1 - \tfrac{3}{2}x + x^2 - \tfrac{1}{4}x^3 - \tfrac{3}{8}\frac{\alpha\Delta\phi(0)}{fx}\left(1 - x + \tfrac{1}{3}x^2\right)\right], \tag{II.B.2}$$

where $E_0 = \frac{4\pi}{3}\mu^2 f^2 R_{\rm T}^3$ and we have defined

$$\alpha \equiv \frac{4}{(\mu R_{\rm T})^2}\,. \tag{II.B.3}$$

During the formation of the system, $R_{\rm T}$ is small and therefore $\alpha \gg 1$. Minimization of the energy with respect to both $\Delta\phi(0)$ and x yields $x = 1$ and

$$\frac{\Delta\phi(0)}{f} = \frac{1}{\alpha}\,. \tag{II.B.4}$$

Therefore, we find a proto-bubble ($R_i = 0$) in which the field displacement at the origin is $\Delta\phi(0)/f \sim (\mu R_{\rm T})^2$, which is the result of an optimal balance between the gradient and potential energies. Parametrically, this matches the result in Eq. (8.22), albeit with a different numerical coefficient. As soon as the slowly-growing star is large enough that the in-density minimum $(\phi_+)_n$ can be reached, which happens when $\alpha \leqslant f/((\phi_+)_n - \phi_-)$, it should be energetically favorable for the profile to develop a core where the scalar value is fixed to $\phi(0) = (\phi_+)_n$. Then, minimization of the energy with respect to x leads to

$$x = \frac{1}{2}\sqrt{\frac{\alpha((\phi_+)_n - \phi_-)}{f}} + O(\alpha)\,, \tag{II.B.5}$$

This matches the result in Eq. (8.26), except for a numerical factor. Likewise, the energy of the bubble in the thin-wall limit $\alpha \ll f/((\phi_+)_n - \phi_-)$ is given by Eq. (8.28) where ϵ and σ scale as in Eqs. (8.29), (8.30) respectively, $\epsilon = \mu^2 f((\phi_+)_n - \phi_-)$ and $\sigma = ((\phi_+)_n - \phi_-)\sqrt{\epsilon}$.

The linear profile Eq. (II.B.1) has the advantage that it is simple to estimate the importance of departures from the approximation of a linear potential, Eq. (8.1), we have worked under in the main text. In particular, we can compute the effects of including the barrier term in Eq. (8.1) at finite density, i.e. with $\Lambda_{\rm B} \to \Lambda_{\rm B}(n)$. While ϵ remains unchanged in the thin-wall limit, the tension receives a correction

$$\frac{\Delta\sigma}{\sigma} = \frac{\sqrt{3}}{10}\frac{\Lambda_{\rm B}^4(n)}{\Lambda_{\rm R}^4}\,, \tag{II.B.6}$$

where we have assumed that the bubble is thin enough as to probe a fixed density.

II.B.2 Gravitational Force

In the equation of motion of the bubble, Eq. (8.37), we have neglected the gravitational force that the star exerts on the wall. While this does not change the conclusions we derived in the main text, it can lead to $O(1)$ numerical changes of the bubble's escape condition, at least for the densest stars, i.e. neutron stars.

In the non-relativistic and weak-field limits, the gravitational force of the star on the bubble wall per unit area (i.e. the pressure), is given by

$$F_{\rm G}(R) = -\frac{1}{8\pi M_{\rm P}^2}\frac{m(R)\sigma}{R^2}\,, \tag{II.B.7}$$

where $m(R)$ is the enclosed mass of the star and σ the wall tension. Using a simple estimate for the neutron star number density $n \sim m_n^3$ and radius $R_{\rm NS} \sim \sqrt{8\pi}M_{\rm P}/m_n^2$, obtained by equating

(Fermi-degeneracy) kinetic and gravitational energy densities and where m_n is the neutron mass, we find $m(R) \sim 8\pi M_{\rm P}^2 R^3/R_{\rm NS}^2$. Therefore, for a neutron star

$$\text{NS}: \quad F_{\rm G}(R) \sim \frac{\sigma R}{R_{\rm NS}^2}\,, \tag{II.B.8}$$

while for less dense stars the gravitational force is much smaller, i.e. for white dwarfs it is suppressed by m_e/m_p. This additional force leads to a modification of the bubble wall equation of motion, in the non-relativistic limit (weak-field) and for $R \leqslant R_{\rm NS}$

$$\sigma \ddot{R} \simeq \epsilon - \frac{2\sigma}{R}\left(1 + \frac{R^2}{2R_{\rm NS}^2}\right) - \sigma'\,, \tag{II.B.9}$$

which is subleading to the tension force except for $R \sim R_{\rm NS}$. Likewise, once if the bubble leaves the star, the enclosed mass is the total mass of star and therefore for $R \geqslant R_{\rm NS}$

$$\sigma \ddot{R} \simeq \epsilon - \frac{2\sigma}{R}\left(1 + \frac{R_{\rm NS}}{2R}\right)\,, \tag{II.B.10}$$

which once again introduces an $O(1)$ change only when $R \sim R_{\rm NS}$.

II.B.3 Linear Tension Approximation

The simplest modelling of $\sigma(R)$, that is a constant σ', allows us to analytically derive the condition Eq. (8.40). Let us then consider a linear increase of the tension with R, starting at $R_{\rm T}$ and ending at $R_{\rm S} = R_{\rm T} + \Delta R_{\rm T}$, thus with $\sigma' = [\sigma(R_{\rm S}) - \sigma(R_{\rm T})]/\Delta R_{\rm T}$ constant. The equilibrium position of the bubble wall is determined by $\ddot{R}(R = R_{\rm eq}) = 0$, and reads

$$R_{\rm eq} = \frac{2[\sigma' R_{\rm T} - \sigma(R_{\rm T})]}{3\sigma' - \epsilon}\,, \qquad R_{\rm T} > \sigma(R_{\rm T})/\sigma' \quad \text{and} \quad 3\sigma' > \epsilon\,, \tag{II.B.11}$$

where the inequalities ensure that this is indeed an equilibrium position, i.e. with $E''(R_{\rm eq}) > 0$, where $E(R)$ is the energy of the bubble (note that $\ddot{R} \propto -E'$). For consistency, we should also require $R_{\rm eq} \geqslant R_{\rm T}$, since that means that the bubble can in fact enter the transition region, where $\sigma' \neq 0$. This happens only if the star has grown large enough

$$R_{\rm T} > \frac{2\sigma(R_{\rm T})}{\epsilon - \sigma'}\,. \qquad \text{(entry transition region)} \tag{II.B.12}$$

This condition is equivalent to the requirement $\ddot{R}(R_{\rm T}) \not< 0$,[20] and it only makes sense for $\epsilon > \sigma'$. If the condition Eq. (II.B.12) is not satisfied, it just means that $R_{\rm eq} = R_{\rm T}$ and the bubble is trapped inside the star. In addition, note that whenever the bubble is able to enter the transition region but the conditions in Eq. (II.B.11) are not satisfied, then the bubble automatically escapes the star, since there is no stable radius $R > R_{\rm T}$ for which $\ddot{R} = 0$ and $E'' > 0$. If instead the conditions in Eqs. (II.B.11), (II.B.12) are satisfied, then there is indeed an equilibrium position at $R_{\rm eq} > R_{\rm T}$, which increases as the star gets larger. This last fact generically leads to a smaller force from the term $2\sigma/R$ in Eq. (8.37). Eventually, the equilibrium condition is lost when the position of the wall reaches the outer edge of the star, i.e. $R_{\rm eq} \geqslant R_{\rm S}$. This takes place when

$$R_{\rm T} > \frac{3\sigma(R_{\rm S}) - \sigma(R_{\rm T}) - \epsilon \Delta R_{\rm T}}{\epsilon - \sigma'}\,. \qquad \text{(exit transition region)} \tag{II.B.13}$$

[20] This requirement does not depend on σ' being constant, and the condition on $R_{\rm T}$ in Eq. (II.B.12) holds in general with $\sigma' \to \sigma'(R_{\rm T})$, under our approximation that σ' turns on at $R_{\rm T}$.

With the linear approximation for $\sigma(R)$ we then conclude that, as long as the volume energy of the bubble is larger than the rate of change of the tension, there is a minimum transition radius such that the bubble can permeate through the transition region, Eq. (II.B.12), and another for which the bubble can reach the surface of the star, Eq. (II.B.13). From that point outwards the bubble expands throughout the whole universe, since $\ddot{R}(R > R_{\rm S}) > 0$. Moreover, we also learn that if $\epsilon > 3\sigma'$, the only equilibrium position is $R_{\rm eq} = R_{\rm T}$, and this is lost as soon as the star is large enough as to satisfy Eq. (II.B.12). Importantly, let us note that when $\epsilon > 3\sigma'$, Eq. (II.B.12) is in fact approximately the same as the condition for the formation of the bubble, Eq. (II.B.4), thus in this case the formation and escape of the bubble take place simultaneously.

II.B.4 Ultra-high Densities

In Sec. 8.1.3 we centered our discussion of the bubble dynamics on the case where densities in the core of the star, while above critical, are not much larger than n_c. This is because a fully formed bubble for which the field at its center is $(\phi_+)_n \sim \phi_+$ already allows for the possibility of a classical phase transition to the true vacuum.

In this appendix we extend our analysis to the case of ultra-high densities, by which we mean $\zeta \to 1$. In this situation, the only minimum of the in-medium potential is found at $(\phi_+)_n \gg \phi_+$, see Eq. (8.7). As we explain in the following, we find that the escape of a bubble of the true vacuum can take place regardless of the scalar inside the star reaching the in-density minimum of the potential, i.e. $\phi(0) < (\phi_+)_n$, but it is enough that the field displacement is at least $\Delta\phi(0) \gtrsim \phi_+ - \phi_-$. As a matter of fact, if the star is large enough as to allow $\phi(0) \gg \phi_+$, the correspondingly large field displacement inside the (proto)-bubble makes it easier for a bubble to escape from the star.

The key point is that, for what concerns the possibility of a bubble of the true vacuum escaping from the star, one only needs to focus on a "sub-bubble" with a field displacement $\Delta\phi_{\rm sub} = \phi_+ - \phi_- \approx 2f$. The energy density of such a sub-bubble is simply $\epsilon_{\rm sub} \sim \Lambda_{\rm R}^4$, while its tension scales as

$$\sigma_{\rm sub}(R_{\rm T}) \sim \sqrt{\Delta\phi(0) f}\,\Lambda_{\rm R}^2 \,. \tag{II.B.14}$$

The latter is enhanced by a factor $(\Delta\phi(0)/\Delta\phi_{\rm sub})^{1/2}$ with respect to the naive expectation, due to the higher potential energy difference of the large (proto-)bubble that contains the sub-bubble, $|\langle \Delta V \rangle| \sim \Delta\phi(0)\Lambda_{\rm R}^4/f$. This simple estimate holds as well if we assume that the in-density minimum is reached, i.e. $\phi(0) = (\phi_+)_n$.

Such an enhancement of the tension facilitates the escape of the sub-bubble, since it decreases the contracting force associated with σ' in Eq. (8.37). In particular, we now have $\sigma'_{\rm sub} \sim [\sigma(R_{\rm S}) - \sigma_{\rm sub}(R_{\rm T})]/\Delta R_{\rm T}$, which is smaller than when $\phi(0) \sim \phi_+$, see Eqs. (8.38), (8.39); in fact it could even be negative. Notice that instead the force associated with the surface tension of the wall at the transition radius, $2\sigma_{\rm sub}(R_{\rm T})/R_{\rm T}$, remains constant, since $R_{\rm T} \sim \sqrt{\Delta\phi(0)/f}\mu^{-1}$. Therefore, the net result is that it is much easier for the escape condition Eq. (8.40) to be satisfied. The larger (proto-)bubble supporting the sub-bubble helps the latter permeate through the entire star. The proper condition that determines if the sub-bubble of true vacuum expands throughout the whole universe is then

$$R_{\rm S} \gtrsim \frac{2\sigma(R_{\rm S})}{\epsilon} \,. \tag{II.B.15}$$

We have explicitly verified this result via our numerical simulations. For a bubble connecting shallow minima, $\delta^2 \ll 1$, this condition translates into

$$R_{\rm S} \gtrsim \frac{f}{\Lambda_{\rm R}^2} \,, \qquad \text{(sub-bubble; shallow)} \tag{II.B.16}$$

a requirement that is automatically satisfied given that $R_{\rm S} > R_{\rm T}$. For a bubble connecting deep minima, $\delta^2 \approx 1$, we find instead

$$R_{\rm S} \gtrsim \frac{f}{\Lambda_{\rm R}^2} \frac{1}{\sqrt{1-\delta^2}} \,. \qquad \text{(sub-bubble; deep)} \tag{II.B.17}$$

This is similar to the escape condition for a deep bubble, Eq. (8.42), yet on $R_{\rm S}$ instead of $\Delta R_{\rm T}$.

II.B.5 Sudden Approximation

We have been assuming that the bubble, during either its formation or expansion through the star, is always found in a nearly-static ($\dot{R} = 0$) equilibrium position, with its radius evolving slowly only because $R_{\rm T} = R_{\rm T}(\bar{t})$ does, as the star is being formed. Only at the point where equilibrium is lost, $\ddot{R} > 0$ and the bubble is free to gain kinetic energy. This was justified in Sec. 8.1.2 on the basis that the characteristic reaction time of the scalar field, μ^{-1}, is much shorter than the evolution time of the star $T_{\rm S}$. In this section we wish to comment on the opposite situation, where $\mu T_{\rm S} \ll 1$.

In this limit, the star is formed instantaneously, with a large region $r < R_{\rm T}$ where the in-density potential allows for the scalar field to start classically rolling. If such a region was of infinite extent, i.e. if the system was spatially homogeneous, the field would roll, accelerate, and finally oscillate around the true minimum. However, in a finite-size system, one needs to crucially take into account the contribution of the spatial gradient to the energy of the field configuration. Indeed, ϕ moves in an effective potential $V(\phi) + \frac{1}{2}\phi'^2$ that becomes large towards the transition region, where the field must return to its vacuum value ϕ_-. Therefore, the sudden formation of the star and the corresponding gain of kinetic energy $\frac{1}{2}\dot{\phi}^2$ does not automatically imply that a first order phase transition will proceed via the escape of a scalar bubble from the dense system. As a matter of in fact, the situation is not much different that in the quasi-static case, as we now explain.

Concerning the formation of the bubble, the main difference with respect to our discussion in Sec. 8.1.3 can be phrased in terms of the maximal value that $\Delta\phi(0) = \phi(0) - \phi_-$, the field displacement at the center of the star, can take. Indeed, because of the kinetic energy the field acquires by rolling down the in-medium potential, $\Delta\phi(0)$ will generically be larger than what found in Eq. (8.22) for the same $R_{\rm T}$, yet oscillating in time. Accordingly, the whole scalar profile will necessarily oscillate in time as well. Then, if the size of star, specifically $R_{\rm T}$, is still not large enough for $\phi(0)$ to reach ϕ_+, the field value corresponding to the true minimum of the scalar potential in vacuum, then such an oscillating scalar profile remains trapped within the star, in a sort of oscillon that, even after eventually losing its kinetic energy,[21] remains as a confined static bubble (see e.g. [267] for a recent discussion of such type of field configurations in vacuum).

Otherwise, if $\Delta\phi(0) \gtrsim 2f$, then whether the scalar bubble remains confined to the dense region or escapes to infinity follows from the same analysis as in Sec. 8.1.3, yet with the properties of the bubble, i.e. the potential energy difference between the two sides of the bubble wall and the tension, now oscillating in time.

We stress again that the main difference between the quasi-static and sudden scenarios concerns the value of $R_{\rm T}$ for which a given field displacement is attained. Another way to interpret this fact is to compare, for the same value of $R_{\rm T}$, the dynamics of the bubble wall between the two scenarios. Because of the larger field displacement in the sudden case, the maximum values of $\epsilon(t)$ and $\sigma(R,t)$ will both be larger, while $\sigma'(R,t)$ will be smaller, than in the quasi-static case. This situation resembles the quasi-static evolution of a bubble in the

[21] This could proceed via radiation of ϕ quanta, or because of the interactions of ϕ with the environment.

limit that $n \gg n_c$, discussed in App. II.B.4. Therefore, we could similarly conclude that in the sudden approximation and for $R_{\rm T} \gg \mu^{-1}$, the condition that determines if the bubble expands indefinitely is

$$R_{\rm S} \gtrsim \frac{2\sigma(R_{\rm S})}{\epsilon}\,. \tag{II.B.18}$$

II.B.6 Formation and Escape of $N \gg 1$ Bubbles

In the main text we have concentrated on bubbles interpolating between two consecutive relaxion minima, located at the period ℓ_* outside the bubble and at ℓ_*+1 inside it. However, the relaxion displacement at the core of the star could be much larger than $2\pi f$, in particular $\Delta\phi(0) \sim 2\pi f N$ with $N \gg 1$ is expected to naturally occur for relaxion bubbles at densities significantly above the critical one, see Eq. (8.65). In this appendix we provide a discussion of the fate of the relaxion bubbles in such a situation, following closely [12] while avoiding the detailed derivation presented there.

For the first in-density minimum to be reached, the energy in the in the field's gradient, $\sim (2\pi f N/R_{\rm T})^2$, needs to be compensated by the gain in potential energy inside the bubble, $\sim 2\pi\Lambda_{\rm R}^4 N$. This can only happen if the core of the star is large enough

$$R_{\rm T} \gtrsim \frac{\sqrt{N}}{\mu}\,, \tag{II.B.19}$$

where we recall that $\mu = \Lambda_{\rm R}^2/f$. If this is the case, a large bubble with a field displacement of $\Delta\phi(0) \sim 2\pi f N$ is fully formed. The properties of such a bubble, that is its volume energy density and tension can be simply estimated as,

$$\epsilon \sim \mu^2 f \Delta\phi(0) \sim 2\pi\Lambda_{\rm R}^4 N\,, \tag{II.B.20}$$

$$\sigma \sim \Delta\phi(0)\sqrt{\epsilon} \sim \Lambda_{\rm R}^2 f (2\pi N)^{3/2}\,. \tag{II.B.21}$$

This large relaxion bubble can be thought as made of a series of N sub-bubbles, each corresponding to a field displacement w.r.t. to the next of $2\pi f$, see Fig. II.B.1. This is motivated by the fact that in vacuum each relaxion minimum is separated by a potential barrier, so the escape of relaxion bubbles from the star takes place in discrete steps, starting with the outermost bubble, within which the relaxion sits just one period away, i.e. at ℓ_*+1, from its in-vacuo value. This sub-bubble has then a volume energy density and tension

$$\epsilon_{\rm sub} \sim 2\pi\Lambda_{\rm R}^4\,, \tag{II.B.22}$$

$$\sigma_{\rm sub}(R_{\rm T}) \sim \Lambda_{\rm R}^2 f (2\pi N)^{1/2}\,. \tag{II.B.23}$$

Note in particular that the wall tension is enhanced by a factor $\sqrt{N}$ w.r.t. the one of a standard relaxion bubble. It is this enhancement that facilitates the sub-bubble escape from the star. Indeed, the characteristic contracting force of bubbles propagating through a star, $\sigma' \sim \Delta\sigma/\Delta R_{\rm T}$ associated with a radius-dependent tension, is mitigated because $\Delta\sigma \sim \sigma_{\rm sub}(R_{\rm S}) - \sigma_{\rm sub}(R_{\rm T})$ decreases (or could even become negative) at large N. We have explicitly verified this effect via numerical simulations of the sub-bubble's dynamics.

The condition for the expansion, beyond the confines of the star and towards infinity, of this $2\pi f$ bubble then coincides with the condition that the bubble does not contract in vacuum, $\epsilon_{\rm sub} \gtrsim 2\sigma_{\rm sub}(R_{\rm S})/R_{\rm S}$, where $\sigma_{\rm sub}(R_{\rm S})$ is the tension of the wall in vacuum. For shallow minima,

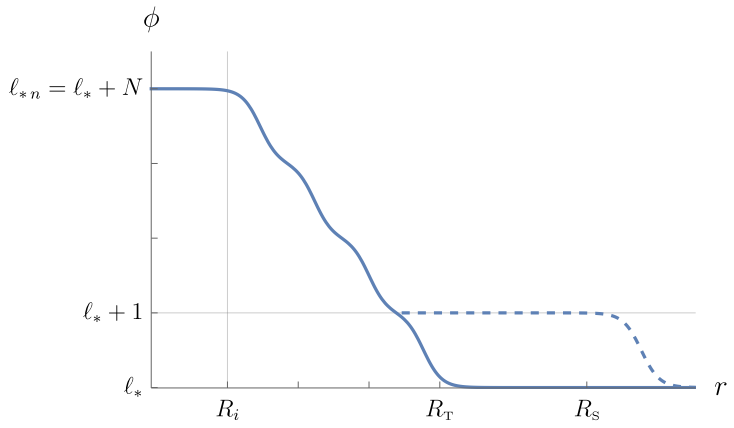

Figure II.B.1: $N \gg 1$ bubble in equilibrium at $R \sim R_{\rm T}$ (solid) and sub-bubble that has already escaped from the star (dashed).

since the potential barrier Eq. (8.62) is very small, this tension is simply $\sigma_{\rm sub}(R_{\rm S}) \sim 2\pi f\sqrt{\epsilon_{\rm sub}}$. Therefore, the condition reads

$$R_{\rm S} \gtrsim \frac{f}{\Lambda_{\rm R}^2}\,, \qquad \text{(sub-bubble; shallow)} \tag{II.B.24}$$

which is automatically satisfied given that $R_{\rm S} > R_{\rm T}$ and Eq. (II.B.19). Instead, for deep minima we can use the thin-wall approximation to compute the wall's tension $\sigma_{\rm sub}(R_{\rm S}) \simeq 8f\Lambda_{\rm B}^2$, and the correct condition is then

$$R_{\rm S} \gtrsim \frac{f}{\Lambda_{\rm R}^2}\frac{1}{\sqrt{1-\delta^2}}\,. \qquad \text{(sub-bubble; deep)} \tag{II.B.25}$$

Finally, let us note that if the conditions for a sub-bubble to escape are satisfied, this will also be the case for subsequent sub-bubbles (with $N \to N-1$), up until N becomes so small that the enhancement in the sub-bubble tension $\sigma_{\rm sub}$ is not enough to guarantee that $\epsilon \gtrsim \sigma'$, that is that the outwards pressure due to the gain in ground state energy is not enough to overcome the tension's gradient.

II.B.7 Opposite-sign Back-reaction

The discussion in the main text has been restricted to densities that, while allowing for the field to classically move inside the star, i.e. $\zeta(n) > \zeta_c = \delta^2$, are still such that the back-reaction term in the potential is non-vanishing, even if negligibly small. In this section we want to consider instead the possibility that $\zeta(n) > 1$, such that the wiggles not only vanish but change sign in some region inside the star.

In this situation, we can identify another inner core radius $R'_{\rm T}$, such that for $r < R'_{\rm T}$, minima of the in-density potential reappear due to opposite-sign barriers. This is fixed by $\zeta(R'_{\rm T}) = 2-\delta^2$, where δ is defined, as in vacuum, as the difference between the size of the rolling and back-reaction terms at the minimum of interest, see Eq. (8.58). Because of the different sign of the back-reaction term, the minima are now shifted by π with respect to those for $\zeta < 1$, i.e. they are located at $(2\pi\ell_{*n} + \theta_{*n} + \pi)f$. The field displacement, or equivalently the value of ℓ_{*n} where the relaxion sits for $r < R'_{\rm T}$, is determined by the size of the region between the two core radii, $\Delta R'_{\rm T} \equiv R_{\rm T} - R'_{\rm T}$. This difference sets, in the same fashion as Eq. (II.B.19), the field

displacement from the in-vacuo value, $\Delta\phi(R'_{\rm T})/f \sim (\mu \Delta R'_{\rm T})^2$. From this point on, the fate of the bubble (or sub-bubble) is not much different than what already discussed in Sec. 8.2.2.A and App. II.B.6. In particular, if $\Delta R'_{\rm T} \gg \mu^{-1}$, the relevant dynamics is that of a $2\pi f$ sub-bubble, for which the condition Eq. (II.B.24) determines if it escapes the star and expands to infinity. The only subtlety arises for $\Delta\phi(R'_{\rm T}) = \pi f$. In this case the potential energy density of the bubble receives a contribution from the back-reaction term in addition to the rolling term. We find $\epsilon \simeq \pi\Lambda_{\rm R}^4 + 2(\zeta-1)\Lambda_{\rm B}^4$, where we recall that we are dealing with densities such that $\zeta > 1$. While for sufficiently large ζ this extra contribution naively helps the bubble expand, as soon as the bubble wall goes through the outer transition region of the star, $r > R_{\rm T}$, ϵ decreases because the relaxion value inside the bubble, $(2\pi\ell_* + \pi)f$, is not a minimum of the potential in vacuum. This eventually prevents the bubble from escaping. This type of confined bubble (yet with $\Lambda_{\rm R} = 0$) has been found to be a plausible consequence of the QCD axion [118], or special deformations thereof [119], in neutron stars.

II.B.8 Bubble Interactions with the Environment

In the main text we have treated the density profile as a non-dynamical classical background field, upon which a non-trivial scalar field develops. In this appendix we study in some more detail the interactions of the scalar bubble with the dense environment.

Let us discuss first the force exerted by individual nucleons, N, on the bubble wall. We focus on the case of the QCD relaxion, since the interactions of non-QCD relaxions with protons and neutrons are much weaker, being mediated by Higgs exchange. The interaction with nucleons is of the form $\sim \sigma_{\pi N} \bar{N} N \cos(\phi/f)$. This constitutes a contribution to their mass that depends on the relaxion field, and therefore on space-time, $m_{\pi N}(r) \sim \sigma_{\pi N} \cos(\phi(r)/f)$. Recall that most of the mass of a nucleon comes from a term independent of the quark masses and thus independent of ϕ, $m_N = M_B + m_{\pi N}$ with $M_B \gg m_{\pi N}$. It is precisely this interaction of the relaxion with nucleons that gives rise to the leading linear correction to the back-reaction term in the limit of small baryonic densities, after substituting $\bar{N}N \to n_b$, as given in Eq. (8.74). Note however that for this treatment to hold, one is implicitly assuming that the scalar field interacts classically with the density profile, or in other words that single nucleons are able to penetrate the bubble wall with negligible quantum-mechanical reflection.

Let us have a look then at the one-dimensional quantum mechanics of a nucleon in the potential associated with its space-time dependent mass, $m_{\pi N}(r)$. This follows the discussion in [212], with some important modifications. Before proceeding, let us note there are two qualitatively different types of potentials depending on the relaxion profile. For bubbles in which the scalar field displacement is $\Delta\phi(0) = 2\pi f$ (our focus in the main text) the overall change of the nucleon mass between inside and outside the bubble vanishes, while at the center of the bubble wall, where $\Delta\phi = \pi/2$, $m_{\pi N} \sim -\sigma_{\pi N}$; the potential thus resembles a well. If instead the field displacement is $\Delta\phi(0) = \pi f$ (briefly discussed in App. II.B.7), we have that the change from outside to inside the bubble $\Delta m_N \sim -2\sigma_{\pi N}$, and the potential is a downwards step. In any of these cases, in order to properly compute the force that the nucleons exert on the bubble wall, it is important to realize that the relevant scales of the problem are the thickness of the wall, of order $\mu^{-1} \sim f/\Lambda_{\rm R}^2$, and the nucleon wavelength, given by $\lambda_N \sim 1/m_N v$, where v is the relative velocity of the nucleons with respect to the wall, which we expect to be non-negligible (either because of their Fermi momentum, temperature, or the initial yet small velocity that the bubble acquires when it forms). We therefore expect $\lambda_N \mu \ll 1$, which already indicates that the nucleons interact with the potential classically. Focussing for concreteness on the step-like potential, we can go further and split it in J small patches, each of them of size λ_N, where quantum mechanical effects become important. In each step the nucleon mass decreases

by an amount $\delta m_N = |\Delta m_N|/J \sim 2\sigma_{\pi N}/J$. Therefore, for each step the quantum-mechanical reflection coefficient is given by

$$\mathbb{R}_1 = \frac{(k-k')^2}{(k+k')^2} \simeq \frac{\delta m_N^2}{4m_N^2 v^4}\,, \tag{II.B.26}$$

where k is the momentum of the nucleon before traversing the wall, and k' its momentum once inside the bubble. In the second equality we have taken the non-relativistic limit, $k \simeq mv$ and $k' \simeq \sqrt{k^2 + 2m_N \delta m_N}$, and expanded in δm_N. Taking into account all the J barriers, the total reflection coefficient is bounded by

$$\mathbb{R} \lesssim J\mathbb{R}_1 \simeq \frac{\Delta m_N^2}{4m_N^2 v^4 J}\,, \tag{II.B.27}$$

which vanishes in the limit $J \gg 1$. This agrees then with the naive expectation that for $\lambda_N \mu \ll 1$ the system behaves classically, without reflection. In fact, one can also compute the total force on the bubble wall associated with the gain in momentum of the nucleons as they pass through it. For a single nucleon, after going down all the J steps, the force is $f_N = J(k'-k)\mathbb{T} \simeq |\Delta m_N|/v$. Therefore, for an ensemble of nucleons with density n_b, the total force reads

$$F_N = n_b v f_N \sim 2\sigma_{\pi N} n_b\,. \tag{II.B.28}$$

This precisely matches the piece of the volume force associated with the change of the potential barriers derived in App. II.B.7 (opposite-sign back-reaction), $\sim 2\zeta\Lambda_{\rm B}^4 \sim 2\sigma_{\pi N} n_b$. For the potential-well case (i.e. for $2\pi f$ bubbles), with this quantum-mechanical treatment we find, as expected, $F_N = 0$. However, given that the wall appears to the individual nucleons as a classical potential well, these tend to accumulate at the wall, i.e. the density (as well as temperature) increases at the wall; this in turn means that the wall gets thicker. Therefore, it appears that as the bubble expands through the star, it carries with it a local (of size μ^{-1}) increase in density. However, for most of the star the density profile remains unaltered.

II.C Backreaction of Light Scalars on Stellar Remnants

II.C.1 Negligible Gradient Approximation in TOV Equations

It is useful to rewrite the equations of motions in terms of dimensionless quantities, which we define as

$$\begin{aligned} &\hat{p} \equiv p/m^4\,, \quad \hat{\varepsilon} \equiv \varepsilon/m^4\,, \quad \hat{r} = r/R\,, \\ &\hat{V} \equiv V/\Lambda^4\,, \quad \hat{m}_*(\theta) \equiv m_*(\theta)/m\,, \quad \hat{\rho}_s \equiv (m\rho_s)/\Lambda^4\,, \end{aligned} \tag{II.C.1}$$

where Λ^4 is the typical scale associated with the potential. The equations of motion are then given by

$$\hat{p}' = -\frac{(\hat{p}+\hat{\varepsilon})e^{2\lambda}}{2\hat{r}}\left(c_1\hat{r}^2\hat{p} + c_2\hat{r}^2 e^{-2\lambda}\theta'^2 + 1 - e^{-2\lambda}\right) - \theta' c_3\left(\frac{\partial\hat{V}}{\partial\theta} + \hat{\rho}_s\frac{\partial\hat{m}_*}{\partial\theta}\right)\,, \tag{II.C.2}$$

$$\left(\hat{r}e^{-2\lambda}\right)' = 1 - \left(c_1\hat{r}^2\hat{\varepsilon} + c_2\hat{r}^2 e^{-2\lambda}\theta'^2\right)\,, \tag{II.C.3}$$

$$e^{-2\lambda}\theta'' + \frac{1}{\hat{r}}\theta'\left(1 + e^{-2\lambda} - \frac{c_1\hat{r}^2}{2}\left(\hat{\varepsilon} - \hat{p}\right)\right) = c_4\left(\frac{\partial\hat{V}}{\partial\theta} + \hat{\rho}_s\frac{\partial\hat{m}_*}{\partial\theta}\right)\,, \tag{II.C.4}$$

where we identifies three relevant dimensionless coefficients

$$c_1 \equiv \frac{\alpha^2 m^4}{M_{\rm pl}2}\,, \quad c_2 \equiv \frac{f^2}{2M_{\rm pl}2}\,, \quad c_3 \equiv \Lambda^4/m^4 \;\text{ and }\; c_4 \equiv \frac{c_1 c_3}{2c_2} = \frac{\alpha^2\Lambda^4}{f^2}. \tag{II.C.5}$$

where α is an arbitrary length scale. The typical size of a gravitationally-bound star is determined by the condition $c_1(\alpha = R_{\rm star}) = 1$, which implies $R_{\rm star} = M_{\rm pl}/m^2$. On the other hand, the typical scale associated with the scalar field is given by the condition $c_4 \mathrm{Max}\{1, \hat{\rho}_s\}(\alpha = \lambda_\phi) = 1$, which strictly speaking is a locally defined property since $\hat{\rho}_s$ depends on $\hat{r}$. This typical scale of the scalar field, which as we just argued changes with density, is what we shall later refer to as the Compton wavelength of the field.

An important approximation used in Eq. (9.11) involves regions where θ varies smoothly in finite region comparable to the size of the star, where the effects of the gradient of the field are neglected. This is justified when considering the equations using the scale $R = R_{\rm star}$ ($c_1 = 1$). In this case, it is clear that for $\theta' \sim \mathcal{O}(1)$ and $e^{-2\lambda} \sim \mathcal{O}(1)$, the energy density and pressure associated with the gradient of the scalar field are negligible as long as $c_2 \ll 1$, or in other words

$$f \ll M_{\rm pl}\,. \tag{II.C.6}$$

The negligible gradient approximation and in-medium wavelength

To understand the negligible gradient approximation, let us look at Eq. (II.C.4)

$$\theta'' + \frac{2}{\hat{r}}\theta' = c_4 \left(\frac{\partial \hat{V}}{\partial \theta} + \hat{\rho}_s \frac{\partial \hat{m}_*}{\partial \theta} \right). \tag{II.C.7}$$

where we neglected the $\mathcal{O}(1)$ deformation of the scalar derivatives due to gravity, as they will not play a significant role in the following discussion. Over a region of size $\Delta\hat{r}$ where θ changes by $\Delta\theta$, the LHS scales as $\sim \frac{\Delta\theta}{(\Delta\hat{r})^2}$. This is true both in the case where the transition happens at $\hat{r} \gg \Delta\hat{r}$ (in which case the θ' term is $\mathcal{O}(\Delta\hat{r}/\hat{r})$ suppressed w.r.t to the θ'' term) or when when the transition happens where $\hat{r} \sim \Delta\hat{r}$ (in which case the θ' and θ'' term scale the same).

Consider the field profile $\theta(r)$ implied by the approximate solution of the system Eq. (9.11), which relies on the EOS deduced from Eq. (9.9). By construction it insures that the RHS of Eq. (II.C.7) vanishes, but it is a good approximation for the full EOM only if the corrections due to the field derivatives on the LHS can be considered small. We separate the discussion into two qualitatively different regions of $\theta(r)$, (1) regions where θ varies smoothly in a finite region and (2) the transition region where θ instantly jumps from value to another, the so-called bubble wall. In both of these regions, we argue that while θ' and θ'' do not vanish, $\theta(r)$ can nonetheless be considered a good approximate solution under certain conditions. We shall derive an upper bound on f which insures the validity of this approximation, with the strongest bound coming from the condition for the formation of the bubble wall.

As a warm up exercise, we start with region of $\theta(r)$ where θ varies smoothly in a finite region. While it is easier to characterize the gradient corrections in this regions, as we will show below, they will typically provide weaker bounds on f. Consider a region where $\theta(r)$ changes slowly from $\bar{\theta} - \Delta\theta/2$ to $\bar{\theta} + \Delta\theta/2$ such that the transition region $\Delta\hat{r}$ is a large finite region, comparable to the total size of the object R. It should be understood that such a relatively flat part of the field profile is not part of the transition region, if one exists. The LHS of Eq. (II.C.4)

scales simply like $\Delta\theta$, where we set $\Delta\hat{r} \approx 1$ in our units of our object size R. In the region around $\bar{\theta}$ where the field changes by $\Delta\theta \ll \bar{\theta}$, it is sensible to use a Taylor expansion on the RHS of Eq. (II.C.4) to find the condition for negligible gradient energy

$$\frac{f^2}{R^2} \ll \Lambda^4_{\rm eff}(\bar{\theta}) \quad \text{where} \quad \Lambda^4_{\rm eff}(\bar{\theta}) \equiv \frac{\partial}{\partial\theta}\left(\frac{\partial V(\theta)}{\partial\theta} + \rho_s \frac{\partial m_*}{\partial\theta}\right)\bigg|_{\theta=\bar{\theta}}. \tag{II.C.8}$$

The term f^2/R^2 can be easily identified as the gradient energy density associated with the smooth change of the field, while the effective scale $\Lambda^4_{\rm eff}(\bar{\theta})$ is identified with the gain in potential energy.

Another typically stronger upper bound on f can be derived from the fast transition region of $\theta(r)$, or the bubble wall. It represent the stronger condition for the negligible gradient energy limit, since the gradient energy density associated with the bubble is typically larger and scales like f^2/λ_ϕ^2, where λ_ϕ is the in-medium wavelength characterizing the transition region, to be defined below. Therefore, when $\lambda_\phi \ll R$, the energy density associated with the bubble wall is $(R/\lambda_\phi)^2$ enhanced compared to the gradient energy in the smoothly changing region described in the previous paragraph.

As oppose to the smooth-varying region, the transition region is, by definition, a small region where θ undergoes an $\mathcal{O}(1)$ change in its value from θ_0 to θ_∞ such that $\bar{\theta} \equiv (\theta_\infty + \theta_0)/2 \sim \Delta\theta \equiv \theta_\infty - \theta_0 \sim \mathcal{O}(1)$. Therefore, the Taylor expansion approach used above is not very useful to capture the scaling of the RHS of Eq. (II.C.7) in regions comparable to the transition length. Instead, we use an estimate which is rough yet adequate in the determination of the size of the transition region, characterized by two wavelengths. At low densities, we define the **low-density wavelength** as

$$\lambda_\phi^{\rm low} \equiv \frac{\sqrt{\Delta\theta} f}{\sqrt{(\partial V/\partial\theta)|_{\theta=\bar{\theta}}}}\,. \tag{II.C.9}$$

By using this definition, as oppose to using the vacuum Compton wavelength defined as $m_\phi^{-1} \equiv f/\sqrt{(\partial^2 V/\partial\theta^2)|_{\theta=\theta_0}}$, we avoid potentially misidentifying the relevant scaling of the RHS of Eq. (II.C.7), which can be dominated by higher order terms in the potential once θ is sufficiently far away from θ_0. This can occur for scalar potential which feature more than one scale, like in the quadratic coupling model discussed in Sec. 9.1.2.B. In this example, the potential can be dominated by the quartic term in the potential. This effect, which admittedly requires some fine-tuning in the potential, is nonetheless captured by the definition in Eq. (II.C.9). In natural potentials, defined by a single scale, $\lambda_\phi^{\rm low}$ reduced to m_ϕ^{-1} as expected, like in the ALP model.

We emphasize that $\lambda_\phi^{\rm low}$ *does not* play an important role in determining the upper bound on f in the negligible gradient energy limit, but rather the high-density effective wavelength λ_ϕ which we define below. $\lambda_\phi^{\rm low}$ is still interesting in cases where $\lambda_\phi^{\rm low} \sim \mathcal{O}(R)$. The presence of a non-trivial axion profile outside the star could have interesting implications, such as long rang forces between stars [119]. Note that for hybrid stars, where the our transition region is contained (at least partially) inside the star, $\lambda_\phi^{\rm low}$ receives corrections from the finite density background, but those are at most $\mathcal{O}(1)$, since the crust of the hybrid star is the region where $V(\theta)$ dominates.

The most important scale for the negligible gradient energy limit is the **in-medium** or high-

density **effective wavelength**, defined as

$$\lambda_\phi = \frac{\sqrt{\Delta\theta} f}{\sqrt{\rho_s^{\rm typ}(\partial m/\partial\theta)|_{\theta=\bar\theta}}}\,, \tag{II.C.10}$$

where $\rho_s^{\rm typ}$ is the typical scalar density at the internal edge of the transition region, i.e. the scalar density at the lowest pressure of the internal phase. If the internal state is the new ground state, this would be the scalar density at zero pressure, namely $\rho_s(\theta^{\rm NGS}, \rho^{\rm NGS})$. For a hybrid star, the internal pressure in the critical pressure where the transition occurs. $\rho_s^{\rm typ}$ is usually model dependent and can be determined using the various approximation used *e.g.* in Secs. 9.1.2.A and 9.1.2.B. Let us illustrate how to determine $\rho_s^{\rm typ}$ in a few simple cases:

1. In models where the high-density phase is fixed around θ_∞ where $m_*(\theta_\infty) = 0$, the parameters of the internal phase $\{\theta, \rho\}$ live on the curve of constant scalar density defined by $\rho_s(\theta, \rho) = \rho_{s,\infty}$, where $\rho_{s,\infty}$ is defined in Eq. (9.13). Plugging in Eq. (9.13) in the definition of Eq. (II.C.10), namely $\rho_s^{\rm typ} \approx \rho_{s,\infty}$, one finds that in this case $\lambda_\phi \sim \lambda_\phi^{\rm low} \sim \mathcal{O}(m_\phi^{-1})$ (where the last similarity assumes the potential is not tuned, see discussion below Eq. (II.C.9)). This apply to the quadratic coupling model discussed in Sec. 9.1.2.B, as well as some of the parameters space in the ALP model of Sec. 9.1.2.A, namely the regions where the internal phase is expected to be ultra-relativistic. These are shown in Fig. 9.4 as the dark red and dark green regions, and it is also the case in the $g \gtrsim 1$ region no shown in the plot.

2. In models where the high-density phase is fixed around θ_∞ where $(\frac{\partial m_*(\theta)}{\partial\theta})|_{\theta=\theta_\infty} = 0$, it is generally harder to make a model-independent determination of λ_ϕ. Since most of the $g < 1$ parameter space considered in the ALP model of Sec. 9.1.2.A is relevant for this discussion, we use it as an example. For the different regions in the ALP model, we find

$$\lambda_\phi \approx \frac{f}{\Lambda^2}\begin{cases} \frac{(\Lambda/m)^{4/5}}{g^{1/2}(1-g)^{3/10}} & \text{NR NGS} \\ \frac{(\Lambda/m)^2}{g^{1/2}(1-g)^{3/2}} & \text{UR NGS} \end{cases}, \tag{II.C.11}$$

   For the NR NGS (light-green region of Fig. 9.4) and UR NGS (dark-green and $\theta^{\rm NGS} = \pi$ region of Fig. 9.4), we used the results derived in Eqs. (9.40), (9.41) while neglecting $\mathcal{O}(1)$ factors. From Eq. (II.C.11) it is clear that in certain parts of parameter space one finds that $\lambda_\phi \gg \lambda_\phi^{\rm low} \sim (m_\phi^{\rm ALP})^{-1} \equiv f/\Lambda^2$. As we discussed above, in these situations the scalar profile may survive in the region outside the star, resulting in an axion halo and potentially interesting effects like long-range forces.

Having determined λ_ϕ, we can now conclude that the gradient energy associated with the formation of the bubble wall can be neglected as long as

$$\lambda_\phi \ll R\,, \tag{II.C.12}$$

where R is the size of the object. Note that this implies an upper bound on f using the definition in Eq. (II.C.10). Importantly, when the gradient energy is comparable to the potential energy, i.e. $\lambda_\phi \sim R$, its effects are no longer negligible and the full coupled system of Eq. (9.7) must be solved. For $\lambda_\phi \gg R$, the formation of the bubble is not energetically favorable leading to trivial $\theta = \theta_0$ solutions, equivalent to the decoupling limit $f \to \infty$. Therefore, $\lambda_\phi \lesssim R$, along with the requirement that the object is dense enough, are the condition for the formation of a bubble. Lastly, we note that Eq. (II.C.12) insures we can safely approximate the transition in the field profile $\theta(r)$ as instantaneous compared to the scale of the star, verifying our thin-well description [12, 212].

II.C.2 Temperature Dependence of WD M - R Relation

The M - R relationship for white dwarfs is temperature dependent, a fact that we have neglected so far. However, the effective temperature of some of the heaviest white dwarf with an EOS independent measurement is not too large with $T_{\rm eff} \lesssim 3 \times 10^4\,{\rm K}$. At these temperatures, the M - R relationship only deviates little from the zero temperature limit, see e.g. in Fig. 9 of [253] and references therein.

Detailed studies of the mass of a white dwarf at given core density for different central temperatures can be found e.g. in [268, 269]. To compare this with our data sets one has to find the central temperature from the given effective surface temperature. In order to do so, one needs to know the temperature gradient (i.e. the heat flux) from the core to the surface of the white dwarf. We use the empirical formula, $T_{\rm eff}/g = 2.05 \times 10^{-10} T_c^{2.56}$, to estimate the central temperature [270], which is also used in [268, 269]. Note that $g = GM_{\rm WD}/R_{\rm WD}^2$ is the surface gravity.

For some of the heaviest white dwarfs under consideration we find central temperatures of $T_c \lesssim O({\rm few})10^7{\rm K}$. Following [268, 269], at these temperatures at the same central density one finds modification of the mass of the order of 10%. This modest temperature dependence of some of the heaviest white dwarfs under consideration demonstrates the robustness of our bounds against temperature modifications of the EOS.

Part III

Conclusions

Despite the clear theoretical and experimental evidence that the Standard Model is incomplete, physics beyond the Standard Model has so far evaded our detection. The absence of any signal at the LHC pushed some extensions of the SM like composite Higgs and supersymmetry into the fine-tuned region of the parameter space. On the weakly interacting frontier, in recent years more and more experiments to hunt for the QCD axion and ALPs are being built. Both these directions have been addressed in this thesis: in the first part of the thesis, we explored the phenomenology of a model that addresses the EW Hierarchy Problem without the introduction of light colored states, a composite twin Higgs model. In the second part of the thesis, we explored the rich phenomenology of weakly interacting light scalars, the QCD axion and ALPs, due to their coupling to Standard Model density.

In part I, we studied twin Higgs models, which enjoy phenomenological signatures that, while linked to the naturalness of the electroweak scale, significantly differ from those of the standard TeV solutions of the Hierarchy Problem.

Instead of collider signals associated with the production of colored particles, e.g. top partners, stops and gluinos, that subsequently decay to top/bottom and Higgs/EW gauge bosons or missing energy, in the twin Higgs scenario the phenomenology at low energies is dominated by states that predominantly couple to the SM via the Higgs, thus giving rise for instance to exotic Higgs decays or heavy Higgs-like signatures. These kind of signals are more difficult to detect at colliders such as the LHC, which is the reason why current constrains are mild. More important is however the fact that large luminosities, expected to be delivered by the LHC in the forthcoming years, could potentially set the scales even.

In in Chapter 3, we focused on a model based on the coset $SO(7)/G_2$. As a consequence of the symmetry structure of the strong sector, the Higgs and its twin both carry hypercharge. The coupling to the top and the twin top, which both have electric charge of $2/3$ eliminates the leading sensitivity of the Higgs mass to the cutoff. The misalignment $\xi = \frac{v^2}{f^2}$ between the EW scale and the Higgs decay constant is common to all composite Higgs scenarios. Higgs couplings deviate from those of an elementary Higgs proportionally to ξ, and these departures are constrained by EW precision as well as Higgs coupling measurements.

The novel features of our model however come from the fact that the twins carry hypercharge. While the fraternal scenario with a relatively light Z' is experimentally disfavored, the minimal scenario where we only have a twin top and bottom is much more compelling: it leads to the correct Higgs mass with only a mild amount of tuning. Our model predicts electrically charged scalars that are long-lived on collider scales as well as quirks: these the twin fermions which are charged under a confining gauge group and cannot hardonize. Once pair produced, they form bound states that lose their energy until they decay either to twin glueballs or to SM fermions. The production cross sections are small but detection prospects at HL-LHC are promising. Some of the glueballs are long-lived and decay to di-photons, thus could potentially picked up by a detector like MATHUSLA.

In part II, we switched our focus to light scalar particles. Light scalars are ubiquitous in models beyond the standard model: as a solution to the strong $\mathcal{CP}$ problem, a DM candidate, a dynamical solution to the EW Hierarchy Problem or as dark energy. In this part, we focused on the interaction of light scalar particles with background density, such as dense stars. We studied both the effect that density has on the scalar field as well as the back-reaction of the scalar on the dense object.

The QCD axion as a solution to the strong $\mathcal{CP}$ problem is one of the best motivated particles beyond the standard model, and there is growing experimental effort to detect it. Some of the best constraints on the couplings of the QCD axion to matter come from the observation of the neutrino signal from the SN1987A. In Chapter 7, we studied the density dependence of the

couplings of the QCD axion to nucleons in a systematic expansion in Fermi momentum over cutoff within heavy baryon chiral perturbation theory.

We find large changes in the axion-proton as well as on the axion-neutron coupling at densities and temperatures typical of supernovae as well as of neutron stars. The effect is especially large for the KSVZ axion, where the axion-neutron coupling at zero density is small and even compatible with zero due to an accidental cancellation: at finite density the cancellation is lifted and the coupling goes towards its natural size. This can lead to exciting changes in the bound on axions from SN1987A as well as from neutron star cooling, which we are currently investigating. A future direction is to study the density dependence of the couplings of astrophobic axions, in which the couplings at zero density are tuned small. While this can still be done at loop level, at least naively this seems to breaks down at densities occurring in different astrophysical systems.

In Chapter 8, we looked at models of light scalars with a metastable ground state. To make the physics as transparent as possible, in the first part of this Chapter we focused on a simple two minima potential of Coleman. We derived conditions on when the interaction with matter leads to a destabilisation of the potential in the dense environment, and in addition, when this leads to an escape of a scalar bubble outside of the star and therefore to a phase transition in the universe after star formation.

Crucially, we found that for a bubble to form, the object not only has to be dense enough s.t. the field can classically overcome the barrier, but also large enough such that gradient effects can be overcome. If the metastable minimum is very shallow, all bubbles that form can also escape. However in the generic case of a deep minimum, there also exists another possibility: a scalar bubble can form but is confined to the dense object unless the dense object is large enough to also fulfil the more stringent escape condition.

The density induced phase transitions can only happen after the formation of the first stars, so at redshifts of $z \lesssim 30$, which makes them tightly constrained: one key parameter that determines if scalar bubbles form and escape is the change of vacuum energy between the true and false minimum. At the same time, measurements of the cosmological constant in the early vs late universe constrains a change in the vacuum energy at these times to be $\Delta\rho \lesssim 10^3\rho_0$. Nevertheless, if the distance in field space between the minima is small, we showed that phase transitions triggered by the largest known stars can be consistent with cosmological data. Any evidence of a phase transition seeded by the formation of stars would be revolutionary to our understanding of physics.

In the second part of Chapter 8, we studied the same effect in some benchmark relaxion models. By construction, the relaxion is in a metastable minimum and it is precisely the connection with the Higgs what is behind the sensitivity of the relaxion to Standard Model density. If the barriers are generated by QCD dynamics, it is the density dependence of the quark condensate that leads to a destabilisation at finite density, while if the barriers are generated by some new confining dynamics, it is the change in the Higgs VEV due to the background nucleons that can lead to a destabilisation. Note that especially in the non-QCD case, the change of the scalar potential is small, however, the relaxion minima are dynamically tuned to be very shallow, such that even tiny deformations can destabilise it. We also showed that not only matter density but an electromagnetic background can destabilise a metastable vacuum.

Together with the above mentioned constraint from the change in vacuum energy this allowed us to put novel constraints on these kind of models. Relaxion phase transitions with a very small change in vacuum energy appear to be allowed from all cosmological considerations. These could be induced by either the largest known stars in the universe or by dark stars made out of non-SM fermions. Finally, the new bound on relaxion models derived above can also have non-trivial implications for other landscapes in case these are subject to density modifications.

In Chapter 9 we looked at bubbles of a scalar field that do not have lower vacuum energy, and thus are only preferred at finite density. These bubbles are always confined to the star sourcing them. In particular we studied the back-reaction of the scalar field on the star, which, due to collective effects can be large. For simplicity we focused on the structure of stellar remnants, neutron stars and white dwarfs, and solve the full coupled system. We investigated the coupling of a scalar in a shift-symmetry breaking fashion to a fermion via the fermion mass term. We began this chapter with a simple free Fermi gas of just one fermion, the neutron. This is used as a toy model for neutron stars. The inclusion of the new scalar field can drastically change the structure of neutron stars. This is due to the fact that in the phase where the scalar field is sourced neutrons are lighter, and, to have the same energy density, more neutrons are needed which in turn have more Fermi pressure. While for a linear coupling of the scalar to neutrons, fifth force bounds exclude all the relevant parameter space, in case of a quadratic coupling or an axion-like coupling, the parameter space is largely unconstrained.

This is a novel way to increase the mass of neutron stars, even beyond the so-called causal bounds. While causal bounds assume that equation of state is known at low energies due to nuclear physics, our model also reproduces nuclear physics, however only on a meta-stable branch. In our model, nuclei are only meta-stable and the true ground state of matter is at some finite density with the scalar field sourced. This ground state is however not accessible in small and dilute systems as nuclei or regular stars while dense systems like neutron stars can exist in this new ground state. Depending on the parameters of our model, the neutron stars can also have long range scalar tails.

These features are very exciting in light of the growing catalogue of stellar remnants due to the measurement of gravitational waves from binary systems. The first observed NS-NS merger, GW170817, was already used to put novel constraints on neutron star properties. In the near future many more mergers are expected constraining the properties of neutron stars, thereby probing the parameter space of light scalar fields.

White dwarfs are less dense, however they are much better understood than neutron stars. They consist of a free Fermi gas of electrons with nuclei following them due to charge neutrality. The white dwarf equation of state is well tested for a large ranges of masses and radii. We can use these measurements of white dwarf properties to put novel constraints on light scalars. If a new ground state phase is accessible within white dwarfs, there is some region in the mass-radius curve that cannot be populated: it is in between the meta-stable branch and the new ground state. We can exclude parameter space where this region falls within measured masses and radii of white dwarfs. In the second part of Chapter 9 we used a light QCD axion as a case study to find that white dwarfs exclude a large region of previously unconstrained parameter space. Future tests of the white dwarf mass radius relation with more data will probe more parameter space of light QCD axions.

The interplay between light scalar fields and matter density opens up many new avenues to pursue. In the future we want to study systematically the influence of density dependent couplings of different QCD axion realizations using realistic models of supernovae and neutron stars. The phenomenology of phase transitions seeded from stars is another compelling direction that we are currently investigating, where the imprint of the gravitational wave signal on the CMB might be a smoking gun signal.

Another direction that we are exploring are phase transitions that are seeded from collisions of relaxion bubbles: neglecting non-linearities, due to the superposition principle every collision of bubbles in relaxion models lead to a jump to the next minimum. It seems naively that once relaxion bubbles are formed, this leads to a cascade of phase transitions that only stops in the global minimum. It is ongoing work to quantify the influence of non-linearities and determine

the consequences on various relaxion models. Yet another direction that is worth to explore is the new ground state of neutrons with a scalar field that described above. Currently we are also exploring a formation mechanism of such neutron balls in the early universe and check if, in fact, they can make up the dark matter abundance in our universe.

Acknowledgements

First and foremost I want like to thank my supervisor Andreas Weiler for giving me the opportunity to pursue my doctoral studies in his group. I want to thank him for his constant support, advice and guidance as well as his encouragement to explore different directions during my PhD. This definitely made me a better physicist.

I want to thank Javi Serra for the countless discussions that we had. Without your constant guidance I would not be the physicist I am.

I also want to thank Michael Geller and the whole Tel Aviv theory group for their hospitality and kindness during my visit to Tel Aviv University.

During my PhD I had the pleasure of collaborating and discussing with many excellent scientists, including Reuven Balkin, Konstantin Springmann, Peter Fierlinger, Ennio Salvioni, Michael Geller and Andrea Caputo. I would like to thank all of them for the amazing work atmosphere and the inspiring discussions.
I especially thank Konstantin Springmann for proof-reading parts of the thesis.

My whole PhD would not have been as much fun without my colleagues, fellow PhD students and office mates Konstantin Springmann, Reuven Balkin, Tobias Theil, Max Ruhdorfer, Michael Stadlbauer, Elena Kaiser, Dominik Haslehner, and many others at TUM. It was really an amazing time and I hope we can keep up some of our traditions, like the yearly Weihnachtsmarkt crawl and the Oktoberfest visit.

I want to thank my friends for always being there for me. You made this time special to me.

I want to thank my girlfriend Lina. Thank you for all your love and support.

Finally I want to thank my parents, Erika und Franz, and my brother Christian for their constant support along this journey. Without you this would not have been possible.

Bibliography

[1] ATLAS collaboration, *Observation of a new particle in the search for the Standard Model Higgs boson with the ATLAS detector at the LHC*, *Phys. Lett. B* **716** (2012) 1 [arXiv:1207.7214].

[2] CMS collaboration, *Observation of a New Boson at a Mass of 125 GeV with the CMS Experiment at the LHC*, *Phys. Lett. B* **716** (2012) 30 [arXiv:1207.7235].

[3] B.W. Lee, C. Quigg and H.B. Thacker, *Weak interactions at very high energies: The role of the higgs-boson mass*, *Phys. Rev. D* **16** (1977) 1519.

[4] R. Peccei and H.R. Quinn, *CP Conservation in the Presence of Instantons*, *Phys. Rev. Lett.* **38** (1977) 1440.

[5] R. Peccei and H.R. Quinn, *Constraints Imposed by CP Conservation in the Presence of Instantons*, *Phys. Rev. D* **16** (1977) 1791.

[6] S. Weinberg, *A New Light Boson?*, *Phys. Rev. Lett.* **40** (1978) 223.

[7] F. Wilczek, *Problem of Strong P and T Invariance in the Presence of Instantons*, *Phys. Rev. Lett.* **40** (1978) 279.

[8] P.W. Graham, D.E. Kaplan and S. Rajendran, *Cosmological Relaxation of the Electroweak Scale*, *Phys. Rev. Lett.* **115** (2015) 221801 [arXiv:1504.07551].

[9] G. Dvali and A. Vilenkin, *Cosmic attractors and gauge hierarchy*, *Phys. Rev. D* **70** (2004) 063501 [arXiv:hep-th/0304043].

[10] J. Serra, S. Stelzl, R. Torre and A. Weiler, *Hypercharged Naturalness*, *JHEP* **10** (2019) 060 [arXiv:1905.02203].

[11] R. Balkin, J. Serra, K. Springmann, S. Stelzl and A. Weiler, *Runaway relaxion from finite density*, *JHEP* **06** (2022) 023 [arXiv:2106.11320].

[12] R. Balkin, J. Serra, K. Springmann, S. Stelzl and A. Weiler, *Density Induced Vacuum Instability*, arXiv:2105.13354.

[13] K. Springmann, M. Stadlbauer, S. Stelzl and A. Weiler, "QCD axion couplings at finite density." in preparation.

[14] R. Balkin, J. Serra, K. Springmann, S. Stelzl and A. Weiler, "Heavy Neutron Stars from Light Scalars." in preparation.

[15] R. Balkin, J. Serra, K. Springmann, S. Stelzl and A. Weiler, "White Dwarfs as a Probe of light QCD Axions." in preparation.

[16] Z. Chacko, H.-S. Goh and R. Harnik, *The twin higgs: Natural electroweak breaking from mirror symmetry*, *Phys.Rev.Lett.* **96** (2006) [arXiv:hep-ph/0506256].

[17] R. Barbieri, T. Gregoire and L.J. Hall, *Mirror world at the large hadron collider*, arXiv:hep-ph/0509242.

[18] Z. Chacko, Y. Nomura, M. Papucci and G. Perez, *Natural little hierarchy from a partially goldstone twin higgs*, *JHEP* **01** (2006) 126 [arXiv:hep-ph/0510273].

[19] Z. Chacko, H.-S. Goh and R. Harnik, *A twin higgs model from left-right symmetry*, *JHEP* **01** (2006) 108 [arXiv:hep-ph/0512088].

[20] N. Arkani-Hamed, T. Cohen, R.T. D'Agnolo, A. Hook, H.D. Kim and D. Pinner, *Solving the hierarchy problem at reheating with a large number of degrees of freedom*, *Phys.Rev.Lett.* **117** (2016) 251801 [arXiv:1607.06821].

[21] R. Contino, *The Higgs as a Composite Nambu-Goldstone Boson*, in *Theoretical Advanced Study Institute in Elementary Particle Physics: Physics of the Large and the Small*, pp. 235–306, 2011, DOI [arXiv:1005.4269].

[22] B. Bellazzini, C. Csáki and J. Serra, *Composite Higgses*, *Eur. Phys. J. C* **74** (2014) 2766 [arXiv:1401.2457].

[23] G. Panico and A. Wulzer, *The Composite Nambu-Goldstone Higgs*, vol. 913, Springer (2016), 10.1007/978-3-319-22617-0, [arXiv:1506.01961].

[24] ATLAS collaboration, *Combination of the searches for pair-produced vector-like partners of the third-generation quarks at $\sqrt{s}$ = 13 tev with the atlas detector*, *Phys.Rev.Lett.* **121** (2018) 211801 [arXiv:1808.02343].

[25] CMS collaboration, *Search for vector-like quarks in events with two oppositely charged leptons and jets in proton-proton collisions at $\sqrt{s}$ = 13 tev*, *Eur.Phys.J.C* **79** (2019) 364 [arXiv:1812.09768].

[26] G. Burdman, Z. Chacko, R. Harnik, L. de Lima and C.B. Verhaaren, *Colorless top partners, a 125 gev higgs, and the limits on naturalness*, *Phys.Rev.D* **91** (2015) 055007 [arXiv:1411.3310].

[27] N. Craig, A. Katz, M. Strassler and R. Sundrum, *Naturalness in the dark at the lhc*, *JHEP* **07** (2015) 105 [arXiv:1501.05310].

[28] D. Curtin and P. Saraswat, *Towards a no-lose theorem for naturalness*, *Phys.Rev.D* **93** (2016) 055044 [arXiv:1509.04284].

[29] R. Barbieri, L.J. Hall and K. Harigaya, *Minimal mirror twin higgs*, *JHEP* **11** (2016) 172 [arXiv:1609.05589].

[30] Z. Chacko, C. Kilic, S. Najjari and C.B. Verhaaren, *Collider signals of the mirror twin higgs through the hypercharge portal*, arXiv:1904.11990.

[31] G. Burdman, Z. Chacko, H.-S. Goh and R. Harnik, *Folded supersymmetry and the lep paradox*, *JHEP* **02** (2007) 9 [arXiv:hep-ph/0609152].

[32] H. Cai, H.-C. Cheng and J. Terning, *A quirky little higgs model*, *JHEP* **05** (2009) 45 [arXiv:0812.0843].

[33] R. Barbieri, *Electroweak theory after the first Large Hadron Collider phase*, *Phys. Scripta T* **158** (2013) 014006 [arXiv:1309.3473].

[34] G.F. Giudice, *Naturally Speaking: The Naturalness Criterion and Physics at the LHC*, arXiv:0801.2562.

[35] G. 't Hooft, *Naturalness, chiral symmetry, and spontaneous chiral symmetry breaking*, *NATO Sci. Ser. B* **59** (1980) 135.

[36] S. Dimopoulos and L. Susskind, *Mass Without Scalars*, .

[37] L. Susskind, *Dynamics of Spontaneous Symmetry Breaking in the Weinberg-Salam Theory*, *Phys. Rev. D* **20** (1979) 2619.

[38] S. Weinberg, *Baryon and Lepton Nonconserving Processes*, *Phys. Rev. Lett.* **43** (1979) 1566.

[39] S. Dimopoulos and J. Preskill, *Massless Composites With Massive Constituents*, *Nucl. Phys. B* **199** (1982) 206.

[40] D.B. Kaplan and H. Georgi, *SU(2) x U(1) Breaking by Vacuum Misalignment*, *Phys. Lett. B* **136** (1984) 183.

[41] T. Banks, *CONSTRAINTS ON SU(2) x U(1) BREAKING BY VACUUM MISALIGNMENT*, *Nucl. Phys. B* **243** (1984) 125.

[42] H. Georgi and D.B. Kaplan, *Composite Higgs and Custodial SU(2)*, *Phys. Lett. B* **145** (1984) 216.

[43] D.B. Kaplan, H. Georgi and S. Dimopoulos, *Composite Higgs Scalars*, *Phys. Lett. B* **136** (1984) 187.

[44] M.J. Dugan, H. Georgi and D.B. Kaplan, *Anatomy of a Composite Higgs Model*, *Nucl. Phys. B* **254** (1985) 299.

[45] C. Csáki, S. Lombardo and O. Telem, *TASI Lectures on Non-supersymmetric BSM Models*, in *Proceedings, Theoretical Advanced Study Institute in Elementary Particle Physics : Anticipating the Next Discoveries in Particle Physics (TASI 2016): Boulder, CO, USA, June 6-July 1, 2016*, R. Essig and I. Low, eds., pp. 501–570, WSP (2018), DOI [arXiv:1811.04279].

[46] S.R. Coleman, J. Wess and B. Zumino, *Structure of phenomenological Lagrangians. 1.*, *Phys. Rev.* **177** (1969) 2239.

[47] C.G. Callan, Jr., S.R. Coleman, J. Wess and B. Zumino, *Structure of phenomenological Lagrangians. 2.*, *Phys. Rev.* **177** (1969) 2247.

[48] D.B. Kaplan, *Flavor at SSC energies: A New mechanism for dynamically generated fermion masses*, *Nucl. Phys. B* **365** (1991) 259.

[49] R. Contino, D. Greco, R. Mahbubani, R. Rattazzi and R. Torre, *Precision tests and fine tuning in twin higgs models*, *Phys.Rev.D* **96** (2017) [arXiv:1702.00797].

[50] M. Geller and O. Telem, *Holographic twin higgs model*, *Phys.Rev.Lett.* **114** (2015) [arXiv:1411.2974].

[51] M. Low, A. Tesi and L.-T. Wang, *Twin higgs mechanism and a composite higgs boson*, *Phys.Rev.D* **91** (2015) [arXiv:1501.07890].

[52] R. Barbieri, D. Greco, R. Rattazzi and A. Wulzer, *The composite twin higgs scenario*, *JHEP* **08** (2015) 161 [arXiv:1501.07803].

[53] J. Mrazek, A. Pomarol, R. Rattazzi, M. Redi, J. Serra and A. Wulzer, *The Other Natural Two Higgs Doublet Model*, *Nucl. Phys. B* **853** (2011) 1 [arXiv:1105.5403].

[54] M. Chala, $h \to \gamma\gamma$ *excess and Dark Matter from Composite Higgs Models*, *JHEP* **01** (2013) 122 [arXiv:1210.6208].

[55] G. Ballesteros, A. Carmona and M. Chala, *Exceptional Composite Dark Matter*, *Eur. Phys. J. C* **77** (2017) 468 [arXiv:1704.07388].

[56] J. Serra and R. Torre, *Neutral naturalness from the brother-higgs model*, *Phys.Rev.D* **97** (2018) 035017 [arXiv:1709.05399].

[57] C. Csáki, T. Ma and J. Shu, *Trigonometric parity for composite higgs models*, *Phys.Rev.Lett.* **121** (2018) 231801 [arXiv:1709.08636].

[58] N. Craig, S. Knapen, P. Longhi and M. Strassler, *The vector-like twin higgs*, *JHEP* **07** (2016) 2 [arXiv:1601.07181].

[59] D. Greco and K. Mimouni, *The rg-improved twin higgs effective potential at nnll*, *JHEP* **11** (2016) 108 [arXiv:1609.05922].

[60] C. Csaki, M. Geller, O. Telem and A. Weiler, *The flavor of the composite twin higgs*, *JHEP* **09** (2016) 146 [arXiv:1512.03427].

[61] B. Keren-Zur, P. Lodone, M. Nardecchia, D. Pappadopulo, R. Rattazzi and L. Vecchi, *On partial compositeness and the cp asymmetry in charm decays*, *Nucl.Phys.B* **867** (2013) 394 [arXiv:1205.5803].

[62] M. Frigerio, M. Nardecchia, J. Serra and L. Vecchi, *The bearable compositeness of leptons*, *JHEP* **10** (2018) 17 [arXiv:1807.04279].

[63] J. Kang and M.A. Luty, *Macroscopic strings and 'quirks' at colliders*, *JHEP* **11** (2009) 65 [arXiv:0805.4642].

[64] G. Burdman, Z. Chacko, H.-S. Goh, R. Harnik and C.A. Krenke, *The quirky collider signals of folded supersymmetry*, *Phys.Rev.D* **78** (2008) 075028 [arXiv:0805.4667].

[65] R. Barbieri, A. Pomarol, R. Rattazzi and A. Strumia, *Electroweak symmetry breaking after lep-1 and lep-2*, *Nucl.Phys.B* **703** (2004) 127 [arXiv:hep-ph/0405040].

[66] O. Domenech, A. Pomarol and J. Serra, *Probing the sm with dijets at the lhc*, *Phys.Rev.D* **85** (2012) 074030 [arXiv:1201.6510].

[67] M. Farina, G. Panico, D. Pappadopulo, J.T. Ruderman, R. Torre and A. Wulzer, *Energy helps accuracy: electroweak precision tests at hadron colliders*, *Phys.Lett.B* **772** (2017) 210 [arXiv:1609.08157].

[68] D.S.M. Alves, J. Galloway, J.T. Ruderman and J.R. Walsh, *Running electroweak couplings as a probe of new physics*, *JHEP* **02** (2015) 7 [arXiv:1410.6810].

[69] G.F. Giudice, C. Grojean, A. Pomarol and R. Rattazzi, *The Strongly-Interacting Light Higgs*, *JHEP* **06** (2007) 045 [arXiv:hep-ph/0703164].

[70] A. Martin, W. Stirling, R. Thorne and G. Watt, *Parton distributions for the lhc*, *Eur.Phys.J.C* **63** (2009) 189 [arXiv:0901.0002].

[71] ATLAS collaboration, *Search for heavy charged long-lived particles in the atlas detector in 36.1 fb^{-1} of proton-proton collision data at $\sqrt{s} = 13$ tev*, *Phys.Rev.D* **99** (2019) [arXiv:1902.01636].

[72] ALEPH and DELPHI and L3 and OPAL and SLD and LEP Electroweak Working Group and SLD Electroweak Group and SLD Heavy Flavour Group collaboration, *Precision electroweak measurements on the z resonance*, *Phys.Rept.* **427** (2006) 257 [arXiv:hep-ex/0509008].

[73] ALEPH and DELPHI and L3 and OPAL and LEP Electroweak collaboration, *Electroweak measurements in electron-positron collisions at w-boson-pair energies at lep*, *Phys.Rept.* **532** (2013) 119 [arXiv:1302.3415].

[74] R. Harnik and T. Wizansky, *Signals of new physics in the underlying event*, *Phys.Rev.D* **80** (2009) 075015 [arXiv:0810.3948].

[75] H.-C. Cheng, E. Salvioni and Y. Tsai, *Exotic electroweak signals in the twin higgs model*, *Phys.Rev.D* **95** (2017) 115035 [arXiv:1612.03176].

[76] L. Li, E. Salvioni, Y. Tsai and R. Zheng, *Electroweak-charged bound states as lhc probes of hidden forces*, *Phys.Rev.D* **97** (2018) 015010 [arXiv:1710.06437].

[77] V.D. Barger, E. Glover, K. Hikasa, W.-Y. Keung, M. Olsson, I. Suchyta, C.J. et al., *Superheavy quarkonium production and decays: A new higgs signal*, *Phys.Rev.D, Phys.Rev.D* **35, 38** (1987) 3366.

[78] K. Cheung, W.-Y. Keung and T.-C. Yuan, *Phenomenology of iquarkonium*, *Nucl.Phys.B* **811** (2009) 274 [arXiv:0810.1524].

[79] R. Fok and G.D. Kribs, *Chiral quirkonium decays*, *Phys.Rev.D* **84** (2011) 035001 [arXiv:1106.3101].

[80] ATLAS collaboration, *Search for new high-mass phenomena in the dilepton final state using 36 fb^{-1} of proton-proton collision data at $\sqrt{s} = 13$ tev with the atlas detector*, *JHEP* **10** (2017) 182 [arXiv:1707.02424].

[81] ATLAS collaboration, *Search for high-mass dilepton resonances using 139 fb^{-1} of pp collision data collected at $\sqrt{s}$ =13 tev with the atlas detector*, arXiv:1903.06248.

[82] H.-C. Cheng, L. Li, E. Salvioni and C.B. Verhaaren, *Singlet Scalar Top Partners from Accidental Supersymmetry*, *JHEP* **05** (2018) 057 [arXiv:1803.03651].

[83] Working Group 3 collaboration, *Beyond the standard model physics at the hl-lhc and he-lhc*, arXiv:1812.07831.

[84] ATLAS collaboration, *Search for heavy resonances decaying to a photon and a hadronically decaying $z/w/h$ boson in pp collisions at $\sqrt{s} = 13$ TeV with the atlas detector*, *Phys.Rev.D* **98** (2018) 032015 [arXiv:1805.01908].

[85] ATLAS collaboration, *Search for new phenomena in high-mass diphoton final states using 37 fb^{-1} of proton–proton collisions collected at $\sqrt{s} = 13$ tev with the atlas detector*, *Phys.Lett.B* **775** (2017) 105 [arXiv:1707.04147].

[86] T. Cohen, N. Craig, G.F. Giudice and M. Mccullough, *The Hyperbolic Higgs*, *JHEP* **05** (2018) 091 [arXiv:1803.03647].

[87] J.E. Juknevich, D. Melnikov and M.J. Strassler, *A pure-glue hidden valley i. states and decays*, *JHEP* **07** (2009) 55 [arXiv:0903.0883].

[88] J.E. Juknevich, *Pure-glue hidden valleys through the higgs portal*, *JHEP* **08** (2010) 121 [arXiv:0911.5616].

[89] G. Burdman and G. Lichtenstein, *Displaced vertices from hidden glue*, *JHEP* **08** (2018) 146 [arXiv:1807.03801].

[90] D. Curtin, M. Drewes, M. McCullough, P. Meade, R.N. Mohapatra, J. Shelton et al., *Long-lived particles at the energy frontier: The mathusla physics case*, arXiv:1806.07396.

[91] V.V. Gligorov, S. Knapen, M. Papucci and D.J. Robinson, *Searching for long-lived particles: A compact detector for exotics at lhcb*, *Phys.Rev.D* **97** (2018) 015023 [arXiv:1708.09395].

[92] V.V. Gligorov, S. Knapen, B. Nachman, M. Papucci and D.J. Robinson, *Leveraging the alice/l3 cavern for long-lived particle searches*, *Phys.Rev.D* **99** (2019) 015023 [arXiv:1810.03636].

[93] ATLAS collaboration, *Search for long-lived, weakly interacting particles that decay to displaced hadronic jets in proton-proton collisions at $\sqrt{s} = 8$ tev with the atlas detector*, *Phys.Rev.D* **92** (2015) [arXiv:1504.03634].

[94] C. Csaki, E. Kuflik, S. Lombardo and O. Slone, *Searching for displaced higgs boson decays*, *Phys.Rev.D* **92** (2015) 073008 [arXiv:1508.01522].

[95] HL/HE WG2 group collaboration, *Higgs physics at the hl-lhc and he-lhc*, arXiv:1902.00134.

[96] D. Curtin and C.B. Verhaaren, *Discovering uncolored naturalness in exotic higgs decays*, *JHEP* **12** (2015) 72 [arXiv:1506.06141].

[97] Z. Chacko, D. Curtin and C.B. Verhaaren, *A quirky probe of neutral naturalness*, *Phys.Rev.D* **94** (2016) 011504 [arXiv:1512.05782].

[98] A. Coccaro, D. Curtin, H. Lubatti, H. Russell and J. Shelton, *Data-driven model-independent searches for long-lived particles at the lhc*, *Phys.Rev.D* **94** (2016) 113003 [arXiv:1605.02742].

[99] C. Kilic, S. Najjari and C.B. Verhaaren, *Discovering the twin higgs boson with displaced decays*, *Phys.Rev.D* **99** (2019) 075029 [arXiv:1812.08173].

[100] ATLAS collaboration, *Search for long-lived neutral particles in pp collisions at $\sqrt{s} = 13$ tev that decay into displaced hadronic jets in the atlas calorimeter*, arXiv:1902.03094.

[101] CMS collaboration, *Search for long-lived particles decaying to photons and missing energy in proton-proton collisions at $\sqrt{s} = 7$ tev*, *Phys.Lett.B* **722** (2013) 273 [arXiv:1212.1838].

[102] ATLAS collaboration, *Search for nonpointing and delayed photons in the diphoton and missing transverse momentum final state in 8 tev pp collisions at the lhc using the atlas detector*, *Phys.Rev.D* **90** (2014) 112005 [arXiv:1409.5542].

[103] I.G. Irastorza and J. Redondo, *New experimental approaches in the search for axion-like particles*, *Prog. Part. Nucl. Phys.* **102** (2018) 89 [arXiv:1801.08127].

[104] S.R. Coleman, *The Fate of the False Vacuum. 1. Semiclassical Theory*, *Phys. Rev. D* **15** (1977) 2929.

[105] J. Callan, Curtis G. and S.R. Coleman, *The Fate of the False Vacuum. 2. First Quantum Corrections*, *Phys. Rev. D* **16** (1977) 1762.

[106] A.D. Linde, *Fate of the False Vacuum at Finite Temperature: Theory and Applications*, *Phys. Lett. B* **100** (1981) 37.

[107] A.D. Linde, *Decay of the False Vacuum at Finite Temperature*, *Nucl. Phys. B* **216** (1983) 421.

[108] S. Weinberg, *Anthropic Bound on the Cosmological Constant*, *Phys. Rev. Lett.* **59** (1987) 2607.

[109] R. Bousso and J. Polchinski, *Quantization of four form fluxes and dynamical neutralization of the cosmological constant*, *JHEP* **06** (2000) 006 [arXiv:hep-th/0004134].

[110] L. Susskind, *The Anthropic landscape of string theory*, arXiv:hep-th/0302219.

[111] V. Agrawal, S.M. Barr, J.F. Donoghue and D. Seckel, *Viable range of the mass scale of the standard model*, *Phys. Rev. D* **57** (1998) 5480 [arXiv:hep-ph/9707380].

[112] N. Arkani-Hamed, S. Dimopoulos and S. Kachru, *Predictive landscapes and new physics at a TeV*, arXiv:hep-th/0501082.

[113] A. Arvanitaki, S. Dimopoulos, V. Gorbenko, J. Huang and K. Van Tilburg, *A small weak scale from a small cosmological constant*, *JHEP* **05** (2017) 071 [arXiv:1609.06320].

[114] N. Arkani-Hamed, R.T. D'Agnolo and H.D. Kim, *The Weak Scale as a Trigger*, arXiv:2012.04652.

[115] T.D. Cohen, R. Furnstahl and D.K. Griegel, *Quark and gluon condensates in nuclear matter*, *Phys. Rev. C* **45** (1992) 1881.

[116] M.G. Alford, K. Rajagopal and F. Wilczek, *QCD at finite baryon density: Nucleon droplets and color superconductivity*, *Phys. Lett. B* **422** (1998) 247 [arXiv:hep-ph/9711395].

[117] J. Khoury, *Chameleon Field Theories*, *Class. Quant. Grav.* **30** (2013) 214004 [arXiv:1306.4326].

[118] R. Balkin, J. Serra, K. Springmann and A. Weiler, *The QCD axion at finite density*, *JHEP* **07** (2020) 221 [arXiv:2003.04903].

[119] A. Hook and J. Huang, *Probing axions with neutron star inspirals and other stellar processes*, *JHEP* **06** (2018) 036 [arXiv:1708.08464].

[120] LIGO Scientific, Virgo collaboration, *GWTC-1: A Gravitational-Wave Transient Catalog of Compact Binary Mergers Observed by LIGO and Virgo during the First and Second Observing Runs*, *Phys. Rev. X* **9** (2019) 031040 [arXiv:1811.12907].

[121] LIGO Scientific, Virgo collaboration, *GWTC-2: Compact Binary Coalescences Observed by LIGO and Virgo During the First Half of the Third Observing Run*, *Phys. Rev. X* **11** (2021) 021053 [arXiv:2010.14527].

[122] LIGO Scientific, VIRGO, KAGRA collaboration, *GWTC-3: Compact Binary Coalescences Observed by LIGO and Virgo During the Second Part of the Third Observing Run*, arXiv:2111.03606.

[123] A. Hook, *Solving the Hierarchy Problem Discretely*, *Phys. Rev. Lett.* **120** (2018) 261802 [arXiv:1802.10093].

[124] L. Di Luzio, B. Gavela, P. Quilez and A. Ringwald, *An even lighter QCD axion*, *JHEP* **05** (2021) 184 [arXiv:2102.00012].

[125] A. Hook, *TASI Lectures on the Strong CP Problem and Axions*, *PoS* **TASI2018** (2019) 004 [arXiv:1812.02669].

[126] C. Vafa and E. Witten, *Parity Conservation in QCD*, *Phys. Rev. Lett.* **53** (1984) 535.

[127] S. Coleman, *Aspects of Symmetry: Selected Erice Lectures*, Cambridge University Press (1985), 10.1017/CBO9780511565045.

[128] J.M. Pendlebury et al., *Revised experimental upper limit on the electric dipole moment of the neutron*, *Phys. Rev. D* **92** (2015) 092003 [arXiv:1509.04411].

[129] M. Pospelov and A. Ritz, *Theta vacua, QCD sum rules, and the neutron electric dipole moment*, *Nucl. Phys. B* **573** (2000) 177 [arXiv:hep-ph/9908508].

[130] T. Donnelly, S. Freedman, R. Lytel, R. Peccei and M. Schwartz, *Do Axions Exist?*, *Phys. Rev. D* **18** (1978) 1607.

[131] J.E. Kim, *Weak Interaction Singlet and Strong CP Invariance*, *Phys. Rev. Lett.* **43** (1979) 103.

[132] M.A. Shifman, A. Vainshtein and V.I. Zakharov, *Can Confinement Ensure Natural CP Invariance of Strong Interactions?*, *Nucl. Phys. B* **166** (1980) 493.

[133] M. Dine, W. Fischler and M. Srednicki, *A Simple Solution to the Strong CP Problem with a Harmless Axion*, *Phys. Lett. B* **104** (1981) 199.

[134] A. Zhitnitsky, *On Possible Suppression of the Axion Hadron Interactions. (In Russian)*, *Sov. J. Nucl. Phys.* **31** (1980) 260.

[135] P. Svrcek and E. Witten, *Axions In String Theory*, *JHEP* **06** (2006) 051 [arXiv:hep-th/0605206].

[136] G. Grilli di Cortona, E. Hardy, J. Pardo Vega and G. Villadoro, *The QCD axion, precisely*, *JHEP* **01** (2016) 034 [arXiv:1511.02867].

[137] S. Scherer, *Introduction to chiral perturbation theory*, *Adv. Nucl. Phys.* **27** (2003) 277 [arXiv:hep-ph/0210398].

[138] V. Bernard, N. Kaiser and U.-G. Meissner, *Chiral dynamics in nucleons and nuclei*, *Int. J. Mod. Phys. E* **4** (1995) 193 [arXiv:hep-ph/9501384].

[139] H. Georgi, *Weak interactions and modern particle theory*, 1984.

[140] F. Capozzi and G. Raffelt, *Axion and neutrino bounds improved with new calibrations of the tip of the red-giant branch using geometric distance determinations*, *Phys. Rev. D* **102** (2020) 083007 [arXiv:2007.03694].

[141] O. Straniero, C. Pallanca, E. Dalessandro, I. Dominguez, F.R. Ferraro, M. Giannotti et al., *The RGB tip of galactic globular clusters and the revision of the axion-electron coupling bound*, *Astron. Astrophys.* **644** (2020) A166 [arXiv:2010.03833].

[142] G.G. Raffelt, *Axion Constraints From White Dwarf Cooling Times*, *Phys. Lett. B* **166** (1986) 402.

[143] M.M. Miller Bertolami, B.E. Melendez, L.G. Althaus and J. Isern, *Revisiting the axion bounds from the Galactic white dwarf luminosity function*, *JCAP* **10** (2014) 069 [arXiv:1406.7712].

[144] M. Koshiba, *Observational neutrino astrophysics*, *Physics Reports* **220** (1992) 229.

[145] R. Bollig, N. Yadav, D. Kresse, H.T. Janka, B. Müller and A. Heger, *Self-consistent 3D Supernova Models From −7 Minutes to +7 s: A 1-bethe Explosion of a ∼19 $M_\odot$ Progenitor*, *Astrophys. J.* **915** (2021) 28 [arXiv:2010.10506].

[146] G.G. Raffelt, *Astrophysical methods to constrain axions and other novel particle phenomena*, *Phys. Rept.* **198** (1990) 1.

[147] R.P. Brinkmann and M.S. Turner, *Numerical Rates for Nucleon-Nucleon Axion Bremsstrahlung*, *Phys. Rev. D* **38** (1988) 2338.

[148] P. Carenza, T. Fischer, M. Giannotti, G. Guo, G. Martínez-Pinedo and A. Mirizzi, *Improved axion emissivity from a supernova via nucleon-nucleon bremsstrahlung*, *JCAP* **10** (2019) 016 [arXiv:1906.11844].

[149] M.V. Beznogov, E. Rrapaj, D. Page and S. Reddy, *Constraints on Axion-like Particles and Nucleon Pairing in Dense Matter from the Hot Neutron Star in HESS J1731-347*, *Phys. Rev. C* **98** (2018) 035802 [arXiv:1806.07991].

[150] K. Hamaguchi, N. Nagata, K. Yanagi and J. Zheng, *Limit on the Axion Decay Constant from the Cooling Neutron Star in Cassiopeia A*, *Phys. Rev. D* **98** (2018) 103015 [arXiv:1806.07151].

[151] A. Sedrakian, *Axion cooling of neutron stars*, *Phys. Rev. D* **93** (2016) 065044 [arXiv:1512.07828].

[152] J. Keller and A. Sedrakian, *Axions from cooling compact stars*, *Nucl. Phys. A* **897** (2013) 62 [arXiv:1205.6940].

[153] J. Espinosa, C. Grojean, G. Panico, A. Pomarol, O. Pujolàs and G. Servant, *Cosmological Higgs-Axion Interplay for a Naturally Small Electroweak Scale*, *Phys. Rev. Lett.* **115** (2015) 251803 [arXiv:1506.09217].

[154] E. Hardy, *Electroweak relaxation from finite temperature*, *JHEP* **11** (2015) 077 [arXiv:1507.07525].

[155] A. Hook and G. Marques-Tavares, *Relaxation from particle production*, *JHEP* **12** (2016) 101 [arXiv:1607.01786].

[156] N. Fonseca, E. Morgante and G. Servant, *Higgs relaxation after inflation*, *JHEP* **10** (2018) 020 [arXiv:1805.04543].

[157] N. Fonseca, E. Morgante, R. Sato and G. Servant, *Relaxion Fluctuations (Self-stopping Relaxion) and Overview of Relaxion Stopping Mechanisms*, *JHEP* **05** (2020) 080 [arXiv:1911.08473].

[158] A. Nelson and C. Prescod-Weinstein, *Relaxion: A Landscape Without Anthropics*, *Phys. Rev.* **D96** (2017) 113007 [arXiv:1708.00010].

[159] A. Banerjee, H. Kim, O. Matsedonskyi, G. Perez and M.S. Safronova, *Probing the Relaxed Relaxion at the Luminosity and Precision Frontiers*, *JHEP* **07** (2020) 153 [arXiv:2004.02899].

[160] N.K. Glendenning, *Compact stars: Nuclear physics, particle physics, and general relativity*, Springer New York (1997).

[161] J.M. Lattimer, *The nuclear equation of state and neutron star masses*, *Ann. Rev. Nucl. Part. Sci.* **62** (2012) 485 [arXiv:1305.3510].

[162] P. de Forcrand, *Simulating QCD at finite density*, *PoS* **LAT2009** (2009) 010 [arXiv:1005.0539].

[163] NANOGrav collaboration, *Relativistic Shapiro delay measurements of an extremely massive millisecond pulsar*, *Nature Astron.* **4** (2019) 72 [arXiv:1904.06759].

[164] J. Menendez, D. Gazit and A. Schwenk, *Chiral two-body currents in nuclei: Gamow-Teller transitions and neutrinoless double-beta decay*, *Phys. Rev. Lett.* **107** (2011) 062501 [arXiv:1103.3622].

[165] S. Weinberg, *Phenomenological Lagrangians*, *Physica A* **96** (1979) 327.

[166] S. Weinberg, *Nuclear forces from chiral Lagrangians*, *Phys. Lett. B* **251** (1990) 288.

[167] S. Weinberg, *Effective chiral Lagrangians for nucleon - pion interactions and nuclear forces*, *Nucl. Phys. B* **363** (1991) 3.

[168] S. Weinberg, *Three body interactions among nucleons and pions*, *Phys. Lett. B* **295** (1992) 114 [arXiv:hep-ph/9209257].

[169] H. Krebs, *Nuclear Currents in Chiral Effective Field Theory*, *Eur. Phys. J. A* **56** (2020) 234 [arXiv:2008.00974].

[170] E. Epelbaum, *Four-nucleon force using the method of unitary transformation*, *Eur. Phys. J. A* **34** (2007) 197 [arXiv:0710.4250].

[171] R.J. Furnstahl and B.D. Serot, *Covariant Feynman rules at finite temperature: Time-path formulation*, *Phys. Rev. C* **44** (1991) 2141.

[172] M. Quiros, *Finite temperature field theory and phase transitions*, in *ICTP Summer School in High-Energy Physics and Cosmology*, pp. 187–259, 1, 1999 [arXiv:hep-ph/9901312].

[173] J.W. Holt, M. Rho and W. Weise, *Chiral symmetry and effective field theories for hadronic, nuclear and stellar matter*, *Phys. Rept.* **621** (2016) 2 [arXiv:1411.6681].

[174] T. Vonk, F.-K. Guo and U.-G. Meißner, *Precision calculation of the axion-nucleon coupling in chiral perturbation theory*, *JHEP* **03** (2020) 138 [arXiv:2001.05327].

[175] D. Siemens, V. Bernard, E. Epelbaum, A.M. Gasparyan, H. Krebs and U.-G. Meißner, *Elastic and inelastic pion-nucleon scattering to fourth order in chiral perturbation theory*, *Phys. Rev. C* **96** (2017) 055205 [arXiv:1704.08988].

[176] V. Bernard, N. Kaiser and U.-G. Meissner, *Aspects of chiral pion - nucleon physics*, *Nucl. Phys. A* **615** (1997) 483 [arXiv:hep-ph/9611253].

[177] P. Gysbers et al., *Discrepancy between experimental and theoretical β-decay rates resolved from first principles*, *Nature Phys.* **15** (2019) 428 [arXiv:1903.00047].

[178] R. Bollig, H.T. Janka, A. Lohs, G. Martinez-Pinedo, C.J. Horowitz and T. Melson, *Muon Creation in Supernova Matter Facilitates Neutrino-driven Explosions*, *Phys. Rev. Lett.* **119** (2017) 242702 [arXiv:1706.04630].

[179] P. Brax and C. Burrage, *Screening the Higgs portal*, arXiv:2101.10693.

[180] R. Balkin, J. Serra, K. Springmann, S. Stelzl and A. Weiler, *to appear*, .

[181] R. Foot, *Have mirror stars been observed?*, *Phys. Lett. B* **452** (1999) 83 [arXiv:astro-ph/9902065].

[182] G. Narain, J. Schaffner-Bielich and I.N. Mishustin, *Compact stars made of fermionic dark matter*, *Phys. Rev. D* **74** (2006) 063003 [arXiv:astro-ph/0605724].

[183] D. Spolyar, K. Freese and P. Gondolo, *Dark matter and the first stars: a new phase of stellar evolution*, *Phys. Rev. Lett.* **100** (2008) 051101 [arXiv:0705.0521].

[184] F. Sandin and P. Ciarcelluti, *Effects of mirror dark matter on neutron stars*, *Astropart. Phys.* **32** (2009) 278 [arXiv:0809.2942].

[185] C. Kouvaris and N.G. Nielsen, *Asymmetric Dark Matter Stars*, *Phys. Rev. D* **92** (2015) 063526 [arXiv:1507.00959].

[186] M.I. Gresham and K.M. Zurek, *Asymmetric Dark Stars and Neutron Star Stability*, *Phys. Rev. D* **99** (2019) 083008 [arXiv:1809.08254].

[187] D. Curtin and J. Setford, *Signatures of Mirror Stars*, *JHEP* **03** (2020) 041 [arXiv:1909.04072].

[188] D. Curtin and J. Setford, *How To Discover Mirror Stars*, *Phys. Lett. B* **804** (2020) 135391 [arXiv:1909.04071].

[189] M. Hippert, J. Setford, H. Tan, D. Curtin, J. Noronha-Hostler and N. Yunes, *Mirror Neutron Stars*, arXiv:2103.01965.

[190] S. Shapiro and S. Teukolsky, *Black holes, white dwarfs, and neutron stars: The physics of compact objects* (1983).

[191] J. Lattimer and M. Prakash, *The physics of neutron stars*, *Science* **304** (2004) 536 [arXiv:astro-ph/0405262].

[192] J. Pons, S. Reddy, M. Prakash, J. Lattimer and J. Miralles, *Evolution of protoneutron stars*, *Astrophys. J.* **513** (1999) 780 [arXiv:astro-ph/9807040].

[193] G.W. Anderson and L.J. Hall, *The Electroweak phase transition and baryogenesis*, *Phys. Rev. D* **45** (1992) 2685.

[194] E.J. Weinberg, *Classical solutions in quantum field theory: Solitons and Instantons in High Energy Physics*, Cambridge Monographs on Mathematical Physics, Cambridge University Press (9, 2012), 10.1017/CBO9781139017787.

[195] W.A. Hiscock, *Can Black Holes Nucleate Vacuum Phase Transitions?*, *Phys. Rev. D* **35** (1987) 1161.

[196] D.R. Green, E. Silverstein and D. Starr, *Attractor explosions and catalyzed vacuum decay*, *Phys. Rev. D* **74** (2006) 024004 [arXiv:hep-th/0605047].

[197] R. Gregory, I.G. Moss and B. Withers, *Black holes as bubble nucleation sites*, *JHEP* **03** (2014) 081 [arXiv:1401.0017].

[198] K. Mukaida and M. Yamada, *False Vacuum Decay Catalyzed by Black Holes*, *Phys. Rev. D* **96** (2017) 103514 [arXiv:1706.04523].

[199] N. Oshita, M. Yamada and M. Yamaguchi, *Compact objects as the catalysts for vacuum decays*, *Phys. Lett. B* **791** (2019) 149 [arXiv:1808.01382].

[200] K.-M. Lee and E.J. Weinberg, *Tunneling without barriers*, *Nucl. Phys. B* **267** (1986) 181.

[201] I.K. Affleck and F. De Luccia, *Induced Vacuum Decay*, *Phys. Rev. D* **20** (1979) 3168.

[202] B. Grinstein and C.W. Murphy, *Semiclassical Approach to Heterogeneous Vacuum Decay*, *JHEP* **12** (2015) 063 [arXiv:1509.05405].

[203] P. Madau and M. Dickinson, *Cosmic Star Formation History*, *Ann. Rev. Astron. Astrophys.* **52** (2014) 415 [arXiv:1403.0007].

[204] J. Garriga and A. Vilenkin, *Solutions to the cosmological constant problems*, *Phys. Rev. D* **64** (2001) 023517 [arXiv:hep-th/0011262].

[205] M. Pospelov, S. Pustelny, M. Ledbetter, D. Jackson Kimball, W. Gawlik and D. Budker, *Detecting Domain Walls of Axionlike Models Using Terrestrial Experiments*, *Phys. Rev. Lett.* **110** (2013) 021803 [arXiv:1205.6260].

[206] L. Abbott, *A Mechanism for Reducing the Value of the Cosmological Constant*, *Phys. Lett. B* **150** (1985) 427.

[207] L. Verde, T. Treu and A. Riess, *Tensions between the Early and the Late Universe*, 7, 2019, DOI [arXiv:1907.10625].

[208] L. Knox and M. Millea, *Hubble constant hunter's guide*, *Phys. Rev. D* **101** (2020) 043533 [arXiv:1908.03663].

[209] T. Karwal and M. Kamionkowski, *Dark energy at early times, the Hubble parameter, and the string axiverse*, *Phys. Rev. D* **94** (2016) 103523 [arXiv:1608.01309].

[210] J. Yoo and R.J. Scherrer, *Big bang nucleosynthesis and cosmic microwave background constraints on the time variation of the Higgs vacuum expectation value*, *Phys. Rev.* **D67** (2003) 043517 [arXiv:astro-ph/0211545].

[211] G. D'Amico, A. Strumia, A. Urbano and W. Xue, *Direct anthropic bound on the weak scale from supernovæ explosions*, *Phys. Rev. D* **100** (2019) 083013 [arXiv:1906.00986].

[212] A. Hook and J. Huang, *Searches for other vacua. Part I. Bubbles in our universe*, *JHEP* **08** (2019) 148 [arXiv:1904.00020].

[213] T. Flacke, C. Frugiuele, E. Fuchs, R.S. Gupta and G. Perez, *Phenomenology of relaxion-Higgs mixing*, *JHEP* **06** (2017) 050 [arXiv:1610.02025].

[214] R. Budnik, H. Kim, O. Matsedonskyi, G. Perez and Y. Soreq, *Probing the relaxed relaxion and Higgs-portal with S1 \& S2*, arXiv:2006.14568.

[215] S. Chang, J. Galloway, M. Luty, E. Salvioni and Y. Tsai, *Phenomenology of Induced Electroweak Symmetry Breaking*, *JHEP* **03** (2015) 017 [arXiv:1411.6023].

[216] R. Harnik, K. Howe and J. Kearney, *Tadpole-Induced Electroweak Symmetry Breaking and pNGB Higgs Models*, *JHEP* **03** (2017) 111 [arXiv:1603.03772].

[217] B. Garbrecht and J. McDonald, *Axion configurations around pulsars*, *JCAP* **07** (2018) 044 [arXiv:1804.04224].

[218] A.K. Harding, *The Neutron Star Zoo*, *Front. Phys. (Beijing)* **8** (2013) 679 [arXiv:1302.0869].

[219] CAST collaboration, *New CAST Limit on the Axion-Photon Interaction*, *Nature Phys.* **13** (2017) 584 [arXiv:1705.02290].

[220] OSQAR collaboration, *New exclusion limits on scalar and pseudoscalar axionlike particles from light shining through a wall*, *Phys. Rev. D* **92** (2015) 092002 [arXiv:1506.08082].

[221] T.C. Bachlechner, K. Eckerle, O. Janssen and M. Kleban, *Multiple-axion framework*, *Phys. Rev. D* **98** (2018) 061301 [arXiv:1703.00453].

[222] A. Strumia and D. Teresi, *Relaxing the Higgs mass and its vacuum energy by living at the top of the potential*, *Phys. Rev. D* **101** (2020) 115002 [arXiv:2002.02463].

[223] LIGO Scientific, Virgo collaboration, *GW190814: Gravitational Waves from the Coalescence of a 23 Solar Mass Black Hole with a 2.6 Solar Mass Compact Object*, *Astrophys. J. Lett.* **896** (2020) L44 [arXiv:2006.12611].

[224] B. Margalit and B.D. Metzger, *Constraining the Maximum Mass of Neutron Stars From Multi-Messenger Observations of GW170817*, *Astrophys. J. Lett.* **850** (2017) L19 [arXiv:1710.05938].

[225] M. Shibata, E. Zhou, K. Kiuchi and S. Fujibayashi, *Constraint on the maximum mass of neutron stars using GW170817 event*, *Phys. Rev. D* **100** (2019) 023015 [arXiv:1905.03656].

[226] A. Nathanail, E.R. Most and L. Rezzolla, *GW170817 and GW190814: tension on the maximum mass*, *Astrophys. J. Lett.* **908** (2021) L28 [arXiv:2101.01735].

[227] LIGO Scientific, Virgo collaboration, *GW170817: Observation of Gravitational Waves from a Binary Neutron Star Inspiral*, *Phys. Rev. Lett.* **119** (2017) 161101 [arXiv:1710.05832].

[228] C.E. Rhoades, Jr. and R. Ruffini, *Maximum mass of a neutron star*, *Phys. Rev. Lett.* **32** (1974) 324.

[229] V. Kalogera and G. Baym, *The maximum mass of a neutron star*, *Astrophys. J. Lett.* **470** (1996) L61 [arXiv:astro-ph/9608059].

[230] P. Brax, S. Fichet and G. Pignol, *Bounding Quantum Dark Forces*, *Phys. Rev. D* **97** (2018) 115034 [arXiv:1710.00850].

[231] J.R. Oppenheimer and G.M. Volkoff, *On massive neutron cores*, *Phys. Rev.* **55** (1939) 374.

[232] R.C. Tolman, *Relativity, Thermodynamics, and Cosmology*, Oxford, The Clarendon Press (1934).

[233] S. Weinberg, *Gravitation and Cosmology: Principles and Applications of the General Theory of Relativity*, John Wiley and Sons, New York (1972).

[234] S.R. Coleman, *The Uses of Instantons*, *Subnucl. Ser.* **15** (1979) 805.

[235] E. Witten, *Cosmic separation of phases*, *Phys. Rev. D* **30** (1984) 272.

[236] J.M. Lattimer and M. Prakash, *Neutron star structure and the equation of state*, *Astrophys. J.* **550** (2001) 426 [arXiv:astro-ph/0002232].

[237] B. Bellazzini, C. Csaki, J. Hubisz, J. Serra and J. Terning, *Cosmological and Astrophysical Probes of Vacuum Energy*, *JHEP* **06** (2016) 104 [arXiv:1502.04702].

[238] N.K. Glendenning, *Fast pulsars, strange stars: an opportunity in radio astronomy*, *Modern Physics Letters A* **05** (1990) 2197 [arXiv:https://doi.org/10.1142/S021773239000250X].

[239] J.L. Friedman, J.R. Ipser and L. Parker, *Implications of a half-millisecond pulsar*, *Phys. Rev. Lett.* **62** (1989) 3015.

[240] P. Haensel and J.L. Zdunik, *A submillisecond pulsar and the equation of state of dense matter*, *Nature* **340** (1989) 617.

[241] F. Weber and N.K. Glendenning, *Application of the Improved Hartle Method for the Construction of General Relativistic Rotating Neutron Star Models*, *Astrophysical Journal* **390** (1992) 541.

[242] G.G. Raffelt, *Astrophysical axion bounds*, *Lect. Notes Phys.* **741** (2008) 51 [arXiv:hep-ph/0611350].

[243] C.E. Rhoades and R. Ruffini, *Maximum mass of a neutron star*, *Phys. Rev. Lett.* **32** (1974) 324.

[244] J.M. Lattimer and M. Prakash, *The Equation of State of Hot, Dense Matter and Neutron Stars*, *Phys. Rept.* **621** (2016) 127 [arXiv:1512.07820].

[245] A.B. Migdal, *Pi condensation in nuclear matter*, *Phys. Rev. Lett.* **31** (1973) 257.

[246] D.B. Kaplan and A.E. Nelson, *Kaon Condensation in Dense Matter*, *Nucl. Phys. A* **479** (1988) 273c.

[247] C. Gao and A. Stebbins, *Structure of Stellar Remnants with Coupling to a Light Scalar*, arXiv:2110.07012.

[248] C.A.J. O'Hare and E. Vitagliano, *Cornering the axion with CP-violating interactions*, *Phys. Rev. D* **102** (2020) 115026 [arXiv:2010.03889].

[249] A. Bédard, P. Bergeron and G. Fontaine, *Measurements of Physical Parameters of White Dwarfs: A Test of the Mass–Radius Relation*, *The Astrophysical Journal* **848** (2017) 11.

[250] P.-E. Tremblay, N. Gentile-Fusillo, R. Raddi, S. Jordan, C. Besson, B.T. Gänsicke et al., *The Gaia DR1 mass–radius relation for white dwarfs*, *Monthly Notices of the Royal Astronomical Society* **465** (2016) 2849.

[251] H.E. Bond, R.L. Gilliland, G.H. Schaefer, P. Demarque, T.M. Girard, J.B. Holberg et al., *Hubble Space Telescope Astrometry of the Procyon System*, *The Astrophysical Journal* **813** (2015) 106.

[252] H.E. Bond, G.H. Schaefer, R.L. Gilliland, J.B. Holberg, B.D. Mason, I.W. Lindenblad et al., *The Sirius System and Its Astrophysical Puzzles: Hubble Space Telescope and Ground-based Astrometry*, *The Astrophysical Journal* **840** (2017) 70.

[253] S.G. Parsons, B.T. Gänsicke, T.R. Marsh, R.P. Ashley, M.C.P. Bours, E. Breedt et al., *Testing the white dwarf mass–radius relationship with eclipsing binaries*, *Monthly Notices of the Royal Astronomical Society* **470** (2017) 4473 [arXiv:https://academic.oup.com/mnras/article-pdf/470/4/4473/19179437/stx1522.pdf].

[254] N.P.G. Fusillo, P.-E. Tremblay, E. Cukanovaite, A. Vorontseva, R. Lallement, M. Hollands et al., *A catalogue of white dwarfs in Gaia EDR3*, *Monthly Notices of the Royal Astronomical Society* **508** (2021) 3877.

[255] Madej, J., Nalezyty, M. and Althaus, L. G., *Mass distribution of DA white dwarfs in the First Data Release of the Sloan Digital Sky Survey*, *A&A* **419** (2004) L5.

[256] Nalezyty, M. and Madej, J., *A catalogue of isolated massive white dwarfs*, *A&A* **420** (2004) 507.

[257] Koester, D. and Kepler, S. O., *Carbon-rich (DQ) white dwarfs in the Sloan Digital Sky Survey*, *A&A* **628** (2019) A102.

[258] F.M. Jimé nez-Esteban, S. Torres, A. Rebassa-Mansergas, G. Skorobogatov, E. Solano, C. Cantero et al., *A white dwarf catalogue from gaia-DR2 and the virtual observatory*, *Monthly Notices of the Royal Astronomical Society* **480** (2018) 4505.

[259] P. Bergeron, P. Dufour, G. Fontaine, S. Coutu, S. Blouin, C. Genest-Beaulieu et al., *On the measurement of fundamental parameters of white dwarfs in the Gaia era*, *The Astrophysical Journal* **876** (2019) 67.

[260] C. Genest-Beaulieu and P. Bergeron, *A comprehensive spectroscopic and photometric analysis of DA and DB white dwarfs from SDSS and Gaia*, *The Astrophysical Journal* **871** (2019) 169.

[261] M. Durant, O. Kargaltsev, G.G. Pavlov, P.M. Kowalski, B. Posselt, M.H. van Kerkwijk et al., *THE SPECTRUM OF THE RECYCLED PSR j0437–4715 AND ITS WHITE DWARF COMPANION*, *The Astrophysical Journal* **746** (2012) 6.

[262] D. Mata Sánchez, A.G. Istrate, M.H. van Kerkwijk, R.P. Breton and D.L. Kaplan, *PSR J1012+5307: a millisecond pulsar with an extremely low-mass white dwarf companion*, *Monthly Notices of the Royal Astronomical Society* **494** (2020) 4031 [arXiv:https://academic.oup.com/mnras/article-pdf/494/3/4031/33149104/staa983.pdf].

[263] Bassa, C. G., van Kerkwijk, M. H., Koester, D. and Verbunt, F., *The masses of psr j1911-5958a and its white dwarf companion*, *A&A* **456** (2006) 295.

[264] A. Arvanitaki, M. Baryakhtar and X. Huang, *Discovering the QCD Axion with Black Holes and Gravitational Waves*, *Phys. Rev. D* **91** (2015) 084011 [arXiv:1411.2263].

[265] N. Fettes, U.-G. Meissner, M. Mojzis and S. Steininger, *The Chiral effective pion nucleon Lagrangian of order p**4*, *Annals Phys.* **283** (2000) 273 [arXiv:hep-ph/0001308].

[266] E. Epelbaum, A. Nogga, W. Gloeckle, H. Kamada, U.G. Meissner and H. Witala, *Three nucleon forces from chiral effective field theory*, *Phys. Rev. C* **66** (2002) 064001 [arXiv:nucl-th/0208023].

[267] J. Ollé, O. Pujolàs and F. Rompineve, *Oscillons and Dark Matter*, *JCAP* **02** (2020) 006 [arXiv:1906.06352].

[268] S.i.P. Nunes, J.D.V. Arbañil and M. Malheiro, *The Structure and Stability of Massive Hot White Dwarfs*, *Astrophys. J.* **921** (2021) 138 [arXiv:2108.08238].

[269] S.M. de Carvalho, M. Rotondo, J.A. Rueda and R. Ruffini, *Relativistic Feynman-Metropolis-Teller treatment at finite temperatures*, *Phys. Rev. C* **89** (2014) 015801.

[270] D. Koester, *Convective Mixing and Accretion in White Dwarfs*, *aap* **52** (1976) 415.